PERFORMANCE EVALUATION OF NATURAL DRAUGHT COOLING TOWERS WITH ANISOTROPIC FILLS

by
Hanno Carl Rudolf Reuter

Thesis presented in fulfilment of the requirements for the degree
PhD in Engineering at the
University of Stellenbosch

Promoter: Prof Detlev G. Kröger
Department of Mechanical and Mechatronic Engineering

December 2010

DECLARATION

By submitting this thesis/dissertation electronically, I declare that the entirety of the work contained therein is my own, original work, and that I have not previously in its entirety or in part submitted it for obtaining any qualification.

December 2010

ABSTRACT

In the design of a modern natural draught wet-cooling tower (NDWCT), structural and performance characteristics must be considered. Air flow distortions and resistances must be minimised to achieve optimal cooling which requires that the cooling towers must be modelled two-dimensionally and ultimately three-dimensionally to be optimised. CFD models in literature are found to be limited to counterflow cooling towers packed with film fill, which is porous in one direction only and generally has a high pressure drop, as well as purely crossflow cooling towers packed with splash fill. This simplifies the analysis considerably as the effects of flow separation at the air inlet are minimised and fill performance is determined using the method of analysis originally employed to determine the fill performance characteristics from test data. Many counterflow cooling towers are, however, packed with trickle and splash fills which have anisotropic flow resistances, which means the fills are porous in all flow directions and thus air flow can be oblique through the fill, particularly near the cooling tower air inlet. This provides a challenge since available fill test facilities and subsequently fill performance characteristics are limited to purely counter- and crossflow configuration.

In this thesis, a CFD model is developed to predict the performance of NDWCTs with any type of spray, fill and rain zone configuration, using the commercial code *FLUENT*®. This model can be used to investigate the effects of different: atmospheric temperature and humidity profiles, air inlet and outlet geometries, air inlet heights, rain zone drop size distributions, spray zone performance characteristics, variations in radial water loading and fill depth, and fill configurations or combinations on cooling tower performance, for optimisation purposes. Furthermore the effects of damage or removal of fill in annular sections and boiler flue gas discharge in the centre of the tower can be investigated.

The CFD modelling of NDWCTs presents various options and challenges, which needed to be understood and evaluated systematically prior to the development of a CFD model for a complete cooling tower. The main areas that were investigated are: spray and rain zone performance modelling by means of an Euler-Lagrangian model; modelling of air flow patterns and flow losses; modelling of fill performance for oblique air flow; modelling of air pressure and temperature profiles outside and inside the cooling tower.

The final CFD results for the NDWCT are validated by means of corresponding one-dimensional computational model data and it is found that the performance of typical NDWCTs can be enhanced significantly by including protruding platforms or roundings at the air inlet, reducing the mean drop size in the rain zone, radially varying the fill depth and reducing the air inlet height.

Keywords:

Wet-cooling tower, Merkel, natural draught, CFD, inlet losses, rain, spray, drops, optimisation.

SAMEVATTING

By die ontwerp van ‘n moderne natuurlike trek nat koeltoring (NTNK), moet strukturele en werkverrigtings eienskappe in ag geneem word. Wanverdeelde lugvloei en vloeiweerstande moet geminimaliseer word om optimale verkoeling te bewerkstellig, wat vereis dat die koeltorings twee-dimensioneel en uiteindelik driedimensioneel gemodelleer moet word om hulle te kan optimeer. Dit is gevind dat berekeningsvloeidinamika (BVD of “CFD” in engels) modelle in die literatuur, beperk is tot teenvloei koeltorings gepak met film tipe pakking, wat net in een vloeirigting poreus is en boonop gewoonlik ook ‘n hoë drukval het, sowel as suiwer dwarsvloei koeltorings met spatpakking. Hierdie vergemaklik die analise aansienlik omdat die effekte van vloeiwegbreking by die luginlaat verklein word en die pakking se werkverrigtingsvermoë bereken kan word met die analise metode wat oorspronklik gebruik is om die pakkingseienskappe vanaf toets data te bepaal. Baie teenvloei koeltorings het egter drup- (“trickle”) of spatpakkings met anisotropiese vloeiweerstand, wat beteken dat die pakking poreus is in alle vloeirigtings en dat die lug dus skuins deur die pakking kan vloei, veral naby die koeltoring se lug inlaat. Hierdie verskaf ‘n uitdaging aangesien beskikbare pakking toetsfasiliteite, en dus ook pakking karakteristieke, beperk is tot suiwer teenvloei en dwarsvloei konfigurasie.

‘n BVD model word in hierdie tesis ontwikkel wat die werkverrigtingsvermoë van NTNK’s kan voorspel vir enige sproei, pakking en reënsone konfigurasie deur van die kommersiële sagteware *FLUENT*® gebruik te maak. Hierdie model kan gebruik word om die effekte van verskillende: atmosferiese temperatuur- en humiditeitsprofiele, lug inlaat en uitlaat geometrië, lug inlaat hoogtes, reënsone druppelgrootteverdelings, sproeisone werkverrigtingskarakteristieke, variasie in radiale waterbelading en pakking hoogte, en pakking konfigurasies of kombinasies op koeltoringvermoë te ondersoek vir optimerings doeleindes. Verder kan die effekte van beskadiging of verwydering van pakking in annulêre segmente, en insluiting van ‘n stoomketel skoorsteen in die middel van die toring ondersoek word.

Die BVD modellering van NTNK bied verskeie moontlikhede en uitdagings, wat eers verstaan en sistematies ondersoek moes word, voordat ‘n BVD model van ‘n algehele NTNK ontwikkel kon word. Die hoof areas wat ondersoek is, is: sproei- en reënsone modellering mbv ‘n Euler-Lagrange model; modellering van lugvloeipatrone en vloeiverliese; modellering van pakking verrigting vir skuins lugvloeie; modellering van lugdruk- en temperatuurprofiele buite en binne in die koeltoring.

Die BVD resultate word mbv van data van ‘n ooreenstemmende eendimensionele berekeningsmodel bevestig en dit is bevind dat die werkverrigting van ‘n tipiese NTNK beduidend verbeter kan word deur: platforms wat uitstaan of rondings by die luginlaat te installeer, die duppelgrootte in die reënsone te verklein, die pakkingshoogte radiaal te verander, en die luginlaathoogte te verlaag.

Sleutelwoorde: Nat koeltoring, Merkel, natuurlike trek, BVD, inlaatverliese, reën, sproei, druppels, optimering.

Dedicated to

Ilse

Ingo, Luca and Sabine

ACKNOWLEDGEMENTS

Thank you my heavenly Father for all the blessings bestowed upon me, for giving me the opportunities, ability, health, strength and perseverance to complete this thesis.

My promoter Prof. Detlev Kröger, for incredible guidance, support, friendship, patience, and countless discussions. I had the opportunity of a lifetime to learn from the best, for which I am eternally grateful.

GEA, NRF Thrip, NRF Thuthuka, Stellenbosch University Sub-committee B, and Eskom for their financial support.

My wife and best friend, Ilse, for her unconditional love and support.

My children, Ingo, Luca and Sabine, for being my pride and joy.

My parents, for their eternal love and support.

Cobus Zietsman for his friendship and help with the experimental work.

All the students, who contributed towards certain aspects of this thesis.

My family and friends for their interest and support.

TABLE OF CONTENTS

LIST OF FIGURES

LIST OF TABLES

LIST OF SYMBOLS

A	Area, m^2, or coefficient
a	Surface area per unit volume, m^{-1}, or coefficient
B	Breadth, m, or coefficient
b	Coefficient, or exponent
b_T	Temperature inversion exponent
C	Coefficient, loss coefficient matrix, correction factor, or heat capacity rate mc_p, W/K
c	Specific heat, J/kgK, concentration, kg/m^3, coefficient, or constant
c_F	Friction factor
c_N	Constant for turbulence level
c_p	Specific heat at constant pressure, J/kgK
c_v	Specific heat at constant volume, J/kgK
D	Diffusion coefficient, m^2/s
$DALR$	Dry adiabatic lapse rate, K/m
d	Diameter, m, or coefficient
E	Aspect ratio
e	Effectiveness
F	Force, N
f	Function
G	Mass velocity, kg/m^2s, gas mass velocity, kg/m^2s
g	Gravitational acceleration, m/s^2
g_{YS}	Nusselt and Sherwood number correction factor
H	Height, m
h	Heat transfer coefficient, W/m^2K
h_D	Mass transfer coefficient, m/s
h_d	Mass transfer coefficient, kg/m^2s
i	Unit vector in the x-direction, enthalpy, J/kg, or equation number
i_{fg}	Latent heat, J/kg
j	Unit vector in the y-direction
K	Loss coefficient, or constant
k	Unit vector in the z-direction, or thermal conductivity, W/mK
L	Length, m, or height, m, liquid mass velocity, kg/m^2s
LS	Left side
l	Characteristic length
M	Mass, kg, or molecular weight, kg/mole
m	Mass flow rate, kg/s
N	Unit number, units
NTU	Number of transfer units
n	Number of units, units, or unit rate, units/s
P	Power, W
p	Pressure, N/m^2 or Pa
Q	Volume flow rate, m^3/s, or heat transfer rate, W
q	Heat flux, W/m^2
R	Gas constant, J/kgK, or cumulative mass fraction,
RS	Right side
Ry	Characteristic flow parameter, m^{-1}
r	Radial coordinate, m, or radius, m

S	Source term
s	Displacement, m
T	Temperature, °C or K
Tu	Turbulence level
t	Time, s, or thickness, m
u	Internal energy, J/kg, or Cartesian velocity component
V	Volume flow rate, m^3/s, molecular volume, $m^3/kmol$, or volume, m^3
v	Velocity, m/s, or Cartesian velocity component, m/s
W	Work, J, or width, m
w	Humidity ratio, kg water vapor/ kg dry air, or Cartesian velocity component, m/s
X	Adjustment factor, or cross-to-counterflow Merkel number ratio
x	Spacial coordinate, m
y	Spacial coordinate, m
y^+	Dimensionless coordinate
z	Spacial coordinate, m, or elevation, m, or exponent

Greek Symbols

α_e	Kinetic energy coefficient
Δ	Differential
δ	Thickness, differential, or deviation
ε	Dissipation rate of turbulent kinetic energy
θ	Angle, °
η	Efficiency
μ	Dynamic viscosity, kg/ms
ν	Kinematic viscosity, m^2/s
ξ_T	Temperature lapse rate, K/m
ρ	Density, kg/m^3
$\Sigma\Delta$	Constant
σ	Surface tension, N/m
τ	Shear stress, N/m^2
Φ	Angle, °
φ	Angle, °
ϕ	Shape factor, relative humidity, or property
ψ	Angle, °

Dimensionless Groups

Eo	Eotvos number, $gd^2(\rho_w-\rho_a)/\sigma_d$
Fr_D	Desimetric Froude number, $\rho v^2/(\Delta\rho dg)$
Le	Lewis number, $k/(\rho c_p D)$, or Sc/Pr
Le_f	Lewis factor, $h/(c_p h_d)$
Me	Merkel number, $h_d a_{fi} L_{fi}/G_w$
Nu	Nusselt number, hL/k
Pr	Prandtl number, $c_p\mu/k$
Re	Reynolds number, $\rho vL/\mu$
Sc	Schmidt number, $\mu/(\rho D)$
Sh	Sherwood number, $h_D L/D$

Subscripts

A	Air, species
abs	Absolute
annulus	Annulus
atm	Atmospheric
b	Species
B	Buoyancy
BC	Boundary condition
bucket	Bucket
c	Convection heat transfer, condensing, or critical
cc	Correction cell
core	Core
counter	Counterflow
cross	Crossflow
ct	Cooling tower
ctc	Cooling tower contraction
cte	Cooling tower expansion
cup	Cup
D	Drag, diffusion
d	Drop, diffusion, drag, or discharge
da	Dry air
db	Dry bulb
de	Drift eliminator
dif	Diffuser
draft	Draught
e	Energy, effective, expansion
evap	Evaporation
f	Liquid, friction, or film
fi	Fill
fr	Frontal
fs	Fill support
G	Gravity
g	Gravitational acceleration, m/s^2, Gas
gross	Gross
he	Heat exchanger
ITD	Initial temperature difference, ºC
i	Step or increment number, inlet, index
j	Index
LHS	Left hand side
losses	Losses
LS	Left side
Me	Merkel theory
Max	Maximum
m	Mean, or mass transfer
max	Maximum
min	Minimum
mom	Momentum
net	Net

norz	No rain zone
o	Outlet, initial, or reference at 0 ºC
r	Radial coordinate
p	Platform
q	Heat source
RHS	Right hand side
RS	Right side
RR	Rosin Rammler
Ref	Reference
Res	Residence
rz	Rain zone
s	Saturation, shell, or surface
sep	Separation point
sp	Spray
sphere	Sphere
ss	Supersaturated
T	Terminal
TTD	Terminal temperature difference
t	Total, turbulence
total	Total
ts	Tower support
up	Upstream
v	Vapour
vc	Vena contracta
w	Water
wb	Wetbulb
wd	Water distribution system
x	Coordinate
y	Coordinate
z	Coordinate, variable

Superscripts

t	Timestep

Abbreviations

ADL	Adiabatic lapse rate
CFD	Computational fluid dynamics
CT	Cooling tower
DALR	Dry adiabataic lapse rate
DPM	Discrete phase model
EM	Expanded metal
HP	High pressure
IP	Intermediate pressure
LP	Low pressure
NDWCT	Natural draught wet-cooling tower
UDF	User defined function
UDM	User defined memory

1. INTRODUCTION

1.1 NATURAL DRAUGHT WET-COOLING TOWERS

Natural draught wet-cooling towers (NDWCTs) are used mainly in power plants and in some industries to reject large quantities of waste heat from re-circulating cooling water, which serves as a transport medium for heat transfer between the source and the sink, to the atmosphere. Figure 1.1 shows a schematic of a counterflow NDWCT used to reject heat from a water-cooled condenser (WCC) of a steam turbine.

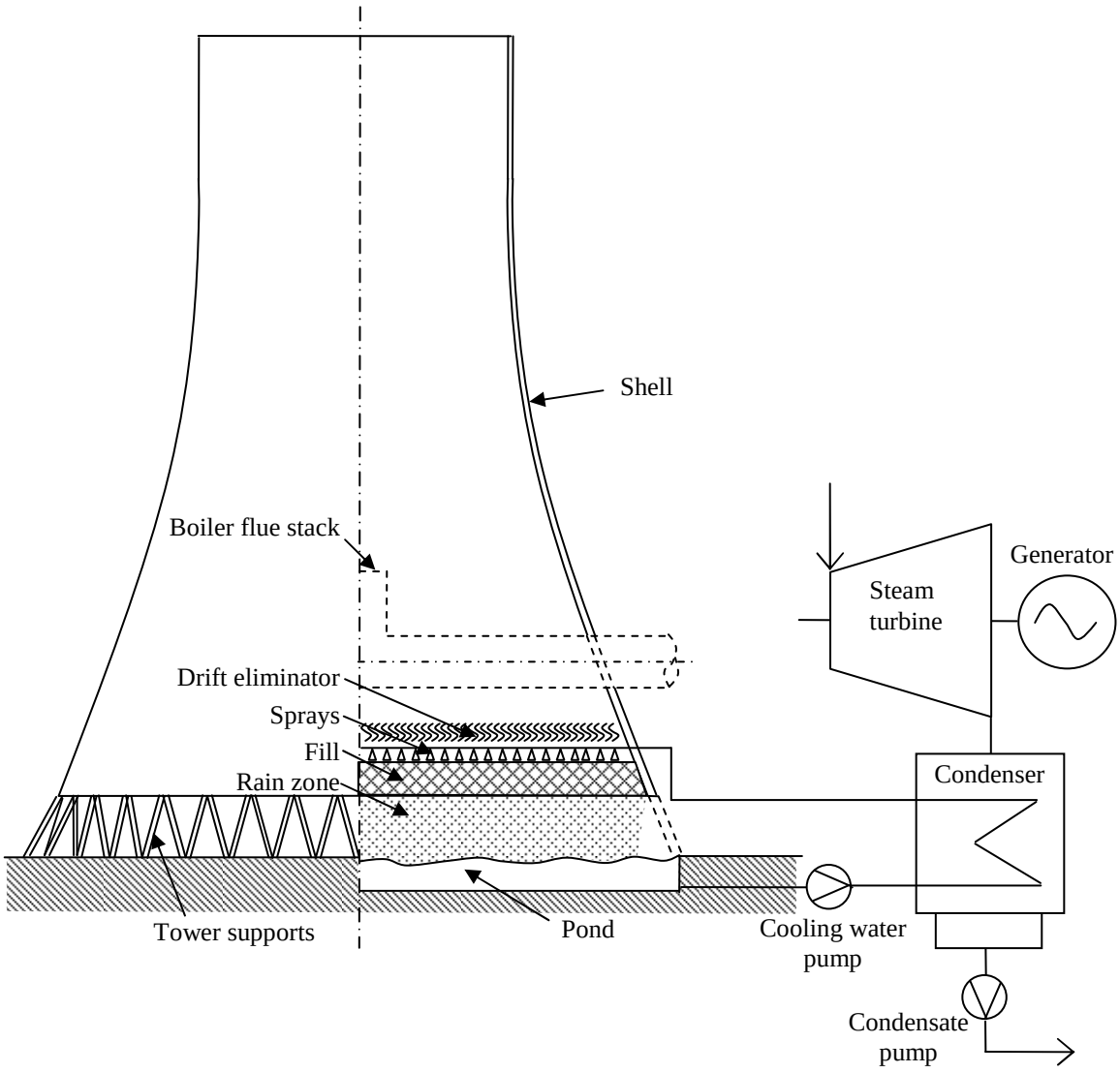

Figure 1.1 : Schematic of a wet-cooling system for a steam turbine comprising a counterflow natural draught wet-cooling tower (NDWCT) and a water-cooled condenser (WCC).

Wet steam from the steam turbine exhaust is condensed into liquid in a surface or shell-and-tube condenser, to allow it to be pumped back to the boiler. The latent heat removed from the steam is transferred to re-circulating cooling water passing through tubes in the condenser. The heated cooling water leaving the condenser is pumped to the cooling tower where it is sprayed uniformly onto a fill or packing material by means of a water distribution system consisting of a grid of spray nozzles. Depending on the type of nozzle, the water is sprayed either up- or downwards with spray patterns of adjacent nozzles generally overlapping. The water then either splashes trickles or runs as a water film through the fill, depending on the type of fill used, and eventually falls freely under gravity through a rain zone into a pond from which it is pumped back to the condenser.

In the cooling tower, sensible and latent heat is transferred from the cooling water to an airstream by means of convection heat transfer and diffusion mass transfer. The purpose of the fill is to enhance the heat and mass transfer by increasing the interfacial transfer area between the water and the air, in direct contact with each other. This is achieved by breaking the water up into smaller drops and retarding the flow, or by spreading the water into thin films on vertical plastic or fibre cement sheets, depending on the type of fill. The factors influencing the choice of fill are its heat transfer performance, operating temperature, quality of water, pressure drop, cost, and durability.

The rain zone performance is dependent on the mean drop size, the rain zone height and the speed and direction of the air flowing through it, which depend on the type of fill and cooling tower design configuration. The air flow is induced by buoyancy in the tall cooling tower shell, due to a density difference between the warm moist air inside and the cold dry air outside the tower. Air enters the tower through the air inlet at the bottom, passing over the fill in either counterflow (Fig. 1.1) or crossflow (Fig. 1.2) configuration, before exiting at the top as a plume of supersaturated warm air. Small drops of cooling water, entrained into the air in the fill region, are removed by means of downstream drift eliminators, to reduce water losses and harmful substances in the cooling water from leaving the cooling tower.

In modern power plants, the boiler flue stack is often located inside the cooling tower to achieve better dispersion of the flue gas. Additional flow losses are partially overcome by the additional flow driving potential due to the higher temperature and speed of the flue gas at the stack outlet.

Wet-cooling tower technology is generally preferred to dry-cooling systems such as mechanical draught direct air-cooled steam condensers or indirect natural draught dry-cooling towers in areas where there is sufficient make-up water and where the highly visible vapour plumes are tolerated by the surrounding communities. This is because the capital costs are known to be significantly lower and power plant efficiencies are higher due to lower steam turbine exhaust pressures and lower auxiliary power consumption.

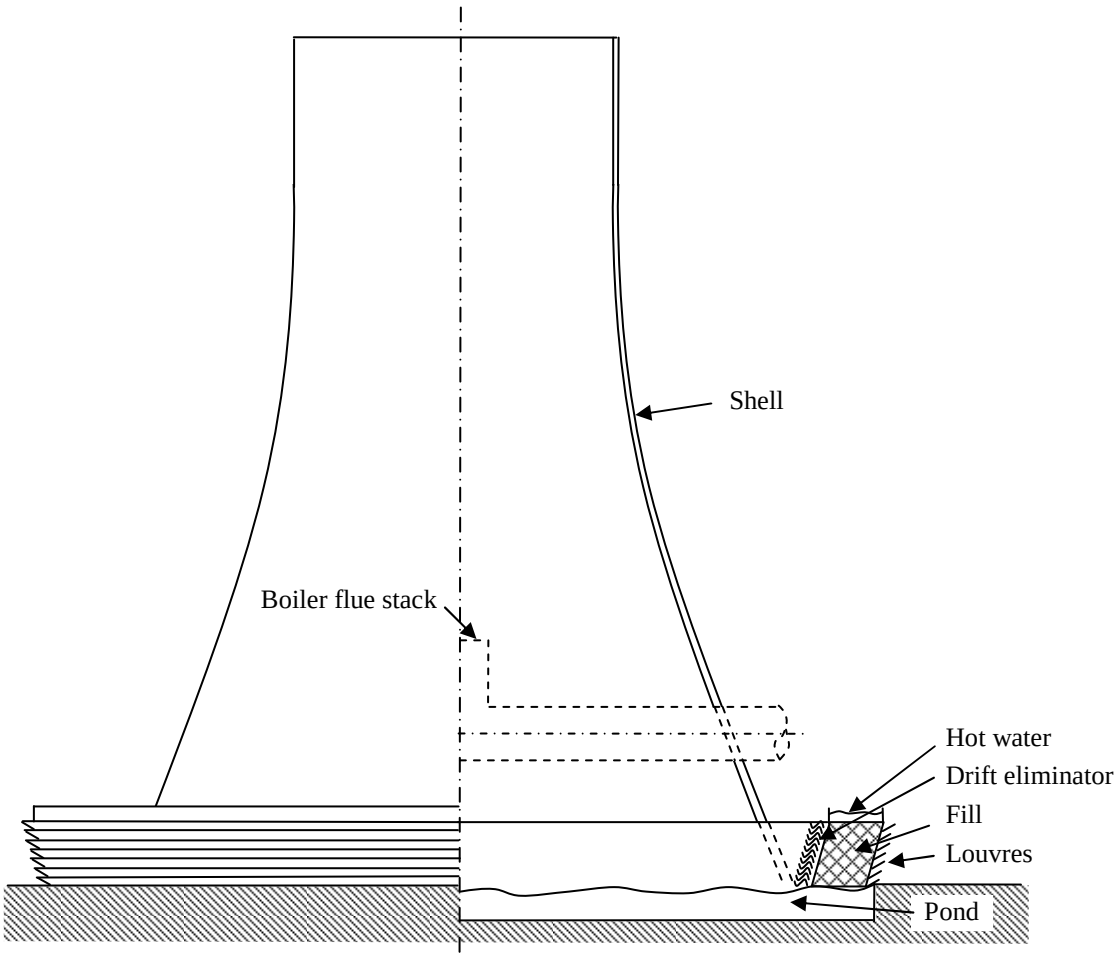

Figure 1.2 : Schematic of a crossflow NDWCT (Kröger, 2004).

From experience, the main suppliers of cooling tower technology make use of simplified one-dimensional computational models for the design of NDWCTs. These models utilise basic models to account for the air flow driving potential and flow losses, and the spray, fill and rain zone transfer characteristics are determined from experimental data measured in counter- and/ or crossflow fill test facilities according to the Merkel (1925), Poppe (Poppe and Rögener, 1991) or e-NTU (Jaber and Webb, 1989) methods of analysis. These one-dimensional models do not take variation of air velocity through the cooling tower into account and therefore do not represent the fluid dynamics and thus the heat and mass transfer processes in a cooling tower accurately. These models can therefore essentially be described as performance adjustment tools, used to scale historical performance acceptance test data of similar existing cooling tower designs in order to predict the performance of new cooling tower designs. Since such practice requires dimensional similitude between the old and new designs, the basic design configuration of cooling towers has remained virtually unchanged over the past decades. Recent developments in computational fluid dynamics (CFD) and continuous improvements in computer technology have, however, now

made it possible to simulate the flow patterns and heat and mass transfer of cooling towers three-dimensionally, allowing for the investigation and optimisation of three-dimensional effects on cooling tower performance.

For a typical modern coal fired power plant, the gross efficiency can be increased by almost $\Delta\eta_{gross}$ = 1 % by reducing the steam turbine exhaust/ condenser temperature by ΔT_{cond} = 3 ºC, which also results in a reduction in condenser heat load of $\Delta Q_{cond}/ Q_{cond}$ x 100 % = 0.8 %, as presented in Appendix R.

To illustrate how such an improvement can be achieved in practice, consider Fig. 1.3 showing a typical T versus ($|Q|/ Q_{cond}$) graph for a wet-cooling system, where the absolute normalised heat transfer ($|Q|/ Q_{cond}$) is calculated from a common physical starting point location. For a wet-cooling system, the common starting point is taken to be the cooling water inlet to the condenser or the cooling water outlet of the cooling tower, which are assumed to be the same. These graphs are effective for determining the heat transfer potential in heat exchangers.

From psychrometrics, there needs to be a difference between the cooling water temperature and the air wet-bulb temperature for heat and mass transfer to take place in a wet-cooling tower. Similarly, from the principles of convection, a temperature difference is necessary for heat transfer to take place from the steam to the cooling water in the condenser. From Fig. 1.3 it can be seen that to obtain a lower steam temperature for a given ambient wet-bulb temperature ($T_{wb,amb}$), the initial temperature difference (ΔT_{ITD}) and the approach (ΔT_{app}) can be reduced. This can possibly be achieved by increasing the performance of the cooling system, by: increasing the heat transfer surface area in the condenser, increasing the size (diameter and shell height) of the cooling tower, increasing the fill volume in the cooling tower, installing more effective fill material, reducing the flow losses, improving the rain zone performance and/ or by increasing the cooling water mass flow rate, hereby reducing the cooling range (ΔT_{cw}).

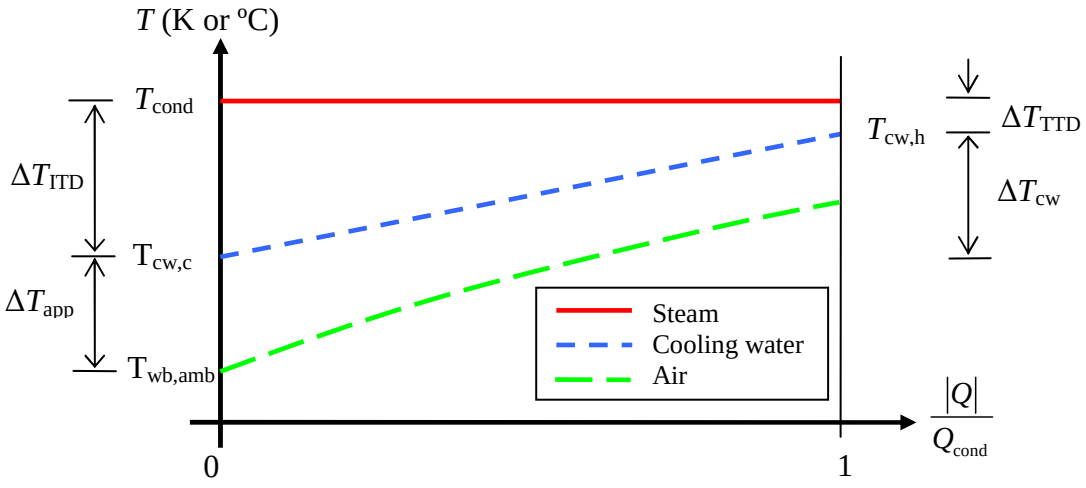

Figure 1.3 : Schematic *T*-|*Q*| graph for a wet-cooled power plant cooling system.

The recent CFD work published on NDWCT performance (Al-Waked, 2006, 2007, 2010, Williamson, 2008a, 2008b, 2008c, and Klimanek, 2008, 2009, 2010), all made use of the commercial CFD code *FLUENT*®. Al-Waked and Williamson applied the Euler-Lagrangian model with species transport to simulate the rain zone, whereas Klimanek used the Euler-Euler multiphase model. These NDWCT models, however, are limited to cooling towers packed with film or orthotropic fills, which are porous in one direction only and have relatively high loss coefficients. This simplifies the numerical analysis considerably due to reduced flow separation at the air inlet and vertical flow through the fill, which can be modelled by means of the simple Merkel (1925) or Poppe (1991) methods of analysis using available fill characteristics. Many cooling towers are, however, packed with trickle and splash fills which have anisotropic flow resistances, which means that the fills are porous in all flow directions and thus air flow can be oblique through the fill, especially near the cooling tower air inlet where the flow turns through about 90º inside the fill after it has entered the tower. An improved model is therefore required with which the performance of NDWCTs packed with any type of fill can be investigated and optimised.

1.2 THESIS OBJECTIVES

In order to develop an improved NDWCT performance model and investigate various alternatives for improving cooling tower performance, the main objectives of this thesis are therefore to:

- ⇨ Gain a better understanding of the modelling options and capabilities of the commercial CFD code *FLUENT*®, and to find optimal methods to calculate the inlet flow losses, thermal performance of the rain, fill and spray zones, and flow driving potential by investigating each separately and comparing the results of different case studies to analytical, numerical, and/ or experimental data.
- ⇨ Develop a one-dimensional computational model to predict NDWCT performance based on Example 7.3.2 in Kröger (2004).
- ⇨ Develop a two-dimensional axisymmetric *FLUENT*® model based on the same design specification as in Example 7.3.2 in Kröger (2004).
- ⇨ Compare the *FLUENT*® and one-dimensional model results obtained for different cooling tower inlet and outlet geometries, inlet heights, rain zone drop diameters and fill types.
- ⇨ Investigate the effects of radially variable water mass velocities and fill heights on NDWCT performance using the new *FLUENT*® model.
- ⇨ Make recommendations on the enhancement of cooling tower performance.

1.3 MOTIVATION

Global warming, which is attributed to elevated concentrations of greenhouse gases in the atmosphere due to the combustion of fossil fuels, is believed to be the main reason for the increasing occurrence and severity of wild fires, heat waves, droughts, hurricanes, floods, and the melting of the polar ice caps and glaciers. This provides sufficient proof that climate change is taking place. The higher concentrations of CO_2, CH_4, NO_x and SO_x also result in higher acidity levels in sea and rain water which has a negative impact on sea and plant life and the general environment. The Kyoto Protocol, initially adopted in 1997, was signed and ratified by 187 states to fight global warming, entering into force in 2005. Under this legally binding protocol, 37 industrialised countries committed themselves to reduce greenhouse and ozone depleting gas emissions by 5.2 % from 1990 levels by the year 2012. The reductions are to be achieved by means of economic incentives through the employment of mechanism such as: international emissions trading (IET), where companies/ countries not meeting their emissions targets trade credits with those who are emitting less than their allowance; clean development mechanism (CDM), where industrialised countries can invest in emission reduction wherever it is cheapest globally; and joint implementation (JI), where in principle existing technology is replaced by improved technology.

In the past, the performance/ efficiency of a power plant was generally the outcome of a design optimisation where the objective was to maximise revenue/ profit while minimising the capital costs to reduce financial risk. Due to the stringent emissions reduction targets of the Kyoto Protocol, ever rising demand for electricity, the higher capital costs due to the current extreme demand for power plants, and higher operating costs due to diminishing fuel and water resources, the focus has shifted towards minimising the power plant life cycle costs (capital, operation, maintenance, and decommissioning costs) while maximising power plant efficiency. This current situation and the significant potential to improve power plant efficiency by improving cooling tower performance and life cycle costs, clearly motivates the research and development of new improved cooling tower technology.

1.4 THESIS OUTLINE

1.4.1 CHAPTER 1

Chapter 1 presents a broad overview of NDWCTs and how they affect power plant performance. The basic terminology and operation of natural draught counter- and crossflow wet-cooling towers used to reject waste heat from steam driven power plants are explained. The objectives and motivation of the thesis are discussed and the thesis outline is presented.

1.4.2 CHAPTER 2

Chapter 2 investigates and discusses the options and capabilities of *FLUENT*® to model: rain and spray zone performance, inlet flow patterns and losses, fill performance, and flow driving potential in order to develop an optimal model to predict the overall performance of natural draught wet-cooling towers.

1.4.3 CHAPTER 3

Chapter 3 discusses the *FLUENT*® CFD model developed in this thesis to predict NDWCT performance and presents a summary of the results obtained for various geometrical changes, changes in mean rain zone drop diameter, compared to one-dimensional model results, and radial variations in water loading and fill height.

1.4.4 CHAPTER 4

Chapter 4 discusses how the main objectives of the thesis were achieved, and gives a summary of all the conclusions drawn and main recommendations made. Finally the ongoing work and research recommended for the future are discussed.

1.4.5 APPENDICES

Most of the research, development and presentation of theoretical and analytical models, equations and computational models are presented in the appendices. Most appendices are self-contained chapters with results and conclusions. The most important results of the appendices are summarised and presented in the main chapters of the thesis while the details of calculations and the methods followed are presented in the appendices.

Comment

In the numerical examples, given in the appendices, values are often given to a large number of decimal places. These numbers are usually as given directly by the computer program output and do not necessarily imply a corresponding degree of accuracy.

2. EVALUATION OF VARIOUS *FLUENT*® MODELS APPLICABLE TO WET-COOLING TOWER PERFORMANCE

2.1 INTRODUCTION

The numerical modelling of natural draught wet-cooling towers (NDWCTs) under no crosswind conditions, using *FLUENT*®, presents various options and challenges, which need to be understood and therefore investigated systematically before developing an overall CFD model for calculating NDWCT performance. These main areas to be investigated are summarised as follows:

a) Spray and rain zone performance modelling by means of an Euler-Lagrangian model. The relevant theory, modelling options and input data required, and different methods to deal with polydisperse drop distributions need to be investigated. Ultimately, a standard modelling procedure is required to predict rain and spray zone performance from measured drop size and flow distribution data.

b) Modelling of air flow patterns and flow losses. Different turbulence models can be used to model inlet flow losses and flow separation at the cooling tower (CT) inlet, which need to be evaluated by comparing the results obtained for different inlet geometries, fill resistances and flow conditions to corresponding experimental data.

c) Modelling of fill performance for oblique air flow. Fill test facilities are limited to counter- and crossflow configurations only, where the air flow is vertical and horizontal respectively. No data therefore exists for cross-counterflow configurations where the airflow is oblique, such as encountered at the CT air inlet. A model must therefore be developed to predict the performance of fills in cross-counterflow configuration and to evaluate fill performance characteristics from experimental data.

d) Modelling of air pressure and temperature profiles outside and inside the cooling tower. The input data required for the flow domain inlet boundary depends on the capabilities of *FLUENT*® to model the atmospheric compression of the air as it descends towards the inlet before entering the cooling tower. Furthermore, the expansion of supersaturated air inside the cooling tower and the condensation of vapour results in a difference in the change in temperature and pressure with elevation compared to outside. This affects the flow driving potential and thus needs to be investigated in order to model the air inlet flow and draught through the cooling tower accurately.

Figure 2.1 shows a temperature contour plot on the left and an air pathline plot on the right of the CT centreline, and illustrates the locations of the above points, which are discussed in the following sections.

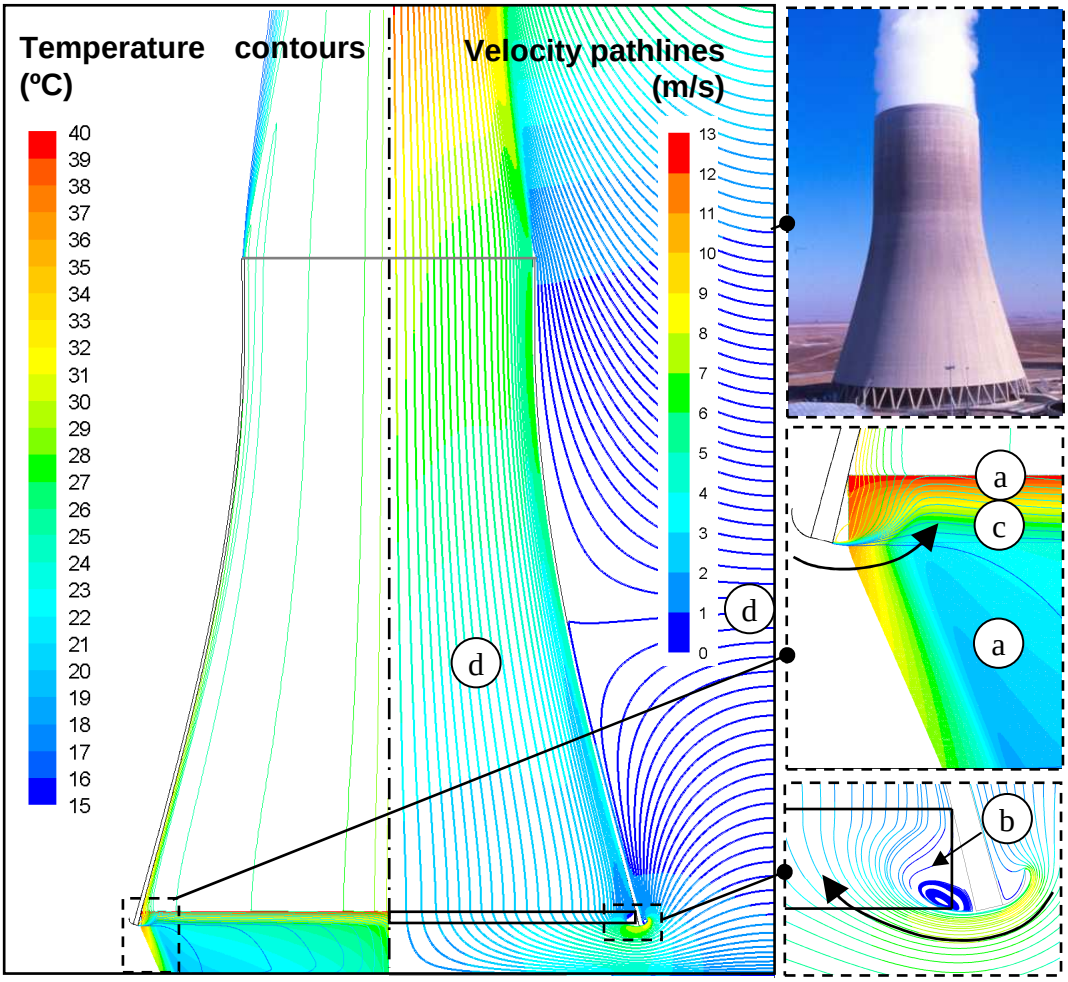

Figure 2.1 : Contour and pathline plots of a natural draught wet-cooling tower to illustrate the regions inside a cooling tower which need to be investigated independently.

2.2 EULER-LAGRANGIAN MODELLING OF SPRAY AND RAIN ZONE PERFORMANCE

Al-Waked (2006, 2007, 2010) and Williamson [2008a, 2008b, 2008c] both made use of the Euler-Lagrangian model, also referred to as the Lagrangian discrete phase model (DPM), to calculate rain and spray zone performance, whereas Klimanek (2008, 2009, 2010) employed the computationally more expensive Euler-Euler multiphase model.

For this thesis, the Euler-Lagrangian model is preferred mainly because it is applicable for both steady and unsteady flow solutions, it is computationally less expensive than the Euler-Euler multiphase model, and provides the flexibility to change the drag, and heat and mass transfer coefficient relations if required. Due to the various alternative options available in *FLUENT*® for the modelling of

spray and rain zone performance, a good understanding of the governing equations, numerical methods, available modelling options, and input data of the Euler-Lagrangian model is required in order to establish an optimal modelling approach and procedure. The independent studies to verify the results and determine the best modelling approach are discussed below.

2.2.1 Numerical analysis of motion and cooling of a single drop falling through a constant velocity air-stream (Appendices B and C)

Firstly, a numerical model was developed for calculating the motion path of a single drop injected into an air-stream and the specific loss coefficient of spray/ rain along a given trajectory, as presented in Appendix B. The model is utilised to verify corresponding *FLUENT*® results and data from literature and to investigate the suitability of the drag models available in *FLUENT*® for the modelling of spray and rain zones. Furthermore, for the design of spray nozzles and analysis of spray zone performance, the effects of the variation of drop diameter, air speed, drop injection speed, and in specific cases drop injection angle on the drop trajectory, horizontal travel distance, drop residence time, specific loss coefficient, maximum spray radius, and maximum radius injection angle, to a given vertical distance below the injection point, are investigated.

For counterflow rain zones, the effects of drop diameter on drop speed, Reynolds number, residence time, and the specific rain zone loss coefficient are investigated for different drop path lengths, air speeds, and initial drop speeds. For crossflow rain zones, the effects of drop diameter and air speed on the horizontal drop displacement, and drop diameter and flow angle on the specific loss coefficient are examined.

The drag models available in the steady flow solver of *FLUENT*® are found to be deficient for rain zone modelling and therefore it is a recommendation that Eq. (B.12), proposed by Dreyer (1994) for accelerating drops with deformation, should be implemented. Equivalent single drop loss coefficient were found to deviate by about 5 % from the values predicted by De Villiers and Kröger (1997) (Eq. B.21) for drop sizes of $d \geq 4$ mm, path lengths of $z_d > 3.5$ m, and atmospheric pressures of $85\,000 \leq p_a \leq 101\,325$ N/m^2. A maximum deviation of 15 % was observed for a drop diameter of d = 2 mm.

To investigate the cooling of a single drop, the numerical drop motion model in Appendix B was extended to include heat and mass transfer, as presented in Appendix C. The model is utilised to verify equivalent *FLUENT*® results and to evaluate the effects of different heat and mass transfer coefficient, diffusion coefficient, Lewis factor, and rate of mass transfer models from literature on drop temperature change and rain zone Merkel number, and data from literature, and to generate useful data for the design of spray nozzles and rain zones. It can be concluded that the Ranz and Marshall (1952) relations for the heat and mass transfer coefficient (Eqs C.12 and C.22) and Eq. (C.5) for determining the rate of mass transfer employed by *FLUENT*®, give conservative results. Furthermore, Eq. (C.42) by Fuller (VDI Wärmeatlas, 2006) and Eq. (B.12) by Dreyer (1994)

should be used for determining the diffusion and drag coefficients respectively. The Lewis factor according to Eq. (C.33) by Bosnjakovic (1960) is found to result in better cooling than the assumption of Merkel (1925) that $Le_f = 1$.

For spray zones, the effects of drop diameter, injection angle and injection speed on drop temperature change and the spray Merkel number are investigated for a given spray zone height, whereas for counter- and crossflow rain zones, the effects of drop diameter on drop temperature change and Merkel number are investigated for different drop path lengths.

The thermophysical properties in *FLUENT*® can be input as polynomial functions. It was found that the drop cooling results are very sensitive to the saturated vapour pressure goodness-of-fit, as *FLUENT*® reduces the coefficients to 7 significant digits, which for higher order polynomials results in significant inaccuracies.

A comparison between single drop Merkel number data and corresponding data generated using the De Villiers (1997) model (Eq. C.40) reveals that for drop diameters of d > 4 mm, the deviation is about 10 % for an atmospheric pressure of p_a = 101 325 N/m^2 and 5 % for p_a = 85 000 N/m^2. For smaller drop sizes $2 \leq d_d \leq 4$ mm, the deviation is seen to be almost 20 %, ascribed to poor curve-fitting.

Figure 2.2 is a graph of the ratio between counterflow rain zone Merkel number and specific loss coefficient plotted against rain zone height for different Sauter mean drop diameters, based on the data of Figs B.11(h) and C.6(c). This graph shows a net improvement in rain zone performance characteristics with a decrease in drop diameter.

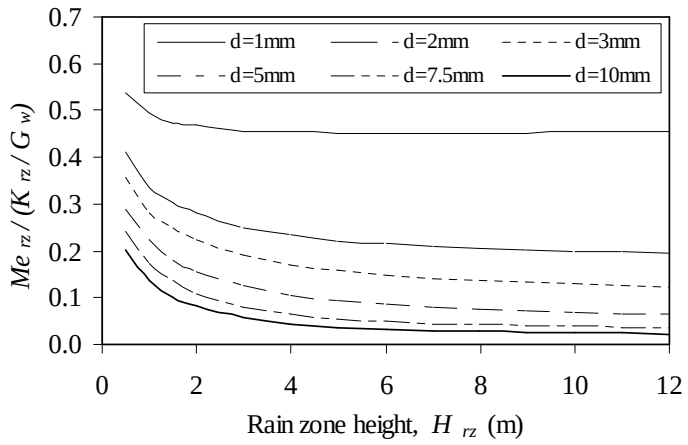

Figure 2.2 : Ratio of Merkel number to specific loss coefficient plotted for different rain zone heights and drop diameters.

2.2.2 Analytical equations for motion and cooling of a single drop falling through a vertical air-stream (Appendices D to G)

In order to gain a better understanding of the physics of counterflow rain zones and the relation of drop motion to variation in drop diameter, air speed, drop injection speed and thermophysical properties in counterflow rain zones, analytical equations are derived in Appendix D for determining absolute drop speed (Eq. D.22), drop path length (Eq. D.25), drop volume fraction (Eq. D.33), void fraction (Eq. D.34), and specific loss coefficient (Eq. D.37). Similarly, analytical equations for single drop temperature change (Eq. E.23) and Merkel number (Eq. E.34) are derived in Appendix E. Important outcomes of this investigation are that the loss coefficient and Merkel number are strong functions of drop diameter and drop residence time, where a reduction in drop diameter results in an increase in Merkel number and specific loss coefficient, however with a significant net gain in thermal performance as shown in Fig. 2.2. The analytical equations in Appendix D and E, however, were considered too elaborate. Simpler analytical equations were therefore derived for the Merkel number and loss coefficients of counterflow rain zones with drops falling at terminal speed, for the extreme cases of constant drag coefficient, applicable to large drops, and Stokes law for low Reynolds number of $Re < 0.5$ applicable to very small drops, as presented in Appendix F. The resultant Merkel number equations (Eqs F.11 to F.13 and F.17 to F.19) expressed in terms of thermophysical properties and fundamental independent variables, reveal that the rain zone Merkel number is independent of water mass velocity but is dependent on atmospheric pressure in addition to being strongly dependent on drop diameter and drop falling distance or rain zone height. According to Kloppers and Kröger [2005(1)], the general form of the Merkel number correlation for fills is given by Eq. (F.1), which includes a term for water mass velocity (G_w), but excludes atmospheric pressure (p_a). Furthermore, Kröger (2004) presents numerous fill Merkel number correlations from literature, which are functions of L/G (G_w/G_a according to the thesis nomenclature). To understand the inclusion of the water mass velocity for fill characteristics and the effect of atmospheric pressure on the Merkel number of film fills, analytical equations (Eqs F.30 to F.32) were also derived for water films running down vertical flat plates at terminal speed in air flowing upwards. It was found that the Merkel number for this case is a function of G_w/ G_a and is independent of atmospheric pressure.

Similarly, the resultant loss coefficient equations (Eqs G.8, G.9, G.12 and G.13), which have the same form as proposed by Kloppers and Kröger (2003) for cooling fills, reveal that the rain zone specific loss coefficient is independent of water mass velocity and dependent on atmospheric pressure, as observed for the Merkel number.

The mechanisms of fills to increase the interfacial surface area between water and air comprise a combination of film and rain flow and therefore correlations for fill Merkel numbers are expected to include the water mass velocity. The effect of atmospheric pressure on splash fills should, however, be investigated further.

2.2.3 Empirical equations for motion and cooling of a single drop falling through a vertical air-stream (Appendices F and G)

To obtain more simplified but accurate relations for the Merkel number and loss coefficient of counter- and crossflow rain zones, the numerical model presented in Appendices B and C was used to generate data, which are correlated in Appendices F and G to yield multi-variable power functions in terms of the fundamental independent variables. From Eqs (F.36) and (F.38), it can be seen that drop diameter, drop path length or rain zone height, atmospheric pressure, and air speed have a significant effect on the Merkel number, with the drop diameter having the highest exponent. Eqs (G.15) and (G.17) reveal that the air speed, drop path length, drop diameter, and atmospheric pressure have the largest effect on the specific loss coefficient, with the air speed having the highest exponent.

2.2.4 CFD analysis of cooling tower rain zones (Appendix I)

As mentioned above, rain zones can be modelled in *FLUENT*® by solving the Lagrangian discrete phase model in addition to the transport equations for the continuous phase. The discrete phase model computes the trajectories of the discrete phase entities as well as heat and mass transfer to/from them and can be coupled to include the impact of the interaction between both the phases.

To gain a better understanding of the capabilities of *FLUENT*® to model rain zone performance, two-dimensional CFD models are developed in Appendix I for purely counterflow and crossflow rain zones, and cross-counterflow rain zones encountered in counterflow natural draught wet-cooling towers. These are employed to investigate the effects of different drop size distributions, methods of dealing with polydisperse drop distributions, and different drop drag, collision and break-up models on the performance of rain zones. The CFD models are validated using the single drop numerical models developed in Appendices B and C, and for counterflow and cross-counterflow rain zones, the cooling range and loss coefficient results are compared with data obtained by solving the semi-empirical model of De Villiers (1998) using the Merkel method of analysis.

From the results, it can be concluded that: *FLUENT*® can be used effectively to model rain zone performance; monodisperse drop distributions based on the Sauter mean drop diameter give representative results for corresponding polydisperse drop distributions; Rosin-Rammler distributions should be avoided; results obtained for the unsteady *FLUENT*® dynamic drag model compare favourably with steady flow results obtained using the Dreyer (1994) deformed drop drag model; the *FLUENT*® drop collision model gives inconsistent results with regard to cooling performance, pressure drop and conservation of mass for the conditions investigated; similar cooling performance can be obtained in a crossflow rain zone as a counterflow rain zone for the same air-side flow power consumption; the rain zone performance model of De Villiers (1998) for cross-

counterflow rain zones gives conservative loss coefficients compared to *FLUENT®;* and a grid size of at least 0.1 x 0.1 m is required with a sufficiently small integration time step to resolve the DPM model.

2.2.5 CFD analysis of cooling tower spray zones (Appendix Q)

Spray zones can be modelled in *FLUENT*® by solving the Lagrangian discrete phase model in addition to the transport equations for the continuous phase, similar to the analysis of rain zones. For the spray zone of a given nozzle, however, the initial drop speed and injection angle must be known for a range of spray trajectories. Appendix Q presents a method, developed in collaboration with Viljoen (2006), to determine spray zone performance for a specific nozzle type from measured drop size, water flow distribution and nozzle inlet pressure data. The single drop models presented in Appendices B and C are used to predict the drop initial speeds and initial angles at the nozzle outlet and drop temperature change along different trajectories by making use of the measured nozzle inlet water pressure as well as water flow distribution and drop size distribution data measured at a specific level below the nozzle. Next, the water distribution produced by a grid of nozzles with overlapping sprays is predicted at a given level and optimised by numerical superposition of single nozzle water distribution data for a given nozzle spacing. The above data is used to firstly develop a CFD model for a single nozzle, which can be verified using the above numerical single drop data. This model is subsequently developed into a multi-nozzle CFD spray zone model for a given nozzle spacing, which is verified with superposition model data. Ultimately a CFD solution is obtained where the continuous and discrete phase models are coupled to simulate the actual performance of the spray zone and the results are used to determine the spray zone transfer characteristics (Merkel numbers) by applying the Merkel method of analysis, and spray zone loss coefficient from the volume flow weighted mean air-side total pressure difference. One of the main outcomes of this investigation is that the single drop model (Appendices B and C) can be used effectively to determine spray zone performance without the use of CFD.

2.3 MODELLING OF THE COOLING TOWER INLET AIR FLOW PATTERNS AND LOSSES

Cooling tower inlet losses are the flow losses or viscous dissipation of mechanical energy affected directly by the cooling tower inlet design, which according to the counterflow natural draught wet-cooling tower performance analysis example given in Appendix K, can be more than 20 % of the total cooling tower flow losses. Flow separation at the lower edge of the shell results in a vena contracta with a distorted inlet velocity distribution that causes a reduction in effective fill or heat exchanger flow area.

In Appendix H, a two-dimensional (axisymmetric) CFD model is developed using *FLUENT*®, to simulate the flow patterns, loss coefficients and effective flow

diameter of circular natural draught cooling tower inlets. The CFD results are compared with axial velocity profile data, tower inlet loss coefficients and effective diameters determined experimentally by Terblanche (1993) on a cylindrical scale sector model as well as applicable empirical relations found in Kröger (2004), determined using the same experimental apparatus as Terblanche. The validated CFD model is used to investigate the effects of grid size, Reynolds number, turbulence model, fill loss coefficient, inlet diameter to inlet height ratio, inlet geometry, fill resistance type, shell wall thickness, and shell wall inclination angle on the flow patterns, inlet loss coefficient and effective diameter of full-scale cooling towers. Ultimately, simple correlations (Eqs H.21 to H.28) are proposed for determining cooling tower inlet loss coefficient and inlet effective flow diameter ratio of full-scale cooling towers without rain zones.

The main conclusions are summarised as follows: results obtained using the k-ε Realizable turbulence model compared favourably with the experimental data from literature; cooling tower inlet losses and effective diameter are independent of the Reynolds number; the inlet diameter to height ratio (d_i/H_i) and fill or heat exchanger loss coefficient (K_{fi}) have the most significant influence on the inlet loss coefficient and effective diameter and the effects of shell thickness and inclination angle are small; there are significant differences between the loss coefficient and effective diameter data of orthotropic and isotropic fill resistances; the fill resistance in cooling towers packed with film type fill, can be a combination of orthotropic and isotropic resistance, depending on the fill orientation relative to the airflow, which should be investigated three-dimensionally; and under no wind conditions, the performance of NDCTs with square inlets can be enhanced significantly by installing round inlets or protruding platforms above the air inlet. From different cooling tower inlet geometries found in industry, it is observed that the frontal area of fills suspended from support beams is generally less than the shell inlet cross-sectional area due to the inclination of the shell wall, which results in a region near the shell wall, which does not contain any fill and therefore reduces the negative impact of flow separation at the inlet on cooling tower performance.

2.4 MODELLING OF HEAT AND MASS TRANSFER IN CROSS-COUNTERFLOW FILLS

In cooling towers packed with trickle or splash fills, which have almost isotropic or anisotropic flow resistance, the air flow through the fill is oblique or in cross-counterflow to the water flow, particularly at the cooling tower inlet when the fill loss coefficient is small or when the fill hangs down into the air inlet region. This results that the fill Merkel number or transfer characteristic for cross-counter flow is between that of purely counter- and crossflow fills.

When using CFD to model natural draught wet-cooling tower performance for isotropic fill resistance, two- or three-dimensional models are therefore required to determine fill performance.

In Appendix J, the governing fundamental partial differential equations are derived in cylindrical and Cartesian co-ordinates to determine the cooling water temperature, water evaporation rate, air temperature and air humidity ratio in two-dimensional cross-counterflow fills for both saturated and supersaturated air. To solve these equations, a relation is proposed to determine Merkel numbers for oblique air flows by linear interpolation and extrapolation of purely cross- and counterflow Merkel numbers in terms of the air flow angle. This model is compared to analytical Merkel numbers obtained for different air flow angles using a single drop trajectory model developed in Appendices B and C.

A computational model, based on a linear upwind spatial discretisation scheme, and an Eulerian *FLUENT*® model were developed to evaluate fill performance characteristics from test data and to model fill performance in cooling towers respectively. The results of these two models are compared and verified with a *FLUENT*® Euler-Lagrange model showing marginal differences.

2.5 MODELLING OF NATURAL DRAUGHT FLOW DRIVING POTENTIAL

The flow driving potential or pressure difference to drive the flow in natural draught wet-cooling towers, required to overcome flow losses, is effectively the aerostatic or total pressure difference between the air inside and outside the tower at fill level, due to the difference in mean density of the colder ambient air outside the tower and the warmer moist air inside the tower. To determine the mean densities, the air temperature and aerostatic pressure must be known as functions of elevation. Different atmospheric temperature and pressure models are presented in Appendix M, which are subsequently used to determine wet-cooling tower flow driving potential based on the air conditions at the tower inlet and fill outlet determined for the reference natural draught wet-cooling tower in Appendix K. The results are ultimately compared to investigate the effect of the different models on the driving potential.

Air flow from a higher to a lower elevation results in compression accompanied by increase in temperature. Modelling of vertical atmospheric air flow using *FLUENT*®, including the effect of gravitational acceleration, however, reveals that the temperature remained constant, as the pressure and kinetic energy terms in the energy equation are not solved. The inlet pressure profile at the air inlet boundary of the CFD model therefore needs to be based on an isothermal model, to be comparable with DALR conditions.

2.6 CONCLUSIONS

The single drop numerical model developed in Appendices B and C is flexible and effective to determine spray and rain zone performance characteristics (Merkel number and loss coefficient) based on constant air velocity, which can be used to calculate spray/ rain zone performance by making use of the Merkel or e-NTU methods of analysis.

It is found that both the Merkel number and specific loss coefficient of rain zones are dependent on atmospheric pressure (p_a), drop diameter (d_d) and air mass velocity (G_a), but independent of water mass velocity (G_w). Fill characteristics in literature are generally independent of atmospheric pressure, which is confirmed to be valid for film fills.

FLUENT® can be used effectively to model spray and rain zone performance, inlet losses and effective flow area, flow driving potential, and fill performance, provided the correct models are implemented as outlined above.

Furthermore it can be seen that the cooling tower performance can be increased by: reducing the inlet flow losses and flow recirculation by installing protruding platforms or roundings, reducing the drop size in the rain zone, and installing additional fill which hangs down into the rain zone below the air inlet height level.

3. CFD MODEL TO PREDICT THE PERFORMANCE OF NATURAL DRAUGHT WET-COOLING TOWERS PACKED WITH ANISOTROPIC FILLS

3.1 INTRODUCTION

In the design of a modern natural draught wet-cooling tower, structural and performance characteristics must be considered. Air flow distortions and resistances must be minimised to achieve optimal cooling which requires that the cooling towers must be modelled two-dimensionally and ultimately three-dimensionally to be optimised. CFD models in literature are limited to counterflow cooling towers packed with film fills, which are porous in one direction only and generally have a high pressure drop, as well as purely crossflow cooling towers packed with splash fill, which simplifies the analysis considerably. Many counterflow cooling towers are however packed with trickle and splash fills which have anisotropic flow resistances, which means the fills are porous in all flow directions and thus air flow can be oblique through the fill, particularly near the cooling tower air inlet. This provides a challenge since available fill test facilities and subsequently fill performance characteristics are limited to purely counter- and crossflow configuration. This section briefly discusses the CFD model developed in this thesis, verification of the results and investigation of various effects on cooling tower performance.

3.2 MODEL DEVELOPMENT AND VERIFICATION

Appendix N presents a *FLUENT*® model of a natural draught wet-cooling tower packed with an isotropic expanded metal fill with low flow resistance, shown in Fig. 3.1, with the same design specification as the one-dimensional model presented in Appendix K. The basic design data are summarised in Table 3.1.

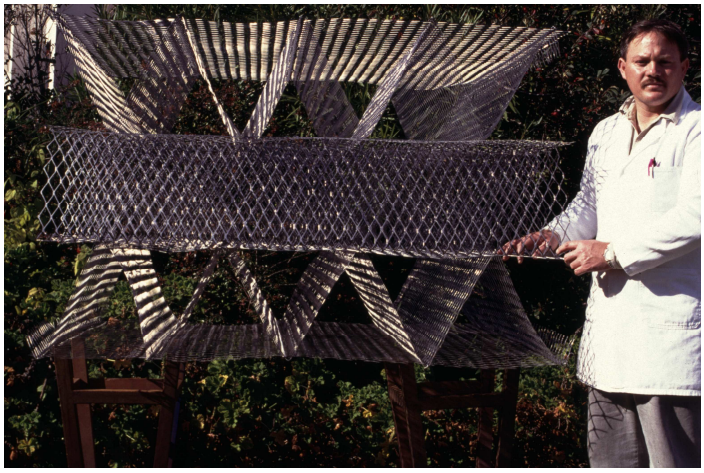

Figure 3.1 : Isotropic expanded metal splash fill.

Table 3.1 : Cooling tower thermal design data for the present investigation.

Description	Symbol	Value	Units
Ambient air:			
Atmospheric pressure:	p_a	84 000	N/m^2
Drybulb temperature at ground level:	T_a	15.5	ºC
Wetbulb temperature at ground level:	T_{wb}	11.1	ºC
Cooling water:			
Mass flow rate:	m_w	12 500	kg/s
Mass velocity/ flux:	G_w	1.5	kg/s m^2
Inlet temperature:	T_{wi}	40	ºC
Cooling range (1-D model of Kröger, 2004):	ΔT_w	18.6	ºC
Cooling range (present CFD model):	ΔT_w	18.5	ºC

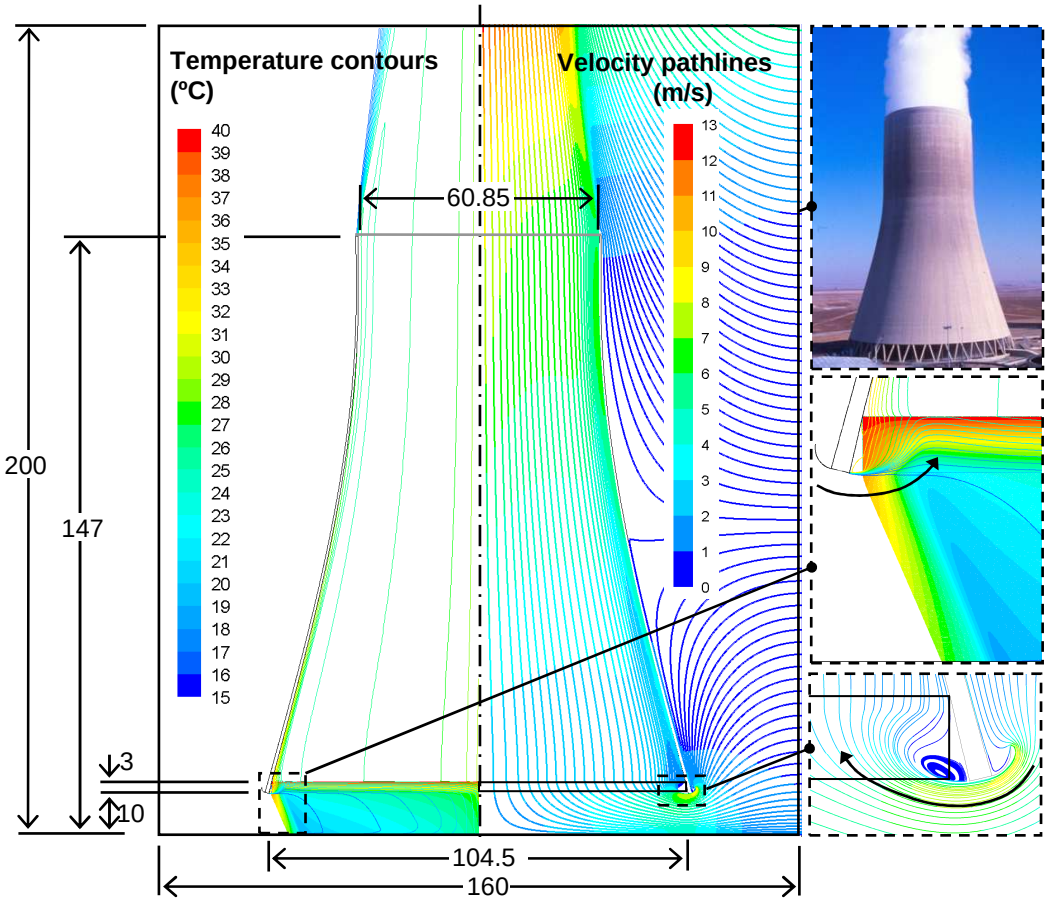

Figure 3.2 : Dimensions, temperature contours, and velocity pathline plots obtained with the *FLUENT*® CFD model for a rounded CT inlet.

Figure 3.2, shows the dimensions of the cooling tower investigated, and typical temperature contour and velocity pathline plots obtained with the CFD model. This model can be used to investigate the effects of different: atmospheric temperature and humidity profiles, air inlet and outlet geometries, air inlet heights, variations in radial water loading and fill depth, fill configurations and combinations, rain zone drop size distributions, and spray zone performance characteristics on cooling tower performance, for optimization purposes.

A sensitivity analysis shows the effects of variation of grid size, fill air outlet saturation level, Merkel number ratio, and wall slip condition on the CFD results, which are presented in Table N.1 and summarised in Table 3.2 below.

Table 3.2 : Sensitivity analysis data showing the effect of different parameters on the CFD results.

Parameter investigated	Changed from → to	Change in cooling range	
		ºC	(%)
Grid size	0.025 → 0.050 mm	0.07	(0.4 %)
Fill air outlet condition	Supersat. → saturated	0.05	(0.3 %)
Merkel number ratio	0.9 → 1.0	-0.19	(-1.0 %)
	0.9 → 0.8	0.21	(1.1 %)
Wall boundary condition	No-slip → slip	0.02	(0.1 %)

The CFD results are validated by means of corresponding one-dimensional computational data obtained using the model in Appendices K and L. Table 3.3 provides a summary of the cooling ranges obtained with the one-dimensional and the CFD models for different air inlet geometries, rain zone drop sizes, and cooling tower inlet heights, which are presented in more detail in Tables N.1 to N.6.

Table 3.3 : Data showing the effects of variation of different design parameters on the one-dimensional and CFD model results, for model comparison and verification.

Parameter investigated	Changed from → to	Change in cooling range			
		1-D model		CFD model	
		ºC	(%)	ºC	(%)
Inlet geometry	round → square	-0.3	(-1.6 %)	-0.6	(-3.3 %)
Rain zone drop size	3.5 → 2.5 mm	1.3	(7.0 %)	1.2	(6.5 %)
	3.5 → 5.5 mm	-1.1	(-6.0 %)	-1.0	(-5.4 %)
	5.5 → 2.5 mm	2.4	(13.0 %)	2.2	(11.9 %)
Inlet height	10 → 9 m	-0.3	(-1.6 %)	-0.1	(-0.5 %)
	10 → 8 m	-0.6	(-3.3 %)	-0.6	(-3.3 %)
Pond	flat → 1 m pondwall	N/A		0.0	(0.0 %)
Tower outlet	cylindrical → stiffener	N/A		-0.3	(-1.6 %)

From the *FLUENT*® and one-dimensional model data, presented in Tables N.1 to N.7, and summarised in Tables 3.2 and 3.3, the following conclusions can be drawn:

- ⇨ A grid size of 0.025 m in the fill region yields energy balances below 1 % and is considered to be sufficiently fine.
- ⇨ A negligible change in performance is observed when changing the properties of the air leaving the fill from supersaturated to saturated conditions (Table N.1).
- ⇨ Depending on the crossflow to counterflow Merkel number ratio, the one-dimensional model for a rounded inlet over-predicts the cooling water outlet temperature marginally compared to corresponding *FLUENT*® data (Table N.1). In the *FLUENT*® model, the higher local Merkel numbers due to oblique flow through the fill appear to neutralise the adverse effects of the flow recirculation. For a sharp air inlet, the differences are found to be more significant (Table N.2).
- ⇨ The difference between using no-slip and slip wall boundaries was found to be negligible (Table N.1).
- ⇨ A rounded inlet results in better performance than a sharp air inlet (Tables N.1 and N.2).
- ⇨ The rain zone drop size has the most significant effect on cooling tower performance (Table N.3).
- ⇨ The inlet height of the cooling tower investigated could be reduced by about $\Delta H_3 = 1$ m without a significant effect on performance (Table N.4).
- ⇨ The effect of a pond wall on cooling water outlet temperature was found to be negligible (Table N.5).
- ⇨ The effect of a stiffening structure inside the shell at the tower outlet should not be ignored (Table N.5).

It should be noted that the physics of the one-dimensional model (Appendix K) and the *FLUENT*® model (Appendix N) differ considerably. In the one-dimensional model, the fill characteristics are determined using the mean vertical air mass velocity and the effect of flow separation on fill performance is not taken into consideration. In the *FLUENT*® model, however, local fill characteristics are calculated for each cell in the rain, fill and spray zones based on absolute mass velocity values, and the entire flow field is solved numerically, including the flow recirculation in the fill due to flow separation at the cooling tower inlet, showing measurable radial variation in cooling water temperature, air flow rate, air temperature and humidity ratio. The following can be concluded from the *FLUENT*® model results presented in Figs N.3 to N.17:

- ⇨ For the reference cooling tower with a rounded inlet, it was observed that the fill performance reduces to $\Delta T_w/\ \Delta T_{w,m}$ = 0.2 in the outer ring region ($r/\ r_{fi}$ > 0.925) against the shell wall, and that the maximum cooling range of $\Delta T_w/\ \Delta T_{w,m} \approx 1.2$ and the minimum of $\Delta T_w/\ \Delta T_{w,m} \approx 0.73$ are at $r/\ r_{fi} \approx 0.925$ and $r/\ r_{fi}$ =0 respectively, changing almost linearly along the radius from maximum to minimum. For square inlets, fill performance in the outer ring region ($r/\ r_{fi}$ < 0.9) is worse than for the round inlet due to the larger flow recirculation region at the inlet, where the maximum cooling range of $\Delta T_w/\ \Delta T_{w,m} \approx 1.3$ and a minimum of $\Delta T_w/\ \Delta T_{w,m} \approx 0.8$ occurs at $r/\ r_{fi} \approx 0.9$ and $r/\ r_{fi}$ = 0 respectively, again changing almost linearly from maximum to minimum.
- ⇨ The rain zone cooling range is consistently about 20 % of the overall cooling range along the radius and a region of high cooling water temperature and thus reduced fill performance is observed near the cooling tower inlet due to flow separation and recirculation.
- ⇨ Atmospheric air is drawn into the tower from a region roughly half the height of the cooling tower, as shown in Fig. 3.2, however, most of the air seems to come from a region closer to the ground.
- ⇨ The radial velocity of the air entering the cooling tower varies significantly with height, being almost double at the upper ring beam to that at ground level.
- ⇨ As shown in Fig. 3.2, the air flow passing through the fill is found to be predominantly oblique, since the fill is isotropic with a low loss coefficient.
- ⇨ Near the cooling tower shell, the axial air mass velocity is very low due to the flow separation and air recirculation, increasing to a maximum at $r/r_{ct,z} \approx 0.94$ before decreasing again to an almost uniform axial mass velocity at $r/r_{ct,z} < 0.82$.

3.3 INVESTIGATION OF THE EFFECTS OF RADIALLY VARIABLE WATER LOADING AND FILL HEIGHT ON NDWCT PERFORMANCE

From the results in Appendix N, it can be seen that the water temperature, air mass velocity, air temperature and humidity ratio vary considerably along the radius and that due to flow separation, there is also significant air recirculation in the fill at the air inlet. In Tables P.1 to P.6 and Figs P.2 to P.4 of Appendix P, the effects of employing two different water mass velocities and two fill heights along the radius on cooling tower performance are investigated for the cooling tower presented in Appendix K. The cross-sectional area of the fill region is therefore divided into a central core area and an annulus and the elevations of the spray and rain zone inlets are kept radially constant. These results are summarised in Table 3.4 below.

The following conclusions can be drawn:

- ⇨ The effect of variable water mass velocity is negligible for the particular cooling tower configuration investigated (Tables P.1 and P.2).

- ⇨ The effect of variable fill height is most significant when the spray and rain zone inlet are at constant elevations, the fill height in the annulus is maximised while the core radius is minimised. (Tables P.3 to P.5)
- ⇨ The water and fill distributions that gave the best results for the expanded metal fill, results in a performance reduction for the trickle fill. It is therefore important to note that cooling tower optimisation studies should be conducted on a case-by-case basis and that the spray and rain zone characteristics play an important role in the outcome of the optimisation. (Table P.6)

Table 3.4 : Summary of the effects of different design parameters on the cooling range predicted by means of the present CFD model.

Parameter investigated	Changed from → to	Change in cooling range ºC	(%)
Radial fill depth	uniform → non-uniform	0.4	(2.2 %)
Radial water loading	uniform → non-uniform	0.0	(0.0 %)

3.4 CONCLUSIONS

The main conclusions of this investigation are summarised as follows:

- ⇨ A new improved and verified *FLUENT*® CFD model was developed for a NDWCT packed with anisotropic flow resistance fills, which can be used for performance prediction and optimisation.
- ⇨ Comparison between equivalent *FLUENT*® and one-dimensional model results, shows that, depending on the Merkel number ratio (X), the deviations are relatively small for a rounded inlet, but more significant for square inlets due to the additional flow recirculation at the air inlet.
- ⇨ The *FLUENT*® model reveals significant differences in the physics between the *FLUENT*® and one-dimensional model, showing measureable variations in water temperature, and air velocity, temperature and humidity ratio along the radius, as well as the effects of flow recirculation at the air inlet.
- ⇨ An investigation of the effect of inlet geometry, inlet height, drop size and fill type, revealed that the outlet water temperature of a typical NDWCT could potentially be decreased by about 3 ºC, by making a few minor and low cost design adjustments, which according to Appendix R could result in a 1 % increase in power plant output and/ or efficiency.
- ⇨ By increasing the fill height in the outer annulus and reducing the fill height in the core to maintain the same fill volume, a further reduction 0.5 ºC in outlet water temperature can be achieved for the cooling tower investigated.

4. CONCLUSION AND RECOMMENDATIONS

4.1 CONCLUSION

An axisymmetric *FLUENT*® CFD model is developed to predict the performance of natural draught wet-cooling towers with any given geometry, and spray, fill and rain zone configuration. The main objectives stated in Chapter 1, which had to be fulfilled in order to achieve this goal, are repeated below:

1. Gain a better understanding of the modelling options and capabilities of the commercial CFD code *FLUENT*® and to find optimal methods to calculate the flow inlet flow losses, thermal performance of the rain, fill and spray zones, and driving potential by investigating each separately and comparing the results of different case studies to analytical, numerical, and experimental data.
2. Develop a one-dimensional computational model to predict NDWCT performance based on Example 7.3.2 in Kröger (2004).
3. Develop a two-dimensional axisymmetric *FLUENT*® model based on the same design specification as for Example 7.3.2 in Kröger (2004).
4. Compare the *FLUENT*® and one-dimensional model results obtained for different cooling tower inlet and outlet geometries, inlet heights, rain zone drop diameters and fill types.
5. Investigate the effects of radially variable water mass velocities and fill heights on NDWCT performance using the new *FLUENT*® model.
6. Make recommendations on how cooling tower performance can be enhanced.

The work done to achieve these goals and the main outcomes are discussed below.

4.1.1 Objective 1

Geldenhuys (1987), Terblanche (1994), and De Villiers (1998) proposed empirical relations for the cooling tower inlet loss coefficient, and Oosthuizen (1995) developed relations for effective flow diameter, determined from experimental data measured on an experimental cooling tower sector model. In Appendix H, the empirical and experimental data from these researchers was used to develop and verify *FLUENT*® models of the different cooling tower inlet configurations investigated. It was found that for different inlet geometries, fill loss coefficients, fill resistance types (orthotropic, anisotropic or isotropic), and cooling tower inlet heights that the k-ε realizable turbulence model results compared well with the data from literature, and that the cooling tower inlet loss coefficient and effective diameter are independent of Reynolds number but dependent on the type of fill flow resistance, which affects the overall flow patterns.

De Villiers (1998, 2001) proposed semi-empirical relations for the Merkel number and loss coefficient for counter- and cross-counterflow rain zones found in rectangular and circular cooling towers, based on the Sauter mean drop diameter. In Appendix I, these relations, the numerical single drop model presented in Appendices B and C, and two measured rain zone drop distributions are used to develop and verify various *FLUENT*® models of counter-, cross- and cross-counterflow rain zones. Models were developed to compare the results for: different drop distribution methods of analysis (Sauter mean monodisperse, polydisperse, and Rosin-Rammler), different drag models (Dreyer (1994), and the *FLUENT*® dynamic drag models) and different discrete phase models (steady, unsteady, stochastic particle tracking, drop collision and drop break-up). In essence it was found that monodisperse drop distributions based on the Sauter mean drop diameter give representative results for corresponding polydisperse drop distributions, but the Rosin-Rammler distribution should be avoided since the correlation of the data is not always adequate. Results obtained for the unsteady *FLUENT*® dynamic drag model compare favourably with results using the steady Dreyer (1994) deformed drop drag model. The effect of stochastic particle tracking is found to be negligible due to the low turbulence levels, large drop size and high void fractions. The *FLUENT*® drop collision model gives inconsistent results with regard to cooling performance, pressure drop and conservation of mass for the conditions investigated, and should be investigated further. Similar cooling performance can be obtained in a crossflow rain zone than for a counterflow rain zone for the same air flow power input. The rain zone performance model of De Villiers (1998) for cross-counterflow rain zones gives conservative loss coefficients compared to *FLUENT*® especially for the enhanced drop distribution. Similar trends are observed for the counterflow models. From a grid independence study a grid size of at least 0.1 x 0.1 m is required and the integration time step should be sufficiently small to resolve the DPM model.

Fill performance characteristics are determined from performance data measured in fill test facilities, which are limited to counter- and crossflow configuration. In cooling towers packed with trickle and splash fills with isotropic or anisotropic fill resistance, where the fill is porous in all flow directions, the air flow through the fill is oblique or in cross-counterflow to the water flow, particularly at the cooling tower inlet and especially when the fill loss coefficient is small, and when the fill is hung below the base or lower ring beam of the tower shell. The fill Merkel number for cross-counter flow will therefore be between that of purely counter- and crossflow fills. In Appendix J, the governing fundamental partial differential equations are derived to determine the cooling water temperature, water evaporation rate, air temperature and air humidity ratio in cross-counterflow fills for unsaturated and supersaturated air. The equations are presented in cylindrical co-ordinates for circular (axisymmetric) cooling towers and Cartesian co-ordinates for rectangular cooling towers. To solve these equations, a relation is proposed to determine Merkel numbers for oblique air flows by linear interpolation and extrapolation of purely cross- and counterflow Merkel numbers in terms of the air flow angle. This relation is compared to analytical Merkel numbers obtained for different air flow angles using the single drop model of

Appendices B and C. A computational model and an Eulerian *FLUENT*® model are developed to model fill performance. The results of the two numerical models are compared and verified with the aid of an Euler-Lagrange *FLUENT*® model and showed minor deviations. The main outcomes of this section are a validated numerical model, which can be used to evaluate fill performance characteristics, an equivalent *FLUENT*® model to model cooling tower performance, and the verification that the single drop model of Appendices B and C can be used effectively to determine rain zone Merkel number for any constant air flow velocity.

Adiabatic inviscid flow of air in a gravitational field results in isentropic compression with an associated increase in temperature according to the adiabatic lapse rate (ALR) for descending air, as opposed to a decrease in temperature for ascending unsaturated air. Upward flow of saturated or supersaturated air however results in further supersaturation due to the decrease in pressure and therefore vapour continues to condense, as evident from the white vapour plumes leaving the top of wet-cooling towers. This condensation process results in a much lower temperature change than the ALR. For incompressible flow with species transport, *FLUENT*® does not solve the pressure (flow work) and kinetic energy terms in the energy equation and therefore the temperature of up or down flowing air remains constant. In Appendix M, different models for determining the driving potential of natural draught wet-cooling towers are therefore compared and it is found that by using the isothermal pressure model inside and outside the tower results in a flow driving potential deviation of about 4 % compared the model used for the one-dimensional model in Appendix K.

Limited data is available in literature on the performance characteristics (Merkel number and loss coefficient) of cooling tower spray zones. Appendix Q therefore proposes a method to determine spray zone performance characteristics for any given spray nozzle from measured pressure, drop size, and flow distribution data, by making use of the numerical single drop model of Appendices B and C, a superposition model, and *FLUENT*®. Ultimately it is found that spray zone performance characteristics can be determined using only the single drop and superposition models i.e. without *FLUENT*®. Spray zone performance can subsequently be determined from the performance characteristics by means of the Merkel or Poppe methods of analysis, depending on the equations of the single drop model.

4.1.2 Objective 2

A one-dimensional computer model, based on Example 7.3.2 in Kröger (2004), was developed to predict NDWCT performance, as presented in Appendices K and L. This example serves as main reference case in this thesis and the model is used mainly to generate data for comparison with CFD results for different cooling tower inlet and outlet geometries, inlet heights, rain zone drop sizes, and fill types.

4.1.3 Objective 3

Appendix N presents a new steady state axisymmetric *FLUENT*® model for a natural draught wet-cooling tower packed with any type of fill (orthotropic, anisotropic, or isotropic fill resistance). This model, which is applicable to general design conditions with no cross-wind, is validated by comparing the results to corresponding one-dimensional data obtained using the models in Appendices K and L for stainless steel expanded metal and trickle fills. The CFD model can be used to optimise the performance of natural draft wet-cooling towers for any given design configuration, and therefore, to investigate the effects of variation of atmospheric temperature distribution, air inlet and outlet geometries, air inlet height, cooling tower diameter, radial water loading and fill height, fill and spray zone configuration, Lewis factor, cross- to counterflow Merkel number ratio, saturation level of the air leaving the fill, and rain zone drop size distribution, on performance. Furthermore the effects of boiler flue gas discharge in the centre of the tower and damage or removal of fill in concentric sections of the cooling tower can be investigated.

For the reference cooling tower with a rounded inlet, it was observed that the fill performance reduces to $\Delta T_w/\ \Delta T_{w,m} = 0.2$ in the outer ring region ($r/\ r_{fi} > 0.925$) and that the maximum cooling range of $\Delta T_w/\ \Delta T_{w,m} \approx 1.2$ and the minimum of $\Delta T_w/\ \Delta T_{w,m} \approx 0.73$ are at $r/\ r_{fi} \approx 0.925$ and $r/\ r_{fi} = 0$ respectively, changing almost linearly along the radius from maximum to minimum. The rain zone cooling range is consistently about 20% of the overall cooling range along the radius and a region of high cooling water temperature and thus reduced fill performance is observed near the cooling tower inlet due to flow separation and recirculation. Atmospheric air is drawn into the tower from a region roughly half the height of the cooling tower, however most of the air seems to come from a zone closer to the ground. The radial velocity varies significantly, being almost double at the upper ring beam to that at ground level. The air flow passing through the fill is found to be predominantly oblique, since the fill is isotropic with a low loss coefficient. Near the cooling tower shell, the axial air mass velocity is very low due to the flow separation and air recirculation, increasing to a maximum at $r/r_{ct,z} \approx 0.94$ before decreasing again to a almost uniform axial mass velocity at $r/r_{ct,z} < 0.82$.

For square inlets, fill performance in the outer ring region ($r/\ r_{fi} < 0.9$) is worse than for the round inlet due to the larger flow recirculation region at the inlet, where the maximum cooling range of $\Delta T_w/\ \Delta T_{w,m} \approx 1.3$ and a minimum of $\Delta T_w/\ \Delta T_{w,m} \approx 0.8$ occurs at $r/\ r_{fi} \approx 0.9$ and $r/\ r_{fi} = 0$ respectively, again changing almost linearly from maximum to minimum.

4.1.4 Objective 4

The difference between *FLUENT*® and one-dimensional model results obtained for different cooling tower inlet and outlet geometries, inlet heights, rain zone drop diameters and fill types are compared in Appendix N and for the reference conditions, it is found that the results obtained for a rounded inlet deviate by

$|\delta(\Delta T_{cw})|/\ \Delta T_{cw} < 0.8$ % and for a square inlet by $|\delta(\Delta T_{cw})|/\ \Delta T_{cw} < 2.9$ %. Larger deviations were found for smaller drop sizes in the rain zone.

The effects of changes to the cooling tower inlet and outlet geometry, inlet height and rain zone drop diameter on the cooling range are summarised in Table N.7.

4.1.5 Objective 5

The effects of radially variable water mass velocities and fill heights on NDWCT performance are investigated in Appendix P using the *FLUENT*® model developed in Appendix N. For the cooling tower investigated, the effect of water distribution was found to be negligible but the effect of fill height variation is significant when the spray and rain zone inlet are at constant elevations. The largest performance enhancement was achieved by maximising the fill height in the annulus while minimising the core radius. When combining the water and fill height distributions that gave the best results, the net increase in cooling range was found to be the sum of the results when each is changed separately.

The water and fill distributions that gave the best results for the expanded metal fill, however results in a performance reduction for the trickle fill. It is therefore important to note that cooling tower optimisation studies should be conducted on a case-by-case basis and that the spray and rain zone characteristics play an important role in the outcome of the optimisation.

4.1.6 Objective 6

Recommendations are given in the following section.

4.2 RECOMMENDATIONS

The above investigations reveal that the performance of cooling towers can be enhanced measurably by means of the following design modifications:

- ⇨ A rounded inlet or protruding platform at the inlet can result in significant improvements in cooling tower performance due to reduced flow recirculation and inlet losses.
- ⇨ In the present investigation, a reduction in inlet height of $\Delta H_3 = 1$ m resulted in a marginal change in performance for a rounded inlet, but either reduces the pumping head or provides space for additional fill. The impact on the cooling tower costs should be investigated.
- ⇨ A reduction in rain zone drop size by installing specially designed splash grids below the fill provides the largest potential for performance enhancement and reduction of life cycle costs of existing and new cooling towers.
- ⇨ The performance of the cooling tower investigated could be enhanced by maximising the annular fill height while minimising the core fill height. Each case should however be investigated independently.

- ⇨ If fill performance characteristics are available for both cross- and counterflow configuration, cooling towers could be designed with fill hanging down to levels below the air inlet height.
- ⇨ The method presented for determining spray nozzle performance characteristics can be used to design new improved spray nozzles as well as to investigate the effect of non-uniform water distribution on fill performance.
- ⇨ The NDWCT investigated in this thesis is a special case. Further investigations should be conducted on cooling towers found in industry.

4.3 FURTHER WORK

Based on the outcomes of this thesis, the following work is being done or should be done in future to continue the optimisation and understanding of cooling tower performance for any given design configuration:

4.3.1 Ongoing research

- ⇨ In Appendix J, it was shown that the Sauter mean drop diameter in the rain zone can be reduced by installing splash grids below the fill which can result in a significant improvement in NDWCT performance, as presented in Appendix N. A new splash grid has been developed and tested to achieve this, yielding promising results.
- ⇨ To verify the accuracy of the models developed in this thesis and to develop a simple model to quantify the economic impact of performance enhancing modifications to cooling towers, online performance tests are being conducted on the power plant units and cooling towers at Eskom Majuba Power Station in South Africa, to monitor performance. A 65 m tall calibrated weather mast, located in an open field about 1200 m away from the power station, is used to measure temperature, humidity and wind velocity profiles, while also measuring atmospheric pressure, solar insolation, and precipitation. This data is measured in conjunction with air temperature and humidity profile measurements at the cooling tower inlet for comparison. Existing measurement devices and instrumentation are used to measure the cooling water temperatures, water mass flow rate, condenser pressure, steam turbine output, and power plant heat input to verify the effect of cooling tower performance on power plant efficiency.
- ⇨ To obtain a better understanding of the effect of drop collision and subsequent agglomeration on the Sauter mean drop diameter in rain zones, high speed video cameras are being used to study drop interaction in rain zones.
- ⇨ To obtain the counter-to-crossflow Merkel number and loss coefficient ratios for different types of fills, performance comparable counter- and crossflow tests are currently being conducted on splash and trickle fills.

- ⇨ To calculate the effect of crosswind on cooling tower performance, flow around cylindrical bodies and cooling tower shells have been investigated numerically and the results obtained are currently used together with this thesis to develop a three-dimensional model for NDWCTs.
- ⇨ To reduce the number of cells in the three-dimensional NDWCT model, an investigation is being conducted to optimise the numerical methods used for the fill analysis.
- ⇨ The method developed to evaluate spray nozzle performance characteristics, has been used effectively to optimise existing commercial spray nozzles and new improved spray nozzles are being developed to achieve uniform water distribution with minimal pumping power consumption.

4.3.2 Future work

Based on the know-how developed in this thesis, the following research can be done in future:

- ⇨ Evaluation, optimisation, and enhancement of existing and new wet-cooling towers to improve plant efficiency.
- ⇨ Development of three-dimensional CFD models for conventional, fan assisted, and hydrid NDWCTs, to ultimately investigate the effect of fans on rain zone performance and plume abatement, and wind effects in order to assist with the development of flow mixing and performance enhancement devices.
- ⇨ Investigate the use of open source CFD codes for the modelling of NDWCTs in order for the CFD model to be globally accessible for commercial use.
- ⇨ Investigate the effects of non-uniform water distribution on fill performance.
- ⇨ Investigate methods to reduce cooling tower outlet losses.
- ⇨ Development of improved splash, film and trickle fill materials.

A

PROPERTIES OF FLUIDS (KRÖGER, 2004)

A.1 THE THERMOPHYSICAL PROPERTIES OF DRY AIR FROM 220K TO 380K AT STANDARD ATMOSPHERIC PRESSURE (101325 N/m^2)

Density:

$$\rho_a = p_a/(287.08\,T),\ \text{kg/m}^3 \tag{A.1.1}$$

Specific heat:

$$c_{pa} = 1.045356\times10^{3} - 3.161783\times10^{-1}\,T + 7.083814\times10^{-4}\,T^{2} - 2.705209\times10^{-7}\,T^{3},\ \text{J/kg K} \tag{A.1.2}$$

Dynamic viscosity:

$$\mu_a = 2.287973\times10^{-6} + 6.259793\times10^{-8}\,T - 3.131956\times10^{-11}\,T^{2} + 8.15038\times10^{-15}\,T^{3},\ \text{kg/s m} \tag{A.1.3}$$

Thermal conductivity:

$$k_a = -4.937787\times10^{-4} + 1.018087\times10^{-4}\,T - 4.627937\times10^{-8}\,T^{2} + 1.250603\times10^{-11}\,T^{3},\ \text{W/m K} \tag{A.1.4}$$

A.2 THE THERMOPHYSICAL PROPERTIES OF SATURATED WATER VAPOUR FROM 273.15K TO 380K.

Vapour pressure:

$$p_v = 10^z, \text{ N/m}^2 \qquad \text{(A.2.1)}$$

$$z = 10.79586(1 - 273.16/T) + 5.02808 \log_{10}(273.16/T) + 1.50474 \times 10^{-4}[1 - 10^{-8.29692\{(T/273.16)-1\}}] + 4.2873 \times 10^{-4}[10^{4.76955(1 - 273.16/T)} - 1] + 2.786118312$$

Specific heat:

$$c_{pv} = 1.3605 \times 10^3 + 2.31334\,T - 2.46784 \times 10^{-10}\,T^5 + 5.91332 \times 10^{-13}\,T^6, \text{ J/kg K} \qquad \text{(A.2.2)}$$

Dynamic viscosity:

$$\mu_v = 2.562435 \times 10^{-6} + 1.816683 \times 10^{-8}\,T + 2.579066 \times 10^{-11}\,T^2 - 1.067299 \times 10^{-14}\,T^3, \text{ kg/s m} \qquad \text{(A.2.3)}$$

Thermal conductivity:

$$k_v = 1.3046 \times 10^{-2} - 3.756191 \times 10^{-5}\,T + 2.217964 \times 10^{-7}\,T^2 - 1.111562 \times 10^{-10}\,T^3, \text{ W/m K} \qquad \text{(A.2.4)}$$

Vapour density:

$$\rho_v = -4.062329056 + 0.10277044T - 9.76300388 \times 10^{-4}\,T^2 + 4.475240795 \times 10^{-6}T^3 - 1.004596894 \times 10^{-8}T^4 + 8.9154895 \times 10^{-12}T^5, \text{ kg/m}^3 \qquad \text{(A.2.5)}$$

Temperature:

$$T = 164.630366 + 1.832295 \times 10^{-3}p_v + 4.27215 \times 10^{-10}p_v^2 + 3.738954 \times 10^3 p_v^{-1} - 7.01204 \times 10^5 p_v^{-2} + 16.161488 \ln p_v - 1.437169 \times 10^{-4}\,p_v \ln p_v, \text{ K} \qquad \text{(A.2.6)}$$

A.3 THE THERMOPHYSICAL PROPERTIES OF MIXTURES OF AIR AND WATER VAPOUR.

Density:

$\rho_{av} = (1 + w)\,[1 - w/(w + 0.62198)]\,p_{abs}/(287.08T)$, kg air-vapour/m^3 (A.3.1)

Specific heat:

$c_{pav} = (c_{pa} + wc_{pv})/(1 + w)$, J/K kg air-vapour (A.3.2a)

or the specific heat of the air-vapour mixture per unit mass of dry air:

$c_{pma} = (c_{pa} + wc_{pv})$, J/K kg dry air (A.3.2b)

Dynamic viscosity:

$\mu_{av} = (X_a\mu_a M_a^{0.5} + X_v\mu_v M_v^{0.5})/\,(X_a M_a^{0.5} + X_v M_v^{0.5})$, kg/m s (A.3.3)

where M_a = 28.97 kg/mole, M_v = 18.016 kg/mole, $X_a = 1/(1 + 1.608\,w)$ and $X_v = w/(w + 0.622)$

Thermal conductivity:

$k_{av} = (X_a k_a M_a^{0.33} + X_v k_v M_v^{0.33})/\,(X_a M_a^{0.33} + X_v M_v^{0.33})$, W/m K (A.3.4)

Humidity ratio:

$$w = \left(\frac{2501.6 - 2.3263(T_{wb} - 273.15)}{2501.6 + 1.8577(T - 273.15) - 4.184(T_{wb} - 273.15)}\right)\left(\frac{0.62509\,p_{vwb}}{p_{abs} - 1.005\,p_{vwb}}\right) - \left(\frac{1.00416(T - T_{wb})}{2501.6 + 1.8577(T - 273.15) - 4.184(T_{wb} - 273.15)}\right) \quad \text{(A.3.5)}$$

Enthalpy:

$i_{av} = [c_{pa}(T - 273.15) + w\{i_{fgwo} + c_{pv}(T - 273.15)\}]/(1 + w)$, J/kg air vapour (A.3.6a)

or the enthalpy of the air-vapour mixture per unit mass of dry air:

$i_{ma} = c_{pa}(T - 273.15) + w[i_{fgwo} + c_{pv}(T - 273.15)]$, J/kg air vapour (A.3.6b)

where the specific heats are evaluated at $(T + 273.15)/2$ and the latent heat i_{fgwo}, is evaluated at 273.15 K according to equation (A.4.5).

A.4 THE THERMOPHYSICAL PROPERTIES OF SATURATED WATER LIQUID FROM 273.15K TO 380K.

Density:

$$\rho_w = (1.49343 \times 10^{-3} - 3.7164 \times 10^{-6} T + 7.09782 \times 10^{-9} T^2 - 1.90321 \times 10^{-20} T^6)^{-1}, \text{ kg/m}^3 \quad \text{(A.4.1)}$$

Specific heat:

$$c_{pw} = 8.15599 \times 10^3 - 2.80627 \times 10\, T + 5.11283 \times 10^{-2} T^2 - 2.17582 \times 10^{-13} T^6, \text{ J/kg K} \quad \text{(A.4.2)}$$

Dynamic viscosity:

$$\mu_w = 2.414 \times 10^{-5} \times 10^{247.8/(T-140)}, \text{ kg/s m} \quad \text{(A.4.3)}$$

Thermal conductivity:

$$k_w = -6.14255 \times 10^{-1} + 6.9962 \times 10^{-3} T - 1.01075 \times 10^{-5} T^2 + 4.74737 \times 10^{-12} T^4, \text{ W/m K} \quad \text{(A.4.4)}$$

Latent heat of vaporisation:

$$i_{fgw} = 3.4831814 \times 10^6 - 5.8627703 \times 10^3 T + 12.139568 T^2 - 1.40290431 \times 10^{-2} T^3, \text{ J/K} \quad \text{(A.4.5)}$$

Critical pressure:

$$p_{wc} = 22.09 \times 10^6, \text{ N/m}^2 \quad \text{(A.4.6)}$$

Surface tension:

$$\sigma_w = 5.148103 \times 10^{-2} + 3.998714 \times 10^{-4} T - 1.4721869 \times 10^{-6} T^2 + 1.21405335 \times 10^{-9} T^3 \quad \text{(A.4.7)}$$

B

ANALYSIS OF DROP MOTION IN AIR FLOW

The drop trajectories and air flow patterns in the spray and rain zones of wet-cooling towers differ considerably from each other. The drops in a spray zone are generally dispersed into air flowing vertically upwards by an array of spray nozzles that distribute the cooling water onto the fill material inside the cooling towers. The spray nozzles generally produce circular overlapping spray patterns and the drops leaving a nozzle therefore have radial and curved trajectories within a nozzle specific included spray angle. In contrast, the drops in a rain zone of a counterflow cooling tower trickle, drip or splash from cooling tower fill material prior to accelerating and freefalling downwards under gravity and the air flow can be either vertical (counterflow), horizontal (crossflow) or in-between (cross-counterflow).

Drop velocity and corresponding position co-ordinates can be determined along the drop trajectories by solving the relevant motion equations. In this section, the governing differential equations for two-dimensional drop motion in moving air are derived and solved numerically using the Euler method, and the analysis is used to determine single drop motion and loss coefficient data for any given drop size, initial drop speed, injection angle, air velocity, distance below or above the injection point as well as different air and drop thermophysical properties. The numerical model is validated with the aid of equivalent CFD data, obtained using *FLUENT*® (6.2.16), and is implemented to investigate the following:

- ⇨ The effect of air speed and drop diameter on the drop trajectories in spray zones.
- ⇨ The effect of injection angle, drop diameter and initial drop speed on the horizontal travel distance, drop residence time and specific loss coefficient in spray zones.
- ⇨ The effects of drop deformation due to acceleration in a gravity field on drop motion.
- ⇨ The effect of drop diameter, air speed, initial drop speed and distance below the injection point on the maximum horizontal travel distance and the corresponding injection angle, applicable to spray zones.
- ⇨ The terminal speeds and terminal Reynolds numbers of different drop diameters.
- ⇨ The effect of diameter, air speed, initial speed and path length on the respective absolute speed, Reynolds number, residence time and specific loss coefficient of drops freefalling vertically in counterflowing air.

⇨ The deviation between relations for spray zone and counterflow rain zone loss coefficient found in literature and corresponding numerical data.

⇨ Horizontal deflection of drops caused by a horizontal air-stream, for different drop diameters.

Although interactions between drops due to collisions are ignored, the data obtained from this investigation provides insight into the performance of spray and rain zones and is used to validate results in subsequent sections.

B.1 GOVERNING DIFFERENTIAL EQUATION OF MOTION

Consider Fig. B.1, showing the velocities and acting forces applicable to a spherical body or water drop falling through air flowing at constant velocity. Assume that the drop has a diameter of d and moves with an absolute speed of v_d at an angle of θ to the horizontal and the air flows at an absolute speed of v_a with an angle of φ. The resultant speed of the air relative to the drop is therefore v at an angle of ψ. The forces acting on the drop are the body force (F_G) due to gravity, the aerodynamic drag force (F_D) and the buoyancy force (F_B).

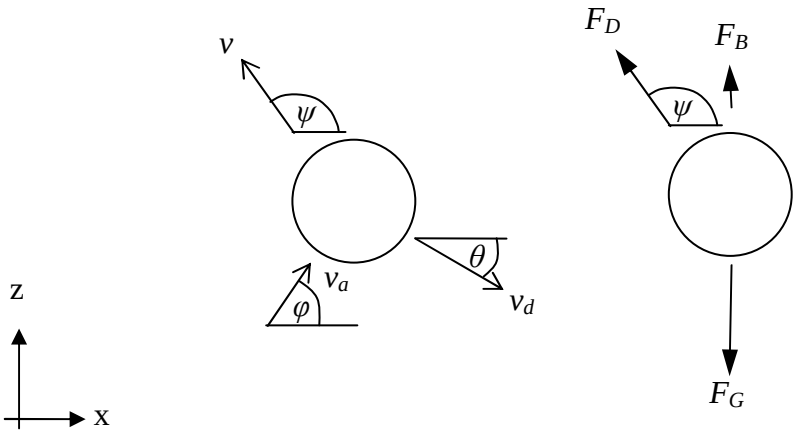

Figure B.1: Velocities and forces acting on a spherical drop falling through moving air.

According to Newton's second law, the rate of change of momentum of a body is proportional to and in the same direction as the resultant force acting on the body. The governing differential equation of motion for a drop falling in air flowing in a two-dimensional plane can therefore be expressed in vector form as

$$\begin{aligned}\frac{d\mathbf{v}_d}{dt} &= \frac{dv_{dx}}{dt}\hat{\mathbf{i}} + \frac{dv_{dz}}{dt}\hat{\mathbf{k}} \\ &= \frac{1}{M_d}\left(C_D A_{fr}\frac{\rho_a v^2}{2}\cos(\psi) - v_{dx}\frac{dM_d}{dt}\right)\hat{\mathbf{i}} \\ &+ \frac{1}{M_d}\left(C_D A_{fr}\frac{\rho_a v^2}{2}\sin(\psi) + V_d(\rho_a - \rho_w)g - v_{dz}\frac{dM_d}{dt}\right)\hat{\mathbf{k}}\end{aligned} \qquad \text{(B.1)}$$

The drop mass (M_d) can also be written in terms of water density and either drop volume or diameter as

$$M_d = \rho_w V_d = \rho_w \left(\frac{\pi d^3}{6} \right) \tag{B.2}$$

The frontal area (A_{fr}) of a drop differs from that of a sphere due to the deformation caused by acceleration in a gravity field. By assuming that the drop has a prolate ellipsoidal shape with an aspect ratio of E, the drop frontal area can be expressed in terms of the diameter (d) of a sphere of the same volume, as

$$A_{fr} = \frac{\pi \left(d\ E^{-1/3} \right)^2}{4} \tag{B.3}$$

where the aspect ratio (E) is defined as

$$E = \frac{d_z}{d_x} \tag{B.4}$$

The air speed relative to the drop is the magnitude of the resultant vector determined from the vector sum of the air velocity and negative drop absolute velocity, expressed as

$$v = \sqrt{\left[v_a \cos(\varphi) + v_d \cos(\theta + 180^o) \right]^2 + \left[v_a \sin(\varphi) + v_d \sin(\theta + 180^o) \right]^2} \tag{B.5}$$

and the corresponding relative flow angle with respect to the horizontal is therefore

$$\psi = \text{a tan} \left[\frac{v_a \sin(\varphi) + v_d \sin(\theta + 180^o)}{v_a \cos(\varphi) + v_d \cos(\theta + 180^o)} \right] \tag{B.6}$$

The fluid properties are calculated using the equations in Appendix A.

B.2 SOLUTION METHOD

The Euler method is used to solve the above equations, comprising a first order Taylor series expression given by Eq. (B.7). The drop trajectory is divided into equal time increments (Δt) and the drop velocity is determined at the next time interval ($t+\Delta t$) by using available velocity and acceleration values from the time interval t, repeating this operation until the required number of iterations are reached.

$$\begin{aligned} \mathbf{v}^{t+\Delta t} &= v_x^{t+\Delta t}\ \hat{\mathbf{i}} + v_z^{t+\Delta t}\ \hat{\mathbf{k}} \\ &= \mathbf{v}^t + \left. \frac{\mathrm{d}\mathbf{v}}{\mathrm{d}t} \right|^t \Delta t = \left(v_x^t + \left. \frac{\mathrm{d}v_x}{\mathrm{d}t} \right|^t \Delta t \right) \hat{\mathbf{i}} + \left(v_z^t + \left. \frac{\mathrm{d}v_z}{\mathrm{d}t} \right|^t \Delta t \right) \hat{\mathbf{k}} \end{aligned} \tag{B.7}$$

The drop trajectory co-ordinates are similarly determined however making use of a second order Taylor series expression, written as

$$\mathbf{s}^{t+\Delta t} = s_x^{t+\Delta t}\hat{\mathbf{i}} + s_z^{t+\Delta t}\hat{\mathbf{k}}$$
$$= \mathbf{s}^t + \mathbf{v}^t \Delta t + \frac{1}{2}\frac{\mathrm{d}\mathbf{v}}{\mathrm{d}t}\bigg|^t \Delta t^2 = \left(x^t + v_x^t \Delta t + \frac{1}{2}\frac{dv_x}{dt}\bigg|^t \Delta t^2 \right)\hat{\mathbf{i}} + \left(z^t + v_z^t \Delta t + \frac{1}{2}\frac{dv_z}{dt}\bigg|^t \Delta t^2 \right)\hat{\mathbf{k}} \tag{B.8}$$

B.3 DRAG COEFFICIENT

Various relations for the drag coefficient of spherical bodies are found in literature (e.g. Brauer 1973, Clift et al. 1978, Ferreira 1997), however one of the best-known is the semi-empirical relation by Turton and Levenspiel (1986), written as

$$C_D = \frac{24\left(1 + 0.173Re^{0.657}\right)}{Re} + \frac{0.413}{1 + 16300Re^{-1.09}} \quad \text{for } Re \leq 200\,000 \tag{B.9}$$

FLUENT® (version 6.2.16) uses another relation by Morsie and Alexander (1972), given as

$$C_D = K_1 + \frac{K_2}{Re} + \frac{K_3}{Re^2} \tag{B.10}$$

where K_1, K_2 and K_3 are constants applicable to certain ranges of Reynolds numbers, as presented in Table B.1.

Table B.1: Values for the constants in Eq. (B.10).

Reynolds numbers	K_1	K_2	K_3
$Re < 0.1$	0	24	0
$0.1 < Re < 1$	3.69	2B.73	0.0903
$1 < Re < 10$	1.222	29.1667	-3.8889
$10 < Re < 100$	0.6167	46.5	-116.67
$100 < Re < 1000$	0.3644	98.33	-2778
$1000 < Re < 5000$	0.357	148.62	-4.75×10^4
$5000 < Re < 10000$	0.46	-490.546	57.87×10^4
$10000 < Re < 50000$	0.5191	-166B.5	5.4167×10^4

The drag experienced by liquid drops however differs from that of equivalent solid spherical bodies due to the influences of internal circulation, oscillation and deformation of the drops. LeClair et al. (1972) found that the effect of internal circulation on the drag experienced by a water drop, which reduces skin friction, is less than 1%. Beard (1977) and Pruppacher and Klett (1978) found that the oscillation frequency of water drops is too high to have a significant effect on drop drag. It is therefore assumed, as done by Dreyer (1994), that the difference between the drag of spheres and drops can be attributed mainly to drop deformation.

FLUENT® (version 6.2.16) provides an option to use the following correlation by Haider and Levenspiel (1989) for deformed drops:

$$C_D = \frac{24\left(1 + b_1 Re^{b_2}\right)}{Re} + \frac{b_3 Re}{b_4 + Re} \tag{B.11}$$

where

$b_1 = \mathrm{e}^{2.3288 - 6.4581\phi + 2.4486\phi^2}$

$b_2 = 0.0964 + 0.5565\phi$

$b_3 = \mathrm{e}^{4.905 - 13.8944\phi + 18.4222\phi^2 - 10.2599\phi^3}$

$b_4 = \mathrm{e}^{1.4681 + 12.2584\phi - 20.7322\phi^2 + 15.8855\phi^3}$

Here the drop shape factor (ϕ) is defined as the ratio of the surface area of a sphere of the same volume as the drop, to the actual surface area of the drop. In *FLUENT®*, the shape factor is a constant input value which must be determined beforehand and also does not change along the drop motion path.

Dreyer (1994) proposes a correlation for the drag coefficient of accelerating drops falling in a gravity field, which includes the effect of changing drop deformation, given as

$$C_D = C_{D,sphere}\left[1 - 0.17185(1-E) + 6.692(1-E)^2 - 6.605(1-E)^3\right] \tag{B.12}$$

where $C_{D,sphere}$ is calculated using Eq. (B.9) and drop deformation is taken into account by the aspect ratio of a prolate ellipsoidal drop, as defined by Eq. (B.4).

According to Dreyer (1994), the deformation of accelerating drops can be obtained from

$$E = 1 - \left(\frac{v_d}{v_T}\right)^2 (1 - E_T) \tag{B.13}$$

where the deformation at terminal velocity (E_T) is determined from a correlation of the data of Beard and Chuang (1987), expressed as

$$E_T = \frac{1}{1 + 0.148 Eo^{0.85}} \tag{B.14}$$

and the Eotvos number is defined as

$$Eo = \frac{g d^2 (\rho_w - \rho_a)}{\sigma_d} \tag{B.15}$$

For comparison, the drag coefficients of Turton and Levenspiel (1986), Morsie and Alexander (1972) and Dreyer (1994) are presented for different Reynolds numbers in Fig. B.2(a). Figure B.2(b) shows that the deviations between models for spherical bodies, compared to Turton and Levenspiel, are small, but that the difference between deformed drops (Dreyer 1994) and spherical bodies can be significant for drop diameters of d > 3 mm.

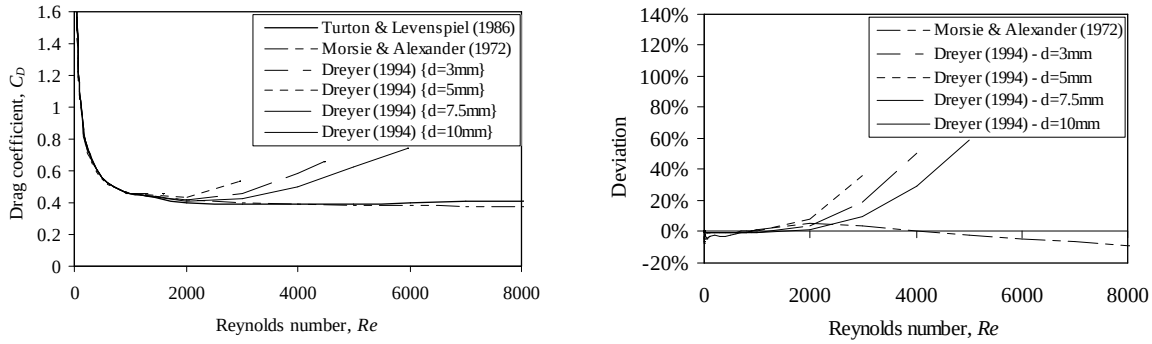

(a) Drag coefficient plotted against Reynolds number. (b) Deviation from Turton and Levenspiel (1986).

Figure B.2: Comparison between different drop drag models.

B.4 LOSS COEFFICIENT

The drop drag forces acting on the air in the opposite direction to the air flow, do negative work on the air-stream, which can be expressed as

$$P = -V_a \Delta p_t$$

$$= -\sum_i F_{D_{ai}} v_{ai} \approx -N_d \frac{1}{t}\int_0^t F_{D_a} v_a \mathrm{d}t = -\frac{6 m_w}{\rho_w \pi d^3}\int_0^t F_{D_a} v_a \mathrm{d}t \qquad \text{(B.16)}$$

where F_{D_a} is the component of the drop drag force in the opposite direction to the air velocity.

For viscous, fully developed, incompressible flow, the loss coefficient is commonly defined as

$$K = \frac{\Delta p_t}{\rho_a v_a^2 / 2} \qquad \text{(B.17)}$$

Substitute Eq. (B.16) into Eq. (B.17) and rearrange to yield the following relation for specific loss coefficient in terms of single drop data:

$$\frac{K}{G_w}\frac{A_{fr,a}}{A_{fr,w}} \approx \frac{12\int_0^t F_{D_a} v_a \mathrm{d}t}{\pi d^3 \rho_w \rho_a v_a^3} \qquad \text{(B.18)}$$

For a single drop falling in a constant velocity air-stream, Eq. (B.18) simplifies to

$$\frac{K}{G_w}\frac{A_{fr,a}}{A_{fr,w}} \approx \frac{12\, t\, \bar{F}_{D_a}}{\pi d^3 \rho_w \rho_a v_a^2} \qquad \text{(B.19)}$$

where for a counterflow rain zone, $A_{fr,a}/A_{fr,w} = 1$.

For the loss coefficient of cooling tower spray zones, Kröger (2004) gives the following correlation based on the data of Lowe and Christie (1961) for d = 1 mm drops in down-spray:

$$K_{sp} = L_{sp}\left[0.4\left(\frac{G_w}{G_a}\right)+1\right] \tag{B.20}$$

For the loss coefficient of purely counterflow rain zones, De Villiers and Kröger (1997) propose the following equation:

$$\begin{aligned} K_{rz} = a_v v_w \Big[& 10645988 a_\mu \mu_a - 130.7774 a_\rho \rho_a - 32.6634 + 888.6645\left\{2.45287\left(a_\mu v_{azo}\right)^{-1.93315} + 0.34\right\} \\ & \times\left\{4.03861\exp\left(-574.542 a_L d_d\right) + 0.493\right\} \\ & \times\exp\left\{\left(65.26215 a_L d_d + 0.74827\right)\ln\left(6.09836\exp\left(0.0767 a_L H_{rz}\right) - 6.1\right)\right\}\Big] \end{aligned} \tag{B.21}$$

where

$a_\mu = 3.061\times10^{-6}\left(\rho_w^4 g^6/\sigma_w\right)^{0.25}$, $a_\rho = 998/\rho_w$, $a_v = 73.298\left(g^5\sigma_w^3/\rho_w^3\right)^{0.25}$

and $a_L = 6.122\left(g\sigma_w/\rho_w\right)^{0.25}$

Eq. (B.21) is valid under the following conditions:

$0\,^\circ\text{C} \le T_a \le 40\,^\circ\text{C}$, $10\,^\circ\text{C} \le T_w \le 40\,^\circ\text{C}$

$0.927\ \text{kg/m}^3 \le \rho_a \le 1.289\ \text{kg/m}^3$, $992.3\ \text{kg/m}^3 \le \rho_w \le 1000\ \text{kg/m}^3$

$1.717\times10^{-5}\ \text{kg/ms} \le \mu_a \le 1.92\times10^{-5}\ \text{kg/ms}$

$0.0696\ \text{N/m} \le \sigma_w \le 0.0742\ \text{N/m}$, $0.002\ \text{m} \le d_d \le 0.008\ \text{m}$, $9.7\ \text{m/s}^2 \le g \le 10\ \text{m/s}^2$

$0.5\ \text{m} \le H_{rz} \le 5.5\ \text{m}$ and $1\ \text{m/s} \le v_{azo} \le 5\ \text{m/s}$

Equations (B.19) to (B.21) are given for comparison later on.

B.5 NUMERICAL DATA AND DISCUSSION OF RESULTS

Fig. B.3(a) shows the spray trajectories for different drop diameters based on the above analysis. These results are compared to equivalent *FLUENT*® data in Fig. B.3(b), showing marginal deviations attributed to differences in the drag models, thermophysical properties and numerical methods used. The data is based on a drop initial speed of v_{d0} = 3.13 m/s; an injection angle of θ = 30º; an air speed of v_a = 2 m/s vertically upwards; an atmospheric pressure of p_a = 101325 Pa; an ambient temperature of T_a = 305.15 K (32 ºC); a relative humidity of φ_a = 100% and a water inlet temperature of T_{wi} = 313.15 K (40 ºC). The initial drop speed is calculated from an assumed dynamic head of 0.5 m, which is low for cooling towers, but with an injection angle of θ = 30º, provides a long and curved trajectory that will best expose any deviations in the results. The other properties are considered to be representative of spray zones in natural draught wet-cooling towers with up-spray nozzles.

For the same conditions, the effect of air speed on the drop trajectories is significant for drop diameters of d = 1 mm, becoming negligible as the drop diameter increases, as shown in Fig. B.4.

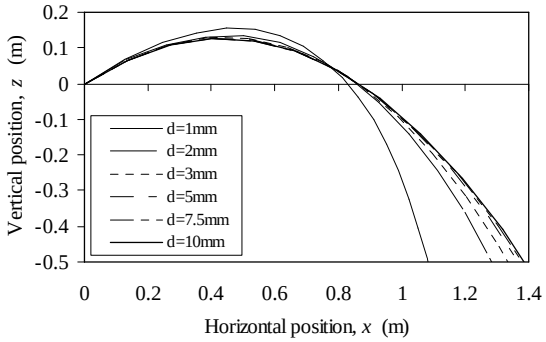

(a) Drop trajectories determined by numerical integration of Eq. (B.1).

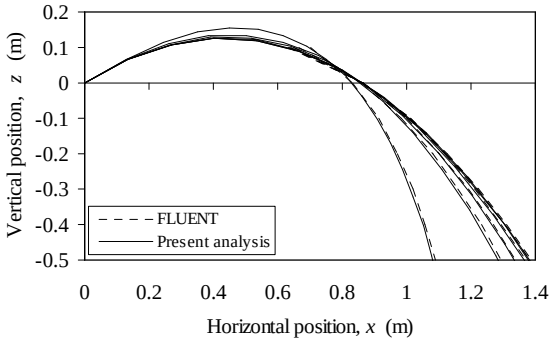

(b) Comparison between the present analysis and FLUENT®.

Figure B.3: Effect of drop diameter on the trajectories of spherical drops injected at a constant angle (θ = 30º) and speed (v_{d0} = 3.13 m/s).

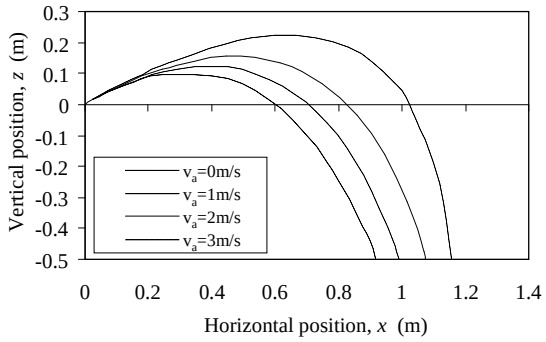

(a) Drop diameter of d = 1 mm.

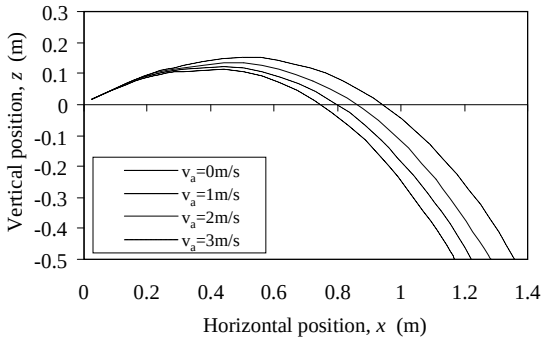

(b) Drop diameter of d = 2 mm.

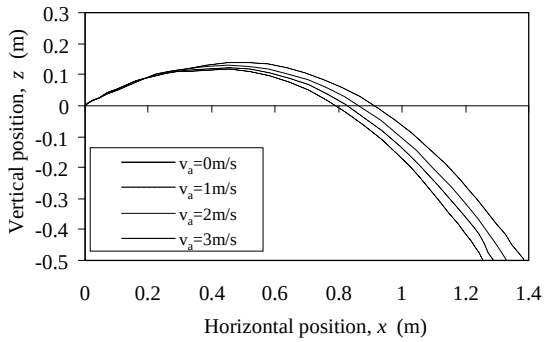

(c) Drop diameter of d = 3 mm.

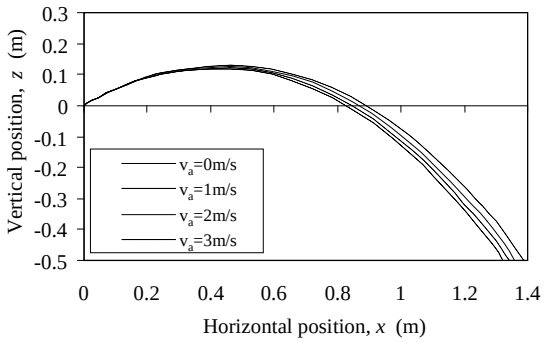

(d) Drop diameter of d = 5 mm.

Fig. B.4: Effect of air speed on a curved up-spray trajectory.

The effects of injection angle on the horizontal travel distance, residence time and specific loss coefficient are presented in Fig. B.5, for a vertical distance below the injection point of z = -0.5 m. In Fig. B.5(a) it can be seen that for injection angles of -90º $\leq \theta \leq$ 0º, referred to as downspray, the horizontal position curves are

clustered together and have an almost linear trend, whereas in upspray ($0^o \leq \theta \leq 90^o$), the curves for the drop diameters d ≤ 3 mm diverge from the other curves, reaching a shorter distance than the larger drops. Figures B.5(b) and B.5(c) show a continuous increase in residence time and specific loss coefficient respectively with injection angle and that the curve for d = 1 mm deviates significantly from the other curves over the whole range of injection angles. Eq. (B.20) is plotted in Fig. B.5(d) for different mass velocity ratios (G_a /G_w), different drop diameters and a spray zone height of 0.5 m. Since this correlation is based on down-spray of d = 1 mm drops, it is compared with present analysis data for d = 1 mm drops and different injection drop speeds and down-spray angles, which are unknown for the experimental data. Eq. (B.20) seems to compare well with data obtained for higher initial drop speeds, generally required to generate small drop sizes.

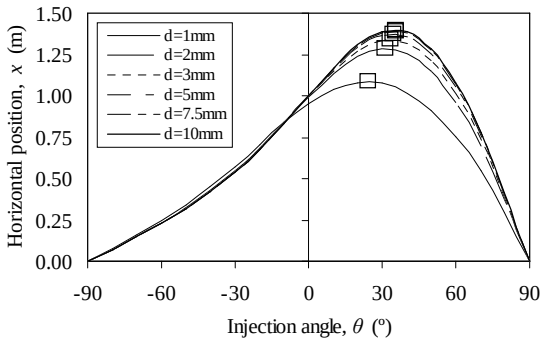

(a) Horizontal travel distance for different injection angles.

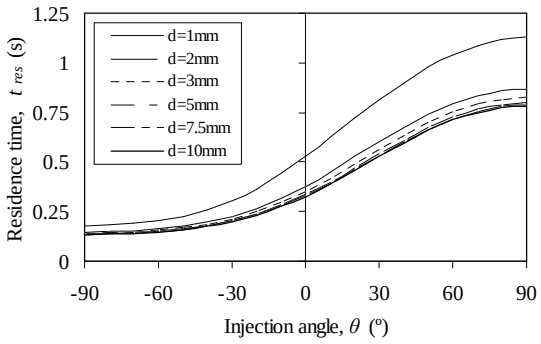

(b) Drop residence time for different injection angles.

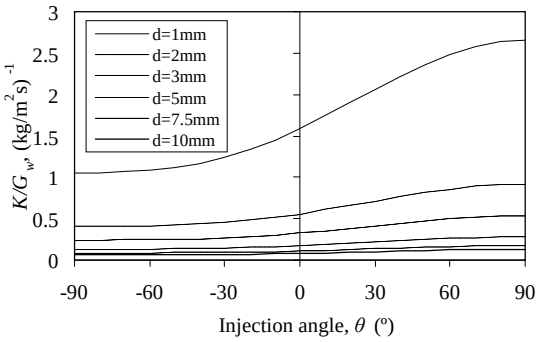

(c) Specific loss coefficient for different injection angles.

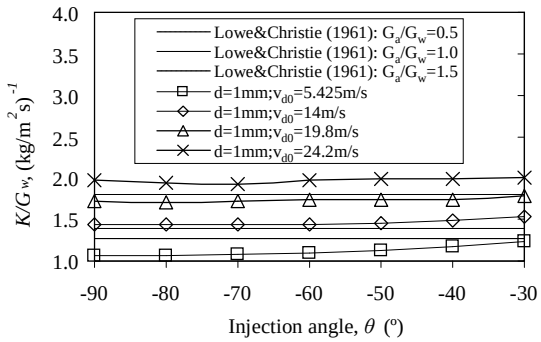

(d) Comparison between Eq. (B.20) by Kröger (2004) based on the data of Lowe and Christie (1961) and present analysis data.

Fig. B.5: Effect of drop injection angle on the horizontal travel distance, drop residence time and specific loss coefficient for different drop diameters.

Fig. B.6 shows that the effect of drop initial speed on the horizontal distance is relatively small for injection angles of $-90^o \leq \theta \leq -30^o$ compared to the large

differences seen for the larger injection angles (θ > -30º). It is also found that an increase in initial drop speed results in marginal decreases in residence time as opposed to marginal increases in specific loss coefficient for θ < 0º and significant increases of both for θ > 0º. This information is important for the design of cooling tower spray nozzles, which must produce a predictable water distribution for a range of water flow rates.

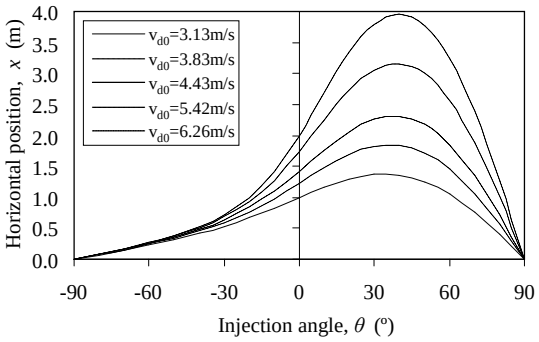

(a) Horizontal travel distance for different injection angles.

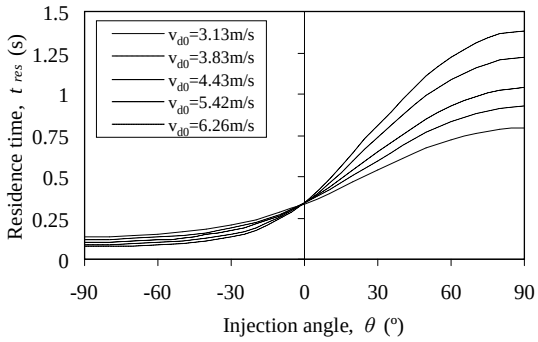

(b) Drop residence time for different injection angles.

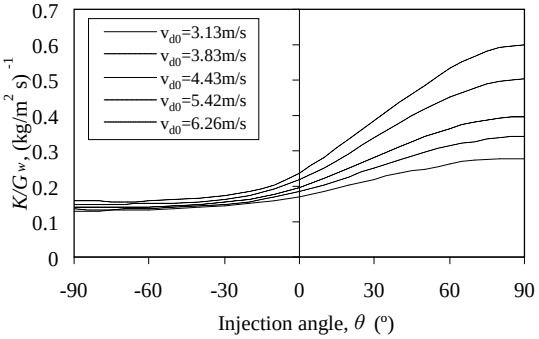

(c) Specific loss coefficient for different injection angles.

Fig. B.6: Effect of drop injection angle and initial drop speed on the horizontal travel distance and drop residence time of a *d* = 5 mm drop.

In Fig. B.7, the effect of drop deformation on the trajectories of d = 5 mm and d = 10 mm drops is found to be negligible. It should be noted that the deformation model is applicable to drops freefalling vertically and accelerating in a gravity field and strictly speaking should not be used for other spray trajectories.

The spray angle that produces the furthest drop trajectory is required to determine the maximum theoretical spray coverage radius attainable for a given drop diameter, initial drop speed (pressure head) and vertical air speed. The common reference conditions for Fig. B.8 are: a drop speed of v_{d0} = 5.42 m/s, corresponding to a dynamic pressure head of 1.5 m; an air speed of v_a = 2 m/s and a spray zone height below the injection point of z = -0.5 m, which are commonly encountered in cooling tower spray zones.

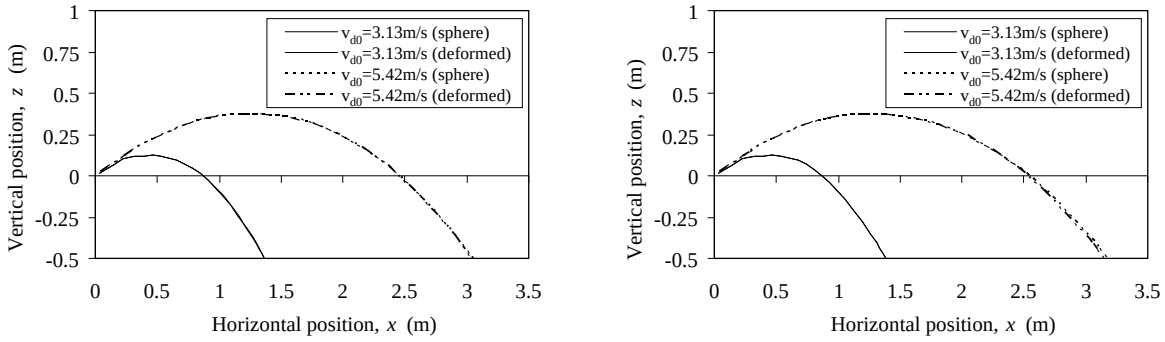

(a) Drop diameter d = 5 mm. (b) Drop diameter d = 10 mm.

Fig. B.7: Comparison between spherical drop and deformed drop trajectories.

It can be seen that the range of injection angles to achieve the maximum radius is between θ_{max} =15º and 40º. The effect of air speed is small, but the effect of drop diameter (d ≤ 3 mm), initial drop speed and vertical distance below the injection point are significant.

In Fig. B.9 the terminal drop speeds and corresponding Reynolds numbers obtained for spherical bodies and deformed drops are plotted for different drop diameters. The terminal speed of deformed drops is almost constant ($v_T \approx 9$ m/s) for drop diameters d > 5 mm, whereas for spherical bodies it continues to rise, reaching a terminal speed of $v_T \approx 16$ m/s at a diameter of d = 10 mm. The terminal Reynolds number of deformed drops is therefore found to be almost linear with drop diameter.

In counter- and crossflow (e.g. at the air inlet of a natural draught counterflow cooling tower) rain zones, which have a maximum height of about H_{rz} = 12 m , the above model is employed to calculate: the Reynolds number at any given moment along the drop motion path, the applicable ranges for different drop sizes; the time it takes for a drop with a certain diameter to fall a given distance, to determine the number of drops and interfacial surface area in the domain at any given moment; the drag force acting on the drop along its motion path, to determine the air-side losses due to the resistive forces acting on the moving air and the horizontal deflection of the drops caused by horizontal air flow applicable to crossflow rain zones.

The data presented in the following figures is based on a drop initial speed of v_{d0} = 0.1 m/s; an injection angle of θ = -90º; an air speed of v_a = 2 m/s vertically upwards (φ = 90º); an atmospheric pressure of p_a = 101325 Pa; an ambient temperature of T_a = 288.15 K (15 ºC); a relative humidity of φ_a = 60 % and a water inlet temperature of T_{wi} = 303.15 K (30 ºC). These conditions are typical for rain zones in counterflow natural draught wet-cooling towers.

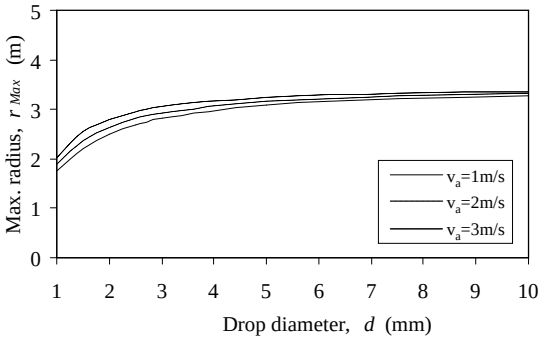

(a_1) Effect of air speed on the maximum spray radius.

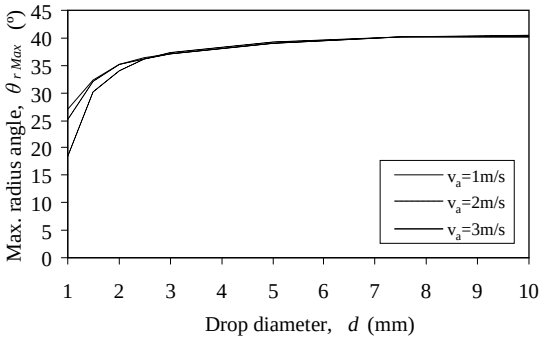

(a_2) Effect of air speed on the angle to achieve maximum spray radius.

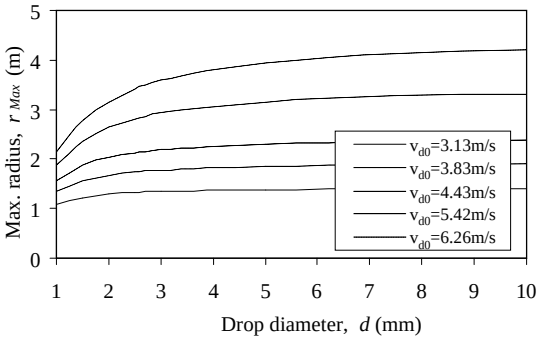

(b_1) Effect of drop speed on the maximum spray radius.

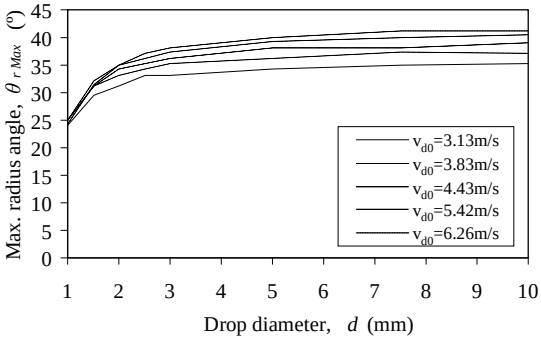

(b_2) Effect of drop speed on the angle to achieve maximum spray radius.

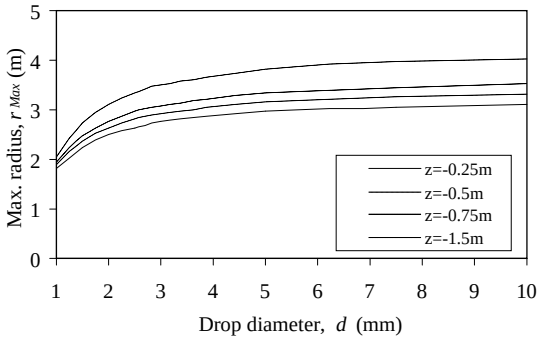

(c_1) Effect of height on the maximum spray radius.

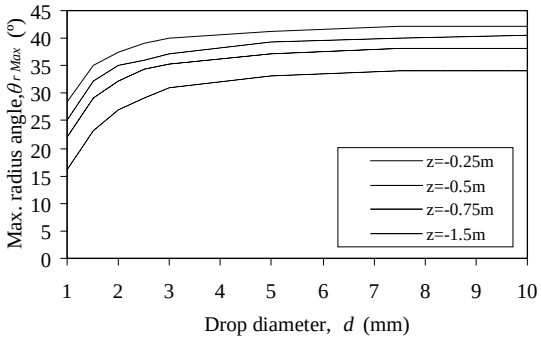

(c_2) Effect of height on the angle to achieve maximum spray radius.

Fig. B.8: Effects of air speed, initial drop speed and distance below the injection point on the maximum spray radius and angle.

Figure B.10(a) shows spherical drop velocity data for different drop diameters plotted against path length, determined using the present analysis. These results are compared to equivalent *FLUENT*® data in Fig. B.10(b), which deviate marginally.

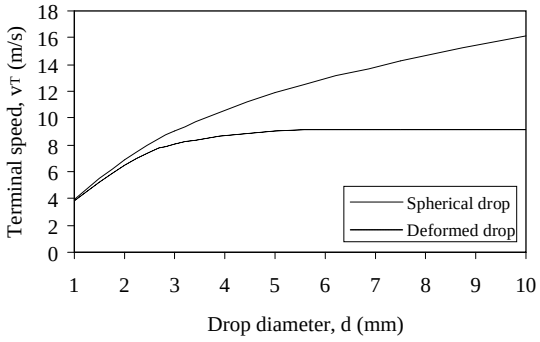

(a) Terminal speed as a function of drop diameter.

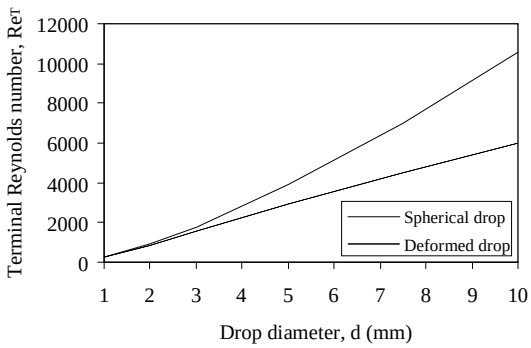

(b) Terminal Reynolds number as a function of drop diameter.

Fig. B.9: Terminal speed and Reynolds number of spherical and deformed drops.

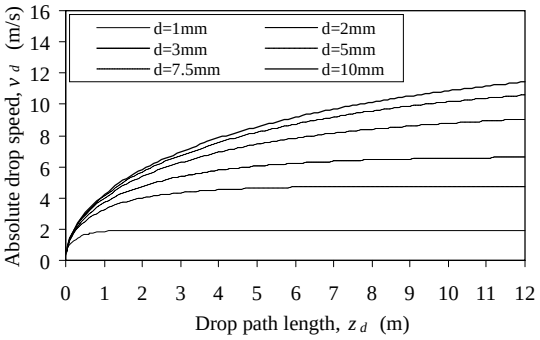

(a) Drop trajectories determined by numerical integration of Eq. (B.1).

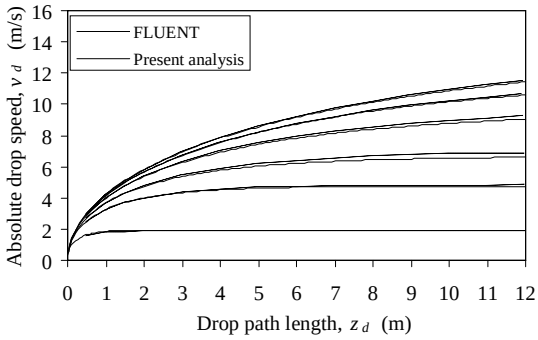

(b) Comparison between present analysis and *FLUENT*® data.

Fig. B.10: Speed of spherical drops falling in counterflow for different drop diameters as a function of path length.

Fig. B.11 shows drop speed, Reynolds number, residence time and loss coefficient plotted against drop path length for spherical and deformed drops. The deformed drops with diameter of $d \geq 5$ mm reach terminal speed at a path length of about $z_d = 5$ m, while the spherical drops do not reach terminal speed over a path length of $z_d = 12$ m. The residence times and loss coefficients of the deformed drops are subsequently higher.

In Fig. B.12, the drop residence time, drop speed and loss coefficient are presented for different air speeds at a path length of $z_d = 10$ m. It can be seen that as the air speed approaches the drop terminal speed of the $d = 1$ mm drop, the residence time rises steeply.

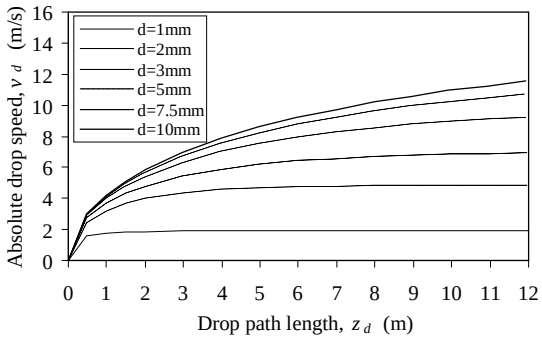

(a) Absolute drop speed (spherical drops).

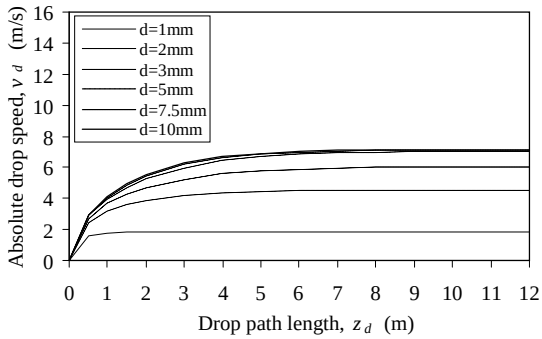

(b) Absolute drop speed (deformed drops).

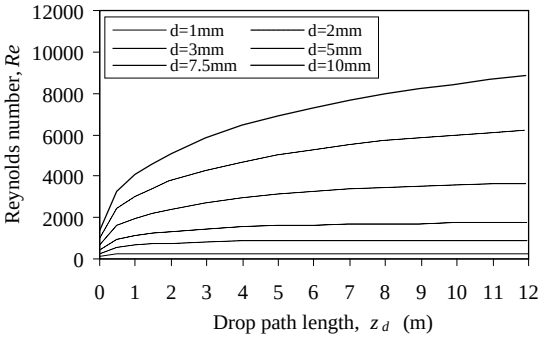

(c) Reynolds number (spherical drops).

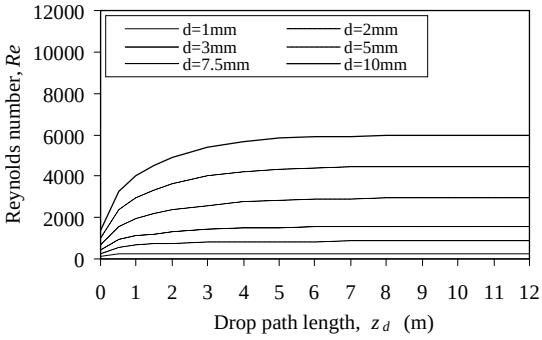

(d) Reynolds number (deformed drops).

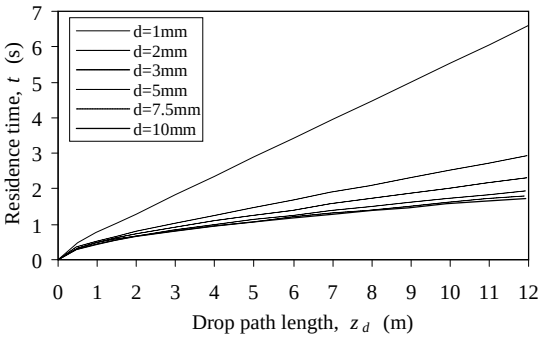

(e) Residence time (spherical drops).

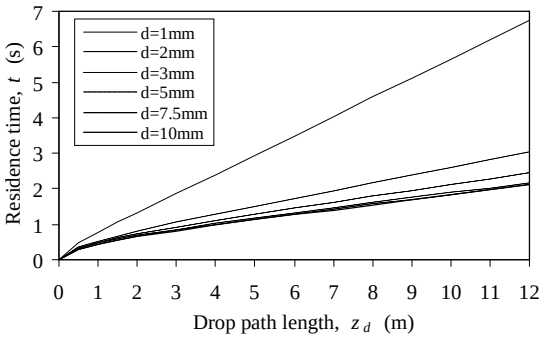

(f) Residence time (deformed drops).

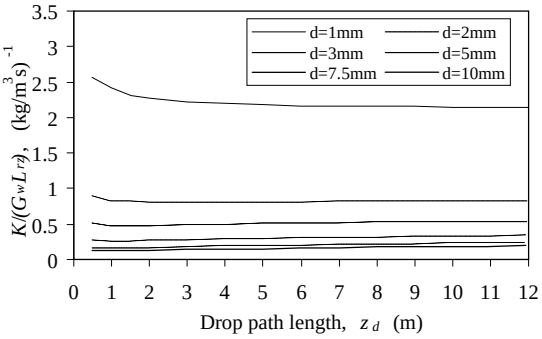

(g) Specific loss coefficient (spherical drops).

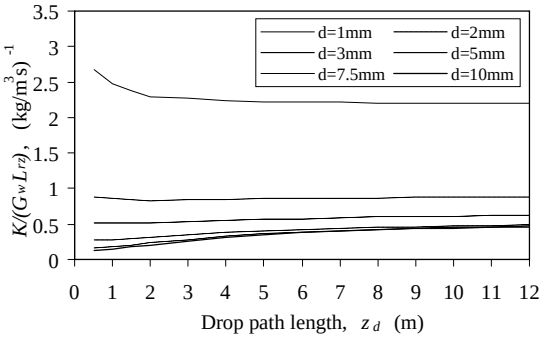

(h) Specific loss coefficient (deformed drops).

Fig. B.11: Drop speed, Reynolds number, residence time and specific loss coefficient plotted against drop path length.

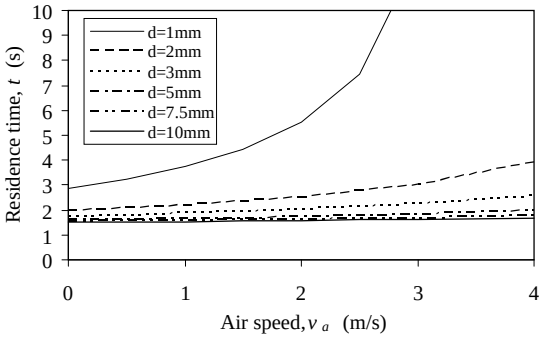

(a) Residence time (spherical drops).

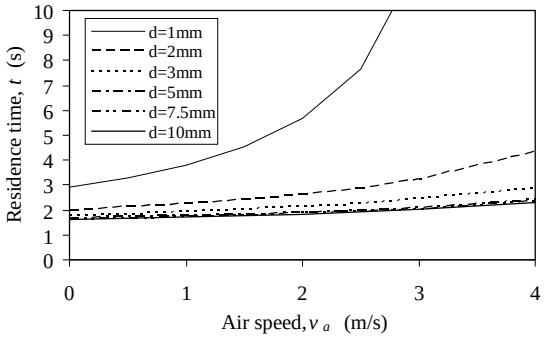

(b) Residence time (deformed drops).

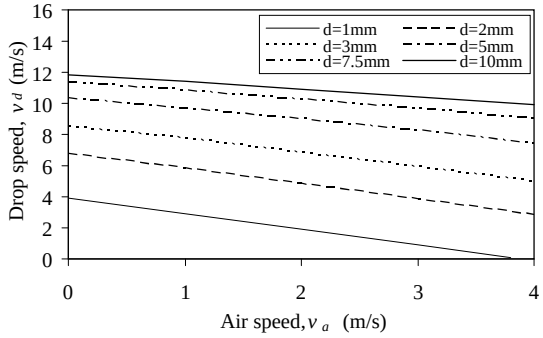

(c) Drop speed (spherical drops).

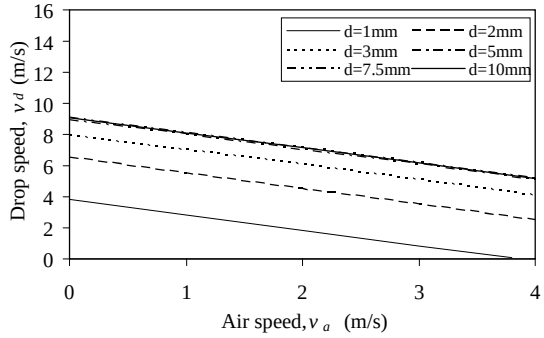

(d) Drop speed (deformed drops).

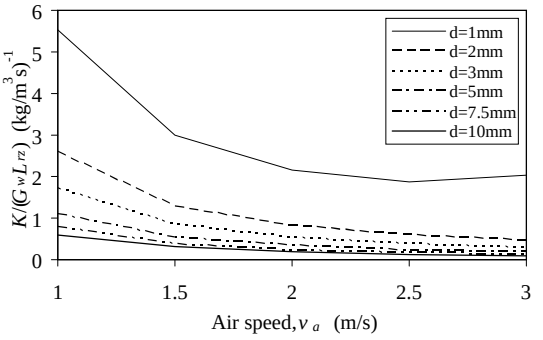

(e) Specific loss coefficient (spherical drops).

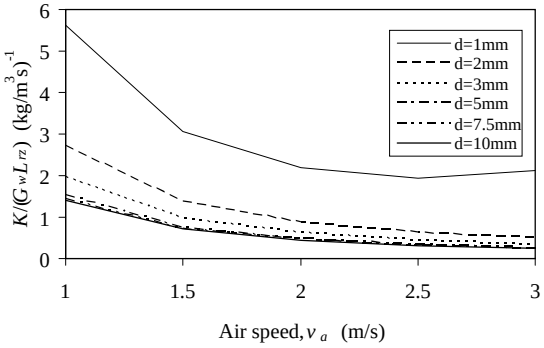

(f) Specific loss coefficient (deformed drops).

Fig. B.12: Effect of air speed on residence time, drop speed and specific loss coefficient determined for a drop motion path length of z_d = 10 m.

Fig. B.13 shows that the effect of initial drop speed on residence time is noticeable, but small with regard to drop speed and loss coefficient.

Fig. B.14 shows the deviation between the loss coefficient data for deformed drops and Eq. (B.21) for different atmospheric pressures and it can be seen that the deviations differ at different atmospheric pressures.

The horizontal deflection of spherical drops due to a horizontal air stream is shown in Fig. B.15 for different drop diameters, where it is found that the deflection of a d = 1 mm drop is twice that of a d = 2 mm drop.

Fig. B.16 shows that the specific loss coefficient for a cross flow rain zone (φ = 0º) is very small and becomes negative at air flow angles of $\varphi \leq$ -5 to -10 º, whereas for a counterflow rain zone the loss coefficient is significant.

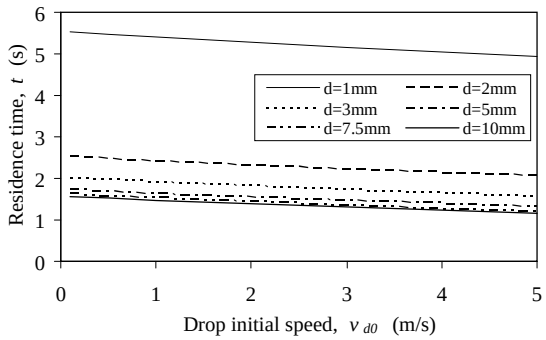

(a) Residence time (spherical drops).

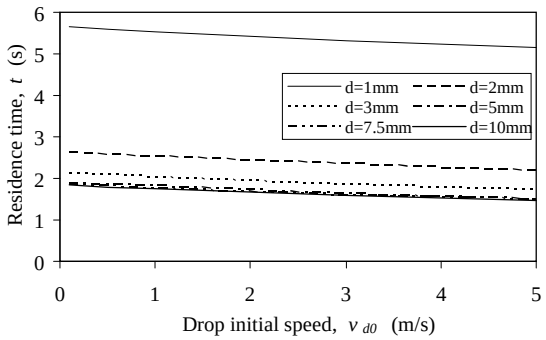

(b) Residence time (deformed drops).

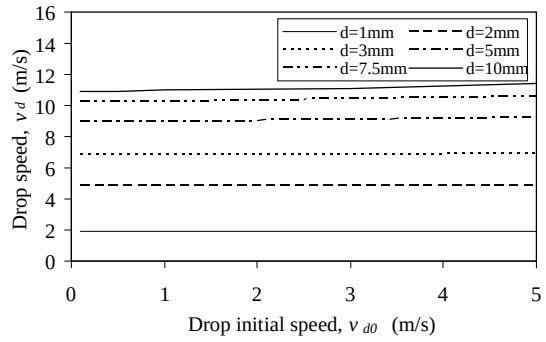

(c) Drop speed (spherical drops).

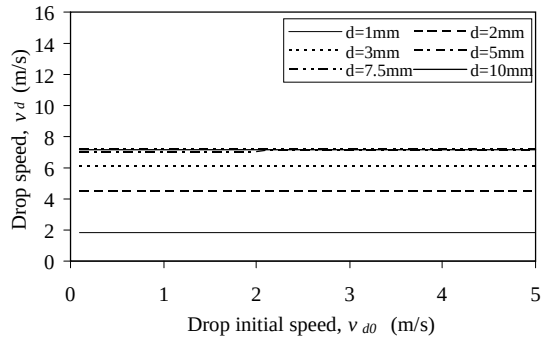

(d) Drop speed (deformed drops).

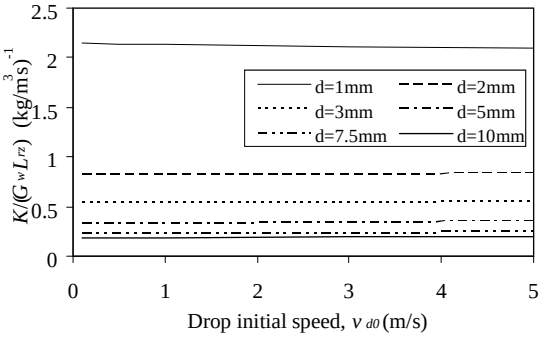

(e) Specific loss coefficient (spherical drops).

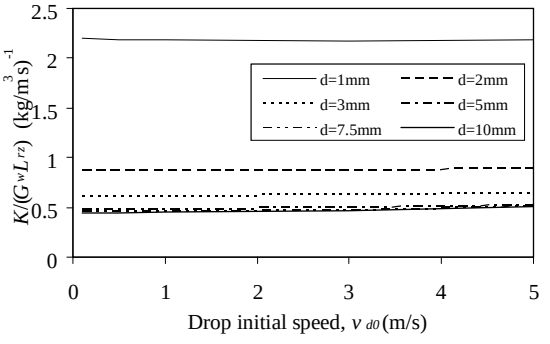

(f) Specific loss coefficient (deformed drops).

Fig. B.13: Effect of initial drop speed on residence time, drop speed and specific loss coefficient determined for a drop motion path length of z_d = 10m.

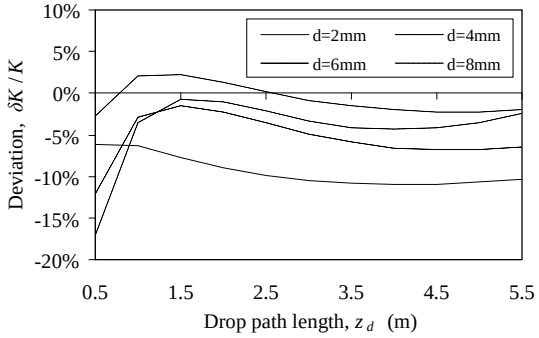

(a) Atmospheric pressure p_a = 101 325 N/m^2.

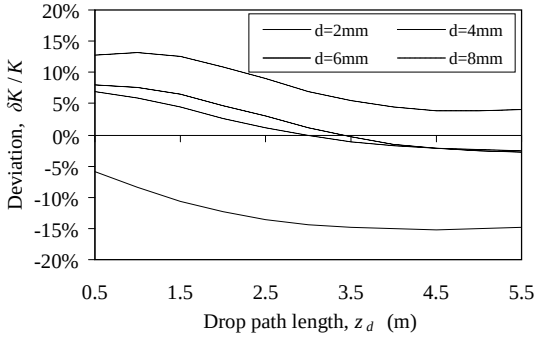

(b) Atmospheric pressure p_a = 85 000 N/m^2.

Fig. B.14: Deviation between loss coefficient data and De Villiers and Kröger (1997) (Eq. B.21).

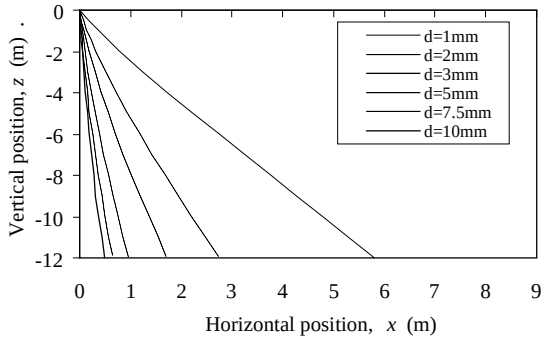

(a) Horizontal air speed v_a = 2 m/s (spherical drops).

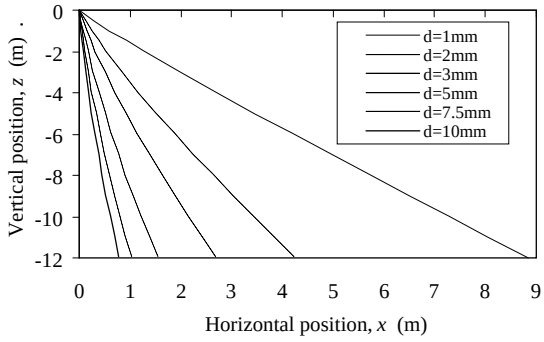

(b) Horizontal air speed v_a = 3 m/s (spherical drops).

Fig. B.15: Horizontal drop deflection caused by horizontal air flow.

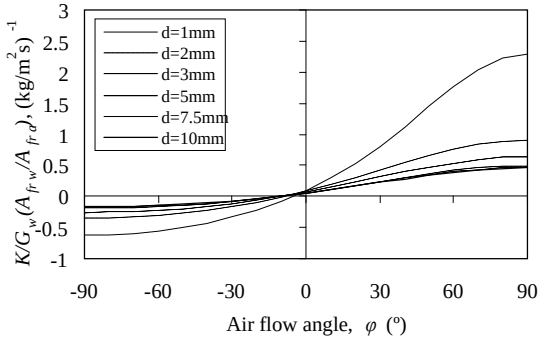

(a) Air speed v_a = 2 m/s (deformed drops).

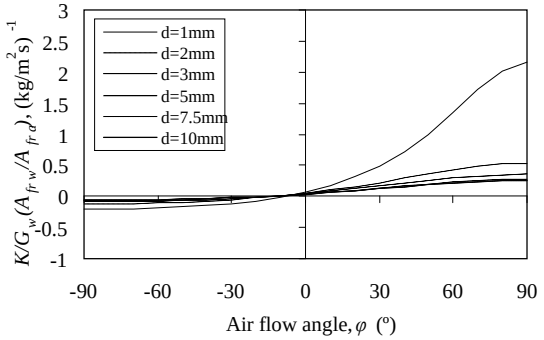

(b) Horizontal air speed v_a = 3 m/s (deformed drops).

Fig. B.16: Specific loss coefficient for different constant air flow angles.

B.6 SUMMARY OF RESULTS

The governing equations of drop motion, based on Newton's 2nd law, are derived and integrated numerically to model single drop motion in a two-dimensional plane for any given drop size, initial drop speed, injection angle, air velocity, vertical distance below the injection point as well as different air and drop thermophysical properties. The results show good comparison with equivalent *FLUENT*® data.

The results obtained for different cases using the above model are summarised as follows:

- ⇨ The effect of air speed on curved up-spray trajectories found in spray zones is significant for small drops (d < 3 mm), however becomes small for larger drop diameters.
- ⇨ The effect of drop diameter on the horizontal travel distance of drops sprayed downwards ($\theta \leq 0^o$) is negligible, whereas for up-spray ($\theta \geq 0^o$) trajectories, the horizontal distance reached by a d = 1 mm drop is considerably less than that of larger drops.
- ⇨ The effect of drop initial speed on the horizontal distance is relatively small for injection angles of $-90^o \leq \theta \leq -30^o$ but is significant for the injection angles of $\theta > -30^o$.
- ⇨ As expected the drop residence time and specific loss coefficient increases with injection angle.
- ⇨ An increase in drop initial speed results in a marginal decrease in drop residence time for injection angles of $\theta < 0^o$ as opposed to large increases for $\theta > 0^o$.
- ⇨ The empirical loss coefficient equation proposed by Kröger (2004), based on the data of Lowe and Christie (1961) compares favourably with corresponding downspray data for a d = 1mm drop at higher initial drop speeds.
- ⇨ The effect of drop deformation on curved spray trajectories is found to be negligible.
- ⇨ The injection angle producing the furthest drop trajectory varies between $15^o \leq \theta_{max} \leq 40^o$ depending on drop diameter, air speed, initial drop speed and distance below the injection point.
- ⇨ The terminal speed of deformed drops is constant for drop diameters d > 5 mm whereas it continues to increase with an increase in diameter in the case of spheres.
- ⇨ In a rain zone with a height of H_{rz} = 12 m, d > 5 mm spherical drops would not reach terminal speed, whereas real (deformed) drops reach terminal speed at about 5 m falling distance.
- ⇨ Deformed drops with drop diameters of d ≥ 5 mm therefore have the same speed, residence time and specific loss coefficient.

- ⇨ The speed, residence time and loss coefficient of spherical and deformed drops with corresponding diameters are the same in the range of drop diameters of $d \leq 3$ mm.
- ⇨ The effect of air speed on drop residence time, drop speed and loss coefficient is particularly large for a d = 1 mm drop as the air speed approaches the drop terminal speed. The effect decreases with an increase in drop diameter.
- ⇨ An increase in initial drop speed shows a slight decrease in residence time, but the effect on drop speed and loss coefficient is negligible.
- ⇨ The deviation between the loss coefficient data and Eq. (B.21) by De Villiers and Kröger (1997), shows that the present analysis generally predicts higher loss coefficients and that atmospheric pressure is not correlated consistently.
- ⇨ The effect of horizontal air speed on the horizontal deflection of spherical drops shows that for v_a = 2 m/s, the deflection ratio of a d = 1 mm drop is about x/z = 0.5 whereas for a d = 2 mm drop it is in the order of x/z = 0.25. For an air speed of v_a = 3 m/s, the displacement ratio of a d = 1 mm drop is about x/z = 0.667 whereas for a d = 2 mm drop it is in the order of x/z = 0.333.
- ⇨ The specific loss coefficient decreases with air flow angle (φ), becoming negative at angles $\varphi < 0^o$. The exact angle is dependent on the absolute air and drop speeds.

B.7 CONCLUSIONS

The trajectories and loss coefficients of small drops (d = 1 to 3mm) are more sensitive to changes in air flow than larger drops. The main reason is that the drop drag to body force ratio increases with a decrease in drop diameter. The body force for a given drop size is essentially constant whereas the drag is a function of the air speed relative to the drop, which is dependent on absolute air velocity and absolute drop velocity.

The main function of a cooling tower spray nozzle system is to distribute water uniformly onto the fill material inside the tower while also enhancing the cooling capability of the cooling tower at minimum life cycle costs. The ultimate spray nozzle must therefore produce small drops with a predictable spray pattern and a large spray radius while consuming minimal pumping power. From the above results it can be seen that down-spray ($\theta \leq 0^o$) drop trajectories are least sensitive to drop diameter, air speed and initial drop speed required for predictable flow patterns, whereas up-spray trajectories ($\theta > 0^o$) give the largest spray radii but also have the largest loss coefficients. Furthermore, it can be seen that a spray radius of r_{max} = 1.4 m can be achieved at a distance z = -0.5 m below the nozzle with a pressure head over the nozzle of 0.5 m.

A rain zone should reject heat without excessive pressure drop. From the above results, it can be seen that loss coefficient of counterflow rain zones increases with a reduction in drop diameter and air speed. For cross-counterflow rain zones, it is

however found that a decrease in air flow angle from $\varphi = 90^{o}$ to -90^{o} results in a decrease in loss coefficient, which actually becomes negative at flow angles $\varphi < 0^{o}$, where the exact angle is a function of the drop diameter and the absolute air and drop speeds. The effect of a reduction in loss coefficient is that higher air speeds can be achieved through the rain zone for the same air-side draught power consumption, depending on the $A_{fr,a}/A_{fr,w}$ ratio.

C

ANALYSIS OF DROP COOLING

In this section, the governing differential equation for cooling of a single drop by air flow is derived and solved numerically simultaneously with the motion equations presented in Appendix B, to determine single drop temperature and transfer characteristic (Merkel number) for any given drop size, initial drop speed, injection angle, air velocity, vertical distance relative to the injection point as well as different air and drop thermophysical properties. This analysis is validated with the aid of equivalent data obtained using *FLUENT*® (version 6.2.16), and is implemented to investigate the effects of the following on drop cooling and transfer characteristics (Merkel number):

- ⇨ Injection angle, injection speed, drop diameter, path length and air velocity.
- ⇨ Different drag coefficient relations.
- ⇨ Different heat and mass transfer coefficient relations.
- ⇨ Different diffusion coefficient relations.
- ⇨ Different definitions for determining the rate of mass transfer.
- ⇨ Different relations for the Lewis factor.

Although interactions between drops due to collisions are ignored, the results obtained provide insight into the performance of spray and rain zones and are also used to validate results in later sections.

C.1 GOVERNING DIFFERENTIAL EQUATION OF DROP COOLING

Consider a control surface defined on the water-air interface of a spherical drop, as shown in Fig. C.1.

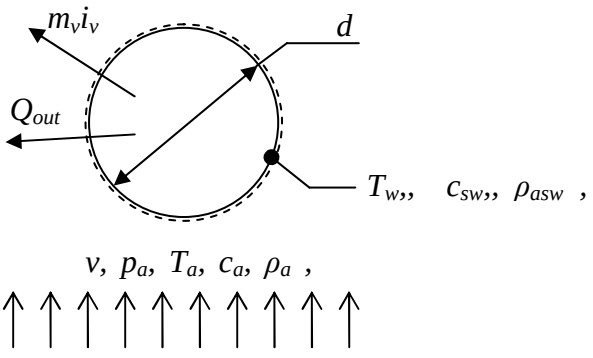

Figure C.1: Control surface around a spherical drop falling through air.

From the first law of thermodynamics, the energy balance for an open system (drop) in an unsteady flow process is given by

$$\begin{aligned}\frac{d\left(M_d u\right)}{dt} &= u\frac{dM_d}{dt} + M_d\frac{du}{dt} \\ &= \left(Q_{in} + W_{in} + \sum m_{in} i_{in}\right) - \left(Q_{out} + W_{out} + \sum m_{out} i_{out}\right)\end{aligned} \tag{C.1}$$

which, for the drop in Fig. C.1, simplifies to

$$u\frac{dM_d}{dt} + M_d\frac{du}{dt} = -Q_{out} - m_v i_v \tag{C.2}$$

By applying Fick's law, the mass transfer from the drop to the surrounding air (mass flow rate of vapour crossing the control surface) may be determined by means of the following relation for isothermal conditions and small partial pressures relative to the absolute pressure,

$$\begin{aligned}\frac{dM_d}{dt} &= -m_v \\ &= -h_D A\left(c_{sw} - c_a\right) = -h_D A\left(\rho_{vsw} - \rho_v\right) \approx -\frac{h_D A}{R_v T}\left(p_{vsw} - p_v\right)\end{aligned} \tag{C.3}$$

For larger partial pressures the following equation, which is used by Bosnjakovic (1965) to determine the Lewis factor, includes the effect of bulk flow away from the drop surface to yield higher mass transfer rates than Eq. (C.3):

$$\frac{dM_d}{dt} = -h_D A\frac{p}{R_v T}\ln\left(\frac{p - p_v}{p - p_{vsw}}\right) \tag{C.4}$$

For non-isothermal mass transfer when there is heat and mass transfer taking place, Incropera and DeWitt (1996) recommend using the following relation, which is also employed by *FLUENT*®:

$$\frac{dM_d}{dt} = -h_D A\left(\rho_{vsw} - \rho_v\right) = -\frac{h_D A}{R_v}\left(\frac{p_{vsw}}{T_w} - \frac{p_v}{T_a}\right) \tag{C.5}$$

Another form may be obtained by assuming that T_w and T_a are approximately equal to the mean temperature $T_{am} = (T_w + T_a)/2$, and it follows that

$$\frac{dM_d}{dt} \approx -\frac{h_D A}{R_v T_{am}}\left(p_{vsw} - p_v\right) \tag{C.6}$$

A alternative definition for the mass transfer coefficient, used in the Merkel (1925) method of analysis for the evaluation of cooling tower fills, is given as

$$\frac{dM_d}{dt} = -h_d A\left(w_{sw} - w\right) \tag{C.7}$$

The heat transfer from the drop to the air (Q_{out}) is attributed mainly to convection, which according to Newton's law of cooling, is defined as

$$Q_{out} = hA(T_w - T_a) \tag{C.8}$$

The specific internal energy of the system is defined as

$$u = c_v T_w \approx c_p T_w \tag{C.9}$$

Substitute equations (C.3), (C.8) and (C.9) into Eq. (C.2) to obtain the following differential equation for the rate of temperature change of the drop:

$$\frac{dT_w}{dt} = \frac{1}{M_d c_{pw}} \left[i_{fg} \frac{dM_d}{dt} - hA\left(T_w - T_a\right) \right] \tag{C.10}$$

The fluid properties are calculated at the mean temperature (T_{am}) using the equations given in Appendix A.

C.2 SOLUTION METHOD

The Euler method, based on a first order Taylor series expression (Eq. C.11), is used to solve the above differential equation. The drop trajectory is divided into equal time increments (Δt) and the drop temperature is determined at a certain time interval ($t+\Delta t$) by using the available temperature and rate of temperature change values for the previously determined time interval t, repeating this operation until the required number of iterations are reached.

$$T^{t+\Delta t} = T^t + \left.\frac{dT}{dt}\right|^t \Delta t \tag{C.11}$$

C.3 HEAT AND MASS TRANSFER COEFFICIENTS

Various semi-empirical relations for the convection heat transfer coefficient of drops or spherical particles moving relative to a surrounding fluid are found in literature. For small single drops suspended in an air-stream, Ranz and Marshall (1952) present the following well-known relation:

$$Nu = 2 + 0.6 Re^{1/2} Pr^{1/3} \quad \text{for} \quad 2 \le Re \le 800 \tag{C.12}$$

A similar relation for spheres given by Rowe et al. (1965) which is valid over a slightly wider range of Reynolds numbers, is written as

$$Nu = 2 + 0.69 Re^{1/2} Pr^{1/3} \quad \text{for} \quad 20 \le Re \le 2000 \tag{C.13}$$

Martin (2005) proposes a relation for spheres that is valid for an extensive range of Reynolds numbers and includes the effect of freestream turbulence on the Nusselt number, expressed as

$$\mathrm{Nu} = 2 + 0.4038\left(\mathrm{c_F\,Re^2\,Pr}\right)^{1/3} \quad \text{for} \quad 10^{-1} \le Re \le 10^6 \quad \text{and} \quad 0.6 \le Sc \le 7000 \tag{C.14}$$

where c_F is a friction factor expressed as

$$c_F = \frac{16}{Re} + \frac{3.73}{Re^{1/2}} + c_N \tag{C.15}$$

The value of the friction factor constant, c_N, corresponds to the free stream turbulence level e.g. c_N = 0.03 for a turbulence level of Tu = 3 %.

Another correlation for spheres, recommended by Whitaker (1972), is

$$Nu = 2 + \left(0.4Re^{1/2} + 0.06Re^{2/3}\right) Pr^{0.4} \left(\frac{\mu}{\mu_s}\right)^{1/4} \quad \text{(C.16)}$$

for $0.71 < Pr < 380$, $3.5 < Re < 7.6\times10^4$ and $1.0 < \mu/\mu_s < 3.2$

The thermophysical properties for Eq. (C.16) are determined at free stream conditions and μ_s at surface conditions, as opposed to the other equations above which are evaluated at mean temperature conditions.

For heat transfer to or from a drop accelerating in air, Yao and Schrock (1976) proposed the following equation:

$$Nu = 2 + g_{YS}\left(0.6Re^{1/2}Pr^{1/3}\right) \quad \text{for} \quad Re < 2500 \quad \text{(C.17)}$$

where

$$g_{YS} = 25\left(z/d\right)^{-0.7} \quad \text{for} \quad 10 < z/d < 600 \quad \text{(C.18)}$$

Erens *et al.* (1994) obtained more accurate correlations for the data of Yao and Schrock (1976), given as

$$g_{YS} = 2.32\left(\frac{z}{d}\right)^{-0.16} \quad \text{for } 10 < \left(\frac{z}{d}\right) < 600 \quad \text{(C.19)}$$

and

$$g_{YS} = 0.22 + 3.15\left[\frac{\left(dv/dt\right)d}{v^2}\right]^{0.2}\left(\frac{d}{d_m}\right)^{0.2} \quad \text{for} \quad \frac{\left(dv/dt\right)d}{v^2} > 5\times10^{-4} \quad \text{(C.20)}$$

where d_m is the maximum stable diameter of a drop before it breaks up, determined from

$$d_m = \sqrt{\frac{16\sigma}{g\left(\rho_w - \rho_a\right)}} \quad \text{(C.21)}$$

According to the analogy between convection heat transfer and mass transfer, limited to isothermal conditions, the above relations may be applied to mass transfer problems by merely replacing *Nu* and *Pr* in Eqs (C.12) to (C.17) with *Sh* and *Sc* respectively to yield the following relations:

Ranz and Marshall (1952):

$$Sh = 2 + 0.6Re^{1/2}Sc^{1/3} \quad \text{for} \quad 2 < Re < 800 \quad \text{(C.22)}$$

Rowe et al. (1965):

$$Sh = 2 + 0.69Re^{1/2}Sc^{1/3} \quad \text{for} \quad 20 < Re < 2000 \quad \text{(C.23)}$$

Martin (2005):

$$Sh = 2 + 0.4038\left[\left(\frac{16}{Re} + \frac{3.73}{Re^{1/2}} + c_N\right) Re^2 Sc\right]^{1/3} \quad \text{for} \quad 10^{-1} \le Re \le 10^6 \quad \text{and} \quad 0.6 \le Sc \le 7000 \tag{C.24}$$

Whitaker (1972):

$$Sh = 2 + \left(0.4 Re^{1/2} + 0.06 Re^{2/3}\right) Sc^{0.4} \left(\frac{\mu}{\mu_s}\right)^{1/4} \tag{C.25}$$

for $0.71 < Pr < 380$, $3.5 < Re < 7.6 \times 10^4$ and $1.0 < \mu/\mu_s < 3.2$

Yao and Schrock (1976):

$$Sh = 2 + g_{YS}\left(0.6 Re^{1/2} Sc^{1/3}\right) \quad \text{for} \quad Re < 2500 \tag{C.26}$$

Çengel (2003) stated that this analogy can be used with confidence in processes that involve the evaporation of water into air, such as in wet cooling towers.

The mass transfer coefficient h_D, in equations (C.3) to (C.6), can be calculated from the Sherwood number, defined as

$$Sh = \frac{h_D d}{D} \tag{C.27}$$

Merkel (1925) theory however utilises the mass transfer coefficient h_d, as defined in Eq. (C.7). The relationship between the mass transfer coefficients h_D and h_d therefore depends on which of the equations (C.3) to (C.6) is employed and can be expressed in terms of either vapour pressure or humidity ratio with the aid of the following relation for vapour pressure:

$$p_v = \frac{p\, w}{w + 0.622} \tag{C.28}$$

From Eqs (C.3) and (C.7), it follows that the relation between h_D and h_d is given by

$$h_d = \frac{h_D}{R_v T}\frac{\left(p_{vsw} - p_v\right)}{\left(w_{sw} - w\right)} = \frac{h_D p}{R_v T\left(w_{sw} - w\right)}\left[\frac{w_{sw}}{\left(w_{sw} + 0.622\right)} - \frac{w}{\left(w + 0.622\right)}\right] \tag{C.29}$$

For Eq. (C.5) the following relation is obtained:

$$h_d = \frac{h_D}{R_v\left(w_{sw} - w\right)}\left(\frac{p_{vsw}}{T_w} - \frac{p_v}{T_a}\right) = \frac{h_D p}{R_v\left(w_{sw} - w\right)}\left[\frac{w_{sw}}{\left(w_{sw} + 0.622\right)T_w} - \frac{w}{\left(w + 0.622\right)T_a}\right] \tag{C.30}$$

For larger mass transfer rates (Eq. C.4), Poppe (1991) derived the following expression based on isothermal conditions:

$$h_d = \frac{h_D}{R_v T\left(w_{sw} - w\right)} ln\left(\frac{p - p_v}{p - p_{vsw}}\right) = \frac{h_D p}{R_v T\left(w_{sw} - w\right)} ln\left(\frac{w_{sw} + 0.622}{w + 0.622}\right) \tag{C.31}$$

The Lewis factor (Le_f) provides a useful direct relationship between the convection heat transfer coefficient (h) and mass transfer coefficient (h_d), defined as

$$Le_f = h/\left(c_{pma} h_d\right) \tag{C.32}$$

In Merkel (1925) theory, extensively used today for the evaluation of fill performance characteristics, the Lewis factor is assumed to be Le_f = 1. Bosnjakovic (1960) derived an equation for the Lewis factor based on Eq. (C.4) and the assumption that the Sherwood number can be expressed by $Sh = C\,Re^m\,Sc^n$, written as

$$Le_f = \frac{h}{h_d\ c_p} = \left(\frac{k_{av}(1+w)}{\rho_{av} c_p D}\right)^{1-n} \left(\frac{v_a}{v_{av}}\right)^{m-n} \left(\frac{w_{sw}+0.622}{w+0.622}-1\right)/ln\left(\frac{w_{sw}+0.622}{w+0.622}\right) \tag{C.33}$$

Kröger (2004) gives the following simplified version of this equation:

$$Le_f \approx 0.866^{0.667}\left(\frac{w_{sw}+0.622}{w+0.622}-1\right)/ln\left(\frac{w_{sw}+0.622}{w+0.622}\right) \tag{C.34}$$

C.4 TRANSFER CHARACTERISTIC OR MERKEL NUMBER

Merkel (1925) proposed the following dimensionless number to characterise fills known as the transfer characteristic or Merkel number, defined as

$$Me = \frac{\bar{h}_d A}{m_w} = \frac{\bar{h}_d a_{fi} A_{fr} L_{fi}}{m_w} = \frac{\bar{h}_d a_{fi} L_{fi}}{G_w} = \int_{T_{wo}}^{T_{wi}} \frac{c_{pw} dT_w}{\left(i_{masw} - i_{ma}\right)} \tag{C.35}$$

For the present single drop analysis, the Merkel number can be obtained by determining the mean mass transfer coefficient from

$$\bar{h}_d = \frac{1}{t}\int_0^t h_d \mathrm{d}t \tag{C.36}$$

and the drop mass flow rate from

$$m_w = \frac{\rho_w \pi d^3}{6\,t} = \frac{\rho_w \pi d^3 z_d}{6\,\bar{v}_d} \tag{C.37}$$

The drop surface area is

$$A = \pi d^2 \tag{C.38}$$

For the characterisation of spray, fill and rain zones from experimental data measured in a test facility or if the air inlet and water inlet and outlet conditions are known, the last term of Eq. (C.35) can be solved by means of the Chebyshev integration method for counterflow conditions, given in Kröger (2004).

For the spray zone above the fill, Kröger (2004) gives a correlation for the data of Lowe and Christie (1961) for down-spray of d = 1mm drops, written as

$$Me_{sp} = 0.2 L_{sp}\left(\frac{G_a}{G_w}\right)^{0.5} \tag{C.39}$$

For a purely counterflow rain zone, De Villiers and Kröger (1997) present the following equation for the Merkel number, based on: Eq. (B.12) for the drag

coefficient of deformed drops; Eqs (C.22) and (C.31) for the mass transfer coefficient; a Lewis factor, Le_f = 1 to determine the convection heat transfer coefficient; and Eq. (41) for the diffusion coefficient:

$$\begin{aligned} Me_{rz} = 3.6&\left(\frac{p_a}{R_v T_a \rho_w}\right)\left(\frac{D}{v_{azo} d_d}\right)\left(\frac{H_{rz}}{d_d}\right) Sc^{0.33}\left[\ln\left(\frac{w_s + 0.622}{w + 0.622}\right)/(w_s - w)\right] \\ &\times\left[5.01134 a_\rho \rho_a - 192121.7 a_\mu \mu_a - 2.57724 + 23.61842\left(0.2539\left(a_v v_{azo}\right)^{1.67} + 0.18\right)\right. \\ &\left.\times\left(0.8366\left(a_L H_{rz}\right)^{-0.5299} + 0.42\right)\left(43.0696\left(a_L d_d\right)^{0.7947} + 0.52\right)\right] \end{aligned} \quad \text{(C.40)}$$

where

$a_\mu = 3.061\times10^{-6}\left(\rho_w^4 g^6/\sigma_w\right)^{0.25}$, $a_\rho = 998/\rho_w$, $a_v = 73.298\left(g^5\sigma_w^3/\rho_w^3\right)^{0.25}$ and $a_L = 6.122\left(g\sigma_w/\rho_w\right)^{0.25}$

Eq. (C.40) is valid under the following conditions:

$0\,^\circ\text{C} \le T_a \le 40\,^\circ\text{C}$, $10\,^\circ\text{C} \le T_w \le 40\,^\circ\text{C}$

$0.927\ \text{kg/m}^3 \le \rho_a \le 1.289\ \text{kg/m}^3$, $992.3\ \text{kg/m}^3 \le \rho_w \le 1000\ \text{kg/m}^3$

$1.717\times10^{-5}\ \text{kg/ms} \le \mu_a \le 1.92\times10^{-5}\ \text{kg/ms}$

$0.0696\ \text{N/m} \le \sigma_w \le 0.0742\ \text{N/m}$, $0.002\ \text{m} \le d_d \le 0.008\ \text{m}$, $9.7\ \text{m/s}^2 \le g \le 10\ \text{m/s}^2$

$0.5\ \text{m} \le H_{rz} \le 5.5\ \text{m}$ and $1\ \text{m/s} \le v_{azo} \le 5\ \text{m/s}$

C.5 DIFFUSION COEFFICIENT

According to Fick's law of steady-state diffusion, which is the molecular transport of mass without flow, the binary diffusion coefficient or mass diffusivity (D) is a constant of proportionality that relates the diffusion mass flux of one species in a stagnant binary gas mixture, consisting of only two species, to the local concentration gradient of that species. Gilliland (1934) proposed a semi-empirical equation for the diffusion coefficients in gases *a* and *b*, based on kinetic theory, given in Kröger (2004) as

$$D = 0.04357\frac{\left(1/M_a + 1/M_b\right)^{0.5}}{\left(V_a^{0.333} + V_b^{0.333}\right)^2}\frac{T^{1.5}}{p} \quad \text{(C.41)}$$

where M is the molecular mass and V is the molecular volume. For air, M_a = 28.97 and V_a = 29.9 and for water vapour, M_b = 18.016 and V_b = 18.8.

This equation is referenced in a number of books (Rohsenow and Choi 1961, Kröger 2004, Perry 1999).

A similar semi-empirical correlation developed by Fuller *et al.* (1966) for air-vapour mixtures is recommended in Bejan (1993), Perry (1999) and the VDI Wärmeatlas (2006), which according to the VDI Wärmeatlas (2006) is expressed as

$$D = 0.0143 \frac{\left(1/M_a + 1/M_b\right)^{0.5}}{\sqrt{2}\left[\left(\sum \Delta_{v_a}\right)^{0.333} + \left(\sum \Delta_{v_b}\right)^{0.333}\right]^2} \frac{T^{1.75}}{p} \qquad \text{(C.42)}$$

where M is the molecular mass and v is the atomic diffusion volume. For air, M_a = 28.9583 g/mol and $\Sigma\Delta_{va}$ = 19.7 and for water vapour, M_v = 18.016 g/mol and $\Sigma\Delta_{vb}$ = 13.1.

Bejan gives a simplified version, written as

$$D \cong D_0 \left(\frac{T}{T_0}\right)^{1.75} \frac{p_0}{p} = 1.233 \times 10^{-4} \frac{T^{1.75}}{p} \qquad \text{(C.43)}$$

where $T_0 = 298\ \text{K}$ and $p_0 = 101325\ \text{Pa}$

According to Mills (1995), the following formula has been used widely for many years particularly for water vapour-air mixtures:

$$D = 1.97 \times 10^{-5} \left(\frac{101325}{p}\right)\left(\frac{T}{256}\right)^{1.685} \quad \text{for} \quad 273\ \text{K} \le T \le 373\ \text{K} \qquad \text{(C.44)}$$

A more recent relation by Marrero and Mason (1972) is expressed as

$$D = 1.895 \times 10^{-5} \frac{T^{2.072}}{p} \quad \text{for} \quad 273\ \text{K} \le T \le 373\ \text{K} \qquad \text{(C.45)}$$

C.6 NUMERICAL DATA AND DISCUSSION OF RESULTS

Fig. C.2(a) shows the values of *Nu* (*Pr* = 0.7) and *Sh* (*Sc* = 0.6) obtained using the equations from Section C.3, for *Re* < 10 000, as applicable to drops in a rain zone. Eq. (C.12) by Ranz and Marshall (1952) is used by *FLUENT*® (version 6.2.16) and is therefore taken as reference to show the deviation between the different models, as presented in Fig. C.2(b). The deviations for *Nu* and *Sh* are virtually the same and therefore no secondary axis is given in this figure.

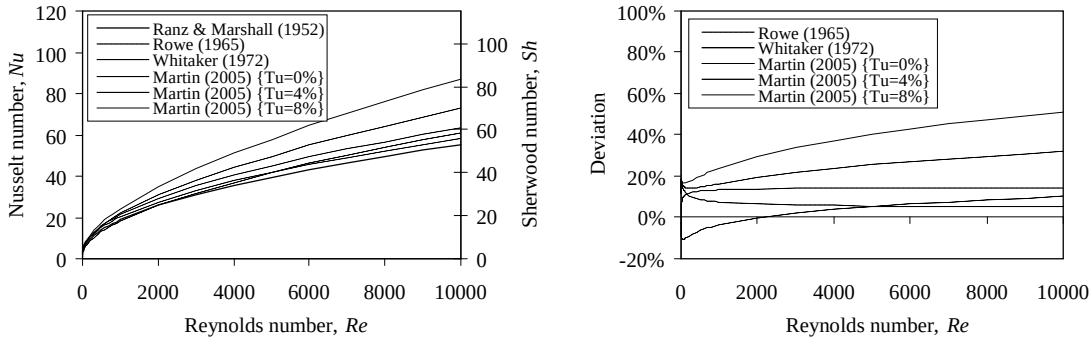

(a) Nusselt and Sherwood number in terms of Reynolds number.

(b) Deviation from Eq. (C.12) (Ranz and Marshall, 1952).

Figure C.2: Comparison between different relations for Nusselt and Sherwood numbers.

It can be seen that the equations of Ranz and Marshall (1952), Whitaker (1972) and Martin (2005) {*Tu* = 0%} differ by less than 10%. At higher free stream turbulence levels (Tu = 4% and 8%), Martin gives respectively up to 20 % and 40 % higher values for *Nu* and *Sh*.

According to Fig. C.3, the diffusion coefficients predicted using the equations in Section C.5 by Fuller, Mills (1995) and Marrero and Mason (1972) are clustered together and differ from Gilliland (1934) by more than 20%.

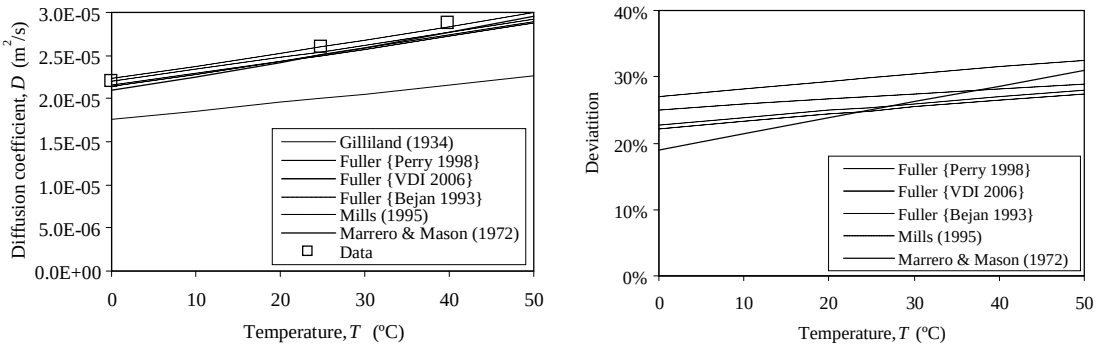

(a) Binary diffusion coefficient in terms of temperature. (b) Deviation from Gilliland (1934).

Figure C.3: Comparison between different relations for the binary diffusion coefficient.

Fig. C.4 shows the temperature change, $\Delta T_w = (T_{wi} - T_w)$ and Merkel number, *Me*, of single drops between the injection point (z = 0 m) and a level z = -0.5 m below it, for different injection angles (θ), drop diameters (d) and initial velocities (v_{d0}). The data in figures C.4(a) and C.4(b) are determined using the above analysis for initial drop speeds of v_{d0} = 3.13 m/s and 5.425 m/s corresponding to a pressure head of 0.5 m and 1.5 m respectively and Fig. C.4(d) shows the temperature deviation between Fig C.4(b_1) and corresponding results obtained with *FLUENT*®, which are seen to be small. As in section B.4, the data is based on an air speed of v_a = 2 m/s vertically upwards; an atmospheric pressure of p_a = 101325 Pa; an ambient temperature of T_a = 305.15 K; a relative humidity of φ_a = 100% and a water inlet temperature of T_{wi} = 313.15 K. For comparison with *FLUENT*® data the following models are used: the Turton and Levenspiel (1986) relation for the drag coefficient (Eq. B.9); the Ranz and Marshall (1952) relations for the heat and mass transfer coefficients (Eqs C.12 and C.22); the Fuller (VDI, 2006) relation for the diffusion coefficient (Eq. C.42); and Eq. (C.5) for determining the rate of mass transfer.

Fig. C.4(c) shows that an increase in initial drop speed results in a smaller temperature change for injection angles $\theta < -10^o$ with respect to the horizontal and larger temperature change for larger angles.

Fig. C.4(a_2) and C.4(b_2) show the transfer characteristics (Merkel numbers) corresponding to the data presented in Fig. C.4(a_1) and C.4(b_1) respectively. It can be seen that the smaller drops ($d \leq 3$ mm) and up-spray trajectories have much

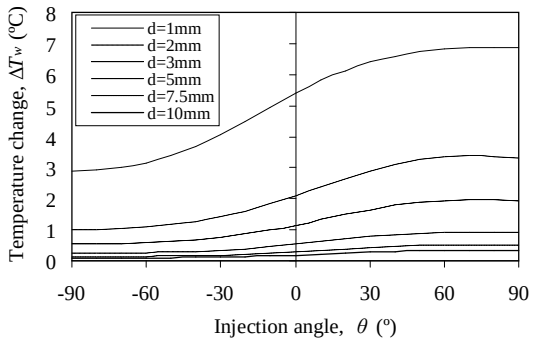

(a_1) Temperature change (initial drop speed of v_{do} = 3.13 m/s).

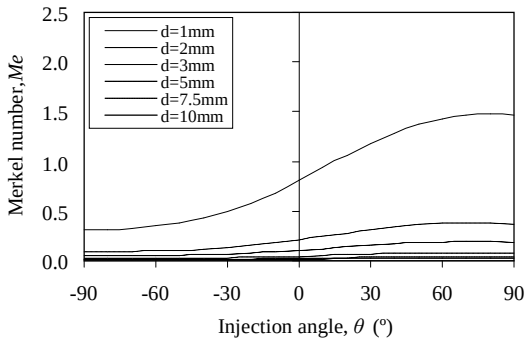

(a_2) Merkel number (initial drop speed of v_{do} = 3.13 m/s).

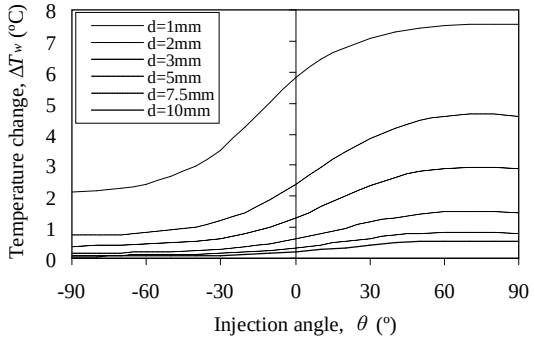

(b_1) Temperature change (initial drop speed of v_{do} = 5.425 m/s).

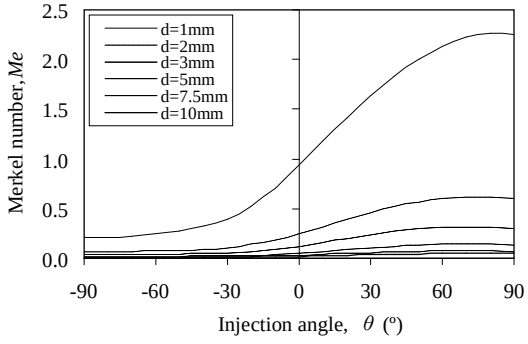

(b_2) Merkel number (initial drop speed of v_{do} = 5.425 m/s).

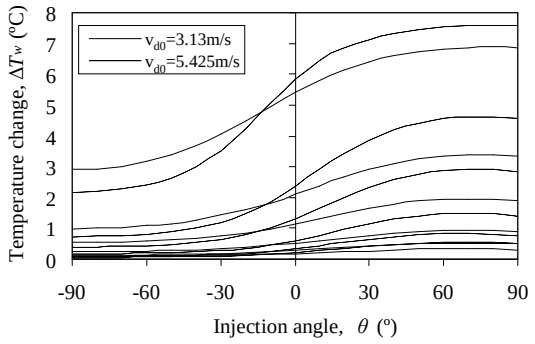

(c_1) Temperature change
(v_{do} = 3.13 m/s and v_{do} = 5.425 m/s).

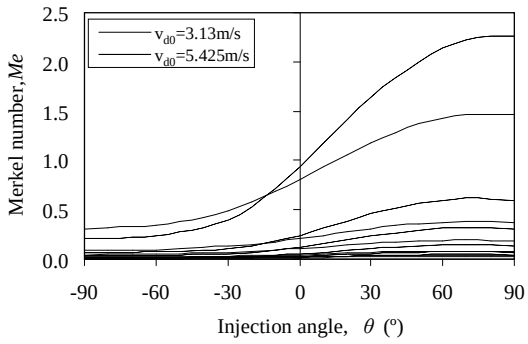

(c_2) Merkel number
(v_{do} = 3.13 m/s and v_{do} = 5.425 m/s).

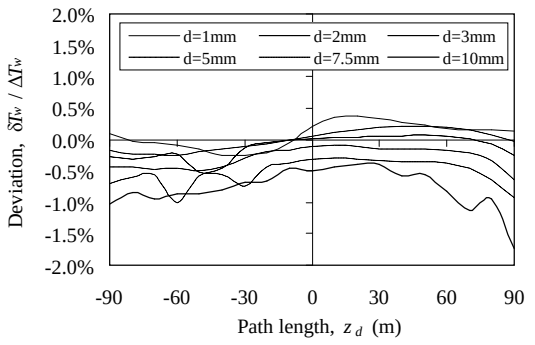

(d) Comparison between the data in (b_1) and *FLUENT*®.

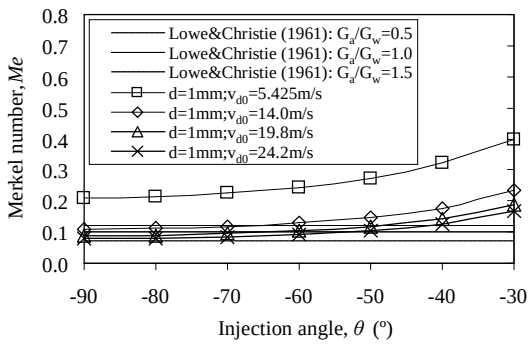

(e) Merkel number {Eq. (C.39) by Kröger (2004) based on the data of Lowe and Christie (1961)}.

Figure C.4: Drop temperature change and Merkel numbers for different injection angles and drop diameters.

higher Merkel numbers than larger drops and down-spray trajectories respectively. The spray zone Merkel number according to Eq. (C.39) (Lowe and Christie 1961), based on down spray data measured for a drop diameter of d = 1 mm, is plotted in Fig. C.4(e) for G_a/ G_w = 0.5, 1 and 1.5. This data is shown to compare favourably with present analysis data determined for initial drop speeds of v_{d0} = 14, 19.8 and 24.2 m/s corresponding to 10, 20 and 30 m water gauge respectively and injection angles of $\theta \leq$ -60 º.

Fig. C.4(c_2) shows that an increase in initial drop speed results in a reduction in Merkel number in down-spray nozzles ($\theta \leq$ -10 º) as opposed to increases for larger injection angles.

The *FLUENT*® trajectories and temperature colour-maps for the cases presented in Fig. C.4 are shown in Fig. C.5.

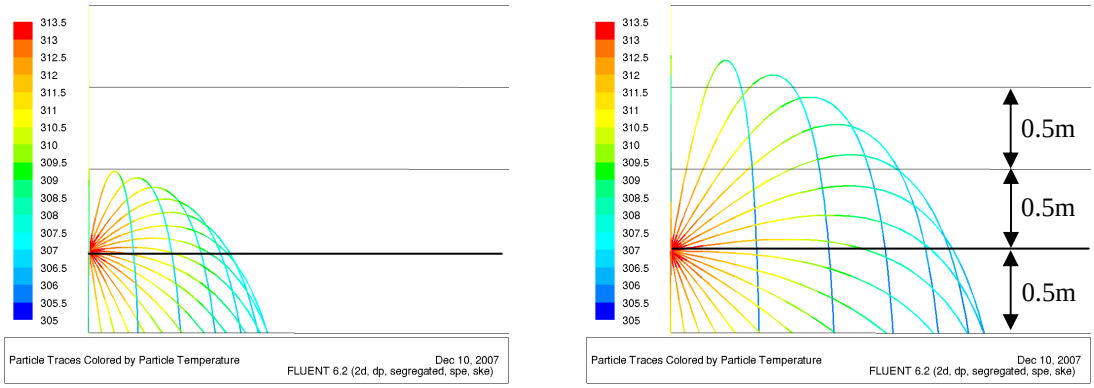

(a) Initial drop speed of v_{d0} = 3.13 m/s.

(b) Initial drop speed of v_{d0} = 5.425 m/s.

Figure C.5: Trajectories and temperatures of single spherical drops (d = 1 mm) injected at constant speed and different injection angles ($\Delta\theta$ = 10º).

For crossflow and counterflow rain zones, which have a maximum height of about H_{rz} = 12 m , the present model is employed to calculate the drop temperature at any given point along the motion path and for different drop sizes, to investigate the effect of using different relations for the drag, diffusion, convection heat transfer and mass transfer coefficients as well as relations for rate of mass transfer and Lewis factor on the calculated drop temperature and Merkel number. The data presented in the following figures is based on an initial drop speed of v_{d0} = 0.1 m/s; an injection angle of θ = -90º; an air speed of v_a = 2 m/s vertically upwards (φ = 90º); an atmospheric pressure of p_a = 101325 Pa; an ambient temperature of T_a = 288.15 K (15 ºC); a relative humidity of φ_a = 60% and a water inlet temperature of T_{wi} = 303.15 K (30 ºC), as was done in section B.4. These conditions are typical for rain zones in natural draught wet cooling towers. For comparison, a reference case is developed which is based on the following models: the Turton and Levenspiel (1986) relation for the drag coefficient (Eq. B.9); the Ranz and Marshall (1952) relations for the heat and mass transfer coefficients (Eqs C.12 and C.22); the Fuller (VDI 2006) relation for the diffusion coefficient (Eq. C.42); and Eq. (C.5) for determining the rate of mass transfer.

In Fig. C.6(a), drop temperatures determined at reference conditions using the above analysis are presented. These results are compared to equivalent *FLUENT*® results in Fig. C.6(b), showing negligible differences.

Corresponding Merkel numbers plotted in Figs C.6(c) and C.6(d) show that the difference between d = 1 mm and d = 3 mm drops is almost a factor of 12. Similar results are obtained for crossflow as presented in Fig. C.7, however it is found that crossflow Merkel numbers are lower than equivalent counterflow values attributed mainly to shorter drop residence times.

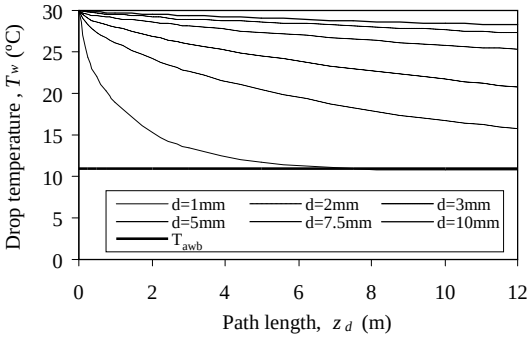

(a) Drop temperature (present analysis).

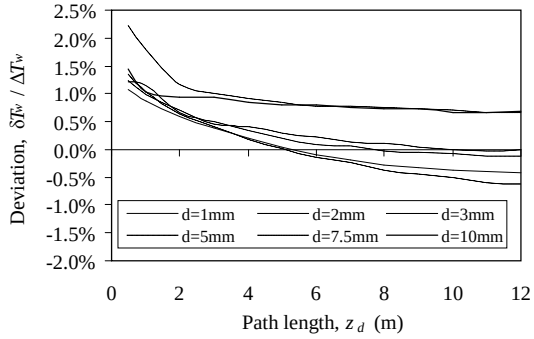

(b) Drop temperature deviation (*FLUENT*®).

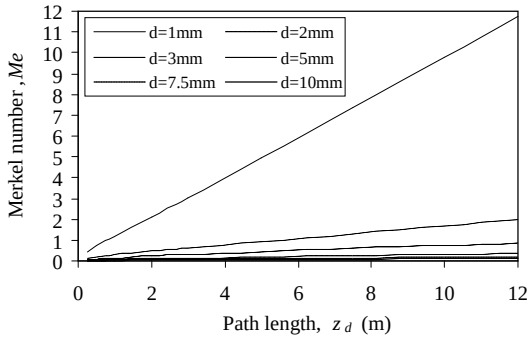

(c) Merkel number (present analysis).

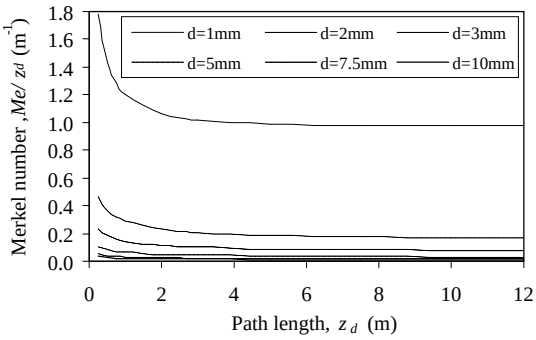

(d) Merkel number per unit path length (present analysis).

Figure C.6: Drop temperatures and Merkel numbers for the counterflow reference case in terms of path length and drop diameter.

Dreyer (1994) developed a drag coefficient relation discussed in Appendix B (Eq. B.12) for accelerating drops falling in a gravity field that includes the effect of changing drop deformation. Fig. C.8(a) shows that the effect on temperature change and Merkel number is relatively small for smaller drops ($d \leq 3$ mm) but becomes significant for larger drops, increasing linearly with path length.

Erens *et al.* (1994) improved the equation of Yao and Schrock (1976) (Eq. C.17) for the heat and mass transfer of accelerating drops, proposing Eqs (C.19) and (C.20) valid for limited range of drop diameters ($3 < d < 6$ mm) and falling distances ($0.18 < z < 2.9$ m). Fig. C.8(b) shows that the deviations from Ranz and

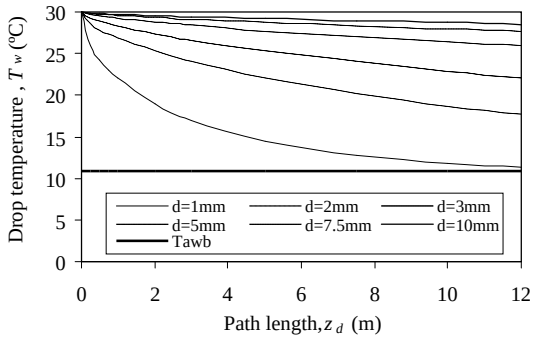

(a) Drop temperature (present analysis).

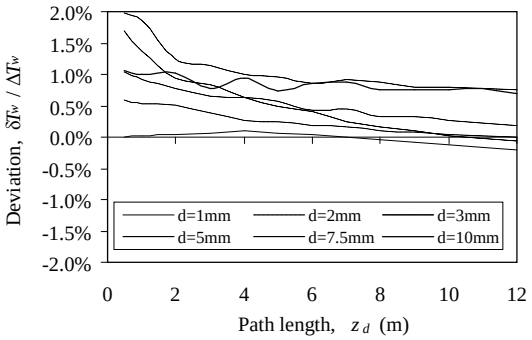

(b) Drop temperature deviation (*FLUENT*®).

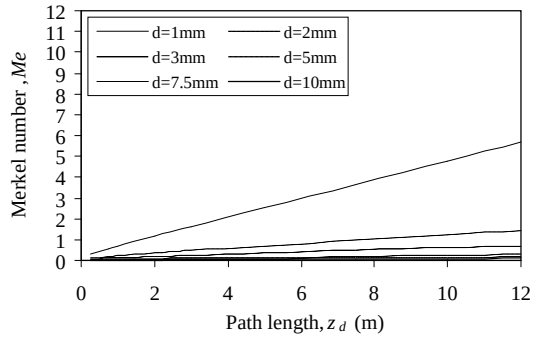

(c) Merkel number (present analysis).

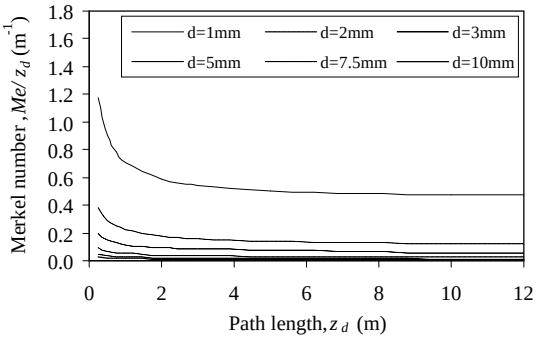

(d) Merkel number per unit path length (present analysis).

Figure C.7: Drop temperatures and Merkel numbers for the crossflow reference case in terms of path length and drop diameter.

Marshall (1952) for the applicable ranges are significant at shorter path lengths but converge as the path length increases.

Fig. C.9 illustrates the effect of using the heat and mass transfer coefficient equations from Section C.3 by Martin (2004) and Whitaker (1972). Martin (2004) predicts lower drop temperatures and subsequently higher Merkel numbers than Ranz and Marshall (1952) for conditions with no free-stream turbulence (Tu = 0%) whereas the temperature values for Whitaker (1972) are higher and the Merkel numbers lower than Ranz and Marshall. The drop temperatures are affected significantly by free-stream turbulence levels, as shown for turbulence levels of Tu = 4% and 8%.

Fig. C.10 shows that the effect of different definitions for determining the rate of mass transfer (equations C.4 to C.6) on drop temperature change and Merkel number is relatively small and that Eq. (C.5) provides conservative results in relation to equations (C.4) and (C.6).

Merkel (1925) theory is based on the simple assumption that the Lewis factor is $Le_f \approx 1$, whereas the more rigorous Poppe and Rögener (1991) model makes use of the Bosnjakovic (1960) equation for the Lewis factor.

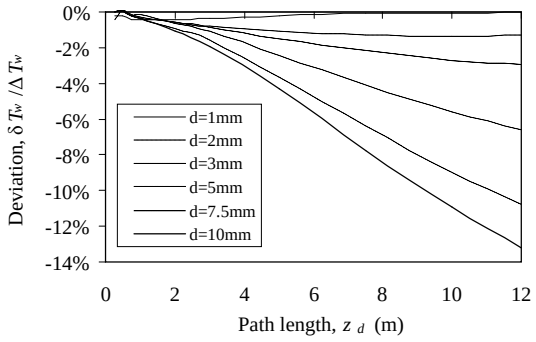

(a_1) Temperature deviation {Eq. (B.12) by Dreyer, (1994)}.

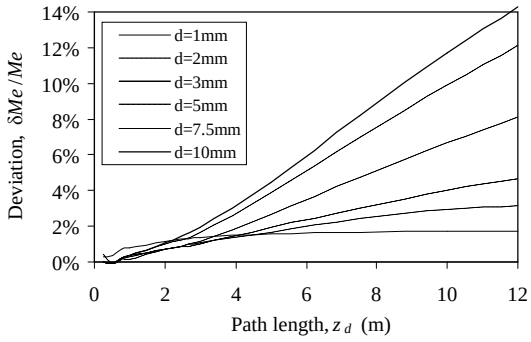

(a_2) Merkel number deviation {Eq. (B.12) by Dreyer, (1994)}.

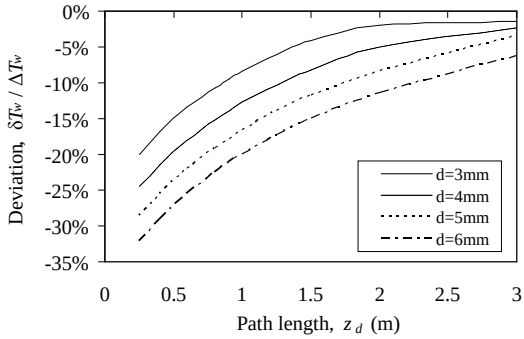

(b_1) Temperature deviation {Eqs (C.17) and (C.26) by Erens *et. al.* (1994)}.

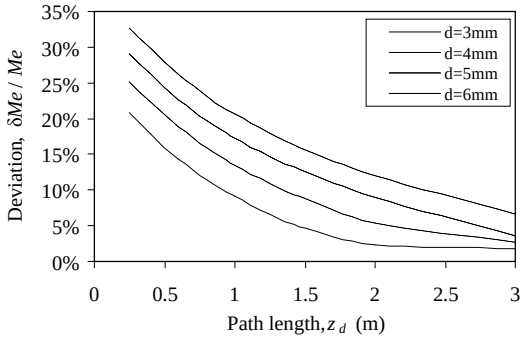

(b_2) Merkel number deviation {Eqs (C.17) and (C.26) by Erens *et. al.* (1994)}.

Figure C.8: Effect of drop deformation and acceleration on drop temperature and Merkel number in terms of path length and drop diameter.

In Fig. C.11(a) it can be seen that the Bosnjakovic relation predicts lower drop temperatures and thus higher Merkel numbers than the reference case while the assumption that $Le_f \approx 1$ [Fig. C.11(c)] is slightly conservative, giving marginally higher values than the reference case. The data in Fig. C.10(b) compare well with the Bosnjakovic results in Fig. C.11(a), which is expected since the derivation of the Bosnjakovic Lewis factor relation is based on the same definition for determining the rate of mass transfer (Eq. C.4).

Kröger (2004) uses the Gilliland (1934) relation (Eq. C.39) for the diffusion coefficient, whereas Bejan (1993), Perry (1999) and the VDI Wärmeatlas (2006) recommend using the relation developed by Fuller (Eq. C.42) for air-vapour mixtures. Fig. C.12 shows the deviation in drop temperature and Merkel number between these equations.

The air thermophysical properties of the reference case are determined at mean air temperature i.e. the average of the air and drop temperatures. FLUENT® however evaluates properties at the continuous phase (air) temperature. The deviation between drop temperature and Merkel number if properties are

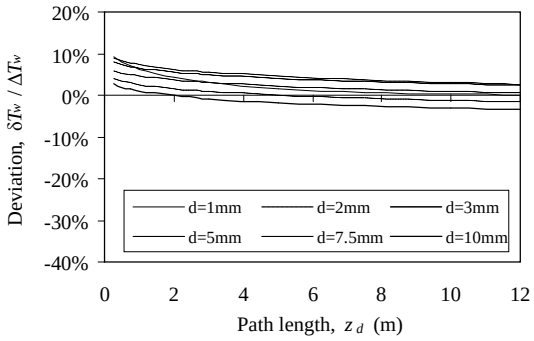

(a_1) Temperature deviation {Eqs (C.16) and (C.25) by Whitaker (1972)}.

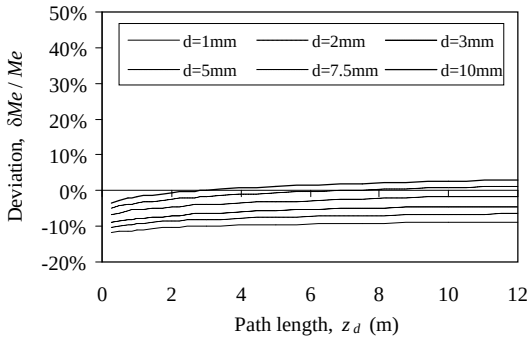

(a_2) Merkel number deviation {Eqs (C.16) and (C.25) by Whitaker (1972)}.

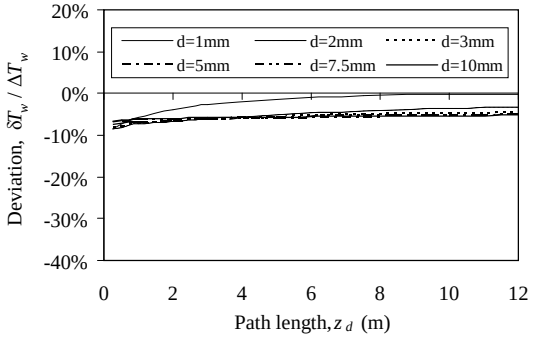

(b_1) Temperature deviation {Eqs (C.14) and (C.24) by Martin (2004) for Tu = 0 %}.

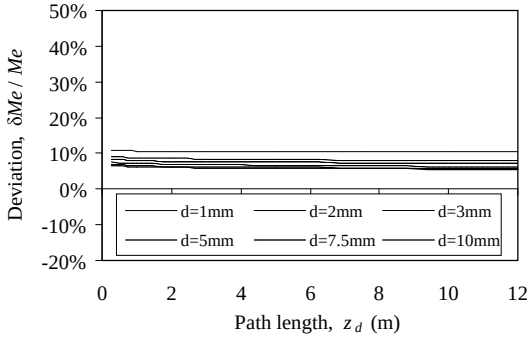

(b_2) Merkel number {Eqs (C.14) and (C.24) by Martin (2004) for Tu = 0 %}.

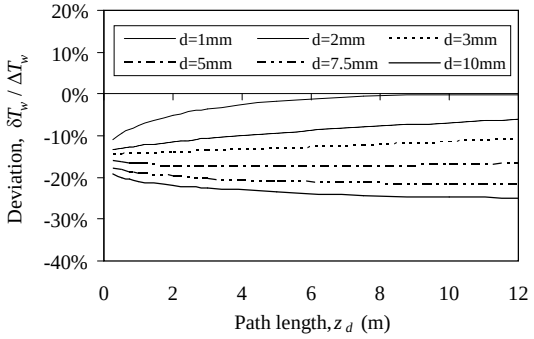

(c_1) Temperature deviation {Eqs (C.14) and (C.24) by Martin (2004) for Tu = 4 %}.

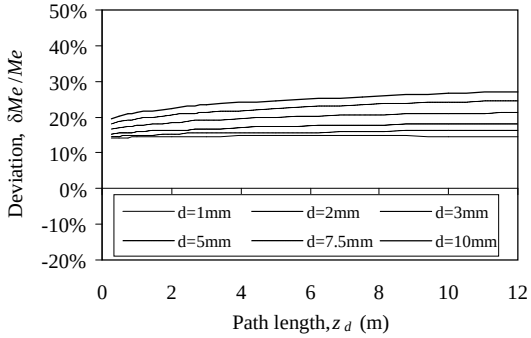

(c_2) Merkel number deviation {Eqs (C.14) and (C.24) by Martin (2004) for Tu = 4 %}.

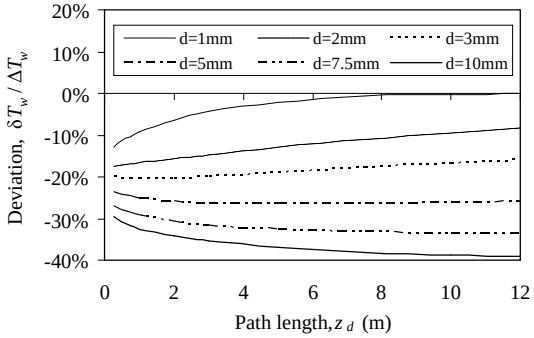

(d_1) Temperature deviation {Eqs (C.14) and (C.24) by Martin (2004) for Tu = 8 %}.

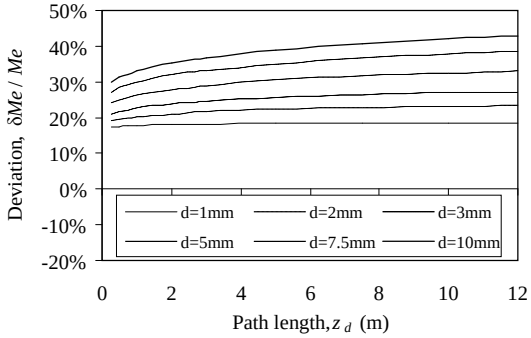

(d_2) Merkel number deviation {Eqs (C.14) and (C.24) by Martin (2004) for Tu = 8 %}.

Figure C.9: Effect of different heat and mass transfer coefficient relations on drop temperature in terms of path length and drop diameter.

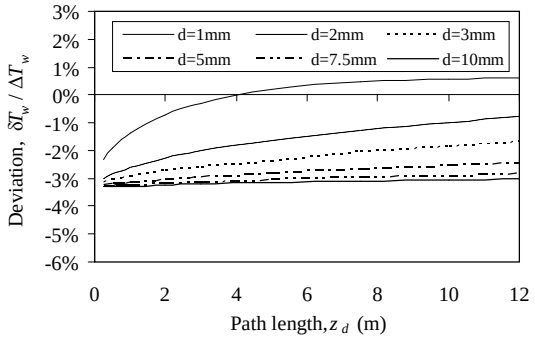

(a_1) Temperature deviation (Eq. C.6).

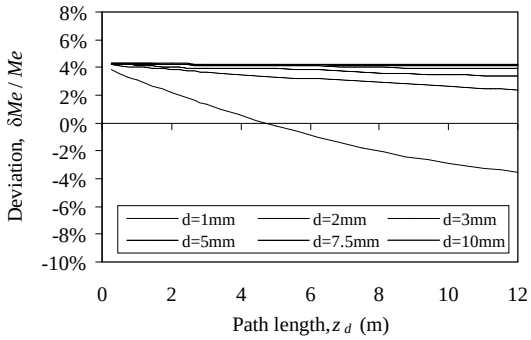

(a_2) Merkel number deviation (Eq. C.6).

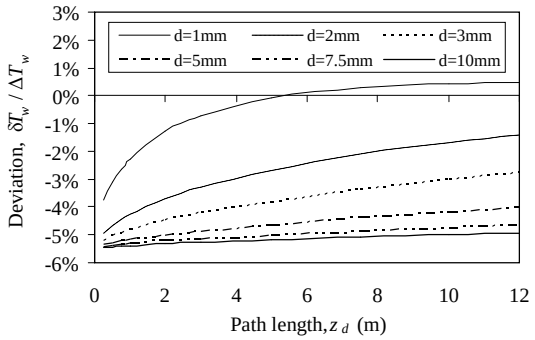

(b_1) Temperature deviation (Eq. C.4).

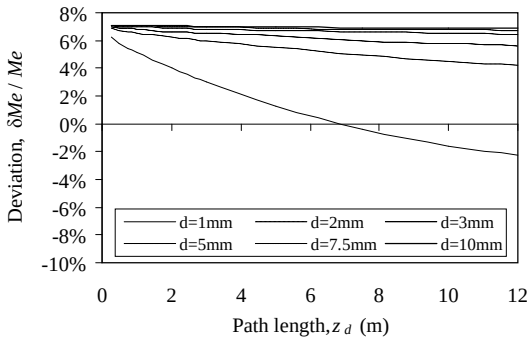

(b_2) Merkel number deviation (Eq. C.4).

Figure C.10: Effect of different mass transfer rate relations on drop temperature and Merkel number in terms of path length and drop diameter.

determined at ambient air temperature instead of mean temperature are shown in Fig. C.13.

In Fig. C.14, the Lewis factor data obtained from the present analysis is compared with Eq. (C.33) of Bosnjakovic (1960), showing that the present analysis gives Lewis factors closer to $Le_f = 1$ than Bosnjakovic.

Fig. C.15 shows that the deviation between Eq. (C.40) by De Villiers (1997) and equivalent Merkel number data determined using the present analysis, based on the drag coefficient relation of Dreyer (1994) (Eq. B.12), the relation by Ranz and Marshall (1952) (Eq. C.12), the mass transfer conversion relation by Poppe (1991) (Eq. C.31), a Lewis factor of unity (Eq. C.32) and the diffusion coefficient relation of Gilliland (1934) (Eq. 41), is between $\delta Me / Me$ = -20 % and 0 % over the valid range, depending on the drop diameter, drop path length and atmospheric pressure and is therefore conservative.

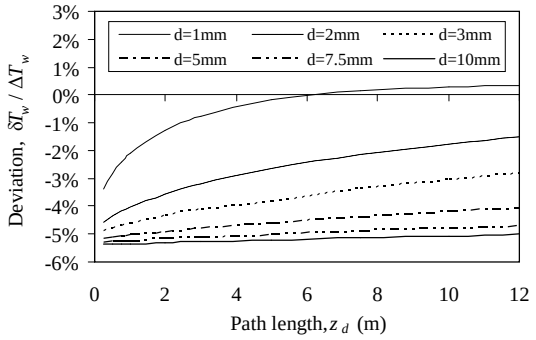

(a_1) Temperature deviation {Eq. (C.7) based on Bosnjakovic (1960) (Eq. C.33)}.

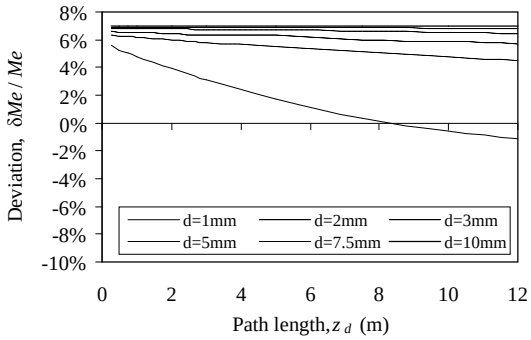

(a_2) Merkel number deviation {Eq. (C.7) based on Bosnjakovic (1960) (Eq. C.33)}.

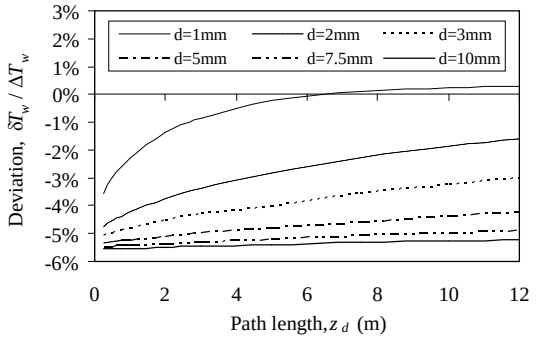

(b_1) Temperature deviation {Eq. (C.7) based on Bosnjakovic (1960) (Eq. C.34)}.

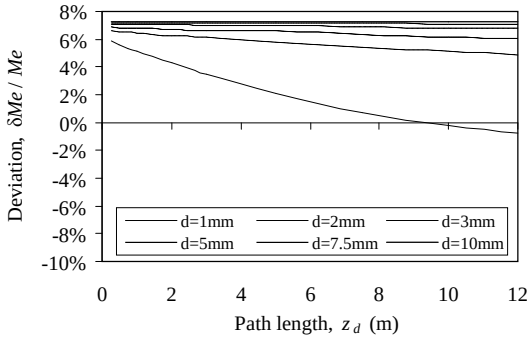

(b_2) Merkel number deviation {Eq. (C.7) based on Bosnjakovic (1960) (Eq. C.34)}.

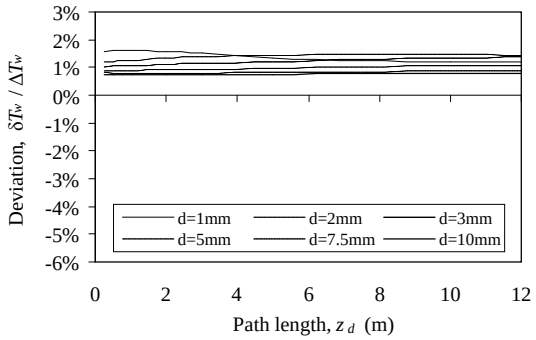

(c_1) Temperature deviation {Eq. (C.7) based on a Lewis factor of $Le_f \approx 1$}.

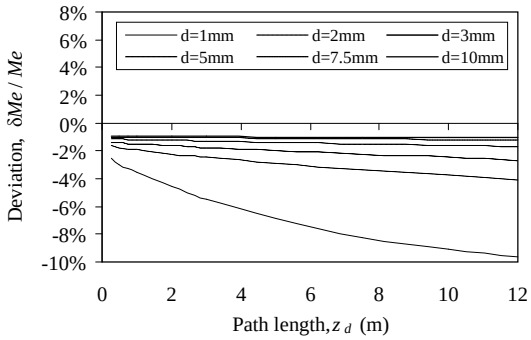

(c_2) Merkel number deviation {Eq. (C.7) based on a Lewis factor of $Le_f \approx 1$}.

Figure C.11: Effect of different Lewis factor relations on drop temperature and Merkel number in terms of path length and drop diameter.

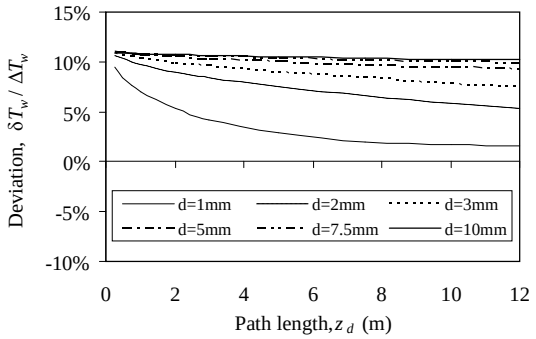

(a) Temperature deviation {Eq. (C.41) by Gilliland (1934)}.

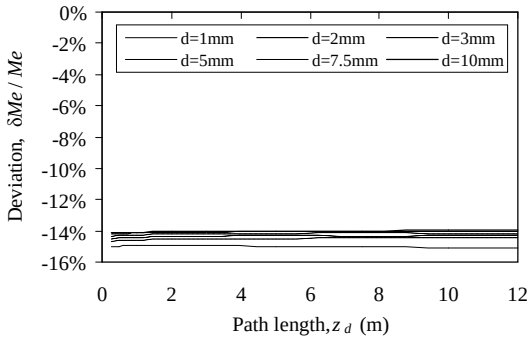

(b) Merkel number deviation {Eq. (C.41) by Gilliland (1934)}.

Figure C.12: Effect of using the Gilliland (1934) diffusion coefficient relation on drop temperature and Merkel number in terms of path length and drop diameter.

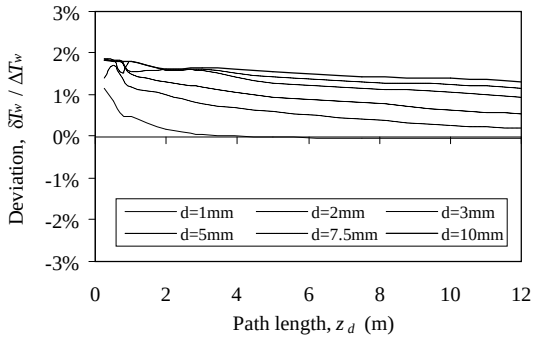

(a) Temperature deviation (Thermophysical properties evaluated at ambient conditions).

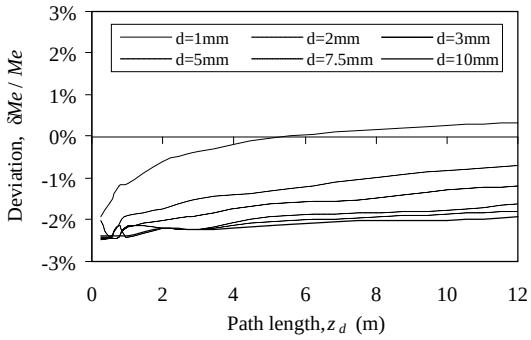

(b) Merkel number deviation (Thermophysical properties evaluated at ambient conditions).

Figure C.13: Effect of evaluating the thermophysical properties at ambient as opposed to mean air temperature on drop temperature and Merkel number in terms of path length and drop diameter.

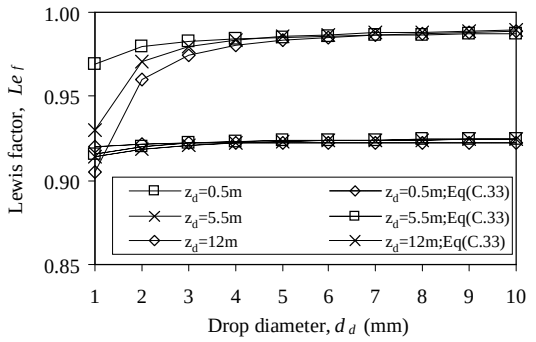

Figure C.14: Lewis factor data from the present analysis compared with Eq. (C.33) by Bosnjakovic (1960).

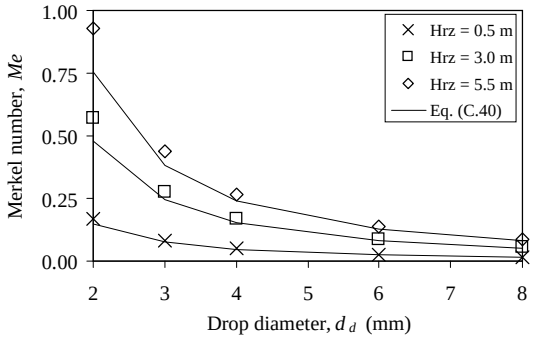

(a) Merkel number (p_a = 101325 N/m^2)

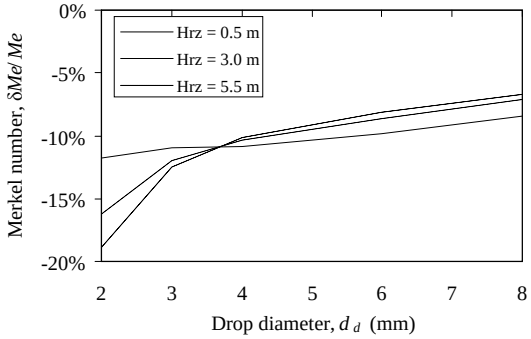

(b) Merkel number deviation (p_a = 101325 N/m^2).

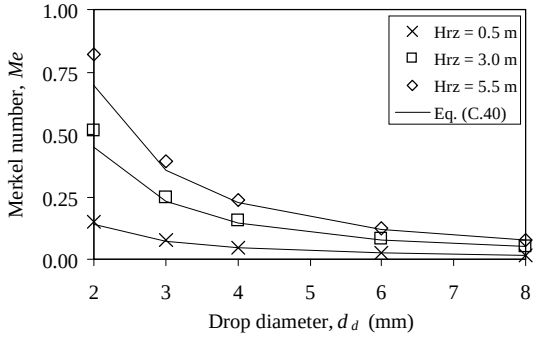

(c) Merkel number (p_a = 85000 N/m^2).

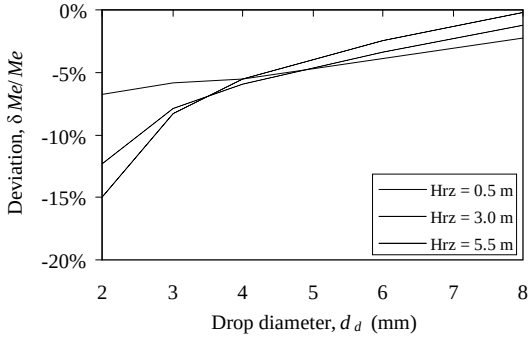

(d) Merkel number deviation (p_a = 85000 N/m^2).

Figure C.15: Comparison between Eq. (C.40) by De Villiers (1997) and equivalent data from the present analysis.

C.7 CONCLUSIONS AND RECOMMENDATIONS

The governing equation is derived for the cooling of a single drop due to relative air flow based on the first law of thermodynamics. This equation is integrated numerically in conjunction with the two-dimensional motion equations presented in Appendix B, to predict the temperature change and Merkel number of a single drop falling in moving air under the effect of gravity for any given drop size, initial drop speed, injection angle, air velocity, vertical distance relative to the injection point as well as different air and drop thermophysical properties. The data show good comparison with equivalent *FLUENT*® results, where the marginal deviations can largely be attributed to curve-fit inaccuracies of the saturated vapour pressure in particular, different drag models and differences in numerical integration methods. Comparing the Nusselt and Sherwood number relations of Ranz and Marshall (1952) to those of Whitaker (1972) and Martin (2004) {Tu = 0 %}, it can be seen that the deviation is less than 15 % for the range of Reynolds numbers applicable to cooling tower rain zones. Martin (2004)

however predicts deviations that are as much as 30 to 50 % higher for free-stream turbulence levels of Tu = 4 % and 8 % respectively.

Kröger (2004) uses the Gilliland (1934) relation for diffusion coefficient based on kinetic theory. For air-vapour mixtures, Bejan (1993), Perry (1999) and the VDI Wärmeatlas (2006) recommend using the equation developed by Fuller, which differs from the Gilliland (1934) equation by more than 20%.

The results obtained for different cases investigated using the above analysis are summarised as follows:

- ⇨ Considering conditions typical for spray nozzles, the temperature change in up-spray ($\theta > 0^o$) configuration can be up to 4 times larger than for down-spray ($\theta < 0^o$) and is significantly higher for smaller drops ($d \leq 3$ mm) than larger drops, increasing with initial drop speed. This can be attributed mainly to differences in drop residence time.
- ⇨ Similarly, the Merkel number in up-spray ($\theta > 0^o$) configuration can be almost 10 times greater than for down-spray ($\theta < 0^o$) and is significantly larger for smaller drops ($d \leq 3$ mm) than larger drops, increasing with initial drop speed.
- ⇨ The maximum height that a drop can be sprayed into the air is almost equal to the initial dynamic head or minimum pressure head over the nozzle.
- ⇨ The spray zone Merkel number according to Eq. (C.39) by Lowe and Christie (1961), based on down spray data measured for a drop diameter of d = 1 mm, is shown to compare favourably with present analysis data for d = 1 mm drops determined for initial drop speeds of v_{d0} = 14, 19.8 and 24.2 m/s corresponding to 10, 20 and 30 m water gauge respectively and injection angles of $\theta \leq$ -60 °. Since these conditions are not generally applicable to cooling tower spray nozzles this equation is unsuitable for general cooling tower analysis.
- ⇨ For the counterflow conditions simulated, a d = 1 mm drop reaches the wet–bulb temperature or maximum possible cooling range after a falling distance of approximately z_d = 7 m, whereas in crossflow configuration it does not reach the cooling limit due to shorter residence times and lower relative air speeds resulting in lower mean heat and mass transfer coefficients and interfacial surface area.
- ⇨ The cooling range of a d = 5 mm drop achieved over a path length of z_d = 12 m is reached by d = 1, 2 and 3 mm drops at falling distances of z_d = 0.2, 1.4 and 3.8 m respectively.
- ⇨ The cooling ranges of d = 2, 3, 5, 7.5 and 10 mm drops at falling distance of z_d = 10 m are respectively $\Delta T_w / \Delta T_{w\,(d=1mm)}$ x 100% = 69, 43, 22, 12 and 8% of the corresponding cooling range of a d = 1 mm drop.
- ⇨ The effect of drop acceleration and subsequent drop deformation results in marginally lower drop temperatures and subsequently higher Merkel numbers. The deviation increases with drop diameter.

- ⇨ Compared to Eqs (C.12) and (C.22) by Ranz and Marshall (1952) for the heat and mass transfer coefficient, Eqs (C.16) and (C.25) of Whitaker (1972) are more conservative, predicting higher drop temperatures, whereas Eqs (C.14) and (C.24) by Martin (2004) predict lower temperatures.
- ⇨ From Eqs (C.14) and (C.24) of Martin (2004), the effect of free stream turbulence is found to be significant.
- ⇨ The effect of using different relations for determining the rate of mass transfer showed that Eq. (C.5), also used by *FLUENT*® 6.2.16, gives slightly conservative results.
- ⇨ The assumption that Lewis factor Le_f = 1 does not result in significant differences at the reference conditions and is considered acceptable for drop diameters of d > 3 mm.
- ⇨ The differences between using Eq. (C.41) by Gilliland (1934) and Eq. (C.42) by Fuller (VDI-Wärmeatlas, 2006) for the diffusion coefficient on drop temperature and Merkel number are measurable.
- ⇨ The differences in Merkel numbers for counterflow and crossflow configurations can be between 100% for a d = 1 mm drop to 15 % for a d = 10 mm drop, depending on the air speed.
- ⇨ For the counterflow reference case, Merkel numbers of d = 2, 3, 5, 7.5 and 10 mm drops at a falling distance of z_d = 10 m are respectively $Me/ Me_{(d=1mm)}$ x 100% = 17, 8, 3, 2 and 1 % of the corresponding Merkel number of a d = 1 mm drop.
- ⇨ A comparison between Eq. (C.40) by De Villiers (1997) and equivalent Merkel numbers determined using the present analysis shows a deviation of between $\delta Me/ Me$ = -20 % and 0 % over the valid range, depending on the drop diameter, drop path length and atmospheric pressure. This deviation is attributed to the omission of the diffusion coefficient from the list of independent variables used for the correlation.

Based on the above results, it can be concluded that the Ranz and Marshall (1952) relations for the heat and mass transfer coefficient (Eqs C.12 and C.22) and the relation for determining the rate of mass transfer (Eq. C.5) employed by *FLUENT*® give conservative results. Furthermore, the relations of Fuller (VDI-Wärmeatlas, 2006) and Dreyer (1994) should be used for determining the diffusion and drag coefficients respectively. In *FLUENT*®, the thermophysical properties can be input as polynomial functions. It was found that the drop cooling results are very sensitive to the saturated vapour pressure goodness-of-fit, as *FLUENT*® reduces the coefficients to 7 significant digits, which for higher order polynomials results in significant inaccuracies.

D

APPROXIMATE ANALYTICAL SOLUTION FOR MOTION OF A SPHERICAL WATER DROP FALLING THROUGH AIR FLOWING UPWARDS

The main objective of this section is to develop approximate analytical equations for determining the absolute drop speed and motion path length of a single spherical water drop falling vertically through upward flowing air and using these equations to determine the counter-flow rain zone loss coefficient. These expressions are obtained by solving the relevant governing differential equations of motion to show the influence of drop diameter on drop speed, path length and loss coefficient for drop diameters of $1 \leq d \leq 5$ mm typically found in cooling tower rain zones. The results are compared to numerical data obtained using the model presented in Appendix B.

D.1 GOVERNING DIFFERENTIAL EQUATION

Consider Eq. (B.1), which for a single drop falling vertically through air simplifies to

$$\frac{dv}{dt} = -\frac{3}{4}\frac{\rho_a}{\rho_w}\frac{C_D}{d}v^2 - g\left(\frac{\rho_a}{\rho_w} - 1\right) \approx -\frac{3}{4}\frac{\rho_a}{\rho_w}\frac{C_D}{d}v^2 + g \tag{D.1}$$

Since the drag coefficient (C_D) is a function of Reynolds number (Re), the above equation can be written in terms of Re as

$$\frac{d\,Re}{dt} = a_1\left(C_D\,Re^2\right) + a_2 \tag{D.2}$$

where

$$a_1 = -\frac{3}{4}\frac{\mu_a}{\rho_w}\frac{1}{d^2} \tag{D.3}$$

$$a_2 = -g\,\frac{\rho_a}{\mu_a}\left(\frac{\rho_a}{\rho_w} - 1\right)d \;\approx \frac{g\rho_a d}{\mu_a} \tag{D.4}$$

The values of a_1 and a_2 are essentially constant for drops of constant diameter and the range of air and water properties typically encountered in wet cooling towers and the drag coefficient (C_D) can be obtained from a number of empirical relations, as discussed in Appendix B. In the present analysis, the equation by Turton and Levenspiel (1986), for spherical bodies, is used:

$$C_D = \frac{24\left(1 + 0.173\,Re^{0.657}\right)}{Re} + \frac{0.413}{1 + 16300\,Re^{-1.09}} \tag{D.5}$$

Substituting Eq. (D.5) into Eq. (D.2) yields

$$\frac{d\,Re}{dt} = a_1\left[24\,Re\left(1+0.173\,Re^{0.657}\right)+\frac{0.413\,Re^2}{1+16300\,Re^{-1.09}}\right]+a_2 \qquad \text{(D.6)}$$

The above equation is not integrable and therefore must be solved numerically, as discussed in Appendix B, to obtain an exact solution.

D.2 DROP SPEED

A fairly accurate analytical solution can be obtained for Eq. (D.2) by approximating the C_DRe^2 term with a suitable function that enables mathematical integration. The simplest solution is obtained if C_DRe^2 is approximated by a linear function of *Re* expressed as

$$C_D\,Re^2 \approx b_1\,Re + b_2 \qquad \text{(D.7)}$$

where b_1 and b_2 are functions of drop diameter (d).

Substitute Eq. (D.7) into Eq. (D.2), to find the following relation:

$$\frac{dRe}{dt} = c_1 Re + c_2 \qquad \text{(D.8)}$$

where

$$c_1 = -\frac{3}{4}\frac{\mu_a}{\rho_w}\left(\frac{b_1}{d^2}\right) \qquad \text{(D.9)}$$

$$c_2 = -\frac{3}{4}\frac{\mu_a}{\rho_w}\left(\frac{b_2}{d^2}\right) - \frac{g\rho_a}{\mu_a}\left(\frac{\rho_a}{\rho_w}-1\right)d \qquad \text{(D.10)}$$

Suitable values for c_1 and c_2 are determined for different drop diameters (d = 1, 2, 3, 4 and 5mm) by linear regression of Eq. (D.6), as shown in Fig. D.1.

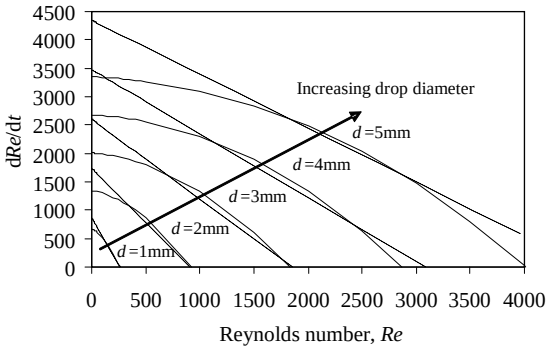

Figure D.1: Rate of change of Reynolds number as a function of Reynolds number.

The terms b_1/d^2 and b_2/d^2 are subsequently calculated from Eqs (D.9) and (D.10) and correlated in terms of drop diameter to yield

$$\frac{b_1}{d^2} = \frac{1.2313\times10^6}{d^{0.76548}} \tag{D.11}$$

$$\frac{b_2}{d^2} = \frac{0.4g\rho_a(\rho_a - \rho_w)d}{\mu_a^2} \tag{D.12}$$

Fig. D.2 shows the exact curve of C_DRe^2 as a function of Re based on Eq. (D.5) and the linear approximation curves (Eq. D.7) for drop diameters of d = 1, 2, 3, 4 and 5 mm.

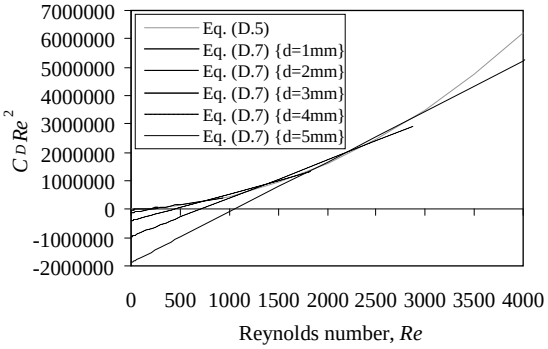

Figure D.2 : C_DRe^2 as a function of Reynolds number

Separation of the variables and integration of Eq. (D.7) yields

$$\int_{Re_0}^{Re} \frac{d\,Re}{c_1\,Re + c_2} = \int_0^t dt \tag{D.13}$$

The following solution is obtained for Reynolds number as a function of time, drop diameter and thermophysical properties of air and water:

$$Re = \left(Re_0 + \frac{c_2}{c_1}\right)e^{c_1 t} - \frac{c_2}{c_1} \tag{D.14}$$

From the definition of Reynolds number (Re), Eq. (D.14) can also be written in terms of relative air speed as

$$v = (v_0 + d_1)e^{c_1 t} - d_1 \tag{D.15}$$

where

$$c_1 = -\frac{3}{4}\frac{\mu_a}{\rho_w}\left(\frac{1.2313\times10^6}{d^{0.76548}}\right) \tag{D.16}$$

$$d_1 = \frac{\mu_a}{\rho_a d}\frac{c_2}{c_1} = 1.4077\times10^{-6}\,\frac{g(\rho_a - \rho_w)d^{0.76548}}{\mu_a} \tag{D.17}$$

The values of c_1 and d_1 can be assumed to be constant. At ISO conditions, i.e. the atmospheric pressure is p_a = 101.325 kPa, the ambient temperature is T_a = 15 ºC and the relative humidity is RH = 60 %, and assuming that the water temperature is the same as the air wet bulb temperature ($T_w = T_{awb}$ = 10.9 ºC), then

$$c_1 = \frac{-0.016471}{d^{0.76548}} \tag{D.18}$$

$$d_1 = -772.552 d^{0.76548} \tag{D.19}$$

Substitute Eqs (D.18) and (D.19) into Eq. (D.15), to find a simplified expression for relative airspeed in terms of initial relative air speed, drop diameter and time.

$$v = \left(v_0 - 772.552 d^{0.76548}\right) \mathrm{e}^{\left(\frac{-0.016471}{d^{0.76548}}\right)t} + 772.552 d^{0.76548} \tag{D.20}$$

The relative air speed can be expressed in terms of absolute air and drop speeds as

$$v = v_a - v_d \tag{D.21}$$

Substitute Eq. (D.21) into Eq. (D.15) to obtain the following expression for absolute drop speed:

$$v_d = \left(v_{d0} - v_a - d_1\right) e^{c_1 t} + \left(d_1 + v_a\right) \tag{D.22}$$

Substitute Eq. (D.18) and Eq. (D.19) into Eq. (D.22) to obtain a relation for absolute drop speed as a function of initial absolute drop speed, absolute air speed, drop diameter and time, written as

$$v_d = \left(v_{d0} - v_a + 772.552 d^{0.76548}\right) \mathrm{e}^{\left(\frac{-0.016471}{d^{0.76548}}\right)t} - \left(772.552 d^{0.76548} - v_a\right) \tag{D.23}$$

For a drop falling from rest through still air, Eq. (D.23) simplifies to

$$v_d = 772.552 d^{0.76548} \left(\mathrm{e}^{\left(\frac{-0.016471}{d^{0.76548}}\right)t} - 1 \right) \tag{D.24}$$

D.3 DROP MOTION PATH LENGTH

Since $v_d = dz/dt$, an approximate analytical equation for drop path length is obtained by integrating Eq. (D.22) with respect to time, which yields

$$z = \frac{\left(v_{d0} - v_a - d_1\right)}{c_1} \left(\mathrm{e}^{c_1 t} - 1\right) + \left(d_1 + v_a\right) t \tag{D.25}$$

Substitute Eq. (D.16) and Eq. (D.17) into Eq. (D.25) to obtain the following relation for drop path length as a function of absolute air speed, initial absolute drop speed, drop diameter and time:

$$z = \left[60.7139 d^{0.76548} \left(v_a - v_{d0}\right) - 46904.6 d^{1.53096} \right] \left(\mathrm{e}^{\left(\frac{-0.016471}{d^{0.76548}}\right)t} - 1 \right) + \left(v_a - 772.552 d^{0.76548}\right) t \tag{D.26}$$

For a drop falling from rest through still air, Eq. (D.26) simplifies to

$$z = -46904.6 d^{1.53096} \left(e^{\left(\frac{-0.016471}{d^{0.76548}} \right) t} - 1 \right) - 772.552 d^{0.76548}\, t \tag{D.27}$$

To obtain an expression for drop path length as a function of absolute drop and air speeds, substitute Eq. (D.22) into Eq. (D.25) to eliminate time, which gives that

$$z = \frac{v_d - v_{d0}}{c_1} + \frac{v_a + d_1}{c_1} \ln\left(\frac{v_a - v_d + d_1}{v_a - v_{d0} + d_1} \right) \tag{D.28}$$

Substitute Eq. (D.16) and (D.17) into Eq. (D.28) which yields the following relation for drop motion path as a function of absolute air speed, initial absolute drop speed, drop diameter and absolute drop speed:

$$z = -60.7139 d^{0.76548} \left[v_d - v_{d0} + \left(v_a - 772.552 d^{0.76548} \right) \ln\left(\frac{v_a - v_d - 772.552 d^{0.76548}}{v_a - v_{d0} - 772.552 d^{0.76548}} \right) \right] \tag{D.29}$$

For a drop falling from rest through still air, Eq. (D.29) simplifies to:

$$z = -60.7139 d^{0.76548} \left[v_d - 772.552 d^{0.76548} \ln\left(\frac{v_d}{772.552 d^{0.76548}} + 1 \right) \right] \tag{D.30}$$

D.4 DROP VOLUME AND VOID FRACTIONS

Consider spherical drops of uniform diameter, mass velocity and inlet speed, introduced into an air-stream. The drop volume fraction at a given point in the rain zone, is defined as

$$\frac{V_w}{V} = \frac{n_d V_d}{v_d A_{fr}} \tag{D.31}$$

The rate at which drops are introduced into the control volume can be determined from

$$n_d = \frac{G_w A_{fr}}{\rho_w V_d} \tag{D.32}$$

Substitute Eq. (D.32) into Eq. (D.31) to find that

$$\frac{V_w}{V} = \frac{G_w}{\rho_w v_d} \tag{D.33}$$

The void fraction, which is the opposite of the volume fraction, is therefore defined as

$$X_{void} = 1 - \frac{V_w}{V} = 1 - \frac{G_w}{\rho_w v_d} \tag{D.34}$$

D.5 SPECIFIC LOSS COEFFICIENT

Consider Eq. (B.19) for the specific loss coefficient of a steady counter-flow rain zone, given as

$$\frac{K}{G_w} \approx \frac{12\ t\ \bar{F}_{D_a}}{\pi d^3 \rho_w \rho_a v_a^2} = \frac{12}{\pi d^3 \rho_w \rho_a v_a^2} \int_0^t F_{Da} \mathrm{d}t = \frac{3\mu_a^2}{2d^3 \rho_w \rho_a^2 v_a^2} \int_0^t \left(C_D Re^2 \right) \mathrm{d}t \tag{D.35}$$

Substitute Eq. (D.2) into Eq. (D.35) and integrate to yield

$$\frac{K}{G_w} \approx \frac{3\mu_a^2}{2d^3 \rho_w \rho_a^2 v_a^2} \int_0^t \left(\frac{1}{a_1} \frac{\mathrm{d}Re}{\mathrm{d}t} - \frac{a_2}{a_1} \right) \mathrm{d}t = \frac{3\mu_a^2}{2d^3 \rho_w \rho_a^2 v_a^2} \left[\frac{1}{a_1} \left(Re - Re_0 \right) - \frac{a_2}{a_1} t \right] \tag{D.36}$$

Substitute Eq. (D.14) into Eq. (D.36), which gives that

$$\frac{K}{G_w} \approx \frac{3\mu_a^2}{2d^3 \rho_w \rho_a^2 v_a^2 a_1} \left[\left(Re_0 + \frac{c_2}{c_1} \right) e^{c_1 t} - a_2 t - \left(\frac{c_2}{c_1} + Re_0 \right) \right] \tag{D.37}$$

Substitute Eqs (D.3), (D.4), (D.9) and (D.10) into Eq. (D.37) to yield

$$\frac{K}{G_w} \approx \left[\begin{array}{l} \left(-\dfrac{2\mu_a Re_0}{d \rho_a^2 v_a^2} - 2.815 \times 10^{-6} \dfrac{\mathrm{g} \left(\rho_a - \rho_w \right) \mathrm{d}^{0.76548}}{\mu_a \rho_a v_a^2} \right) e^{-\left(9.235 \times 10^5 \frac{\mu_a}{\rho_w d^{0.76548}} \right) t} \\ -\dfrac{2g \left(\rho_a - \rho_w \right)}{\rho_w \rho_a v_a^2} \left(t - 1.40773 \times 10^{-6} \dfrac{\rho_w \mathrm{d}^{0.76548}}{\mu_a} \right) + \dfrac{2\mu_a Re_0}{d \rho_a^2 v_a^2} \end{array} \right] \tag{D.38}$$

D.6 RESULTS

Figure (D.3) shows the comparison between Eqs (D.22), (D.28) and (D.38) and the corresponding exact numerical data from the model in Appendix B. The results are based on: an air speed of v_a = 2 m/s; an initial absolute drop speed of v_{d0} = -0.1 m/s; ISO ambient conditions i.e. an atmospheric pressure of p_a = 101 325 N/m^2, an ambient air dry bulb temperature of T_{adb} = 15 ºC and a relative humidity of RH = 60 %; and a water temperature of T_w= T_{awb}=10.9 ºC.

In Fig. D.4, the void fraction is plotted against drop speed for different drop mass velocities.

D.7 CONCLUSION

In this section, the following approximate analytical equations are derived for a single drop falling vertically through upward moving air:

- ⇨ Absolute drop speed (v_d) as a function of drop diameter (d), time (t), initial drop speed (v_{d0}), absolute air speed (v_a) and thermophysical properties.
- ⇨ Drop path length (z_d) as a function drop diameter (d), time (t), initial drop speed (v_{d0}), absolute air speed (v_a) and thermophysical properties.

- ⇨ Drop path length (z_d) as a function of absolute drop diameter (d), drop speed (v_d), initial drop speed (v_{d0}), absolute air speed (v_a) and thermophysical properties.
- ⇨ Drop volume fraction as a function of drop mass velocity (G_w), absolute drop speed (v_d) and drop density (ρ_w).
- ⇨ Void fraction as a function of drop mass velocity (G_w), absolute drop speed (v_d) and drop density (ρ_w).
- ⇨ Counter-flow rain zone loss coefficient as a function of drop diameter (d), time (t), initial drop speed (v_{d0}), absolute air speed (v_a) and thermophysical properties.

Results are presented for the following conditions: drop diameters of d = 1, 2, 3, 4 and 5mm; an air speed of v_a = 2 m/s; an initial absolute drop speed of v_{d0} = -0.1 m/s; ISO ambient conditions i.e. an atmospheric pressure of p_a = 101 325 N/m^2, an ambient air dry bulb temperature of T_{adb} = 15 ºC, a relative humidity of RH = 60 %; and a water temperature of T_w= T_{awb}=10.9 ºC. This data is compared to corresponding numerical data, for path lengths up to z_d = 12 m and the deviations are found to be relatively small.

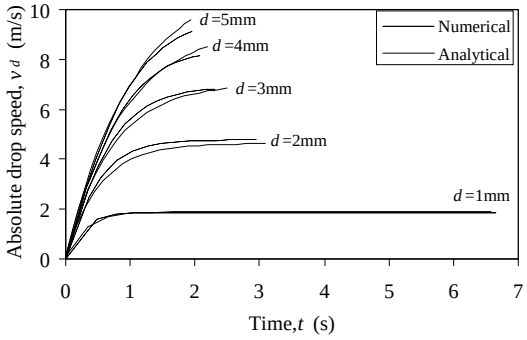

(a) Absolute drop speed as a function of time.

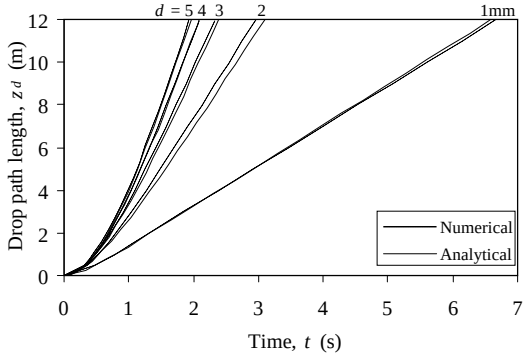

(b) Drop path length as a function of time.

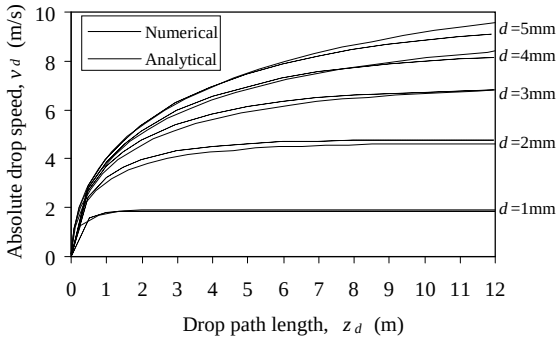

(c) Absolute drop speed as a function of drop path length

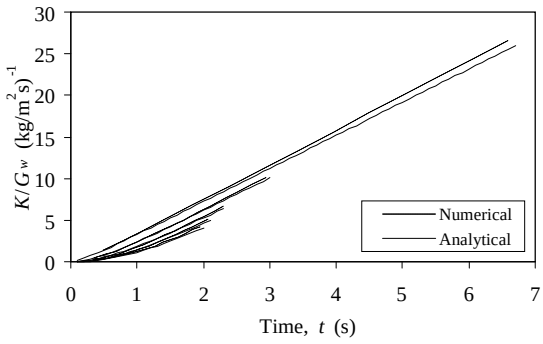

(d) Rain zone loss coefficient as a function of time.

Figure D.3: Comparison between approximate analytical and numerical drop motion data.

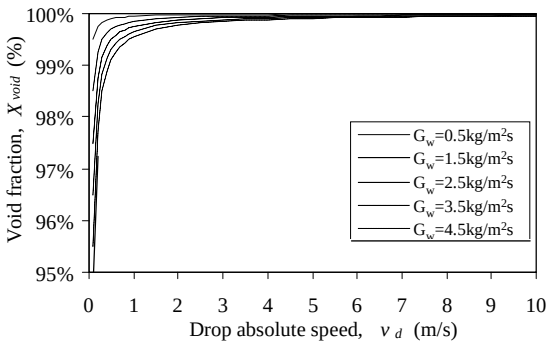

Figure D.4: Void fraction in terms of drop speed and water mass velocity.

E

APPROXIMATE ANALYTICAL SOLUTION FOR THE TEMPERATURE CHANGE AND MERKEL NUMBER OF A SPHERICAL WATER DROP COOLED BY AIR FLOWING UPWARDS

The main objective of this section is to develop approximate analytical equations for determining the temperature and transfer characteristic or Merkel number of a single spherical water drop cooled by air flowing upwards. These expressions are obtained by solving the relevant governing differential equations, to show the influence of drop diameter on drop temperature change and Merkel number (*Me*) for drop sizes ($1 \leq d \leq 5$ mm) typically found in cooling tower rain zones. The results are compared to the exact numerical data determined using the model presented in Appendix C.

E.1 GOVERNING DIFFERENTIAL EQUATION

The following relation for the rate of temperature change of a single drop cooled by means of air, is obtained by substituting Eq. (C.7) into Eq. (C.10):

$$\frac{dT_w}{dt} = -\frac{A}{M_d c_p}\left[h_d\left(w_{sw}-w\right)i_{fg}+h\left(T_w-T_a\right)\right] \tag{E.1}$$

The mass transfer coefficient (h_d) and convection heat transfer coefficient (h) can be determined from a number of empirical relations, as discussed in Appendix C. Merkel (1952) makes the assumption that $Le_f \approx 1$, the effect of which is shown to be small in Fig. C.10. This assumption leads to the following relationship between the convection heat transfer coefficient (h) and the mass transfer coefficient (h_d):

$$Le_f = \frac{h}{c_{pma} h_d} \approx 1 \tag{E.2}$$

In the present analysis, the well-known equation by Ranz and Marshall (1952) for liquid drops suspended in a gas stream is used to determine the Nusselt number, expressed as

$$Nu = 2 + 0.6 Re^{1/2} Pr^{1/3} \tag{E.3}$$

This equation is compared to other equivalent models in Fig. C.2(b), to verify its validity over the entire range of Reynolds numbers applicable to cooling tower rain zones i.e. $Re \leq 10000$.

Substitute equations (E.2) and (E.3) into Eq. (E.1) and simplify it to find

$$\frac{dT_w}{dt} = -\frac{6k_a\left(2+0.6Re^{1/2}Pr^{1/3}\right)}{\rho_w c_{pw} c_{pma} d^2}\left[\left(w_{sw}-w\right)i_{fg}+c_{pma}\left(T_w-T_a\right)\right] \tag{E.4}$$

This equation must be solved numerically, as discussed in Appendix C, to obtain an exact solution for drop temperature as a function of time, as it is not mathematically integrable.

E.2 DROP TEMPERATURE

By separation of the variables, Eq. (E.4) can be written in integral form as

$$\int_{T_{wi}}^{T_w} \frac{\rho_w c_{pw} c_{pma} d^2}{6k_a\left[\left(w_{sw} i_{fg}+c_{pma}T_w\right)-\left(w i_{fg}+c_{pma}T_a\right)\right]} dT_w = -\int_0^t \left(2+0.6Re^{1/2}Pr^{1/3}\right) dt \tag{E.5}$$

A fairly accurate approximate analytical solution can be obtained if the integrands are approximated by functions that can be solved mathematically.

Consider the LHS of Eq. (E.5), expressed as

$$\text{Eq. (E.5)}_{\text{LHS}} = \int_{T_{wi}}^{T_w} \frac{a_1}{\left[\left(w_{sw} i_{fg}+c_{pma}T_w\right)+a_2\right]} dT_w \tag{E.6}$$

where

$$a_1 = \frac{\rho_w c_{pw} c_{pma} d^2}{6k_a} \approx 174\frac{\rho_w c_{pw} d^2}{k_a} \tag{E.7}$$

$$a_2 = -\left(w i_{fg}+c_{pma}T_a\right) \approx -\left(2\,445\,000 w + 1044 T_a\right) \tag{E.8}$$

The values of a_1 and a_2 are assumed constant since the drop diameter and thermophysical properties do not change much.

The sum of the terms that are dependent on water temperature, T_w, can be approximated by means of the following linear function, presented in Fig. E.1:

$$w_{sw} i_{fg} + c_{pma} T_w \approx 3500 \mathrm{T_w} - 680000 \tag{E.9}$$

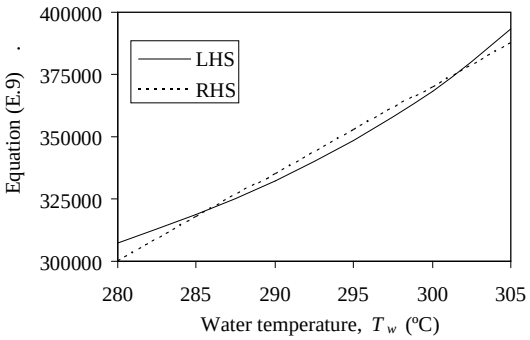

Figure E.1 : LHS and RHS of equation (E.9) as a function of drop temperature.

Substitute Eq. (E.9) into Eq. (E.6) and integrate to find the following solution:

$$\text{Eq.(E.5)}_{\text{LHS}} \approx \int_{T_{wi}}^{T_w} \frac{a_1}{\left[3500T_w + \left(a_2 - 680000\right)\right]} \mathrm{d}T_w = \frac{a_1}{3500} \ln\left[\frac{T_w + \left(a_2/3500 - 194.3\right)}{T_{wi} + \left(a_2/3500 - 194.3\right)}\right] \quad \text{(E.10)}$$

Now consider the RHS of Eq. (E.5), expressed as

$$\text{Eq (E.5)}_{\text{RHS}} = -\int_0^t \left(2 + 0.6Re^{1/2}Pr^{1/3}\right) dt \quad \text{(E.11)}$$

The integrand can be approximated by means of the following linear function of *Re*, as presented in Fig. E.2:

$$2 + 0.6Re^{1/2}Pr^{1/3} \approx b_1 Re + b_2 \quad \text{(E.12)}$$

where

$$b_1 = \frac{2.8\times10^{-5}}{d} \quad \text{(E.13)}$$

$$b_2 = 3000\, d \quad \text{(E.14)}$$

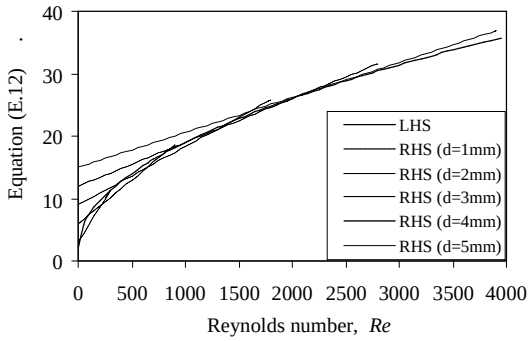

Figure E.2 : LHS and RHS of Eq. (E.12) as a function of Reynolds number.

Substitute the RHS of Eq. (E.12) into Eq. (E.11) to yield,

$$\text{Eq (E.5)}_{\text{RHS}} \approx -\int_0^t \left(b_1 Re + b_2\right) dt \quad \text{(E.15)}$$

The following equation for Reynolds number as a function of time is derived in Appendix D:

$$Re = \left(Re_0 + c_2\right) \mathrm{e}^{c_1 t} - c_2 \quad \text{(D.14)}$$

where

$$c_1 = -9.2348\times10^{5}\,\frac{\mu_a}{\rho_w d^{0.76548}} \tag{E.16}$$

$$c_2 = 1.3796\times10^{-5}\,\frac{\rho_a(\rho_a-\rho_w)d^{1.76548}}{\mu_a^{\,2}} \tag{E.17}$$

$$Re_0 = \frac{\rho_a v_0 d}{\mu_a} = \frac{\rho_a(v_a - v_{d0})\,d}{\mu_a} \tag{E.18}$$

Substitute Eq. (D.14) into Eq. (E.15) and integrate to find the following solution:

$$\text{Eq. (E.5)}_{\text{RHS}} \approx -\int_0^t \left(b_1\left[(\text{Re}_0 + c_2)\,\text{e}^{c_1 t} - c_2\right] + b_2\right)\text{d}t = -\left(d_1 Re_0 + d_2\right)\left(\text{e}^{c_1 t} - 1\right) - \left(b_2 - d_3\right)t \tag{E.19}$$

where

$$d_1 = \frac{b_1}{c_1} = \text{-}3.032\times10^{-11}\,\frac{\rho_w}{\mu_a}\,\frac{1}{d^{0.23452}} \tag{E.20}$$

$$d_2 = \frac{b_1 c_2}{c_1} = \text{-}4.182947\times10^{-16}\,\frac{\rho_w\rho_a(\rho_a-\rho_w)d^{1.53096}}{\mu_a^{\,3}} \tag{E.21}$$

$$d_3 = b_1 c_2 = 3.86288\times10^{-10}\,\frac{\rho_a(\rho_a-\rho_w)d^{0.76548}}{\mu_a^{\,2}} \tag{E.22}$$

Substitute equations (E.10) and (E.17) into Eq. (E.5) and simplify it to obtain an expression for drop temperature as a function of initial drop temperature, diameter and time, written as

$$T_w = \left[T_{wi} + e_1\right]\text{e}^{e_2} - e_1 \tag{E.23}$$

where

$$e_1 = \left(a_2/3500 - 194.3\right) \tag{E.24}$$

$$e_2 = -\frac{3500}{a_1}\left[\left(d_1 Re_0 + d_2\right)\left(\text{e}^{c_1 t} - 1\right) + \left(b_2 - d_3\right)t\right] \tag{E.25}$$

and a_1, a_2, b_2, c_1, d_1, d_2 and d_3 are obtained from equations (E.7), (E.8), (E.14), (E.16), (E.20), (E.21) and (E.22) respectively.

At ISO conditions, the atmospheric pressure is p_a = 101.325 kPa, the ambient temperature is T_a = 15 ºC and the relative humidity is RH = 60 % and Eq. (E.23) can be expressed as

$$T_w = \left[T_{wi} - 284.764\right]\text{e}^{\left(\frac{2.07446\times10^{-10}}{d^{2.2345}}Re_0 - \frac{0.010276}{d^{0.4690}}\right)\left(\text{e}^{-\left(0.016781/d^{0.76548}\right)t} - 1\right) - \left(\frac{3.7297\times10^{-4}}{d} - \frac{1.72439\times10^{-4}}{d^{1.23452}}\right)t} + 284.764 \tag{E.26}$$

Since this equation does not provide clear insight into the effect of drop diameter on drop temperature, Eq. (E.25) is plotted (Fig. E.3) against time for different drop diameters, ISO conditions, v_{d0} = -0.1 m/s, v_a = 2 m/s and a maximum path length of z_d = 12 m.

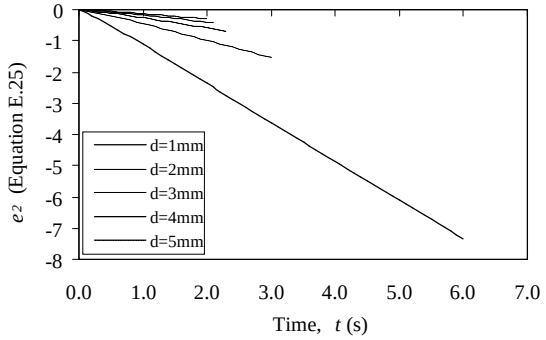

Figure E.3 : Equation (E.25) as a function of residence time for different drop diameters.

A curve fit through the data plotted in Fig. E.3 yields the following relation:

$$e_2 \approx \frac{-0.0001167}{d^{1.34}} t \tag{E.27}$$

Substitute Eq. (E.27) into Eq. (E.23) to yield

$$T_w \approx \left[T_{wi} - 284.764\right] \mathrm{e}^{-\left(\frac{0.0001167}{d^{1.34}}\right) t} + 284.764 \tag{E.28}$$

This equation shows that the strong influence of residence time and diameter on drop temperature as also depicted in Fig. E.4.

E.3 MERKEL NUMBER

The transfer characteristic or Merkel number is defined as

$$Me = \frac{\bar{h}_d A}{m_w} \tag{E.29}$$

From Eq. (E.2) and Eq. (E.3), the mean mass transfer coefficient, $\bar{h}_d$, can be expressed as

$$\bar{h}_d = \frac{1}{t}\int_0^t h_d \,\mathrm{d}t \approx \frac{k_a}{c_{pma} d\, t}\int_0^t (2+0.6 Re^{1/2} Pr^{1/3})\,\mathrm{d}t \tag{E.30}$$

Substitute Eq. (E.19) into Eq. (E.30) to find

$$\bar{h}_d \approx \frac{k_a}{c_{pma} d\, t}\left[\left(d_1 Re_0 + d_2\right)\left(\mathrm{e}^{c_1 t} - 1\right) - \left(d_3 - b_2\right) t\right] \tag{E.31}$$

The drop surface area, A, is expressed as

$$A = \pi d^2 \tag{E.32}$$

and the drop mass flow rate, m_w, is expressed as

$$m_w = \frac{\rho_w \pi d^2}{6\,t} \tag{E.33}$$

Substitute equations (E.31), (E.32) and (E.33) into Eq. (E.29) to yield the following approximate analytical equation for Merkel number:

$$Me = \frac{6\,k_a}{c_{pma}\rho_w d^2}\left[\left(d_1 Re_0 + d_2\right)\left(e^{c_1 t} - 1\right) - \left(d_3 - b_2\right)t\right] \tag{E.34}$$

Again for ISO conditions, this equation can be written as

$$Me = \frac{6\,k_a}{c_{pma}\rho_w d^2}\left[\begin{array}{l}\left(\dfrac{-1.6686\times10^{-3}}{d^{0.76548}}Re_0 + 8.26558\times10^4 d^{1.5310}\right)\left(e^{-(0.16781/d^{0.76548})t} - 1\right)\\ +\left(1.3870\times10^3 d^{0.76548} + 3000d\right)t\end{array}\right] \tag{E.35}$$

Since this equation also does not provide clear insight into the effect of drop diameter on Merkel number, Eq. (E.35) is plotted (Fig. E.5) against time for different drop diameters, ISO conditions, v_{d0} = 0.1 m/s, v_a = 2 m/s and a maximum path length of z_d = 12 m.

A curve fit through this data yields the following relationship between *Me*, drop diameter and time:

$$Me \approx \frac{0.0001382}{d^{1.34}}t \tag{E.36}$$

This relation shows the significant influence of drop diameter and residence time on Merkel number as also illustrated later on in Fig. E.4.

E.4 RESULTS

Figure (E.5) shows the comparison between drop temperatures determined using Eqs (E.26) and (E.28) and the corresponding exact data obtained using the numerical model in Appendix C. The results are based on: an air speed of v_a = 2 m/s; an initial absolute drop speed of v_{d0} = 0.1 m/s; ISO ambient conditions i.e. an atmospheric pressure of p_a = 101 325 N/m^2, an ambient air dry bulb temperature of T_{adb} = 15 ºC and a relative humidity of *RH* = 60 %; an inlet water temperature of T_{wi}= 30 ºC; and a maximum path length of z_d = 12 m.

Figure E.5 shows the Merkel number determined using Eqs (E.35) and (E.36) for the same conditions as above.

E.5 CONCLUSION

In this section, approximate analytical equations are derived for the temperature change and transfer characteristic (Merkel number) of a single drop falling vertically through upward moving air, as functions of residence time (*t*), drop diameter (*d*), initial drop speed (v_{d0}), absolute air speed (v_a) and thermophysical properties.

Results are presented for the following conditions: drop diameters of d = 1, 2, 3, 4 and 5mm; an air speed of v_a = 2 m/s; an initial absolute drop speed of v_{d0} = 0.1 m/s; ISO ambient conditions i.e. an atmospheric pressure of p_a = 101 325 N/m^2, an ambient air dry bulb temperature of T_{adb} = 15 ºC, a relative humidity of RH = 60 %; and a water temperature of T_w= T_{awb}=10.9 ºC. This data is compared to corresponding numerical data, for path lengths up to z_d = 12 m and it is found that the deviations between the approximate analytical and numerical solutions are relatively small. From the approximate analytical solutions, it can be seen that the effect of residence time and drop diameter on drop temperature and Merkel number are significant.

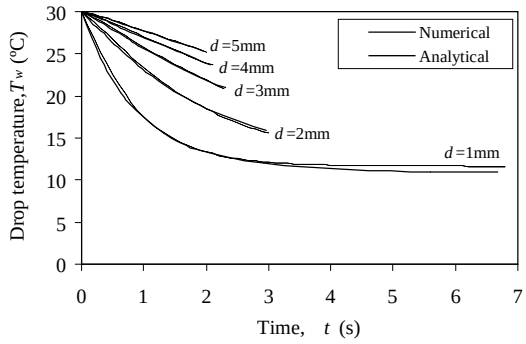

(a) Approximate analytical data based on Eq. (E.26).

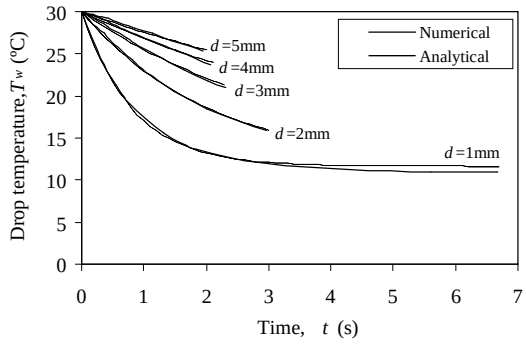

(b) Approximate analytical data based on Eq. (E.28).

Figure E.4 : Comparison between approximate analytical and numerical drop temperature data plotted against residence time.

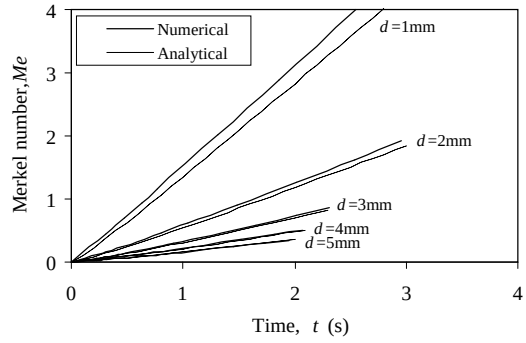

(a) Approximate analytical data based on Eq. (E.35).

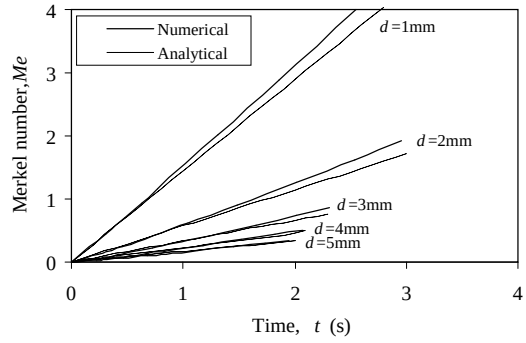

(b) Approximate analytical data based on Eq. (E.36).

Figure E.5: Comparison between approximate analytical and numerical Merkel number data plotted against residence time.

F

ANALYTICAL AND EMPIRICAL RAIN ZONE AND FILL MERKEL NUMBER RELATIONS

Kloppers and Kröger [2005(1)] conducted tests in a counter-flow cooling tower fill test facility, measuring the effects of the following variables on the fill transfer characteristic (Merkel number): water mass velocity (G_w) and air mass velocity (G_a) for splash, trickle and film type fills; fill height (L_{fi}) for trickle and film type fills; and inlet water temperature (T_{wi}), inlet air dry-bulb temperature (T_{ai}) and inlet air wet-bulb temperature (T_{wbi}) for trickle fills. The results showed that the effects of G_w, G_a, L_{fi} and T_{wi} are significant, but that the effects of T_{ai} and T_{wbi} are small and the following general form of the transfer characteristic correlation is proposed:

$$\frac{Me}{L_{fi}} = a_1 G_w^{\,a_2} G_a^{\,a_3} L_{fi}^{\,a_4} T_{wi}^{\,a_5} \tag{F.1}$$

Due to the fixed location and limitations of the test facility used by Kloppers, the effect of air pressure could not be tested. Since many wet-cooled power plants are located high above sea level, it is important to determine the effect of atmospheric pressure on the fill characteristics measured at sea level should this need to be corrected for design purposes.

To investigate the effect of thermophysical properties and fundamental independent variables on the transfer characteristic, analytical equations are derived for the Merkel number based on single drops falling at terminal speed in upward flowing air, since drops free-falling in air flowing at v_a = 2 m/s reach terminal speed at a distance of between z_d = 1 m and 4 m depending on the drop size, as shown in Appendix B. Equations are proposed for the extreme cases of constant drag coefficient, applicable to higher Reynolds numbers (large drops) and Stokes law ($C_D = 24/Re$) for low Reynolds numbers (creeping flow where Re < 0.5) applicable to very small drops. For comparison, an analytical equation is also derived for another interesting case where a water film runs down evenly spaced vertical flat sheets. Ultimately, empirical correlations are proposed for the transfer characteristic of uniform drops accelerating under gravity in counter- and cross-flow configuration, determined using the numerical analysis presented in Appendix C based on the drag coefficient relation of Dreyer (1994) for deformed drops (Eq. B.12), the heat transfer coefficient relation by Ranz and Marshall (1952) (Eq. C.12), a Lewis factor of Le_f = 1, Eq. (C.7) for the rate of mass transfer and the diffusion coefficient relation of Fuller (VDI 2006) (Eq. C.42).

F.1 SINGLE DROP FALLING AT TERMINAL SPEED IN AIR FLOWING UPWARDS

Consider a single drop falling in air flowing vertically upwards. The heat transfer coefficient of the drop can be approximated by

$$\frac{hd}{k_a} \approx a_1 Re_a^{a_2} Pr_a^{a_3} \tag{F.2}$$

For a Lewis factor of $Le_f = 1$, the mass transfer coefficient can be expressed in terms of the heat transfer coefficient as

$$h_d = \frac{h}{c_{pa}\, Le_f} = \frac{k_a}{d\, c_{pa}}\left(a_1 Re^{a_2} Pr^{a_3}\right) = \frac{a_1\, k_a}{d\, c_{pa}}\left(\frac{\rho_a v\, d}{\mu_a}\right)^{a_2}\left(\frac{\mu_a c_{pa}}{k_a}\right)^{a_3} \tag{F.3}$$

From the definition of Merkel number it follows that

$$Me = \frac{\bar{h}_d A_d}{m_w} = \frac{6\bar{h}_d z_d}{\rho_w d\, \bar{v}_d} = 6\, a_1 \frac{k_a^{(1-a_3)}}{c_{pa}^{(1-a_3)} \mu_a^{(a_2-a_3)}} \frac{\rho_a^{a_2}}{\rho_w} \frac{z_d}{d^{(2-a_2)} \bar{v}^{(1-a_2)}} \left(\frac{1}{1-v_a/\bar{v}}\right) \tag{F.4}$$

For $v_a/\bar{v} < 1$, a series approximation can be applied to the last term in brackets, which are compared in Fig. F.1.

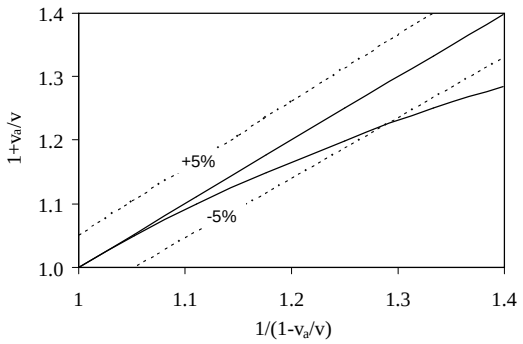

Fig. F.1 : Comparison between the the last term in Eq. (F.4), in brackets, and a series approximation.

Eq. (F.4) can therefore be re-written as

$$Me \approx 6\, a_1 \frac{k_a^{(1-a_3)}}{c_{pa}^{(1-a_3)} \mu_a^{(a_2-a_3)}} \frac{\rho_a^{a_2}}{\rho_w} \frac{z_d}{d^{(2-a_2)}} \left(\frac{1+v_a/\bar{v}}{\bar{v}^{(1-a_2)}}\right) \quad \text{for} \quad v_a \ll \bar{v} \tag{F.5}$$

The exponents of Eq. (F.2) are obtained from a curve-fit of the Ranz and Marshall (1952) relation for the ranges of *Re* and *Pr* typically encountered in rain zones, which yields

$$\frac{hd}{k_a} = 2 + 0.6 Re^{1/2} Pr^{1/3} \approx Re^{0.44} Pr^{0.28} \tag{F.6}$$

Substitute the exponents of Eq. (F.6) into Eq. (F.5) and simplify the resultant equation to obtain

$$Me \approx 6\frac{k_a^{0.72}}{c_{pa}^{0.72}\mu_a^{0.16}}\frac{\rho_a^{0.44}}{\rho_w}\frac{z_d}{d^{1.56}}\left(\frac{1+v_a/\bar{v}}{\bar{v}^{0.56}}\right) \quad \text{for} \quad v_a \ll \bar{v} \tag{F.7}$$

The terminal speed of a drop falling in air is given by

$$v_T = \bar{v} = \left(\frac{4\rho_w d\, g}{3C_D\rho_a}\right)^{0.5} \tag{F.8}$$

The Merkel number for terminal speed therefore becomes

$$Me \approx 2.921625\frac{k_a^{0.72}}{c_{pa}^{0.72}\mu_a^{0.16}}\frac{\rho_a^{0.72}}{\rho_w^{1.28}}\frac{C_D^{0.28}z_d}{d^{1.84}}\left[1+\left(\frac{3C_D\rho_a}{4\rho_w dg}\right)^{0.5}v_a\right] \quad \text{for} \quad v_a \ll v_T \tag{F.9}$$

or in terms of the air mass velocity (G_a) can be written as

$$Me \approx 2.921625\frac{k_a^{0.72}}{c_{pa}^{0.72}\mu_a^{0.16}}\frac{\rho_a^{0.72}}{\rho_w^{1.28}}\frac{C_D^{0.28}z_d}{d^{1.84}}\left[1+\left(\frac{3C_D}{4\rho_a\rho_w dg}\right)^{0.5}G_a\right] \tag{F.10}$$

The Merkel number can also be expressed in terms of fundamental independent variables, by obtaining correlations for the property terms that are functions of T_a and T_w, as follows:

$$Me \approx 6.849177\times10^{-10}\frac{p_a^{0.72}T_{w(K)}^{0.085}}{T_{a(K)}^{0.208}}\frac{C_D^{0.28}z_d}{d^{1.84}}\left[1+0.1233677\left(\frac{T_{a(K)}C_D}{p_a d}\right)^{0.5}T_{w(K)}^{0.0325}G_a\right] \tag{F.11}$$

where $T_{a(K)}$ and $T_{w(K)}$ are in Kelvin.

Since *Me* is generally expressed in terms of temperatures in ºC, the temperatures in Eq. (F.11) are converted to ºC by means of the following correlations:

$$T_{a(K)} = 252.780T_{a(°C)}^{0.04836} \text{ for } T_{a(°C)} \approx 15\ °C \tag{F.12}$$

$$T_{w(K)} = 257.172T_{w(°C)}^{0.04836} \text{ for } T_{w(°C)} \approx 30\ °C \tag{F.13}$$

Substituting Eqs (F.12) and (F.13) into (F.11) yields

$$Me \approx 3.473257\times10^{-10}\frac{p_a^{0.72}T_{w(ºC)}^{0.00411}}{T_{a(ºC)}^{0.0101}}\frac{C_D^{0.28}z_d}{d^{1.84}}\left[1+2.349119\left(\frac{C_D}{p_a d}\right)^{0.5}T_{a(ºC)}^{0.02418}T_{w(ºC)}^{0.00157}G_a\right] \tag{F.14}$$

For large drops, where C_D is a constant and for the case of still air (v_a = 0 m/s), Eqs (F.10), (F.11) and (F.14) therefore simplify to

$$\begin{aligned} Me &\approx 2.921625\frac{k_a^{0.72}}{c_{pa}^{0.72}\mu_a^{0.16}}\frac{\rho_a^{0.72}}{\rho_w^{1.28}}\frac{C_D^{0.28}z_d}{d^{1.84}} \\ &\approx 6.849177\times10^{-10}\frac{p_a^{0.72}T_{w(K)}^{0.085}}{T_{a(K)}^{0.208}}\frac{C_D^{0.28}z_d}{d^{1.84}} \approx 3.473257\times10^{-10}\frac{p_a^{0.72}T_{w(ºC)}^{0.00411}}{T_{a(ºC)}^{0.0101}}\frac{C_D^{0.28}z_d}{d^{1.84}} \end{aligned} \tag{F.15}$$

For very small drops the drag coefficient can be $C_D = 24/Re$ (Stokes law) for the extreme case of creeping flow with no flow separation where $Re < 0.5$ and the terminal drop speed therefore becomes

$$v_T = \left(\frac{\rho_w d^2 g}{18\,\mu_a} \right) \tag{F.16}$$

Substitute Eq. (F.16) into Eq. (F.9) to obtain

$$Me \approx 8.433683 \frac{k_a^{0.72} \mu_a^{0.4}}{c_{pa}^{0.72}} \frac{\rho_a^{0.44}}{\rho_w^{1.56}} \frac{z_d}{d^{2.68}} \left[1 + 1.836735 \frac{\mu_a}{\rho_w d^2} v_a \right] \tag{F.17}$$

or in terms of air mass velocity

$$Me \approx 8.433683 \frac{k_a^{0.72} \mu_a^{0.4}}{c_{pa}^{0.72}} \frac{\rho_a^{0.44}}{\rho_w^{1.56}} \frac{z_d}{d^{2.68}} \left[1 + 1.836735 \frac{\mu_a}{\rho_a \rho_w d^2} G_a \right] \tag{F.18}$$

Expressed in terms of the primary fundamental variables and temperatures in Kelvin, Eq. (F.18) becomes

$$Me \approx 2.608568 \times 10^{-13}\, p_a^{0.44} T_{a(K)}^{0.492} T_{w(K)}^{0.1} \frac{z_d}{d^{2.68}} \left[1 + 9.359233 \times 10^{-8} \frac{T_{a(K)}^{1.75} T_{w(K)}^{0.065}}{p_a d^2} G_a \right] \tag{F.19}$$

and for temperatures in ºC,

$$Me \approx 6.91152 \times 10^{-12}\, p_a^{0.44} T_{a(ºC)}^{0.0238} T_{w(ºC)}^{0.004836} \frac{z_d}{d^{2.68}} \left[1 + 0.002151317 \frac{T_{a(ºC)}^{0.08463} T_{w(ºC)}^{0.003143}}{p_a d^2} G_a \right] \tag{F.20}$$

For still air (v_a = 0 m/s), Eqs (F.17) to (C.20) simplify to

$$\begin{aligned} Me &\approx 8.433683 \frac{k_a^{0.72} \mu_a^{0.4}}{c_{pa}^{0.72}} \frac{\rho_a^{0.44}}{\rho_w^{1.56}} \frac{z_d}{d^{2.68}} \\ &\approx 2.608568 \times 10^{-13}\, p_a^{0.44} T_{a(K)}^{0.492} T_{w(K)}^{0.1} \frac{z_d}{d^{2.68}} \approx 6.91152 \times 10^{-12}\, p_a^{0.44} T_{a(ºC)}^{0.0238} T_{w(ºC)}^{0.004836} \frac{z_d}{d^{2.68}} \end{aligned} \tag{F.21}$$

F.2 A WATER FILM RUNNING DOWN A VERTICAL FLAT PLATE AT TERMINAL SPEED IN AIR FLOWING UPWARDS

Consider a water film of thickness δ running down a vertical flat plate in air flowing upward as shown in Fig. F.2. The shear stress in the water film can be expressed as

$$\tau_x = \mu_w \left. \frac{\partial v_z}{\partial x} \right|_x = g \rho_w (\delta - x) - \tau_\delta \tag{F.22}$$

Assume no shear stress (τ_δ = 0) at $x = \delta$ and integrate Eq. (F.22) by assuming laminar film flow to yield

$$v_z = \frac{g \rho_w \left(\delta x - x^2/2 \right)_\delta}{\mu_w} \tag{F.23}$$

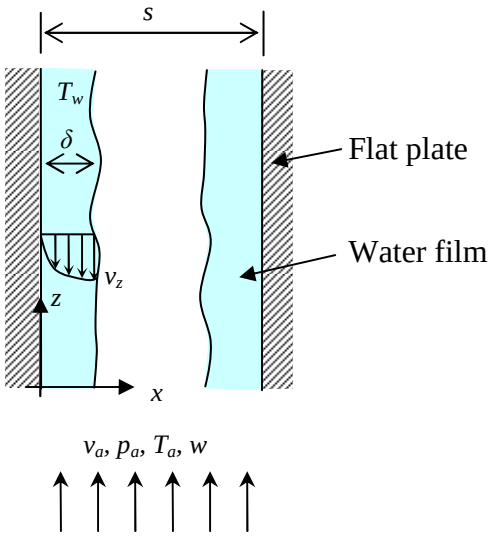

Figure F.2: Water running down a flat plate in air flowing upward.

The film flow rate per unit plate width is then

$$m_w = \rho_w \int_0^{\delta} v_z \mathrm{d}x = \frac{g\rho_w^2}{\mu_w} \int_0^{\delta} \left(\delta x - x^2/2\right) \mathrm{d}x = \frac{g\rho_w^2 \delta^3}{3\mu_w} \tag{F.24}$$

It follows that

$$\delta = \left(\frac{3\mu_w m_w}{g\rho_w^2} \right)^{1/3} \tag{F.25}$$

The absolute speed of the film surface at the air interface is therefore

$$v_{z(\delta)} = \frac{g\rho_w \delta^2}{2\mu_w} = 1.04 \left(\frac{g}{\rho_w \mu_w} \right)^{1/3} m_w^{2/3} \tag{F.26}$$

The following relation by Dittus and Boelter (1930) can be used to determine the air-side heat transfer coefficient for turbulent flow in ducts:

$$\frac{hd}{k_a} \approx 0.0265 Re_a^{\ 0.8} Pr_a^{\ 0.3} \tag{F.27}$$

For a Lewis factor of Le_f = 1, the mass transfer coefficient can be expressed in terms of the heat transfer coefficient as

$$h_d = \frac{h}{c_{pa}} = \frac{0.0265 k_a}{d_e \, c_{pa}} \left(\frac{\rho_a \left(v_a + v_{z(\delta)}\right) d_e}{\mu_a} \right)^{0.8} \left(\frac{\mu_a c_{pa}}{k_a} \right)^{0.3} \tag{F.28}$$

where the effective diameter is twice the distance between two plates i.e. $d_e = 2\,s$.

The Merkel number is defined as

$$Me = \frac{h_d A_d}{m_w} = \frac{h_d 2H_f}{m_w} = \frac{0.053 k_a^{0.7}}{d_e^{0.2} c_{pa}^{0.7} \mu_a^{0.5}} \frac{\left[\rho_a \left(v_a + v_{z(\delta)}\right)\right]^{0.8} H_f}{m_w} \tag{F.29}$$

For typical film fill, consisting of vertical flat sheets spaced 20 – 25 mm apart, it can be found from Eq. (F.26) that $v_a >> v_{z(\delta)}$ and that the Merkel number can therefore be approximated by

$$Me \approx 0.106 \left(\frac{k_a^{0.7}}{c_{pa}^{0.7} \mu_a^{0.5} d_e^{1.2}} \right) \frac{G_a^{0.8}}{G_w} H_f \tag{F.30}$$

Expressed in terms of the primary fundamental variables and temperature in Kelvin, Eq. (F.30) becomes

$$Me \approx 0.003877 \left(\frac{T_{a(K)}^{0.24}}{d_e^{1.2}} \right) \frac{G_a^{0.8}}{G_w} H_f \approx 0.539 \frac{G_a^{0.8}}{G_w} H_f \tag{F.31}$$

For temperature in ºC, Eq. (F.12) is used to convert Eq. (F.31) to

$$Me \approx 0.014627 \left(\frac{T_{a(ºC)}^{0.0116}}{d_e^{1.2}} \right) \frac{G_a^{0.8}}{G_w} H_f \tag{F.32}$$

Fill performance characteristics presented in Kröger (2004), show that for flat sheets spaced s = 25.4 mm apart, the Merkel number is

$$Me = 0.459 \left(\frac{G_a}{G_w} \right)^{0.73} H_f \tag{F.33}$$

F.3 SINGLE DROP ACCELERATING UNDER GRAVITY IN AIR FLOWING UPWARDS

From the above analysis it is clear that the Merkel number can be dependent upon the following fundamental variables:

$$Me = \mathrm{f}\left(p_a, T_a, w, v_a, T_{wi}, v_{d0}, d, z_d\right) \tag{F.34}$$

To clearly show the influence of these variables on the Merkel number of a drop free-falling under gravity in a vertical air-stream, the following empirical relation is obtained by correlation of numerical data obtained from the numerical analysis in Appendix C, based on the drag coefficient relation of Dreyer (1994) for deformed drops (Eq. B.12), the heat transfer coefficient relation by Ranz and Marshall (1952) (Eq. C.12), a Lewis factor of Le_f = 1, Eq. (C.7) for the rate of mass transfer and the diffusion coefficient relation of Fuller (VDI 2006) (Eq. 42):

$$Me \approx 5.589337 \times 10^{-9} \frac{p_a^{0.61} v_a^{0.35} z_d^{0.785}}{T_{a(ºC)}^{0.002176} w^{0.006} T_{wi(ºC)}^{0.009672} d^{1.65} v_{d0}^{0.025}} \tag{F.35}$$

The temperatures in this equation are in ºC and it is valid for the following conditions:

$85000 \le p_a \le 101325$ N/m^2; $10 \le T_a \le 30$ ºC; $0.002 \le w_a = 0.03$ kg/kg d.a.; $1 \le v_a \le 3$ m/s; $25 \le T_{wi} \le 40$ ºC; $0.002 \le d_d \le 0.01$ m; $0.1 \le v_{d0} \le 1.0$ m/s and $3 \le z_d \le 10$ m.

The curve-fit reference data is:

$p_{a(ref)} = 101325$ N/m^2; $T_{a(ref)} = 15$ ºC; $w_{a(ref)} = 0.0064613$ kg/kg d.a.; $v_{a(ref)} = 2$ m/s; $T_{wi(ref)} = 30$ ºC; $d_{d(ref)} = 0.003$ m; $v_{d0(ref)} = 0.1$ m/s and $z_{d(ref)} = 5$ m.

Since *Me* number relations are generally expressed in terms of the air mass velocity (G_a), Eq. (F.35) is also expressed in terms of G_a as

$$Me \approx 2.809431\times10^{-7}\,\frac{p_a^{\,0.25}\,T_{a(^oC)}^{\,0.01475}\,G_a^{\,0.35}\,z_d^{\,0.785}}{w^{0.006}\,T_{wi(^oC)}^{\,0.009672}\,d^{1.65}\,v_{d0}^{\,0.025}} \qquad \text{(F.36)}$$

The deviations between Eqs (F.35) or (F.36) and corresponding numerical data are shown in Fig. F.3 for different air mass velocities, drop diameters, and atmospheric pressures.

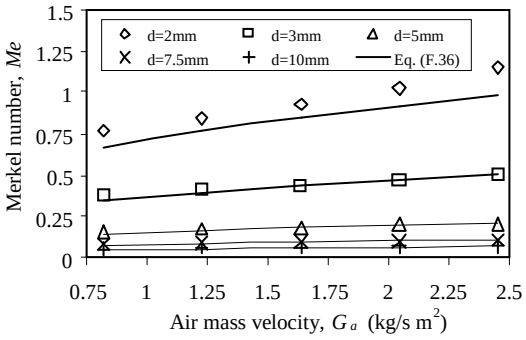

(a_1) Merkel number (p_a=101325 N/m^2).

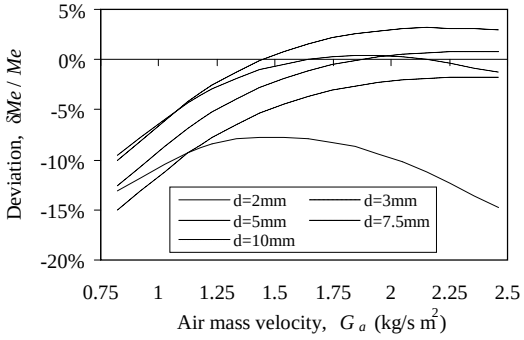

(a_2) Deviation (p_a=101325 N/m^2).

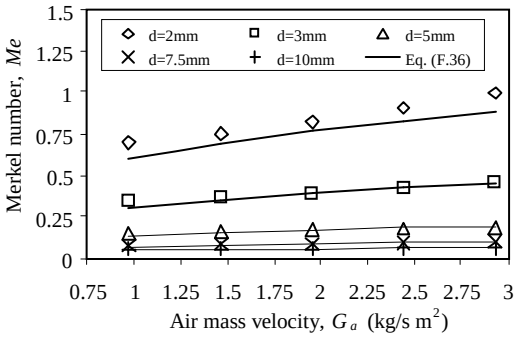

(b_1) Merkel number (p_a=85000 N/m^2).

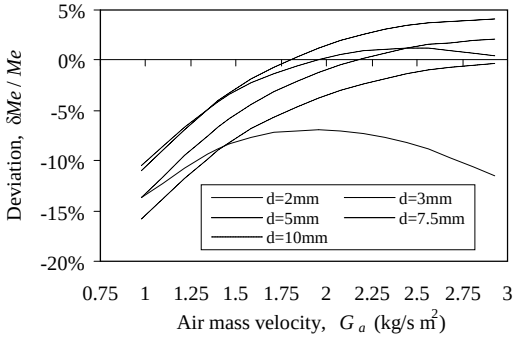

(b_2) Deviation (p_a=85000 N/m^2).

Figure F.3 : Deviation between Eqs (F.35) or (F.36) and corresponding numerical data for different air mass velocities, drop diameters and atmospheric pressures.

F.4 SINGLE DROP ACCELERATING UNDER GRAVITY IN HORIZONTAL AIR FLOW

In exactly the same way and for the same conditions as Eq. (F.35), an empirical relation for Merkel number is obtained for drops falling through air flowing horizontally, given as

$$Me \approx 2.434895\times10^{-8}\,\frac{p_a^{\,0.51}T_{a(^oC)}^{\,0.000242}v_a^{\,0.1}z_d^{\,0.76}}{w^{0.006}T_{wi(^oC)}^{\,0.005803}d^{1.59}v_{d0}^{\,0.025}} \qquad \text{(F.37)}$$

Since *Me* number relations are generally expressed in terms of the air mass velocity (G_a), Eq. (F.37) is also expressed in terms of G_a by

$$Me \approx 7.456839\times10^{-8}\,\frac{p_a^{\,0.41}G_a^{\,0.1}z_d^{\,0.76}}{w^{0.006}T_{a(^oC)}^{\,0.004594}T_{wi(^oC)}^{\,0.005803}d^{1.59}v_{d0}^{\,0.025}} \qquad \text{(F.38)}$$

The deviations between Eqs (F.37) or (F.38) and corresponding numerical data are shown in Fig. F.4 for different air mass velocities, drop diameters, and atmospheric pressures.

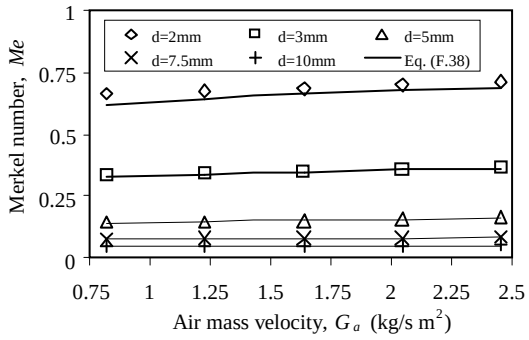

(a_1) Merkel number (p_a=101325 N/m^2).

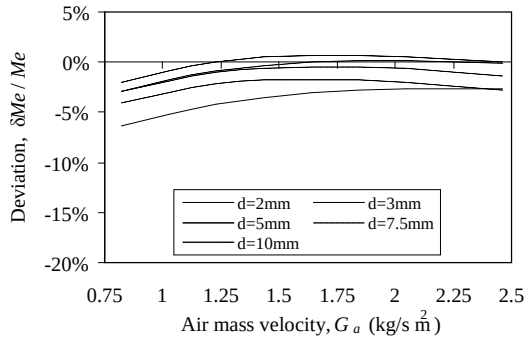

(a_2) Deviation (p_a=101325 N/m^2).

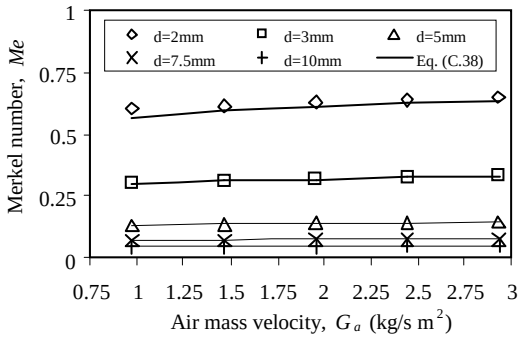

(b_1) Merkel number (p_a=85000 N/m^2).

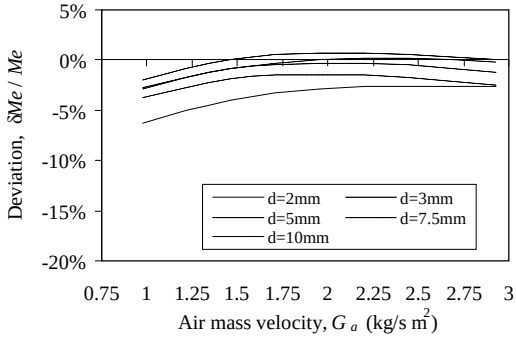

(b_2) Deviation (p_a=85000 N/m^2).

Figure F.4 : Deviation between Eqs (F.37) or (F.38) and corresponding numerical data for different air mass velocities, drop diameters and atmospheric pressures.

F.4 CONCLUSIONS

Analytical equations are derived for the Merkel number of drops falling at terminal speed in upward flowing air and a water film running down uniformly spaced flat sheets in upward flowing air. From the analysis, it is seen that the speed at which drops fall through the air is significantly higher than the speed of a water film running down a flat sheet. To clearly show the influence of the fundamental independent variables on the Merkel number of counter- and crossflow rain zones, empirical relations are obtained using data from the numerical analysis in Appendix C and the deviations are seen to be small. The following conclusions can be made:

- ⇨ The Merkel number of counter- and cross-flow cooling tower rain zones is strongly dependent on drop diameter (d), drop falling distance (z_d) or rain zone height (H_{rz}), air mass velocity (G_a) and the atmospheric pressure (p_a) and is totally independent of the water mass velocity (G_w).
- ⇨ The Merkel number for counter-flow (Eq. F.34) is more sensitive to air mass velocity (G_a) and drop diameter (d), but less sensitive to pressure (p_a) than for cross-flow (Eq. F.36).
- ⇨ In comparison, the Merkel number of water running down flat sheets, as encountered in certain types of film packs, is strongly dependent on the air and water mass velocities (G_a and G_w), the gap between sheets (d_e=2s), the sheet height (H_f) and the air temperature (T_a), but is independent of atmospheric pressure (p_a). The analytical equation also shows that the exponents for G_a and G_w are comparable to those of a corresponding correlation for flat sheet film fill found in Kröger (2004).

G

ANALYTICAL AND EMPIRICAL RAIN ZONE LOSS COEFFICIENT RELATIONS

Kloppers and Kröger (2003) conducted tests in a counter-flow cooling tower fill test facility, as discussed in App. F, measuring the effects of the following variables on the fill loss coefficient: water mass velocity (G_w) and air mass velocity (G_a) for splash, trickle and film type fills; and fill height (L_{fi}) for trickle and film type fills. The results showed that the effects of G_w, and G_a are significant and the following general form of the loss coefficient equation is proposed:

$$K_{fi}=a_1 G_w^{a_2} G_a^{a_3} + a_4 G_w^{a_5} G_a^{a_6} \tag{G.1}$$

By following the same procedure as presented in Appendix F, analytical equations are derived in this section for the loss coefficient of single drops falling at terminal speed in upward flowing air to investigate the effect of thermophysical properties and fundamental independent variables on the loss coefficient. Equations are proposed for the extreme cases of constant drag coefficient, found at higher Reynolds numbers applicable to large drops and Stokes law ($C_D = 24/Re$) at low Reynolds numbers (creeping flow where Re < 0.5) for small drops. Ultimately, empirical correlations are proposed for the loss coefficient of drops accelerating under gravity in counter- and cross-flow configuration, determined using the numerical analysis presented in Appendices B and C based on the drag coefficient relation of Dreyer (1994) for deformed drops (Eq. B.12), the heat transfer coefficient relation by Ranz and Marshall (1952) (Eq. C.12), a Lewis factor of $Le_f = 1$, Eq. (C.7) for the rate of mass transfer and the diffusion coefficient relation of Fuller (VDI 2006) (Eq. C.42).

G.1 SINGLE DROP FALLING AT TERMINAL SPEED IN AIR FLOWING UPWARDS

Consider a rain zone of drops falling in air flowing vertically upwards. The rain zone loss coefficient can be determined from the mean drag force ($\bar{F}_{D_a}$) of a single drop using Eq. (B.19), written as

$$\frac{K_{fdm}}{G_w}\frac{A_{fr_a}}{A_{fr_w}} \approx \frac{12\, t\, \bar{F}_{D_a}}{\pi d^3 \rho_w \rho_a v_a^2} \tag{G.2}$$

where the drag force of a spherical drop is defined as

$$\bar{F}_{D_a} = C_D \pi d^2 \frac{\rho_a \bar{v}^2}{2} \tag{G.3}$$

Substitute Eq. (G.3) into Eq. (G.2) to yield

$$\frac{K_{fdm}}{G_w}\frac{A_{fr_a}}{A_{fr_w}} \approx \frac{6\,C_D z_d}{\rho_w d}\frac{\overline{v}^2}{v_a^2 \overline{v}_d} = \frac{6 C_D z_d}{\rho_w d}\frac{\overline{v}}{v_a^2\left(1\text{-}v_a/\overline{v}\right)} \tag{G.4}$$

By applying the same series approximation to the last term between brackets as for Eq. (F.4), compared in Fig. F.1, Eq. (G.4) can be re-written as

$$\frac{K_{fdm}}{G_w}\frac{A_{fr_a}}{A_{fr_w}} \approx \frac{6\,C_D z_d}{\rho_w d}\frac{\overline{v}\left(1+v_a/\overline{v}\right)}{v_a^2} \quad \text{for } v_a \ll \overline{v} \tag{G.5}$$

Substitute the terminal speed of a drop falling in upward moving air (Eq. F.8) into Eq. (G.5) and take $A_{fr\,a} / A_{fr\,w} = 1$, to find the following relation for a counter-flow rain zone:

$$\frac{K_{fdm}}{G_w z_d} \approx 21.688707\left(\frac{C_D}{\rho_a \rho_w d}\right)^{0.5}\frac{1}{v_a^2} + 6\frac{C_D}{\rho_w d}\frac{1}{v_a} \tag{G.6}$$

or expressed in terms of the air mass velocity (G_a) as

$$\frac{K_{fdm}}{G_w z_d} \approx\ 21.688707\left(\frac{C_D \rho_a^3}{\rho_w d}\right)^{0.5}\frac{1}{G_a^2} + 6\left(\frac{C_D \rho_a}{\rho_w d}\right)\frac{1}{G_a} \tag{G.7}$$

The loss coefficient can also be expressed in terms of fundamental independent variables, by obtaining correlations for the property terms that are functions of T_a and T_w, as follows:

$$\frac{K_{fdm}}{G_w z_d} \approx 1.173577\times10^{-4}\left(\frac{C_D p_a^3 T_{wi(K)}^{0.065}}{T_{a(K)}^3 d}\right)^{0.5}\frac{1}{G_a^2} + 1.447815\times10^{-5}\left(\frac{C_D p_a T_{wi(K)}^{0.065}}{T_{a(K)} d}\right)\frac{1}{G_a} \tag{G.8}$$

where temperatures are in Kelvin.

Since K_{fdm} is generally expressed in terms of temperatures in ºC, the temperatures in Eq. (G.8) are converted to ºC using Eqs (F.12) and (F.13), to yield

$$\frac{K_{fdm}}{G_w z_d} \approx 3.497275\times10^{-8}\left(\frac{C_D p_a^3 T_{wi(ºC)}^{0.003143}}{T_{a(ºC)}^{0.1451} d}\right)^{0.5}\frac{1}{G_a^2} + 8.215522\times10^{-8}\left(\frac{C_D p_a T_{wi(ºC)}^{0.003143}}{T_{a(ºC)}^{0.04836} d}\right)\frac{1}{G_a} \tag{G.9}$$

For large drops falling at terminal speed with high Reynolds numbers, C_D can be assumed constant. For very small drops the drag coefficient can be approximated by $C_D = 24/Re$ (Stokes law) for the extreme case of creeping flow with no flow separation where $Re < 0.5$ and the terminal drop speed is therefore given by Eq. (F.14). Substitute Eq. (F.14) into Eq. (G.6) to obtain

$$\frac{K_{fdm}}{G_w z_d} \approx 3.266667\frac{C_D d}{\mu_a}\frac{1}{v_a^2} + 6\left(\frac{C_D}{\rho_w d}\right)\frac{1}{v_a} \tag{G.10}$$

or in terms of air mass velocity

$$\frac{K_{fdm}}{G_w z_d} \approx 3.266667\frac{C_D \rho_a^2 d}{\mu_a}\frac{1}{G_a^2} + 6\left(\frac{\rho_a C_D}{\rho_w d}\right)\frac{1}{G_a} \tag{G.11}$$

Expressed in terms of the primary fundamental variables and temperatures in Kelvin, Eq. (G.11) becomes

$$\frac{K_{fdm}}{G_w z_d} \approx 154.6953 \frac{C_D p_a^2 d}{T_{a(K)}^{2.75}} \frac{1}{G_a^2} + 1.447829 \times 10^{-5} \left(\frac{C_D p_a \ T_{wi(K)}^{0.065}}{d} \right) \frac{1}{G_a} \tag{G.12}$$

and for temperatures in ºC

$$\frac{K_{fdm}}{G_w z_d} \approx 3.818868 \times 10^{-5} \frac{C_D p_a^2 d}{T_{a(ºC)}^{0.133}} \frac{1}{G_a^2} + 8.215596 \times 10^{-8} \left(\frac{C_D p_a T_{wi(ºC)}^{0.003134}}{T_{a(ºC)}^{0.04837} d} \right) \frac{1}{G_a} \tag{G.13}$$

The above equations are all found to be in the form proposed by Kloppers (2003).

G.2 SINGLE DROP ACCELERATING UNDER GRAVITY IN AIR FLOWING UPWARDS

From the above analysis it is clear that the loss coefficient is dependent upon the following fundamental variables:

$$K_{fdm} = \mathrm{f}\left(p_a \ , T_a \ , G_a \ , G_w \ , T_{wi} \ , d \ , v_{d0} \ , z_d \right) \tag{G.14}$$

To clearly show the influence of these variables on the loss coefficient of a drop free-falling under gravity in a vertical air-stream, the following empirical relation is obtained by correlation of numerical data obtained from the numerical analysis in Appendix C, based on the drag coefficient relation of Dreyer (1994) for deformed drops (Eq. B.12), the heat transfer coefficient relation by Ranz and Marshall (1952) (Eq. C.12), a Lewis factor of Le_f = 1, Eq. (C.7) for the rate of mass transfer and the diffusion coefficient relation of Fuller (1966) (Eq. 42).

$$\frac{K_{fdm}}{G_w} \approx 0.389506 \frac{T_{a(ºC)}^{\ 0.03385} w^{\ 0.002} z_d^{\ 1.1}}{p_a^{\ 0.215} T_{wi(ºC)}^{\ 0.01161} d^{0.63} v_{d0}^{\ 0.0015} v_a^{\ 1.45}} \tag{G.15}$$

The temperatures in this equation are in ºC and it is valid for the following conditions:

$85000 \leq p_a \leq 101325$ N/m^2; $10 \leq T_a \leq 30$ ºC; $0.002 \leq w_a = 0.03$ kg/kg d.a.; $1 \leq v_a \leq 3$ m/s; $25 \leq T_{wi} \leq 40$ ºC; $0.002 \leq d_d \leq 0.01$ m; $0.1 \leq v_{d0} \leq 1.0$ m/s and $3 \leq z_d \leq 10$ m.

The curve-fit reference data is:

$p_{a(ref)} = 101325$ N/m^2; $T_{a(ref)} = 15$ ºC; $w_{a(ref)} = 0.0064613$ kg/kg d.a.; $v_{a(ref)} = 2$ m/s; $T_{wi(ref)} = 30$ ºC; $d_{d(ref)} = 0.003$ m; $v_{d0(ref)} = 0.1$ m/s and $z_{d(ref)} = 5$ m.

Since loss coefficient relations are generally expressed in terms of the air and water mass velocity, Eq. (G.15) is also expressed in terms of G_a and G_w as

$$K_{fdm} \approx 3.486848 \times 10^{-8} \frac{p_a^{\ 1.235} w^{\ 0.002} z_d^{\ 1.1}}{T_{a(ºC)}^{\ 0.03627} T_{wi(ºC)}^{\ 0.01161} d^{0.63} v_{d0}^{\ 0.0015}} \frac{G_w}{G_a^{\ 1.45}} \tag{G.16}$$

The deviations between Eq. (G.15) or Eq. (G.16) and corresponding numerical data within the limits of the valid ranges, is shown in Fig. G.1.

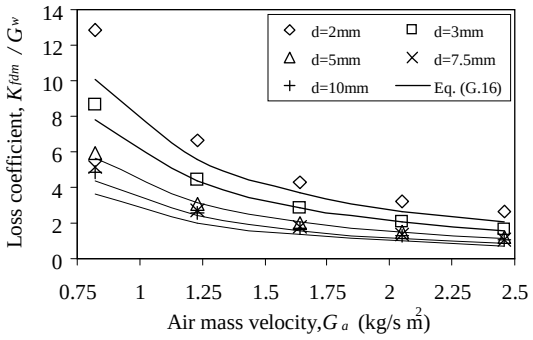

(a_1) Loss coefficient (p_a=101325 N/m^2).

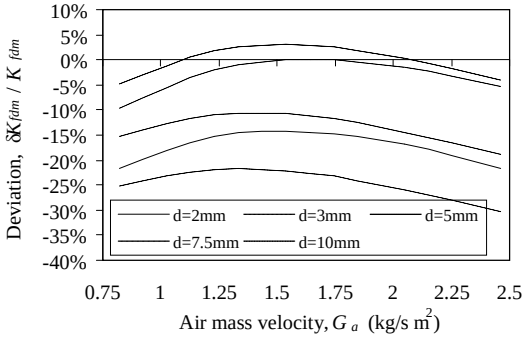

(a_2) Deviation (p_a=101325 N/m^2).

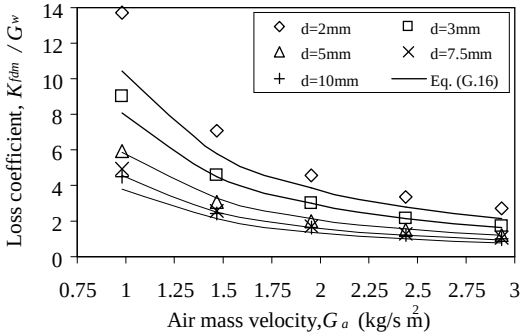

(b_1) Loss coefficient (p_a=85000 N/m^2).

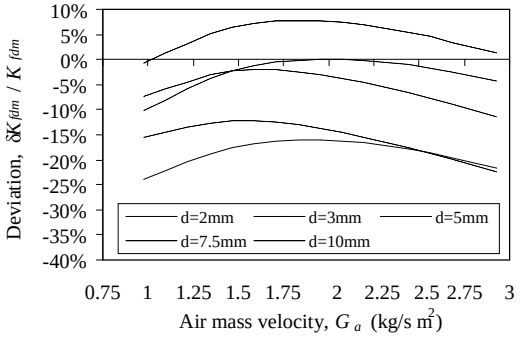

(b_2) Deviation (p_a=85000 N/m^2).

Figure G.1 : Deviation between Eq. (G.15) or (G.16) and corresponding numerical data for different air mass velocities, drop diameters and atmospheric pressures.

G.3 SINGLE DROP ACCELERATING UNDER GRAVITY IN HORIZONTAL AIR FLOW

In exactly the same way and valid for the same conditions as Eq. (G.15), an empirical relation for loss coefficient is obtained for drops falling through air flowing horizontally, given as

$$\frac{K_{fdm}}{G_w}\frac{A_{fr_a}}{A_{fr_w}} \approx 1.350078 \frac{T_{a(^oC)}^{\ 0.03869} w^{\ 0.003} z_d^{\ 0.55}}{p_a^{\ 0.44} T_{wi(^oC)}^{\ 0.00967} d^{0.63} v_{d0}^{\ 0.009} v_a^{\ 0.93}} \qquad \text{(G.17)}$$

and in terms of G_a and G_w as

$$K_{fdm} \approx 4.072540 \frac{p_a^{\ 0.49} w^{\ 0.003} z_d^{\ 0.55}}{T_{a(^oC)}^{\ 0.006285} T_{wi(^oC)}^{\ 0.00967} d^{0.63} v_{d0}^{\ 0.009}} \frac{A_{fr_w}}{A_{fr_a}} \frac{G_w}{G_a^{\ 0.93}} \qquad \text{(G.18)}$$

The deviations between Eq. (G.17) and corresponding numerical data are shown in Fig. G.2, for A_{fra}/ A_{frw}=1, different air mass velocities, drop diameters and atmospheric pressures.

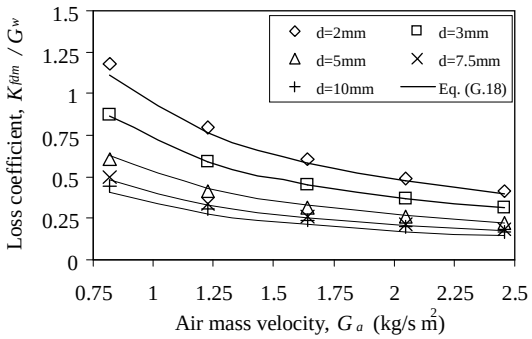

(a_1) Loss coefficient (p_a=101325 N/m^2).

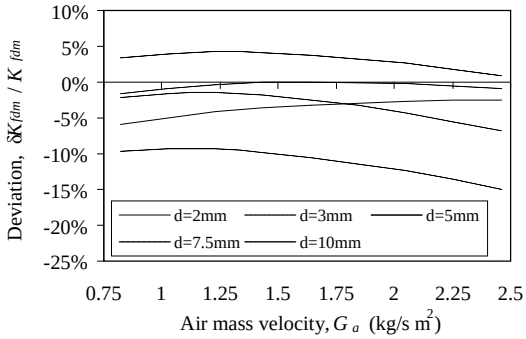

(a_2) Deviation (p_a=101325 N/m^2).

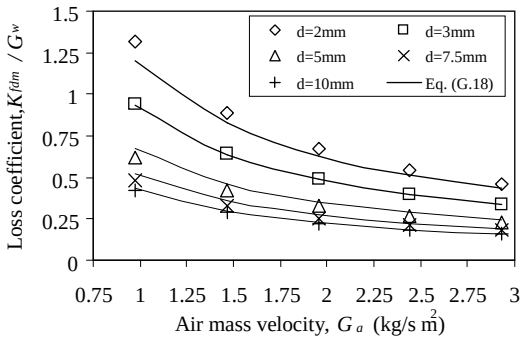

(b_1) Loss coefficient (p_a=85000 N/m^2).

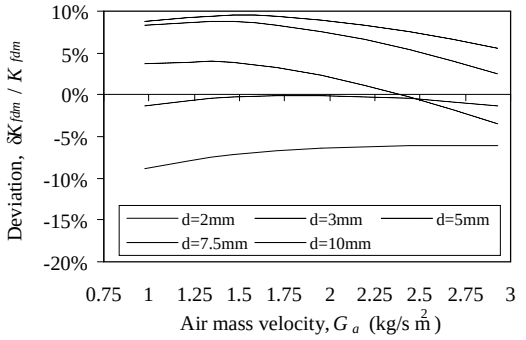

(b_2) Deviation (p_a=85000 N/m^2).

Figure C.2 : Deviation between Eqs (G.17) or (G.18) and corresponding numerical data for different air mass velocities, drop diameters and atmospheric pressures.

G.4 SUMMARY OF RESULTS AND CONCLUSIONS

Analytical equations are derived for the loss coefficient of drops falling at terminal speed in upward flowing air. To clearly show the influence of the fundamental independent variables on the loss coefficient of counter- and cross-flow rain zones, empirical relations are obtained using data from the numerical analysis in Appendix C and the deviations are seen to be significant. The following conclusions can be made:

- ⇨ The loss coefficient of counter- and cross-flow cooling tower rain zones is strongly dependent on the air mass velocity (G_a), water mass velocity (G_w), drop diameter (d), drop falling distance (z_d) or rain zone height (H_{rz}) and the atmospheric pressure (p_a).
- ⇨ The loss coefficient for counter-flow (Eq. G.16) is more sensitive to pressure (p_a), air mass velocity (G_a) and drop falling distance (z_d) than for cross-flow (Eq. G.18).

- ⇨ The cross-flow loss coefficient is also directly proportional to A_{frw}/ A_{fra}.
- ⇨ The correlation for counter-flow loss coefficient deviates significantly from the numerical data, but it is conservative and indicates the sensitivity of the loss coefficient to different variables.

H

CFD ANALYSIS OF COOLING TOWER INLETS

Viscous dissipation of mechanical energy in fluid flow is caused by shear stresses (friction) in the fluid due to velocity gradients, which generally occur in surface boundary layers and core flow turbulence such as in wakes and flow separation or re-circulation regions. The mechanical energy is converted to heat where "mechanical energy" refers to the $p/\rho + \alpha_e v^2/2 + gz$ terms in the equation of the first law of thermodynamics, i.e.,

$$P+Q=m\left[\left(u_2+\frac{p_2}{\rho_2}+\frac{\alpha_{e2}v_2^2}{2}+gz_2\right)-\left(u_1+\frac{p_1}{\rho_1}+\frac{\alpha_{e1}v_1^2}{2}+gz_1\right)\right] \tag{H.1}$$

The subscripts 1 and 2 refer to a control volume for flow between sections 1 and 2 respectively. P and Q represent the mechanical power and the rate of heat inputs into the fluid respectively.

The dimensionless loss coefficient for flow between two cross-sections in a duct system is defined as

$$K=\frac{\left(p_1/\rho_1+\alpha_{e1}v_1^2/2+gz_1\right)-\left(p_2/\rho_2+\alpha_{e2}v_2^2/2+gz_2\right)+P/m}{v^2/2}=\frac{\left(u_2-u_1\right)-Q/m}{v^2/2} \tag{H.2}$$

where v is usually based on conditions at either section 1 or 2. For incompressible flow in horizontal ducts without heat transfer and mechanical energy input or output, Eq. (H.2) becomes

$$\begin{aligned} K&=\frac{\left(p_1/\rho+\alpha_{e1}v_1^2/2\right)-\left(p_2/\rho+\alpha_{e2}v_2^2/2\right)}{v^2/2}\\ &=\frac{\left(p_1+\alpha_{e1}\rho v_1^2/2\right)-\left(p_2+\alpha_{e2}\rho v_2^2/2\right)}{\rho_i v^2/2}=\frac{p_{t1}-p_{t2}}{\rho_i v^2/2}=\frac{p_{t1}-p_{t2}}{\left(m/A\right)^2/(2\rho_i)} \end{aligned} \tag{H.3}$$

where p_t is the total pressure.

From the principle of conservation of mass, the loss coefficient can be referred to any other condition (denoted by subscripts 1 and 2) since the pressure drop is equal at both sets of conditions, which gives

$$\Delta p=K_1\frac{\left(m_1/A_1\right)^2}{2\rho_1}=K_2\frac{\left(m_2/A_2\right)^2}{2\rho_2} \tag{H.4}$$

It follows from equation (H.4) that the loss coefficient K_2 at condition 2 referred to the conditions at 1, is

$$K_2 = K_1 \left(\frac{\rho_2}{\rho_1} \right) \left(\frac{m_1}{m_2} \right)^2 \left(\frac{A_2}{A_1} \right)^2 \qquad \text{(H.5)}$$

Cooling tower inlet losses are the flow losses or viscous dissipation affected directly by the cooling tower inlet design, which according to the cooling tower performance analysis example given in Appendix K, can be more than 20 % of the total flow losses in counterflow cooling towers. Furthermore, flow separation at the lower edge of the shell results in a vena contracta with a distorted inlet velocity distribution that causes a reduction in effective fill or heat exchanger flow area, defined as the core area that satisfies continuity when integrating from the tower axis. Typical flow patterns encountered in cooling towers with square and rounded inlets are shown schematically on the left and right side respectively of Fig. H.1. By decreasing the inlet loss coefficient and increasing the effective flow area (e.g. by installing a rounded inlet), a higher air flow rate and effective heat transfer surface area can be attained which will improve cooling tower performance.

A number of researchers have investigated cooling tower inlets experimentally by conducting scale model tests (Kröger 2004), showing that the inlet loss coefficient and effective diameter are strongly dependent on the fill loss coefficient, fill type, inlet diameter to inlet height ratio and inlet geometry.

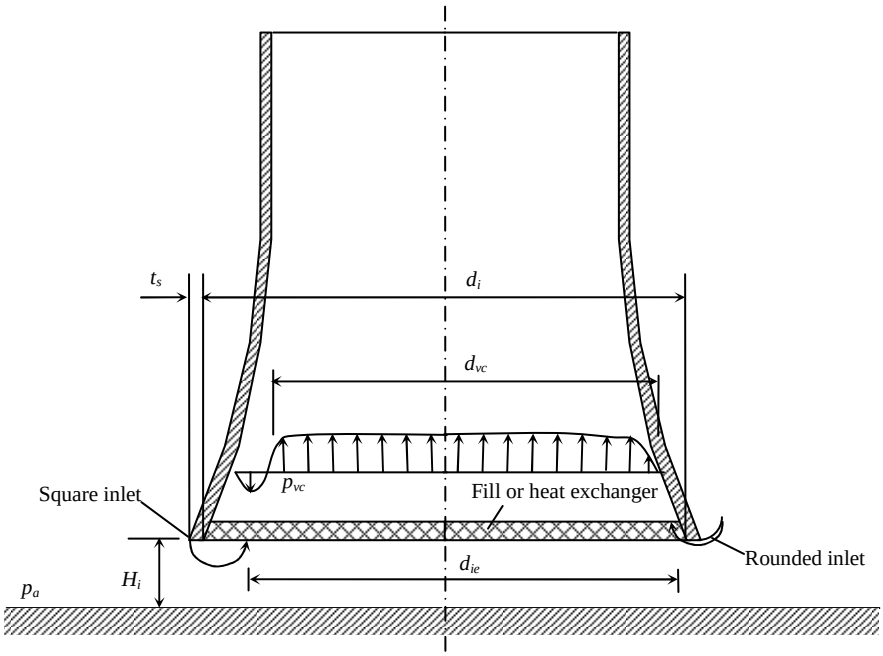

Figure H.1 : Natural draught counterflow cooling tower inlet flow patterns.

The tower support columns also affect the cooling tower inlet flow patterns and losses, especially at the top of the columns near the lower edge of the shell where air speeds are the highest. The columns reduce the cross-sectional flow area resulting in higher air speeds, and the flow separation around these columns

causes form drag and low pressure turbulent wakes downstream of the columns, affecting the airflow through the fill in these regions. It can be seen from Fig. H.2 that these supports can have a V, A, I or X arrangement and the support shape can be round, oval, square or rectangular, where the oval shape is the most streamlined and therefore the most suitable aerodynamic shape.

(a) V-arrangement, round columns and a square shell inlet.

(b) A-arrangement, square columns and a square shell inlet.

(c) I-arrangement, oval columns and a rounded shell inlet.

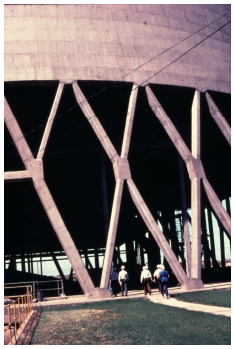

(a) X-arrangement, rectangular columns and a square shell inlet.

Figure H.2 : Photographs of different natural draught wet-cooling tower inlet designs.

In wet-cooling towers, the inlet loss coefficient and effective flow area are also influenced by the drops in the rain zone, due to increased flow resistance, which is investigated in Appendix I.

The main objectives of this appendix are: to develop a validated two-dimensional (axi-symmetric) CFD counterflow cooling tower inlet model with the aid of *FLUENT*®; to investigate the effects of dimensional scaling, shell wall thickness, shell wall inclination angle, fill loss coefficient, fill type, inlet diameter to inlet height ratio and inlet geometry on the inlet flow patterns, loss coefficient and effective diameter, initially neglecting effects of drops in the rain zone; and ultimately to develop simple correlations for the inlet loss coefficient and effective diameter ratio in terms of the above variables.

The cooling tower inlet loss coefficient is determined using the following simplified form of Eq. (H.3) applicable to a horizontal duct and incompressible flow:

$$K_{ct} \approx \frac{p_a - \left(p_{vc} + \alpha_{e,vc} \rho v_{m,vc}^2 / 2 \right)}{\rho v_{m,i}^2 / 2} - K_{fi} \qquad \text{(H.6)}$$

where the kinetic energy correction coefficient for incompressible flow is defined as

$$\alpha_e = \frac{\int_A \left(v^2 / 2 \right) \mathrm{d}m}{m v_m^2 / 2} = \frac{\int_A v^3 \mathrm{d}A}{A v_m^3} \qquad \text{(H.7)}$$

and the mean velocity is determined from

$$v_m = \frac{\int_A v \, dA}{A} = \frac{m}{\rho A} \tag{H.8}$$

The static pressure at the level of the vena contracta, just downstream of the fill or heat exchanger, is not entirely constant along the radius, deviating marginally near the shell wall. Since the product of pressure and volume flow rate has the units of power (J/s), the mean pressure at the vena contracta level is determined from a volume flow rate (V) weighted average, defined as

$$p = \frac{\int_A p \, dV}{V} \tag{H.9}$$

The CFD results are compared to equivalent experimental data from literature and corresponding empirical data obtained using the following relations given in Kröger (2004) for circular counterflow towers, determined experimentally on the same test-rig.

For orthotropic (film type) fill resistance, square-edged cylindrical inlets and the assumption that $\alpha_{e,i} = 1$, Geldenhuys (1987) gives the following equation for the inlet loss coefficient of a cylindrical cooling tower:

$$K_{ct} = 0.05\left(d_i/H_i\right)^{\left[2.24+0.0225\left(d_i/H_i\right)\right]} K_{fi}^{\left[-0.12-0.018\left(d_i/H_i\right)\right]} + 0.4 \tag{H.10}$$

valid for $10 \le d_i/H_i \le 15$ and $10 \le K_{fi} \le 45$.

Terblanche and Kröger (1994) propose a different relation for square-edged cylindrical inlets ($t_s/d_i = 0.0045$) that includes the effect of a distorted velocity profile ($\alpha_{e,i} \ge 1$), given as

$$K_{ct} = \left[100 - 18\left(d_i/H_i\right) + 0.94\left(d_i/H_i\right)^2\right] K_{fi}^{\left[-1.28+0.183\left(d_i/H_i\right)-7.769\times10^{-3}\left(d_i/H_i\right)^2\right]} \tag{H.11}$$

He also proposes the following equation for well-rounded inlets ($r_i/d_i \approx 0.01$):

$$K_{ct} = 1.5\mathrm{e}^{0.2\left(d_i/H_i\right)} K_{fi}^{\left[-0.4645+0.02303\left(d_i/H_i\right)-9.5\times10^{-4}\left(d_i/H_i\right)^2\right]} \tag{H.12}$$

The following relation is obtained for square and rounded inlets up to $r_i/d_i = 0.02$, by modifying Eq. (H.12) based on the experimental data of Terblanche (1994):

$$K_{ct} \approx 0.09422\left[22.265 - 118.168\left(r_i/d_i\right)^{0.635}\right]\mathrm{e}^{0.2\left(d_i/H_i\right)} \times K_{fi}^{\left[-0.4645+0.02303\left(d_i/H_i\right)-9.5\times10^{-4}\left(d_i/H_i\right)^2\right]} \tag{H.13}$$

where all three of these equations are valid for $10 \le d_i/H_i \le 15$ and $5 \le K_{fi} \le 25$.

For isotropic (trickle or splash type) fill resistance, De Villiers (1998) developed a correlation applicable to both square and rounded inlets, written as

$$K_{ct} = 0.011266\,e^{0.093(d_i/H_i)}K_{fi}^2 - 0.3105\,e^{0.1085(d_i/H_i)}K_{fi} + 4.5614\,e^{0.131(d_i/H_i)} - 1.7522$$
$$+\sinh^{-1}\left[\left\{\frac{\left(10970.19\,e^{-0.2442K_{fi}} + 1391.27\right)}{\left(d_i/H_i - 15.7258\right)} + 1205.54\,e^{-0.23K_{fi}} + 109.314\right\}\right. \qquad \text{(H.14)}$$
$$\left.\times\left\{2r_i/d_i - 0.01942/\left(d_i/H_i - 27.929\right) - 0.016866\right\}\right]$$

valid for $7.5 \le d_i/H_i \le 15$, $5 \le K_{fi} \le 25$ and $0 \le r_i/d_i \le 0.02$

The CFD results for effective fill diameter are compared with the following equations determined experimentally by Oosthuizen (1995), which for orthotropic fill resistance and square inlets is given by

$$\frac{d_{ie}}{d_i+2t_s} = 1.2549 - 0.21069\ln\left(\frac{d_i+2t_s}{H_i}\right)$$
$$+\left[0.050673\ln\left(\frac{d_i+2t_s}{H_i}\right) - 0.052085\right]\ln\left(K_{fi}\right) \qquad \text{(H.15)}$$

valid for $5.35 \le (d_i + 2t_s) \le 16$, $3.6 \le K_{fi} \le 49$ and $d_{ie}/d_i \le 1$.

For rounded inlets the following correlation is given:

$$\frac{d_{ie}}{d_i} = 1.27 - 0.16722\ln\left(\frac{d_i}{H_i}\right) + \left[0.043653\ln\left(\frac{d_i}{H_i}\right) - 0.062658\right]\ln\left(K_{fi}\right) \qquad \text{(H.16)}$$

valid for $5.35 \le (d_i/H_i) \le 16$, $3.6 \le K_{fi} \le 49$, $r_i/d_i = 0.01$ and $d_{ie}/d_i \le 1$.

In the above relations, the effective diameter is normalized with respect to the diameter of the flow separation point, which for a square inlet is $d_{sep} = d_i + 2t_s$ and for a rounded inlet is $d_{sep} = d_i$.

In the following sections, a two-dimensional (axi-symmetric) CFD model of the experimental apparatus used to determine the above correlations is developed using the CFD code *FLUENT*®. The results are compared with axial velocity profile data, tower inlet loss coefficients and effective diameters determined experimentally by Terblanche (1994) as well as applicable empirical data. The validated model is then used to investigate the effect of different variables on the inlet flow patterns, loss coefficient and effective diameter of full-scale towers, the results of which are used to develop simple correlations for the inlet loss coefficient and effective diameter ratio in terms of these variables.

The outcomes of the validation and investigation are ultimately implemented in an axi-symmetric CFD model for simulating the performance of a full-scale natural draught wet-cooling tower, presented in Appendix N.

H.1 CFD MODEL OF A COOLING TOWER INLET

The experimental circular counterflow cooling tower sector model used to develop the above empirical relations (Eqs H.10 to H.15), shown in Fig. (H.4), has a sector angle of 5º, an inside radius of $d_i/2$ = 2.621 m and a tower shell wall thickness of t_s = 0.019 m. The apparatus consists of a horizontal table with a transparent perspex cover on top that hinges at the axis. The ground is represented by an adjustable wedge-shaped plank that allows the H_i/d_i ratio of the tower to be variable. The tower shell wall is represented by another plank inserted between the table and the perspex cover.

Plate-finned radiator cores with perforated plates sandwiched between them, to increase the flow resistance, are used to simulate an orthotropic or film type cooling tower fill or finned tube heat exchanger. The sector model air inlets are well-rounded to ensure smooth air inflow. The sector is connected to a wind tunnel which draws air through it by means of a variable speed centrifugal fan and the air flow rate is determined by measuring the pressure difference over flow nozzles in the wind tunnel. The static pressure downstream of the radiator cores is measured by a static pressure tap in the shell wall connected to a Betz water manometer measuring relative to atmosphere. The velocity profile is measured using a Pitot-static tube and an anemometer.

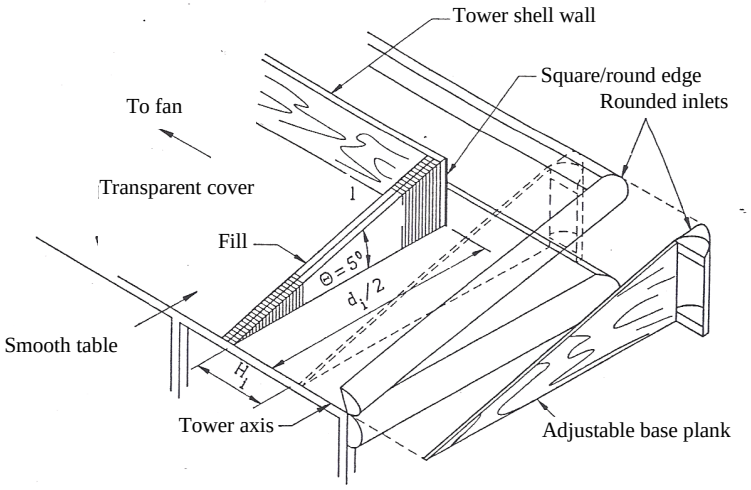

Figure H.3 : Cooling tower sector model for measuring inlet losses and effective flow area.

The computational flow domain of the apparatus is meshed with a uniform structured (quadrilateral) grid and the main dimensions and boundary definitions are depicted in Fig. H.4. The transport equations for mass, momentum, energy, species mixing and turbulence are solved by employing the double precision, axi-symmetric, steady state, segregated solver and the SIMPLE algorithm for the pressure-velocity coupling. To maximize accuracy, second order discretization is employed for all the governing equations. The wall boundaries are defined as slip walls since the boundary layers are negligibly thin and do not influence flow separation at the inlets, as confirmed by De Villiers (1998), Störm (2010), and later on in Appendix N.

Provision is made for future discrete phase (DP) modelling according to the Lagrangian approach, to simulate cooling tower rain zone performance. The grid is therefore uniform and materials properties are defined to simulate species transport i.e. the air properties are based on a mixture of dry air and water vapour and the energy equation is solved.

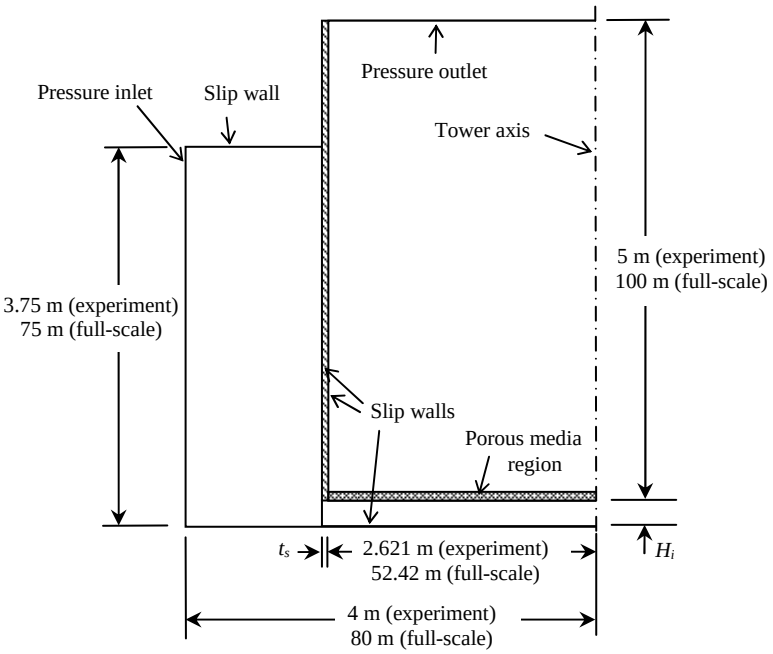

Figure H.4 : Main dimensions and boundary definitions of the CFD flow domain of a cylindrical cooling tower.

The air-side flow resistances due to the cooling tower inlet (and rain zone later) are resolved by solving the flow equations in *FLUENT*®, whereas the flow resistance of the fill is simulated by a porous medium model in the region where the fill is located, which is merely the addition of a momentum source term to the standard flow equations in this region. For inertial (fill) flow losses, the momentum source term is written as

$$S_i = \nabla p = -\sum_{\mathrm{j}=1}^{3} C_{\mathrm{i,j}} \left(\frac{1}{2} \rho |v| v_j \right) \qquad \text{(H.17)}$$

where S_i is the source term for the i^{th} (x, y, or z) momentum equation, C is a prescribed matrix for the loss coefficient, $|v|$ is the velocity magnitude and v_j are the velocity components in the x, y and z directions.

For an isotropic fill resistance where the loss coefficient is the same in all directions, such as assumed for trickle and splash type fills, the source term is only variable to a change in velocity and simplifies to

$$S_i = -\frac{K_{fi}}{L_{fi}} \frac{1}{2} \rho |v| v_i \qquad \text{(H.18)}$$

where K_{fi} is the fill loss coefficient.

For an orthotropic fill resistance, such as film-type fills or the finned-tube radiator cores tested by Geldenhuys (1987) and Terblanche (1994), the oblique flow entering the fill is forced into the vertical direction by the fill sheets and radiator fins respectively. This change of direction can be modelled by means of an anisotropic porous medium model by making at least one of the horizontal loss coefficients in Eq. (H.17) very large to simulate the impermeability of the fill in that direction. This artificial loss coefficient however results in all the horizontal momentum in its direction to be dissipated or removed from the flow, which is not what happens in reality. As illustrated in Fig. H.5, the flow that enters the orthotropic fill undergoes flow separation at the leading edge of the fill sheets/ fins as the flow changes direction, forming a vena contracta with partial static pressure recovery as the flow expands downstream.

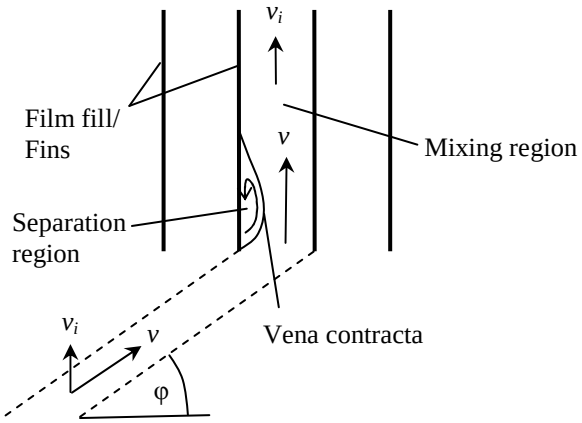

Figure H.5 : Oblique flow entering an orthotropic resistance (Kröger 2004).

The losses determined in porous media are significantly higher than the actual losses for orthotropic fills, and must therefore be adjusted by adding the horizontal momentum removed from the flow as it enters the porous medium region to the vertical momentum and adding a momentum sink for the losses due to oblique inlet flow, determined from the following loss coefficient relation proposed by Moore and Torrence (1977):

$$K_{i\theta} = \left(\frac{1}{\sin \varphi} - 1 \right)^2 \tag{H.19}$$

The following momentum source term is therefore applied to the bottom/ inlet row of cells in the porous medium, referred to as the correction cells:

$$S_z = -\left[\frac{K_{fi}}{L_{fi}} + \frac{2}{L_{cc}} \left(1 - \frac{1}{\sin \varphi} \right) \right] \frac{1}{2} \rho |v| v_i \tag{H.20}$$

where L_{cc} is the length of the correction cells.

Further details on CFD and *FLUENT*® can be obtained from *ANSYS-FLUENT* (2006).

H.2 VALIDATION OF THE CFD RESULTS

The above CFD model is validated by conducting a grid independence study, a turbulence model evaluation and comparison with experimental data from literature. The axial velocity distribution downstream of the fill, tower inlet loss coefficient and effective diameter are determined for different mesh sizes and compared with corresponding experimental data of Terblanche (1994) based on a square inlet, K_{he} = 12.2 and d_i/H_i = 10 to find the optimal mesh size which provides a solution that remains essentially unchanged with further grid refinement. Similarly the results obtained with different turbulence models are compared to the same experimental data, to verify their accuracy and to select the best turbulence model. The grid independence velocity profile results for the experimental apparatus and a scaled-up full-size cooling tower are presented in Figs H.6(a) and H.6(b) respectively and the corresponding loss coefficient and effective diameter data are presented in Table H.1. These results show that the differences between the apparatus and full-scale cylindrical tower data are negligible. The measured loss coefficient (Terblanche 1993) is found to be almost 6 % lower than the CFD data whereas the measured effective diameter is about 2 % larger. The applicable empirical loss coefficient (Eq. H.11) is 1.2 % higher and the empirical effective diameter (Eq. H.15) is 3.2 % larger.

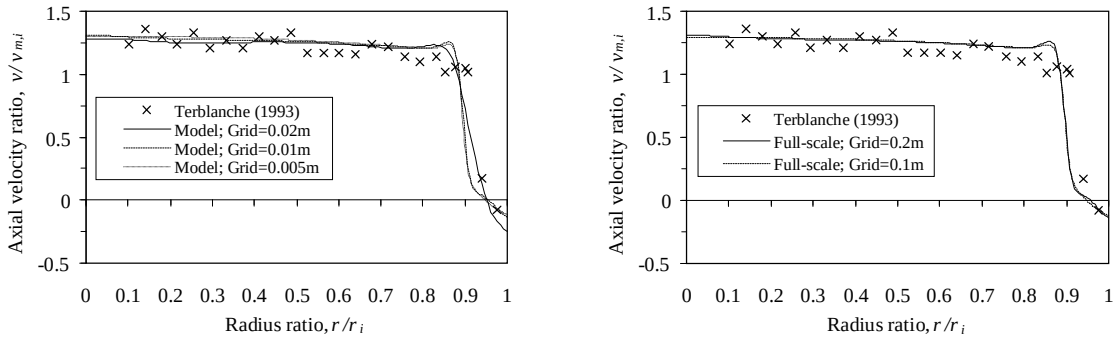

(a) Experimental apparatus. (b) Full-scale cooling tower.

Figure H.6: Effect of physical size and grid size on the velocity profile downstream of the fill for K_{fi} = 12.2 and d_i/H_i = 10.

The cooling tower velocity profiles obtained for different turbulence models are presented in Fig. H.7 and the corresponding loss coefficient and effective diameter data is summarised in Table H.2. It can be seen that the axial velocity profile obtained with the k-ε Realizable turbulence model has a similar trend to the experimental data of Terblanche (1994) in the vicinity of the tower shell, whereas the other models show deviating trends in this region. The Spalart Allmeras and k-ω SST model however seem to predict the core region velocity profile slightly better than the k-ε Realizable model whereas the Standard k-ε model deviates significantly over the entire profile. The loss coefficients and

effective diameters obtained with the different turbulence models do not deviate much from the experimental data. Shih (1995) shows that the k-ε Realizable model, which contains a new improved formulation of the turbulent viscosity (μ_t) and an improved transport equation for the dissipation rate (ε), performs better than the k-ε Standard model in all of the classical test cases used to benchmark these models. Since the k-ε Realizable model is observed to give the best overall results i.e. velocity profile, inlet loss coefficient and effective diameter, it is considered to be the best model for simulation of cooling tower inlets.

Table H.1 : The effect of physical size and grid size on the loss coefficient and effective diameter.

Description	Units	Terblanche (1993)	Experimental apparatus (CFD)			Full-scale tower (CFD)	
Grid size	m	N.A.	0.02	0.01	0.005	0.2	0.1
d_i/H_i	-	10	10	10	10	10	10
$v_{m,i}$	m/s	5.994	6.029	5.820	5.808	1.601	1.597
$\alpha_{e,i}$	-	1.409	1.476	1.522	1.539	1.523	1.527
$v_{m,vc}$	m/s	6.725	7.156	7.031	7.058	1.934	1.940
$\alpha_{e,vc}$	-	1.149	1.043	1.042	1.041	1.043	1.034
(d_{ie}/d_i)	-	0.924	0.916	0.908	0.907	0.908	0.906
$\delta(d_{ie}/d_i)$	%	0%	-0.9%	-1.7%	-1.8%	-1.7%	-1.9%
$(d_{ie}/d_i)_{Eq.(H.15)}$				0.937			
$(p_{atm} - p_i)$	N/m^2	Not given	432.5	443.5	444.2	33.44	33.43
K_{fi}	-	12.2	12.2	12.2	12.2	12.2	12.2
K_{ct}	-	7.387	5.830	7.735	7.841	7.670	7.753
δK_{ct}	%	0%	-21.1%	4.7%	6.1%	3.8%	5.0%
K_{ct} (α_{ei}=1)	-	Not given	6.301	8.256	8.380	8.192	8.280
$K_{ct\text{-}Eq.\ (H.10)}$	-			7.288			
$K_{ct\text{-}Eq.\ (H.11)}$	-			7.937			

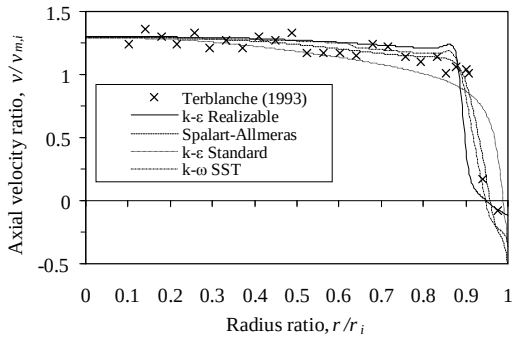

Figure H.7: Effect of the turbulence model on the velocity profile downstream of the fill for K_{fi} = 12.2 and d_i/H_i = 10 for the experimental apparatus.

Table H.2 : The effect of turbulence model on the loss coefficient and effective diameter.

Description	Units	Terblanche (1993)	Experimental apparatus (CFD)			
Turbulence model	-	N.A.	k-ε Realizable	k-ε Standard	Spalart-Allmeras	k-ω SST
Grid size	m	N.A.	0.005	0.005	0.005	0.005
d_i/H_i	-	10	10	10	10	10
$v_{m,i}$	m/s	5.994	5.808	5.894	5.803	5.801
$\alpha_{e,i}$	-	1.409	1.539	1.195	1.410	1.483
$v_{m,vc}$	m/s	6.725	7.058	6.164	6.794	6.988
$\alpha_{e,vc}$	-	1.149	1.041	1.092	1.026	1.020
(d_{ie}/d_i)	-	0.924	0.907	0.977	0.923	0.910
$\delta(d_{ie}/d_i)$	%	0%	-1.8%	5.4%	-0.1%	-1.5%
$(d_{ie}/d_i)_{Eq.(H.15)}$				0.937		
$(p_{atm} - p_i)$	N/m^2	Not given	444.2	443.5	441.9	443.6
K_{fi}	-	12.2	12.2	12.2	12.2	12.2
K_{ct}	-	7.387	7.841	7.523	7.897	7.920
δK_{ct}	%	0%	6.1%	1.8%	6.9%	7.2%
K_{ct} (α_{ei}=1)	-	Not given	8.380	7.718	8.307	8.404
$K_{ct\text{-}Eq.\ (H.10)}$	-			7.288		
$K_{ct\text{-}Eq.\ (H.11)}$	-			7.937		

Figure H.8 shows experimental data (Terblanche 1993) and corresponding CFD curves for the axial velocity ratio profile downstream of the radiator core, determined for different fill loss coefficients (K_{fi}) and inlet diameter to inlet height ratios (d_i/H_i), which have similar trends, but the CFD vena contracta diameters are observed to be slightly smaller resulting in higher core velocities. The inlet loss coefficient and effective diameter data for d_i/H_i = 10 and 15, are given in Tables H.3 and H.4 respectively. The deviations between the experimental and CFD data can be attributed to a combination of possible measurement uncertainties (air flow rate, air velocity, pressure drop and fill loss coefficient), geometric differences (sector vs axi-symmetric) and modelling uncertainties (fill losses and flow turbulence), but are deemed relatively small.

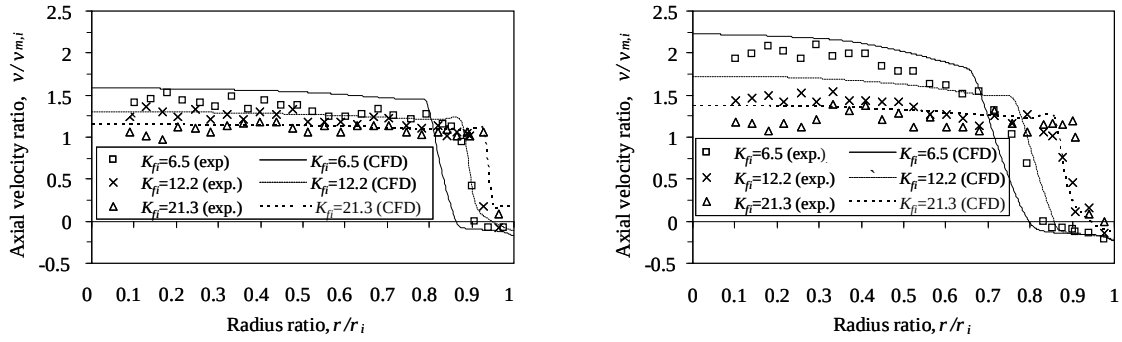

(a) d_i/H_i = 10. (b) d_i/H_i = 15.

Figure H.8: Comparison between experimental and CFD data showing the effect of K_{fi} and d_i/H_i on the velocity profile downstream of the fill for the experimental apparatus.

Table H.3 : Experimental and CFD data for square inlets and d_i/H_i = 10 showing the effect of fill loss coefficient (K_{fi}) on the inlet loss coefficient and effective diameter.

Description	Units	Exp.	CFD	Exp.	CFD	Exp.	CFD
Grid size	m	N.A.	0.005	N.A.	0.005	N.A.	0.005
d_i/H_i	-	10	10	10	10	10	10
$v_{m,i}$	m/s	6.258	6.036	5.994	5.808	5.757	5.545
$\alpha_{e,i}$	-	1.688	2.264	1.409	1.539	1.185	1.205
$v_{m,vc}$	m/s	8.248	8.996	6.725	7.058	5.651	5.545
$\alpha_{e,vc}$	-	1.039	1.015	1.149	1.041	1.185	1.205
(d_{ie}/d_i)	-	0.888	0.819	0.924	0.907	0.975	1.000
$\delta(d_{ie}/d_i)$	%	0%	-7.8%	0%	-1.8%	0%	2.5%
$(d_{ie}/d_i)_{Eq.(H.15)}$		0.896		0.937		0.974	
$(p_{atm} - p_i)$	N/m^2	Not given	-411.3	Not given	444.2	Not given	-530.8
K_{fi}	-	6.5	6.5	12.2	12.2	21.3	21.3
K_{ct}	-	8.389	9.740	7.387	7.841	6.377	5.786
δK_{ct}	%	0%	16.1%	0%	6.1%	0%	-9.2%
K_{ct} (α_{ei}=1)	-	Not given	11.005	Not given	8.380	Not given	5.991
$K_{ct\text{-}Eq.\ (H.10)}$	-	8.719		7.288		6.227	
$K_{ct\text{-}Eq.\ (H.11)}$	-	9.155		7.937		6.994	

Table H.4 : Experimental and CFD data for square inlets and d_i/H_i = 15 showing the effect of fill loss coefficient (K_{fi}) on the inlet loss coefficient and effective diameter.

Description	Units	Exp.	CFD	Exp.	CFD	Exp.	CFD
Grid size	m	N.A.	0.005	N.A.	0.005	N.A.	0.005
d_i/H_i	-	15	15	15	15	15	15
$v_{m,i}$	m/s	5.660	5.467	5.585	5.829	5.528	5.355
$\alpha_{e,i}$	-	3.047	4.006	1.661	2.524	1.408	1.635
$v_{m,vc}$	m/s	9.536	10.635	7.257	9.128	5.485	6.670
$\alpha_{e,vc}$	-	1.215	1.053	1.181	1.024	1.408	1.053
(d_{ie}/d_i)	-	0.790	0.716	0.908	0.798	0.975	0.895
$\delta(d_{ie}/d_i)$	%	0%	-9.4%	0%	-12.1%	0%	-8.2%
$(d_{ie}/d_i)_{Eq.(H.15)}$		0.852		0.905		0.952	
$(p_{atm} - p_i)$	N/m^2	Not given	689.3	Not given	792.0	Not given	-712.5
K_{fi}	-	6.8	6.8	12.4	12.4	21.4	21.4
K_{ct}	-	22.659	27.031	20.496	23.280	16.251	17.687
δK_{ct}	%	0%	19.2%	0%	13.6%	0%	8.8%
K_{ct} (α_{ei}=1)	-	Not given	30.036	Not given	24.803	Not given	18.322
$K_{ct\text{-}Eq.\ (H.10)}$	-	25.893		20.533		16.674	
$K_{ct\text{-}Eq.\ (H.11)}$	-	24.152		20.351		17.438	

Kröger (2004) reveals that the loss coefficient and effective diameter can be improved significantly by attaching a rounding to the lower edge of the cylindrical shell. Figure H.9 shows experimental (Terblanche 1993) and CFD axial velocity profile data for square and rounded inlets and Table H.5 gives the corresponding inlet loss coefficient and effective diameter data. It can be seen that the inlet loss coefficient of the rounded inlet is almost 55% of that of the equivalent square inlet

and the effective diameter is 0.912 compared with 0.79 for square inlets, which are significant improvements.

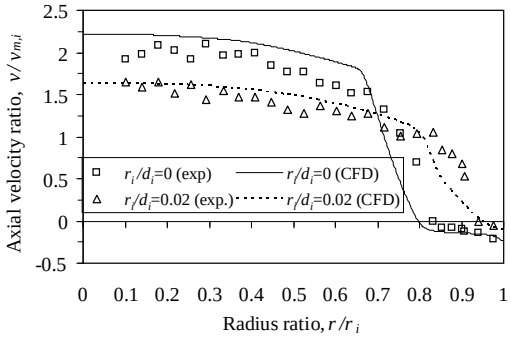

Figure H.9 : Experimental (Terblanche 1993) and CFD axial velocity data for d_i/H_i = 15 and K_{fi} = 6.6.

Table H.5 : Experimental (Terblanche 1993) and CFD inlet loss coefficient and effective diameter data for d_i/H_i = 15 and K_{fi} = 6.6 and a rounded inlet (r_i/d_i=0.02).

Description	Units	Exp.	CFD
r_i/d_i	-	0.02	0.02
Grid size	m	N.A.	0.005
d_i/H_i	-	15	15
$v_{m,i}$	m/s	6.001	5.436
$\alpha_{e,i}$	-	1.641	1.906
$v_{m,vc}$	m/s	7.563	6.577
$\alpha_{e,vc}$	-	1.161	1.302
(d_{ie}/d_i)	-	0.912	0.908
$\delta(d_{ie}/d_i)$	%	0%	-0.4%
$(d_{ie}/d_i)_{Eq.(H.16)}$	-	0.922	
$(p_{atm} - p_i)$	N/m^2	Not given	371.8
K_{fi}	-	6.6	6.6
K_{ct}	-	12.674	12.876
δK_{ct}	%	0%	1.6%
K_{ct} (α_{ei}=1)	-	Not given	13.782
$K_{ct\text{-}Eq.\ (H.13)}$	-	12.533	

The differences in the CFD axial downstream velocity profiles, inlet loss coefficients and effective diameters obtained for orthotropic and isotropic fill resistance are shown in Figure H.10 and Table H.6 for square and rounded (r_i/d_i = 0.02) inlets, K_{fi} = 6.8 or 6.6 and d_i/H_i = 15 and it can be seen that the orthotropic fill resistance reduces both the inlet loss coefficient and effective diameter. Comparing the CFD data for isotropic fill with Eq. (H.14), based on $\alpha_{e,vc}$ = 1, reveals that *FLUENT*® over-predicts the loss coefficient of a square-edged inlet by approximately 4 % whereas it underpredicts a well-rounded inlet by almost 25%.

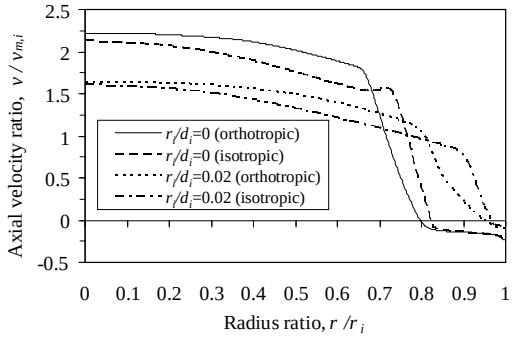

Figure H.10: Comparison between CFD axial velocity profile data for orthotropic and isotropic fill resistance; inlets with and without an inlet rounding of r_i/d_i = 0.02; K_{fi} = 6.8/ 6.6; and d_i/H_i = 15.

Table H.6 : CFD inlet loss coefficient and effective diameter data for orthotropic and isotropic fill resistance; inlets with and without an inlet rounding of r_i/d_i = 0.02; K_{fi} = 6.8 and 6.6; and d_i/H_i = 15.

Description	Units	CFD	CFD	CFD	CFD
r_i/d_i	-	0	0	0.02	0.02
Fill resistance	-	Orthotropic	Isotropic	Orthotropic	Isotropic
Grid size	m	0.005	0.005	0.005	0.005
d_i/H_i	-	15	15	15	15
$v_{m,i}$	m/s	5.467	5.433	5.437	5.422
$\alpha_{e,i}$	-	4.006	3.155	1.906	1.510
$v_{m,vc}$	m/s	10.635	9.390	6.577	6.368
$\alpha_{e,vc}$	-	1.053	1.048	1.302	1.121
(d_{ie}/d_i)	-	0.716	0.760	0.908	0.945
$\delta(d_{ie}/d_i)$	%	0%	6.1%	0%	4.1%
$(d_{ie}/d_i)_{Eq.(H.15)}$	-	0.899	N.A.	N.A.	N.A.
$(d_{ie}/d_i)_{Eq.(H.16)}$	-	N.A.	N.A.	0.922	N.A.
$(p_{atm} - p_i)$	N/m^2	689.3	N.A.	371.8	377.0
K_{fi}	-	6.8	6.8	6.6	6.6
K_{ct}	-	27.031	26.473	12.111	12.895
δK_{ct}	%	0%	6.6%	0%	4.3%
K_{ct} (α_{ei}=1)	-	30.148	28.328	13.017	13.405
$(K_{ct})_{Eq.(H.11)}$	-	24.153	N.A.	N.A.	N.A.
$(K_{ct})_{Eq.(H.13)}$	-	22.263	N.A.	12.533	N.A.
$(K_{ct})_{Eq.(H.14)}$	-	N.A.	27.092	N.A	16.917

Geldenhuys and Kröger (1986) visually observed the flow patterns at the inlet of the experimental sector model for d_i/H_i = 7.5 and different heat exchanger loss coefficients as shown in Fig. H.11.

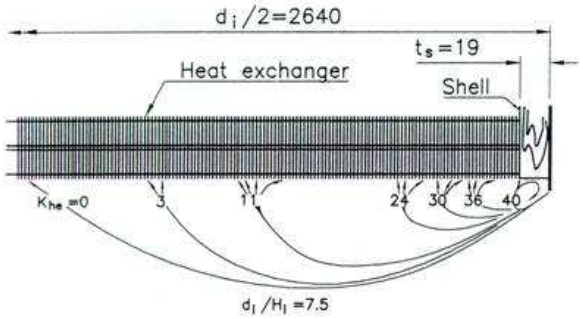

Figure H.11: Visually observed flow patterns at the tower inlet for orthotropic fill resistance.

CFD tower inlet flow patterns for the experimental sector model for d_i/H_i = 10 and different heat exchanger loss coefficients are depicted in Fig. H.12, showing similar trends to Fig. H.11.

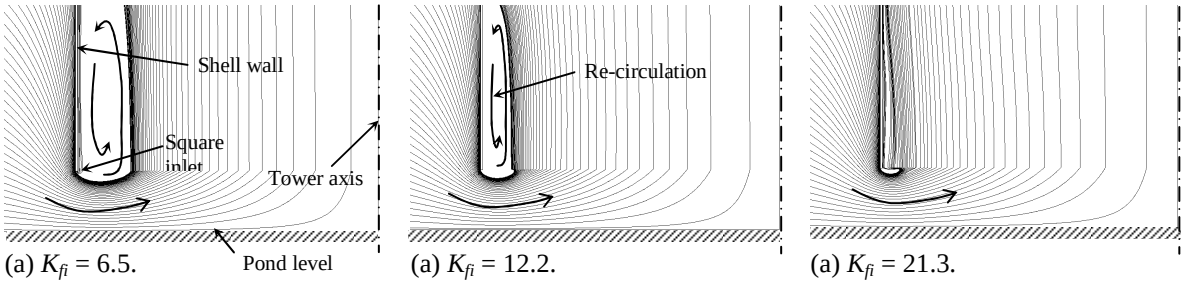

(a) K_{fi} = 6.5. (a) K_{fi} = 12.2. (a) K_{fi} = 21.3.

Figure H.12: CFD pathline flow patterns at the tower inlet (d_i/H_i = 10) for orthotropic fill resistance.

H.3 INFLUENCE OF VARIABLES ON THE INLET FLOW CHARACTERISTICS

In this section, the validated CFD model is used to investigate the effects of different variables on the inlet loss coefficient (K_{ct}) and the effective diameter (d_{ie}) of conical cooling towers. Four reference cases (square and rounded (r_i/d_i = 0.02) inlets both with orthotropic and isotropic fill resistance) are investigated, where the fill material loss coefficient (K_{fi}), ratio of tower inlet diameter to inlet height (d_i/H_i) and radius of the inlet rounding (r_i/d_i) are varied for all the cases and shell wall thickness (t_s) and shell wall inclination angle (θ) are varied for the square inlet cases only. The following common reference conditions, assumed typical for full-scale wet-cooling towers, are used: $t_{s(ref)}$ = 1 m; $\theta_{(ref)}$ = 12 °; $K_{fi(ref)}$ = 12.2 and $(d_i/H_i)_{(ref)}$ = 10.

Table H.7 shows the CFD data determined for the reference cases as well as the relevant empirical data (Eqs H.10 to H.15), for comparison.

Table H.7 : Reference case CFD inlet loss coefficient and effective diameter data.

Description	Units	CFD	CFD	CFD	CFD
r_i/d_i	-	0	0	0.02	0.02
Fill resistance	-	Orthotropic	Isotropic	Orthotropic	Isotropic
Grid size	m	0.1	0.1	0.1	0.1
d_i/H_i	-	10	10	10	10
$v_{m,i}$	m/s	1.539	1.516	1.511	1.622
$\alpha_{e,i}$	-	1.508	1.385	1.054	1.043
$v_{m,vc}$	m/s	1.793	1.730	1.511	1.622
$\alpha_{e,vc}$	-	1.112	1.063	1.054	1.042
(d_{ie}/d_i)	-	0.923	0.932	0.997	0.997
$(d_{ie}/d_i)_{Eq.(H.15)}$	-	0.948	N.A.	N.A.	N.A.
$(d_{ie}/d_i)_{Eq.(H.16)}$	-	N.A.	N.A.	0.980	N.A.
$(p_{atm} - p_i)$	N/m^2	29.837	29.956	28.321	28.627
K_{fi}	-	12.2	12.2	12.2	12.2
K_{ct}	-	7.686	8.569	2.075	5.25
K_{ct} (α_{ei}=1)	-	8.195	8.957	2.129	5.296
$(K_{ct})_{Eq.(H.10)}$	-	7.287	N.A.	N.A.	N.A.
$(K_{ct})_{Eq.(H.11)}$	-	7.937	N.A.	N.A.	N.A.
$(K_{ct})_{Eq.(H.13)}$	-	6.803	N.A.	3.792	N.A.
$(K_{ct})_{Eq.(H.14)}$	-	N.A.	9.838	N.A.	6.140

The CFD data and regression curves for the square inlet and orthotropic fill resistance are presented in Fig. H.13, revealing that the fill loss coefficient and inlet diameter to height ratio have the largest effect.

The following empirical relations are proposed for the loss coefficient [Fig. H.13(a_1)] and effective diameter [Fig. H.13(a_2)] of square inlets and orthotropic fill resistance:

$$K_{ct} = 0.051514\, t_s^{-0.136} \theta^{0.058} K_{fi}^{-0.45} \left(\frac{d_i}{H_i} \right)^{2.6} \tag{H.21}$$

$$\frac{d_{ie}}{d_i + 2t_s} = 1.486175\, t_s^{0.002} \theta^{-0.006} K_{fi}^{0.13} \left(\frac{d_i}{H_i} \right)^{-0.35} \tag{H.22}$$

valid for $0.75 \le t_s \le 1.25$ m, $8 \le \theta \le 16$ º, $6.5 \le K_{fi} \le 30$, $10 \le d_i/H_i \le 15$ and in addition for Eq. (H.22), $d_{ie} \le (d_i - 2L_{fi}\tan\theta)$.

From Fig H.13 it can be seen that a change in diameter to inlet height ratio from d_i/H_i = 10 to 15 results in an increase in the inlet loss coefficient of about 200% and a reduction in the effective diameter of 13%. A change in fill loss coefficient from K_{fi} = 12.2 to 30 results in a decrease in the inlet loss coefficient of about 40% and an increase in the effective diameter ratio from $d_{ie}/(d_i + 2t_s)$ = 0.906 to maximum. In comparison, the effects of shell wall thickness and shell inclination angle are negligibly small. In Fig. H.13(b_1), the above loss coefficient correlation (Eq. H.21) is compared to Eq. (H.11) for a cylindrical cooling tower (θ = 0º)

showing that the deviation is relatively small. Similarly, the above effective diameter correlation (Eq. H.22) is compared to Eq. (H.15) in Fig. H.13(b_2), showing small deviations for d_i/H_i = 10 but significant deviations for d_i/H_i = 15.

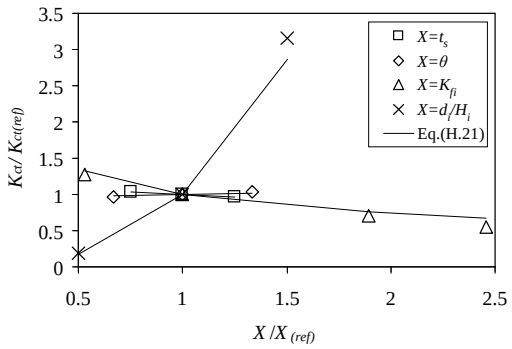

(a_1) CFD inlet loss coefficient data and regression curves.

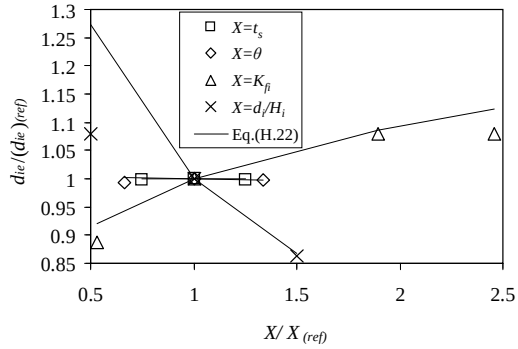

(a_2) CFD effective diameter data and regression curves.

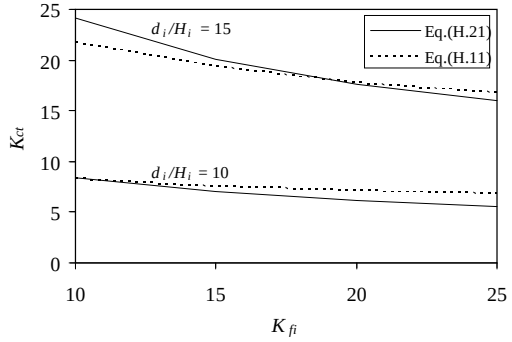

(b_1) Comparison between empirical inlet loss coefficient curves.

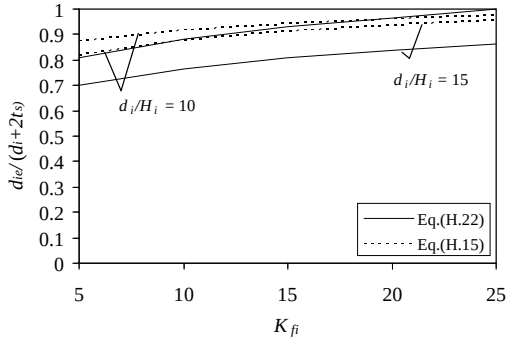

(b_2) Comparison between empirical effective diameter curves.

Figure H.13 : Effects of different variables on the inlet loss coefficient and effective diameter for square inlets and orthotropic fill resistance.

The CFD data and regression curves for the square inlet and isotropic fill resistance are presented in Fig. H.14.

The following empirical relations are proposed for the loss coefficient [Fig. H.14(a_1)] and effective diameter [Fig. H.14(a_2)] of square inlets and isotropic fill resistance:

$$K_{ct} = 0.057391\, t_s^{-0.136} \theta^{0.058} K_{fi}^{-0.45} \left(\frac{d_i}{H_i} \right)^{2.6} \qquad \text{(H.23)}$$

$$\frac{d_{ie}}{d_i + 2t_s} = 1.41247\, t_s^{0.0164} \theta^{-0.006} K_{fi}^{0.09} \left(\frac{d_i}{H_i} \right)^{-0.28} \qquad \text{(H.24)}$$

valid for $0.75 \le t_s \le 1.25$ m, $8 \le \theta \le 16$ º, $6.5 \le K_{fi} \le 30$, $10 \le d_i/H_i \le 15$ and in addition for Eq. (H.24), $d_{ie} \le (d_i - 2L_{fi}\tan\theta)$.

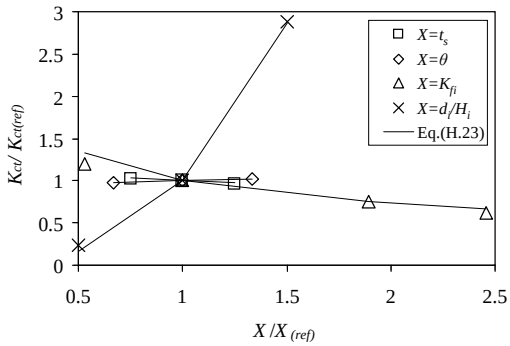

(a_1) CFD inlet loss coefficient data and regression curves.

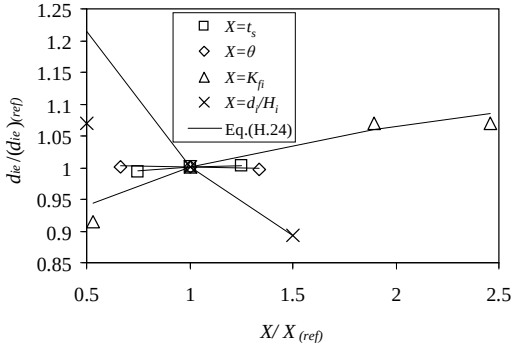

(a_2) CFD effective diameter data and regression curves.

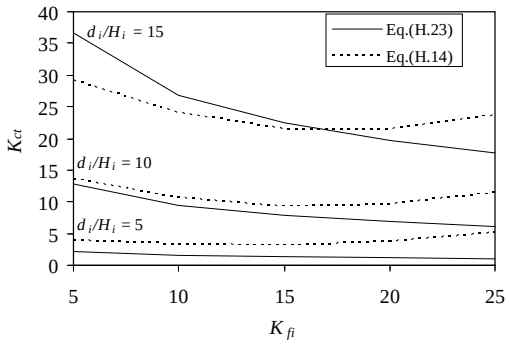

(b_1) Comparison between empirical inlet loss coefficient curves.

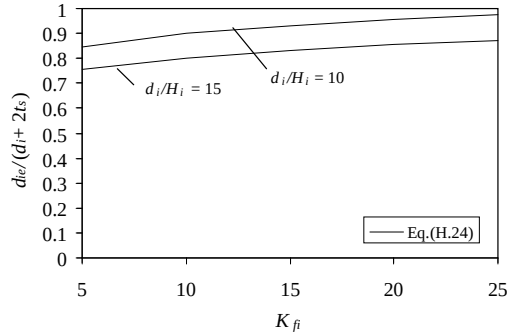

(b_2) Empirical curves for effective diameter.

Figure H.14: Effects of different variables on the inlet loss coefficient for square inlets and isotropic fill.

From Fig. H.14 it can be seen that a change in diameter to inlet height ratio from d_i/H_i = 10 to 15 results in an increase in the inlet loss coefficient of slightly less than 200% and a reduction in the effective diameter of roughly 10%. A change in fill loss coefficient from K_{fi} = 12.2 to 30 results in a decrease in the inlet loss coefficient of about 40% and an increase in the effective diameter ratio from $d_{ie}/(d_i+2t_s)$ = 0.915 to maximum. In comparison, the effects of shell wall thickness and shell inclination angle are negligibly small. In Fig. H.14(b_1), the above loss coefficient correlation (Eq. H.23) is compared to Eq. (H.14) showing that the deviation is larger than for orthotropic fill. The above effective diameter correlation (Eq. H.24) is plotted in Fig. H.14(b_2) but could not be compared with other empirical data.

The CFD data and regression curves for the rounded inlet and orthotropic fill resistance are presented in Fig. H.15.

The following empirical relations are proposed for the loss coefficient [Fig. H.15(a_1)] and effective diameter [Fig. H.15(a_2)] of rounded inlets (r_i/d_i = 0.02) and orthotropic fill resistance:

$$K_{ct} = 0.009687 K_{fi}^{-0.8} \left(\frac{d_i}{H_i} \right)^{3.2} \tag{H.25}$$

$$\frac{d_{ie}}{d_i} = 1.053639 \, K_{fi}^{0.07} \left(\frac{d_i}{H_i} \right)^{-0.1} \tag{H.26}$$

valid for $6.5 \le K_{fi} \le 30$, $10 \le d_i/H_i \le 15$ and in addition for Eq. (H.26), $d_{ie} \le (d_i - 2L_{fi}\tan\theta)$.

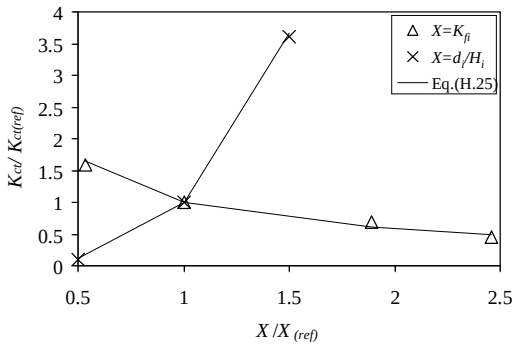

(a_1) CFD inlet loss coefficient data and regression curves.

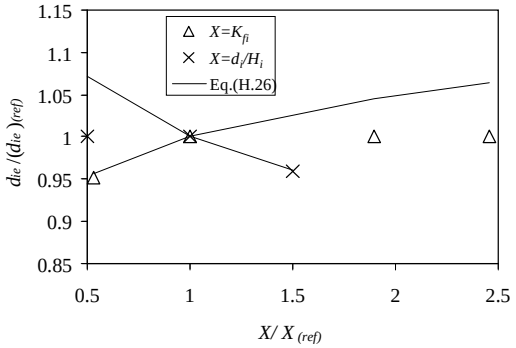

(a_2) CFD effective diameter data and regression curves.

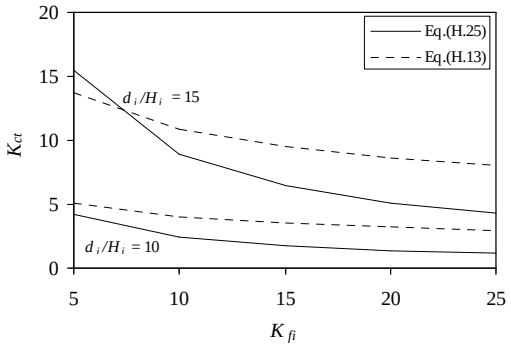

(b_1) Comparison between empirical inlet loss coefficient curves.

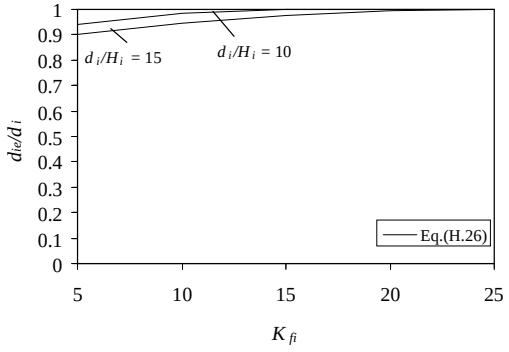

(b_2) Empirical effective diameter curves.

Figure H.15: Effects of different variables on the inlet loss coefficient for rounded inlets (r_i/d_i = 0.02) and orthotropic fill resistance.

From Fig. H.15 it can be seen that a change in diameter to inlet height ratio from d_i/H_i = 10 to 15 results in an increase in the inlet loss coefficient of slightly less than 270% and a reduction in the effective diameter of roughly 5%. A change in fill loss coefficient from K_{fi} = 12.2 to 30 results in a decrease in the inlet loss

coefficient of around 50% and the effective diameter ratio remains at its maximum. In Fig H.15(b_1), the above correlation for loss coefficient (Eq. H.25) is compared to Eq. (H.13) and in Fig H.15(b_2) the effective diameter (Eq. H.26) is plotted, but could not be compared with empirical data.

The CFD data and regression curves for the rounded inlet and isotropic fill resistance are presented in Fig. H.16.

The following empirical relations are proposed for the loss coefficient [Fig. H.16(a_1)] and effective diameter [Fig. H.16(a_2)] of rounded inlets (r_i/d_i = 0.02) and isotropic fill resistance:

$$K_{ct} = 0.111819 K_{fi}^{-0.21} \left(\frac{d_i}{H_i} \right)^{1.9} \tag{H.27}$$

$$\frac{d_{ie}}{d_i} = \frac{d_i - 2L_{fi} \tan\theta}{d_i} \tag{H.28}$$

valid for $6.5 \leq K_{fi} \leq 30$, $10 \leq d_i/H_i \leq 15$.

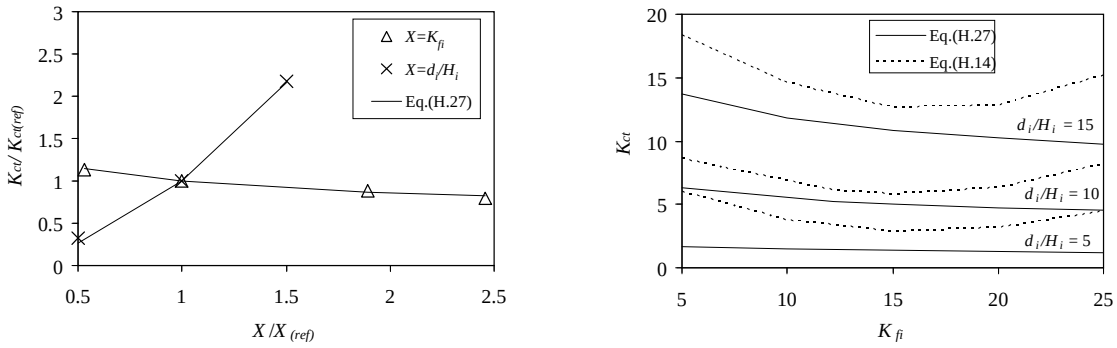

(a) CFD inlet loss coefficient data and regression curves.

(b) Comparison between empirical inlet loss coefficient data.

Figure H.16: Effects of different variables on the inlet loss coefficient for rounded inlets (r_i/d_i = 0.02) and isotropic fill resistance.

From Fig. H.16 it can be seen that a change in diameter to inlet height ratio from d_i/H_i = 10 to 15 results in an increase in the inlet loss coefficient of slightly less than 120%. A change in fill loss coefficient from K_{fi} = 12.2 to 30 results in a decrease in the inlet loss coefficient of around 20%. In Fig. H.16(b) the above correlations for loss coefficient (Eq. H.27)) is compared to Eq. (H.14) showing similar deviations as observed by De Villiers (1998). Since the effective diameter (Eq. H.28) is at its maximum and no valid empirical data is available for isotropic fill resistance, the effective diameter graph is not included in Fig H.16.

The effect of installing a protruding platform on the outside of the cooling tower shell just above the lowest edge of the shell is presented in Fig. H.17 in terms of platform protrusion length (L_p) and installation height (Δz_p) above the shell edge. It can be seen that the lowest inlet loss coefficients are obtained when $L_p = \Delta z_p$. Significant improvements are also observed for the effective diameter ratio. Comparing the protruding platform results to the rounded inlet data shows that the loss coefficients and effective diameters are similar.

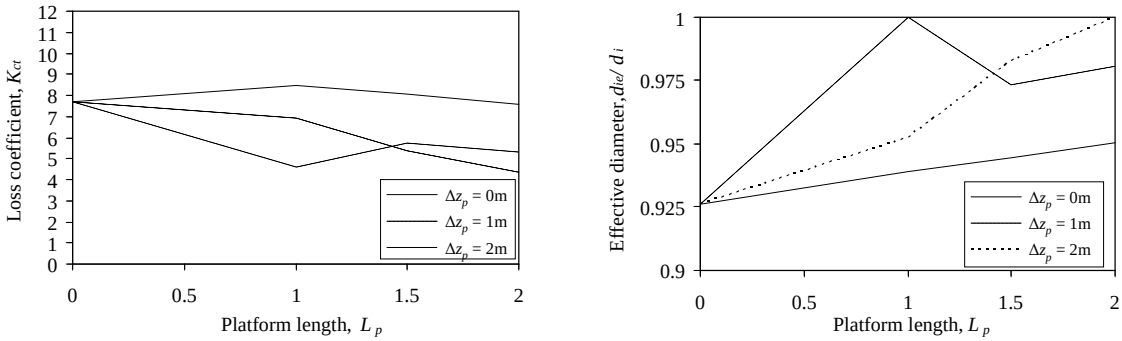

(a) Inlet loss coefficient.

(b) Effective diameter.

Figure H.17: Effects of a protruding platform above the air inlet on the inlet loss coefficient and effective diameter for orthotropic fill resistance.

The CFD flow patterns for square, rounded and protruding platform inlets are shown in Fig. H.18. For the square inlet, flow separation occurs at the square edge, resulting in a vena contracta below the shell base and subsequent higher air velocities entering the tower. This vena contracta can be eliminated by installing a rounding or a protruding platform, hereby reducing the flow recirculation region thus increasing the effective flow area and reducing energy dissipation due to velocity gradients.

4. SUMMARY OF RESULTS

A two-dimensional (axi-symmetric) CFD model of a cooling tower inlet is developed using the CFD code *FLUENT*®. The results are compared with axial velocity profile data, tower inlet loss coefficients and effective diameters determined experimentally by Terblanche (1994) as well as applicable empirical data found in literature. The validation results are summarized as follows:

- ⇨ A grid size of approximately 1% of the cooling tower diameter is found to give results that are essentially grid independent.
- ⇨ The effects of dimensional scaling on the inlet loss coefficient and effective diameter are negligible which confirms that Reynolds number effects are negligible.

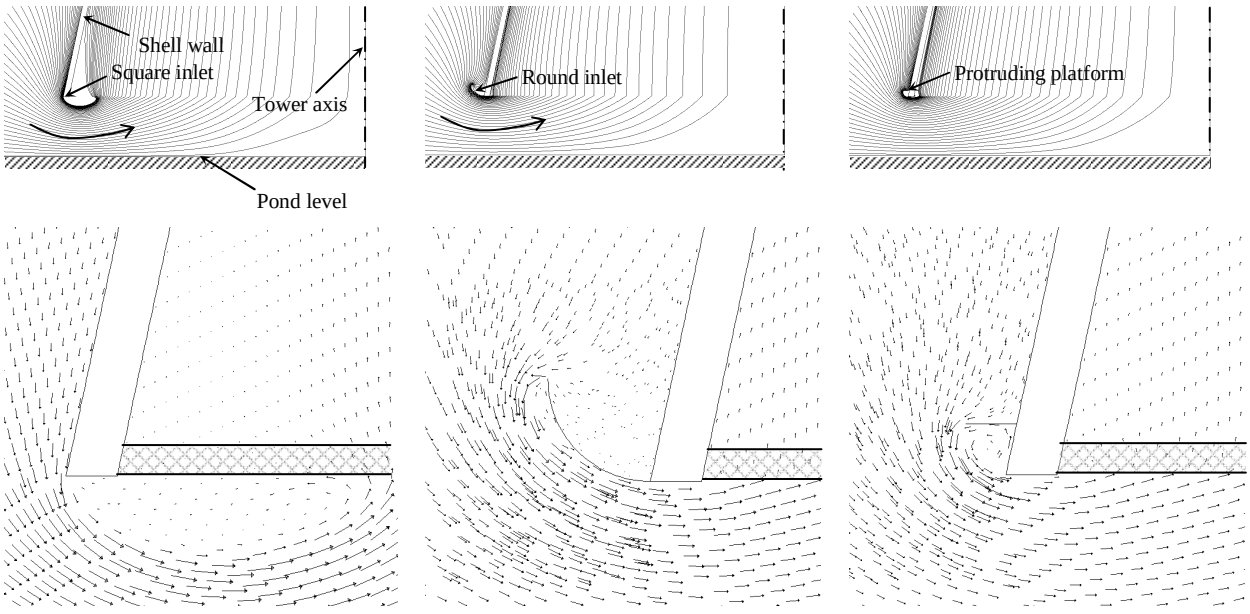

(a) Square inlet.

(b) Round (r_i/d_i = 0.02) inlet.

(c) Protruding platform (L_p = 1m, Δz_p = 1m) inlet.

Figure H.18: CFD pathline flow patterns and vector diagrams for a square, round and protruding platform inlet for d_i/H_i = 10 and K_{fi} = 12.2 and isotropic fill resistance.

- ⇨ Comparing the k-ε Realizable, k-ε Standard, Spalart Allmeras and k-ω SST turbulence models, reveals that the k-ε Realizable model gives the best results with regard to velocity profile, loss coefficient and effective diameter. The Spalart Allmeras and k-ω SST models seem to predict the core velocity profile slightly better than the k-ε Realizable model, but they do not predict the near shell velocity profile well, whereas the k-ε Standard velocity profile deviates considerably from the experimental data over the whole range.
- ⇨ The comparison between the CFD results and the experimental data for a cylindrical cooling tower with a square inlet and orthotropic fill resistance is presented for different fill loss coefficients, inlet height to diameter ratios and inlet designs. It can be seen that the CFD generally predicts smaller vena contracta or effective diameters and therefore over-predicts the inlet loss coefficient, attributed to a combination of measurement uncertainties (air flow rate, air velocity, pressure drop and fill loss coefficient), geometric differences (sector vs axi-symmetric) and modelling uncertainties (fill losses and flow turbulence). The differences are however deemed relatively small.
- ⇨ By installing a round inlet, the inlet loss coefficient and effective flow diameter can be improved significantly.
- ⇨ The differences in the inlet loss coefficient and effective diameter for isotropic and orthotropic fill resistance are found to be significant. For oblique flow, the fill resistance of orthotropic fill is lower than that of isotropic fill for the same

axial fill loss coefficient, resulting in a smaller vena contracta and therefore a higher inlet loss coefficient in accordance with general trends observed.

The validated CFD model is used to investigate the effects of shell wall thickness, shell wall inclination angle, fill loss coefficient, fill type, inlet diameter to inlet height ratio and inlet geometry on the inlet loss coefficient and effective diameter of full-scale towers. The results are used to develop simple correlations for the inlet loss coefficient and effective diameter ratio in terms of these variables and can be summarised as follows:

- ⇨ The effects of shell wall thickness and inclination angle on the inlet loss coefficient and effective diameter are negligible, whereas the effects of fill or heat exchanger loss coefficient and especially diameter to inlet height ratio are significant.
- ⇨ The differences between the inlet loss coefficient correlations and empirical data from literature for square inlets are small whereas for round inlets they are more significant. The general trend is that the relations from literature are more conservative.
- ⇨ The comparison between the effective diameter correlations and empirical data from literature for square inlets shows that the differences are small for d_i/H_i = 10 but significant for d_i/H_i = 15, where the CFD data is the more conservative in this case.
- ⇨ The data presented in Table H.8 for orthotropic fill resistance reveals that an inlet rounding with r_i/d_i = 0.02 reduces the inlet loss coefficient to about a third of the value for a square inlet while maximising the effective diameter ratio. A further observation is that the inlet loss coefficient and effective diameter for d_i/H_i = 15 with a rounded inlet is almost the same as for d_i/H_i = 10 with a square inlet.
- ⇨ For isotropic fill resistance, the difference between the loss coefficients and effective diameter of square and round inlets is slightly less than for orthotropic resistance.

Table H.8 : Data to evaluate the effect of installing a round inlet.

Description	Orthotropic fill resistance				Isotropic fill resistance			
r_i/d_i	0	0.02	0	0.02	0	0.02	0	0.02
d_i/H_i	10	10	15	15	10	10	15	15
K_{he}	12.2	12.2	12.2	12.2	12.2	12.2	12.2	12.2
K_{ct}	7.686	2.075	24.246	7.504	8.569	5.25	24.708	11.463
$d_{ie}/(d_i+2t_s)$	0.906	Max.	0.782	0.957	0.915	Max.	0.818	Max.

- ⇨ The CFD results obtained for a protruding platform attached to the outside of the cooling tower above the lowest part of the shell, reveal that similar loss coefficients and effective diameters can be achieved compared to rounded

inlets. For the conditions investigated, the optimum is found to be when $L_p \approx \Delta z_p$.

- ⇨ Pathline and vector diagrams are presented for square, round and protruding platform inlets. For the sharp inlet, a flow separation region exists below the shell's lowest edge resulting in higher mean inlet velocity. This flow separation region is eliminated by installing a round inlet or protruding platform above the air inlet herewith reducing viscous dissipation due to velocity gradients at the flow recirculation interface and subsequently reducing the loss coefficient.

5. CONCLUSIONS AND RECOMMENDATIONS

The deviations between CFD, experimental and empirical data for cooling tower inlets are found to be relatively small, considering the uncertainties in the experimental data and the numerical models.

From the results, the following can be concluded:

- ⇨ CFD is an excellent tool to model cooling tower inlet flows.
- ⇨ Cooling tower inlet losses and effective diameter are independent of the Reynolds number.
- ⇨ The inlet diameter to height ratio (d_i/H_i) and fill or heat exchanger loss coefficient (K_{fi}) have the most significant influence on the inlet loss coefficient and effective diameter and the effects of shell thickness and inclination angle are small.
- ⇨ There are significant differences between the loss coefficient and effective diameter data of orthotropic and isotropic fill resistances. The fill resistance in cooling towers packed with film type fill, can however be a combination of orthotropic and isotropic resistance, depending on the fill orientation relative to the airflow, which should be investigated three-dimensionally.
- ⇨ Under no wind conditions, the performance of NDCTs with square inlets can be enhanced significantly by installing round inlets or protruding platforms above the air inlet, where the protruding platform is expected to be much cheaper. Future research should however be done to determine the effect of these modifications under windy conditions.
- ⇨ From different cooling tower inlet geometries found in industry, it observed that the fill frontal area of fills suspended from support beams is generally less than the shell inlet cross-sectional area due to the inclination of the shell wall, as shown in Fig. H.19. This results in a region near the shell wall, which does not contain any fill and therefore reduces the negative impact of flow separation at the inlet on cooling tower performance.

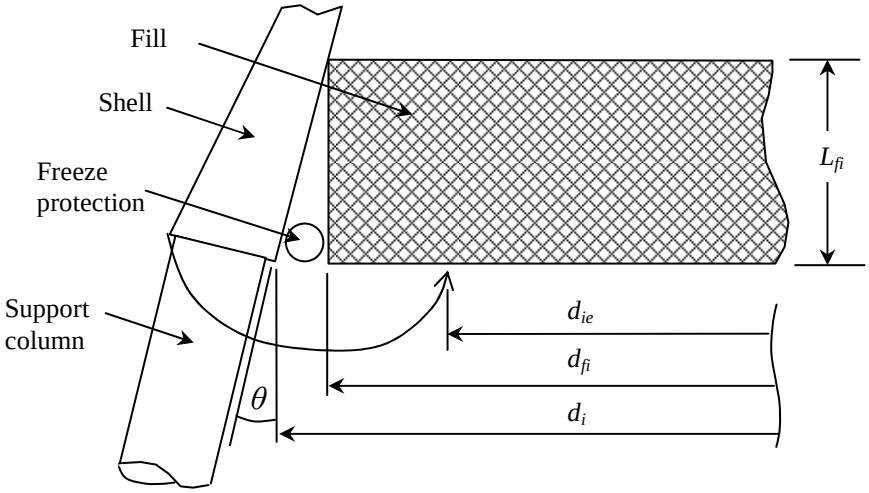

Figure H.19: Schematic of a NDCT inlet showing the difference between inlet and fill diameter.

I

CFD ANALYSIS OF COOLING TOWER RAIN ZONES

In the rain zones of wet-cooling towers, drops fall downwards under gravity through air flowing at different angles relative to the drop motion. In counter-flow cooling towers, the air enters the rain zone horizontally via the cooling tower air inlet, turning through 90º in the rain zone before continuing its flow path vertically upwards through the cooling tower, as shown in Fig. I.1.

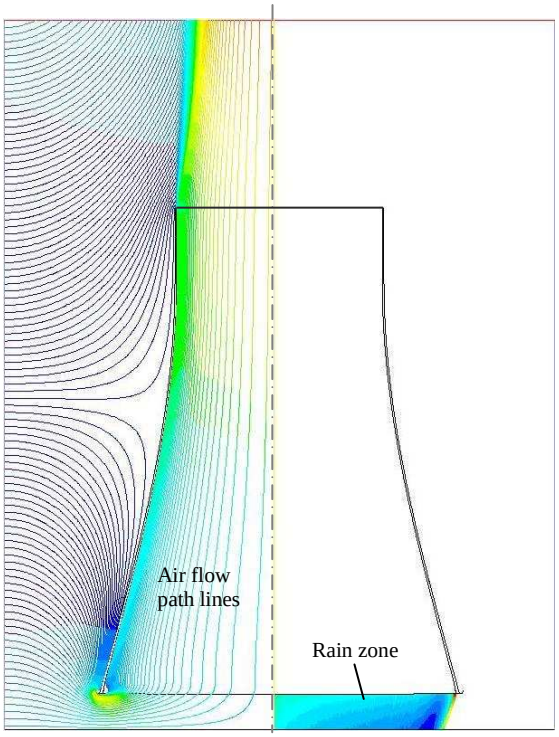

Figure I.1 : Typical flow patterns in a natural draught counterflow wet-cooling tower.

De Villiers (1998) and (2001) developed semi-empirical relations for the Merkel number and loss coefficient for purely counterflow rain zones and cross-counterflow rain zones found in circular and rectangular counterflow cooling towers using CFD and empirical data, and investigated the effect of the rain zone on the inlet loss coefficient of these types of cooling towers, as presented in Kröger (2004).

For purely counterflow rain zones, the Merkel number is given as

$$
\begin{aligned}
Me_{rz} = 3.6&\left(\frac{p_a}{R_v T_a \rho_w}\right)\left(\frac{D}{v_{azo} d_d}\right)\left(\frac{H_{rz}}{d_d}\right) Sc^{0.33}\left[\ln\left(\frac{w_s + 0.622}{w + 0.622}\right)/(w_s - w)\right] \\
&\times\Big[5.01134 a_\rho \rho_a - 192121.7 a_\mu \mu_a - 2.57724 + 23.61842\left(0.2539\left(a_v v_{azo}\right)^{1.67} + 0.18\right) \\
&\times\left(0.8366\left(a_L H_{rz}\right)^{-0.5299} + 0.42\right)\left(43.0696\left(a_L d_d\right)^{0.7947} + 0.52\right)\Big]
\end{aligned}
\tag{I.1}
$$

The corresponding rain zone loss coefficient is given as

$$
\begin{aligned}
K_{rz} = a_v v_w\Big[&10645988 a_\mu \mu_a - 130.7774 a_\rho \rho_a - 32.6634 \\
&+ 888.6645\left\{2.45287\left(a_\mu v_{azo}\right)^{-1.93315} + 0.34\right\}\left\{4.03861\exp\left(-574.542 a_L d_d\right) + 0.492\right\} \\
&\times\exp\left\{\left(65.26215 a_L d_d + 0.74827\right)\ln\left(6.09836\exp\left(0.0767 a_L H_{rz}\right) - 6.1\right)\right\}\Big]
\end{aligned}
\tag{I.2}
$$

where

$a_\mu = 3.061\times10^{-6}\left(\rho_w^4 g^6/\sigma_w\right)^{0.25}$, $a_\rho = 998/\rho_w$, $a_v = 73.298\left(g^5\sigma_w^3/\rho_w^3\right)^{0.25}$ and $a_L = 6.122\left(g\sigma_w/\rho_w\right)^{0.25}$

The above equations are valid for the following conditions:

$0 \le T_a \le 40\ ^\circ\mathrm{C}$, $10 \le T_w \le 40\ ^\circ\mathrm{C}$

$0.927 \le \rho_a \le 1.289\ \mathrm{kg/m^3}$, $992.3 \le \rho_w \le 1000\ \mathrm{kg/m^3}$

$1.717\times10^{-5} \le \mu_a \le 1.92\times10^{-5}\ \mathrm{kg/ms}$

$0.0696 \le \sigma_w \le 0.0742\ \mathrm{N/m}$, $0.002 \le d_d \le 0.008\ \mathrm{m}$, $9.7 \le g \le 10\ \mathrm{m/s^2}$

$0.5 \le H_{rz} \le 5.5\ \mathrm{m}$

$0.00075 \le v_w \le 0.003\ \mathrm{m/s}$ and $1 \le v_{azo} \le 5\ \mathrm{m/s}$

D according to Eq. (C.41) by Gilliland (1934)

For the cross-counterflow rain zone of a counterflow natural draught wet-cooling tower, the Merkel number is given as

$$
\begin{aligned}
Me_{rz} = 12&\left(\frac{p_a}{R_v T_a \rho_w}\right)\left(\frac{D}{v_{azo} d_d}\right)\left(\frac{H_{rz}}{d_d}\right) Sc^{0.33}\left[\ln\left(\frac{w_s + 0.622}{w + 0.622}\right)/(w_s - w)\right] \\
&\times\Big[0.90757 a_\rho \rho_a - 30341.04 a_\mu \mu_a - 0.37564 + 4.04016\left(41.7215\left(a_L d_d\right)^{0.80043} + 0.55\right) \\
&\times\left(3.741\left(a_L H_i\right)^{-1.23456} + 0.713\right)\left(3.11\exp\left(0.15 a_v v_{azo}\right) - 3.13\right)\Big] \\
&\times\exp\Big[\left\{5.3759\exp\left(-0.2092 a_L H_i\right)\right\}\ln\left\{0.3719\exp\left(0.0019055 a_L d_i\right) + 0.55\right\}\Big]\Big]
\end{aligned}
\tag{I.3}
$$

The corresponding rain zone loss coefficient is given as

$$
\begin{aligned}
K_{rz} = {} & 3a_v v_w \left(H_i/d_d\right)\Big[5263.04a_\mu\mu_a - 0.31467a_\rho\rho_a + 0.2246 \\
& + 0.775526\left(1.4824163\exp\left(71.52a_L d_d\right) - 0.91\right) \\
& \times\left(0.39064\exp\left(0.010912a_L d_i\right) - 0.17\right)\left(2.08915\left(a_v v_{azo}\right)^{-1.3944} + 0.14\right) \\
& \times\exp\Big\{\left(0.8449\ln\left(a_L d_i/2\right) - 2.312\right)\left(0.3724\ln\left(a_v v_{azo}\right) + 0.7263\right) \\
& \times\ln\left(206.757\left(a_L H_i\right)^{-2.8344} + 0.43\right)\Big\}\Big]
\end{aligned}
\tag{I.4}
$$

The above equations are valid for the same conditions as Equations (I.1) and (I.2), except for the following:

$4 \le H_{\mathrm{i}} \le 12\ \mathrm{m}$, $30 \le d_{\mathrm{i}}/2 \le 70\ \mathrm{m}$, and $1 \le v_{\mathrm{azo}} \le 3\ \mathrm{m/s}$

For a counterflow natural draught wet-cooling tower with a rain zone, the inlet loss coefficient models presented in Appendix H for circular dry-cooling towers without rain zones, need to be multiplied by the following correction factor proposed by De Villiers (2001) to obtain the effective wet-cooling tower inlet loss coefficient:

$$
\begin{aligned}
C_{rz} = {} & \Big[0.2394 + 80.1\left\{0.0954/\left(d_i/H_i\right) + d_d\right\}\exp\left(0.395G_w/G_a\right) - 0.3195\left(G_w/G_a\right) \\
& \times -966\left\{d_d/\left(d_i/H_i\right)\right\}\exp\left(0.686G_w/G_a\right)\Big]\left(1 - 0.06825G_w\right) \\
& \times K_{\mathrm{fi}}^{0.09667}\exp\left\{8.7434\left(1/d_i - 0.01\right)\right\}
\end{aligned}
\tag{I.5}
$$

valid for the following conditions:

$7.5 \le d_{\mathrm{i}}/H_i \le 20$, $30 \le d_{\mathrm{i}}/2 \le 60\ \mathrm{m}$, $0.003 \le d_{\mathrm{d}} \le 0.006\ \mathrm{m}$, $1 \le G_w \le 3\ \mathrm{kg/sm^2}$, $1.2 \le G_a \le 3.6\ \mathrm{kg/sm^2}$, and $5 \le K_{fi} \le 25$

It is assumed that Eq. (I.5) is valid for rounded inlets (r_i/d_i = 0.02) only since a CFD model of a cooling tower with a rounded inlet is used to develop the relation. The effective wet-cooling tower inlet loss coefficient is therefore expressed as

$$K_{ct(rz)} = C_{rz} K_{ct(norz)} \tag{I.6}$$

Al-Waked (2006, 2007, 2010) and Williamson [2008(1), 2008(2), 2008(3)] developed CFD models to simulate the performance of counter-flow wet-cooling towers, revealing that cooling tower performance can be enhanced significantly by reducing the mean drop size in the rain zone and that limited drop distribution data is available in literature. The effects of drop collisions and break-up due to drop interaction were not investigated by either of them.

The main objectives of this section are: to develop CFD models using *FLUENT*® for determining the performance of counterflow, crossflow and cross-counterflow rain zones; to use these models for investigating the effects of different drop size distributions, drop drag models, and drop interaction models (collision and break-up) on the rain zone performance; and to compare the CFD results to data from previous sections and empirical data from literature.

I.1 CFD MODELS OF COOLING TOWER RAIN ZONES

The two-dimensional computational flow domains of the CFD models are meshed with a uniform structured (quadrilateral) grid (0.1 m x 0.1 m) and the main dimensions and boundary definitions for the counterflow and crossflow models are presented in Fig. I.2.

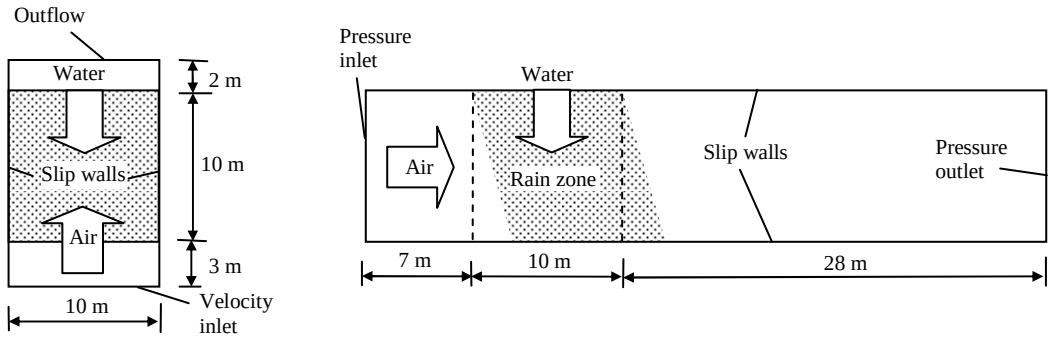

(a) Counterflow rain zone. (b) Crossflow rain zone.

Figure I.2 : Main dimensions of the computational domains for the counter- and crossflow rain zone.

The transport equations for mass, momentum, energy, species mixing and turbulence are solved in the Eulerian frame of reference, employing the two-dimensional, double precision, steady state, segregated solver and the SIMPLE algorithm for the pressure-velocity coupling. To maximize numerical accuracy, second order discretization is employed for all the governing equations.

The rain zone performance is simulated by means of the Lagrangian discrete phase (DP) model, which tracks the drop (dispersed phase) trajectories through the calculated flow field and the exchange of momentum, mass and energy with the air (continuous phase). The grid is therefore uniform and materials properties are defined for simulation of species transport i.e. the air properties are based on a mixture of dry air and water vapour and the energy equation is solved.

The discrete phase (DP) model of *FLUENT*® is limited to volume fractions of less than 10-12%, as applicable to cooling tower rain zones and offers drop collision, drop breakup and stochastic tracking models. Information on these models is given in the *ANSYS-FLUENT*® (2006) Users' Guide, and for brevity is not included in this appendix.

I.2 CFD RESULTS

The data presented in the following figures is based on an atmospheric pressure of p_a = 101325 Pa; an ambient temperature of T_a = 288.15 K (15 ºC); a relative humidity of ϕ_a = 60 %; a water inlet temperature of T_{wi} = 303.15 K (30 ºC); an initial drop speed of v_{d0} = 0.1 m/s; a water mass velocity of G_{wi} = 2.84 kg/m^2; and an injection angle of θ = -90º. These conditions are typical design conditions for rain zones in natural draught counterflow wet-cooling towers. As done in the

previous appendices, a reference case is developed for comparison, based on the following models: the Dreyer (1994) relation for the drag coefficient (Eq. B.12); the Ranz and Marshall (1952) relations for the heat and mass transfer coefficients (Eqs C.12 and C.22); the Fuller (VDI 2006) relation for the diffusion coefficient (Eq. C.42); and Eq. (C.5) for determining the rate of mass transfer.

Since limited drop size distribution data is available in literature, a new counter-flow test rig was designed and built to measure the drop distributions below different counter-flow fill configurations for various water and air flow rates. Terblanche (2009) developed a digital photographic drop size measurement technique for this test rig, including the necessary digital image processing software, and measured drop size distributions below cross-fluted film, trickle and fibre cement sheet film fills, commonly used in natural draught wet-cooling towers as well as different grid configurations installed below these fills to reduce the Sauter mean drop diameter.

For the following CFD investigation of cooling tower rain zones, the drop size distributions measured below a trickle fill as well as a horizontal grid installed 0.6 m below the trickle fill are used, as presented in Table I.1 and Fig I.3. These distributions, measured at a water mass velocity of G_w = 2.84 kg/sm^2, are each based on the sum of 3 digital images and represent a typical and enhanced drop distribution respectively.

Table I.1 : Drop size distribution data.

		Typical drop distribution				Enhanced drop distribution		
d	n	M_d/M_t	R_m	R_{RR}	N	M_d/M_t	R_m	R_{RR}
0.25	5	9.19×10^{-6}	1.0000	1.0000	0	0	1.0000	0.9998
0.75	48	0.0012	0.9988	0.9997	699	0.0234	0.9766	0.9943
1.25	35	0.0040	0.9948	0.9975	358	0.0555	0.9210	0.9737
1.75	27	0.0085	0.9863	0.9908	237	0.1009	0.8201	0.9291
2.25	15	0.0100	0.9762	0.9756	125	0.1131	0.7071	0.8547
2.75	21	0.0257	0.9506	0.9471	60	0.0991	0.6079	0.7500
3.25	10	0.0202	0.9304	0.9005	31	0.0845	0.5234	0.6212
3.75	13	0.0403	0.8901	0.8322	17	0.0712	0.4522	0.4805
4.25	21	0.0947	0.7954	0.7407	17	0.1037	0.3485	0.3433
4.75	18	0.1133	0.6821	0.6285	13	0.1107	0.2379	0.2242
5.25	15	0.1275	0.5545	0.5026	7	0.0805	0.1574	0.1323
5.75	16	0.1787	0.3758	0.3742	2	0.0302	0.1272	0.0699
6.25	11	0.1578	0.2180	0.2558	5	0.0970	0.0303	0.0327
6.75	4	0.0723	0.1457	0.1581	0	0.0000	0.0303	0.0134
7.25	2	0.0448	0.1010	0.0871	1	0.0303	0	0.0047
7.75	0	0	0.1010	0.0419	0	0	0	0.0014
8.25	0	0	0.1010	0.0174	0	0	0	0.0004
8.75	0	0	0.1010	0.0061	0	0	0	0.0001
9.25	1	0.0465	0.0545	0.0017	0	0	0	0
9.75	1	0.0545	0	0.0004	0	0	0	0

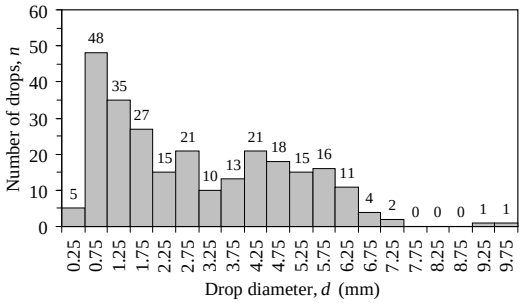

(a_1) Typical drop distribution.

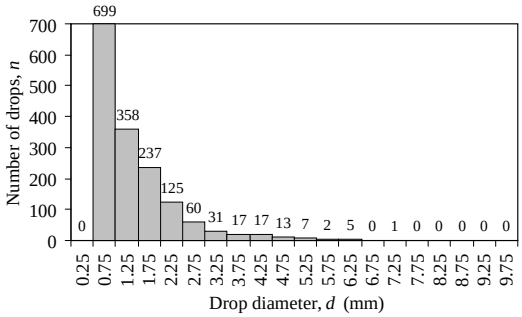

(a_2) Enhanced drop distribution.

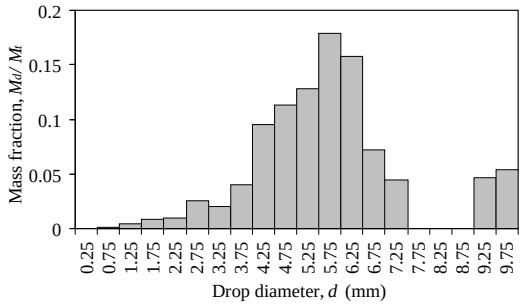

(b_1) Typical mass distribution.

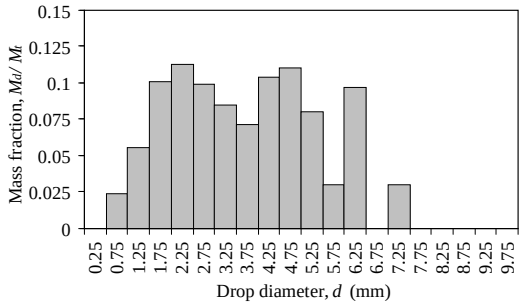

(b_2) Enhanced mass distribution.

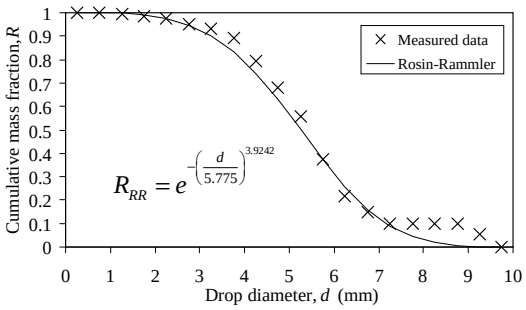

(c_1) Typical cumulative mass distribution and Rosin-Rammler curve.

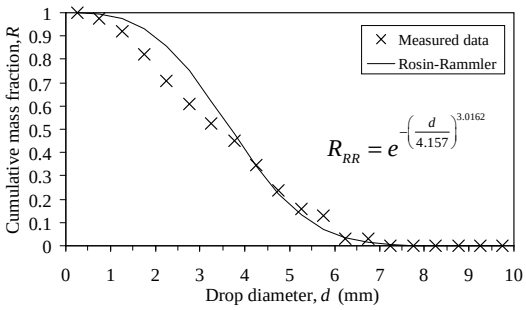

(c_2) Enhanced cumulative mass distribution and Rosin-Rammler curve.

Figure I.3 : Typical and enhanced rain zone inlet polydisperse drop distribution graphs.

The typical distribution has a mean drop size as typically encountered in rain zones below trickle and film fills, whereas the enhanced distribution has smaller drops for rain zone performance enhancement, achieved by allowing the drops leaving the fill to impinge on the slats of a horizontal grid. Fig I.3(c) shows the empirical Rosin-Rammler curve for the experimental cumulative mass fraction data, where R is the cumulative drop mass fraction of drops with a diameter greater than d. The general form of the Rosin-Rammler equation is

$$R_{RR} = e^{\left[-\left(\frac{d}{\bar{d}_{RR}}\right)^{n_{RR}}\right]} \qquad \text{(I.7)}$$

where

$$n_{RR} = \sum_{i=1}^{N} \frac{\ln\left[-\ln\left(R_{m,i}\right)\right]}{\ln\left(d_i / \bar{d}_{RR}\right)} / \mathrm{N} \tag{I.8}$$

Different definitions for mean diameter of a polydisperse drop distribution can be determined from the following general equation (ASTM E799-92):

$$d_{pq}^{(p-q)} = \frac{\sum_i d_i^p}{\sum_i d_i^q} \approx \frac{\sum_j n_j d_j^p}{\sum_j n_j d_j^q} \tag{I.9}$$

According to *ANSYS-FLUENT*® (2006), the following mean diameters are used for comparison and analysis of evaporation processes: mean (d_{10}), overall volume (d_{31}), Sauter mean (d_{32}) and De Brouckere (d_{43}) diameters. Values for these diameters are presented in Table I.2 for the typical and enhanced drop distribution. Pierce (2007) used *FLUENT*® to confirm that the Sauter mean diameter is the most representative monodisperse drop diameter for determining the transfer characteristics and loss coefficient of cooling tower rain zones. He however did not include the effects of drop interaction (collision and break-up) and flow turbulence (drop dispersion) on the *FLUENT*® results in his investigation.

Table I.2 : Monodisperse drop diameter data for the typical and enhanced drop distributions.

Description	Units	Typical drop distribution	Enhanced drop distribution	Field of application *FLUENT*® (2006)
Mean diameter, d_{10}	mm	2.950	1.411	Comparisons
Overall volume diameter, d_{31}	mm	4.684	2.382	Molecular diffusion
Sauter mean diameter, d_{32}	mm	5.137	2.836	Combustion, mass transfer
De Brouckere diameter, d_{43}	mm	5.729	3.720	Combustion equilibrium
Rosin-Rammler diameter, $\bar{d}_{RR}$	mm	5.775	4.157	Rosin-Rammler function

I.2.1 Counterflow rain zone

The *FLUENT*® performance results for a counterflow rain zone (10 m wide x 1 m deep x 10 m high) are presented in this section for an air speed of v_a = 2 m/s vertically upwards (φ = 90º). Fig. I.4 compares the drop speeds and drop temperature changes of the typical and enhanced drop distributions as functions of drop path length, determined using the numerical model for single drops (Appendix B and C) and the *FLUENT*® model excluding momentum, mass and energy exchange between the drops and the airstream, which shows minor differences.

The *FLUENT*® results determined using the time independent DPM model are presented in Fig. I.5 for the typical and enhanced drop distributions. The graphs show drop temperature and air dry- and wet-bulb temperature as well as the loss coefficient for monodisperse (Sauter mean diameter), polydisperse and Rosin-Rammler drop size distributions, including momentum, mass and energy transfer exchange between drops and the airstream. From this data and the summary of results presented in Table I.3, it can be seen that the deviations are generally relatively small, with the largest deviations observed for the loss coefficient of the

monodisperse enhanced distributions and the cooling range of the Rosin-Rammler distribution, which are above 10%. Furthermore, for the conditions investigated, it is found that for the enhanced distribution, the air leaving the rain zone is saturated whereas for the typical distribution it is unsaturated.

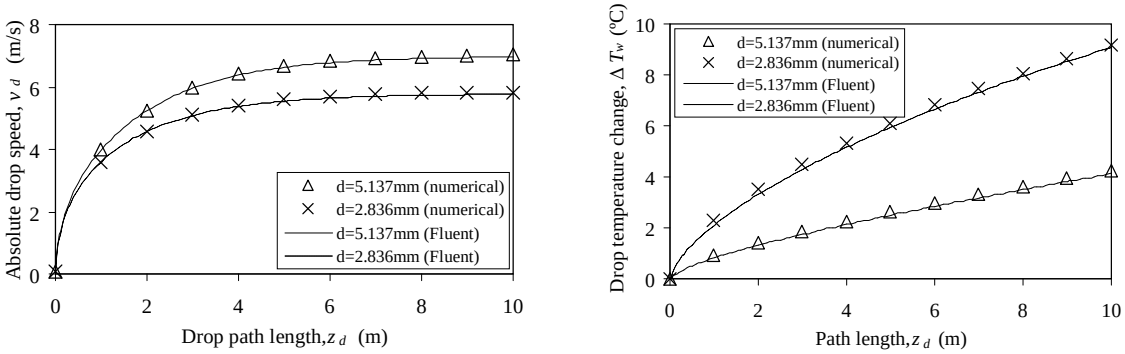

(a) Drop speed. (b) Drop temperature change.

Figure I.4 : Comparison between *FLUENT*® data for a counterflow rain zone without momentum, mass and energy exchange with the air and corresponding numerical single drop data (App. B and C).

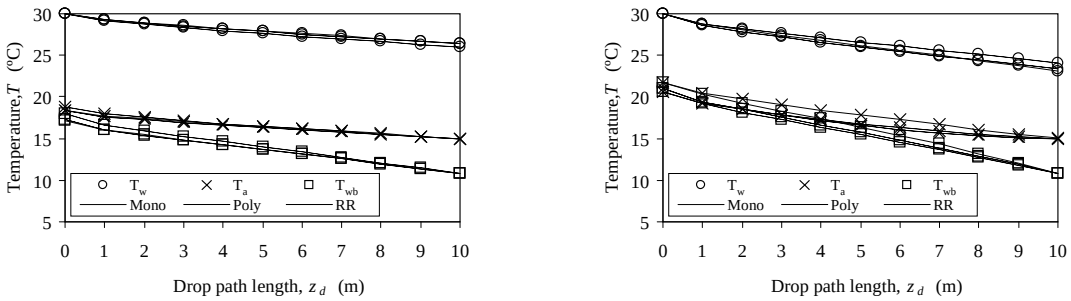

(a_1) Temperatures for the typical drop distribution. (a_2) Temperatures for the enhanced drop distribution.

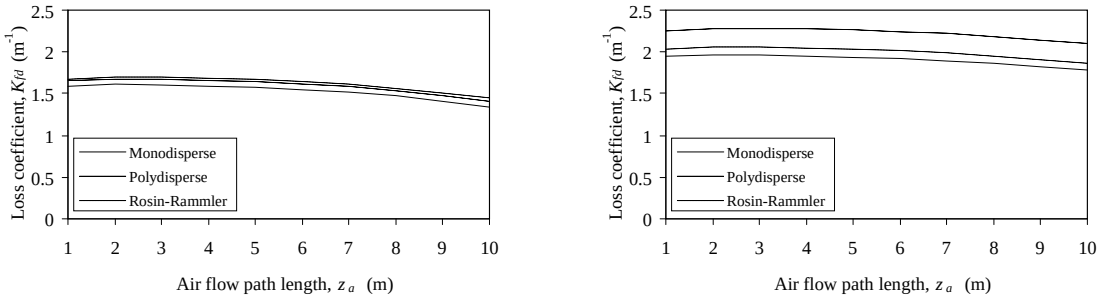

(b_1) Loss coefficient for the typical drop distribution. (b_2) Loss coefficient for the enhanced drop distribution.

Figure I.5 : Counterflow rain zone *FLUENT*® results for different drop distribution definitions.

The drop collision and break-up models in *FLUENT*® require the DPM model to be solved time dependently. The enhanced drop distribution *FLUENT*® results for a time dependent DPM solution with an injection time-step of Δt_d = 0.1 s are compared with corresponding steady DPM results in Fig. I.6, with negligible differences.

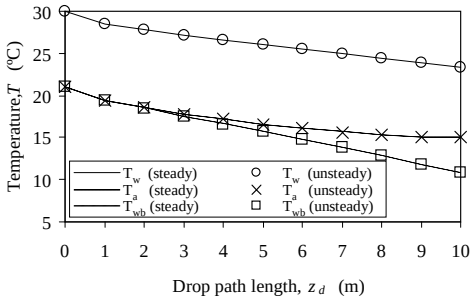

(a) Temperatures for the enhanced drop distribution.

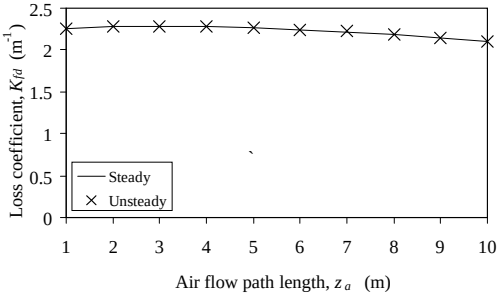

(b) Loss coefficient for the enhanced drop distribution.

Figure I.6 : Effect of the time dependent DPM solution on the *FLUENT*® results.

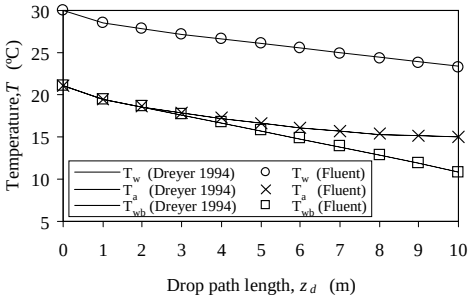

(a) Temperatures for the enhanced drop distribution.

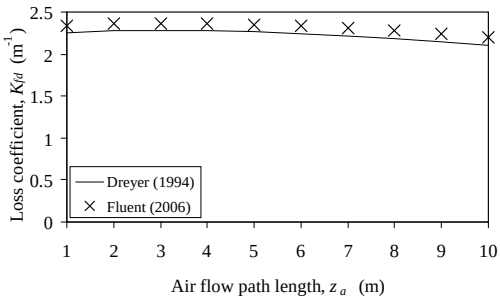

(b) Loss coefficient for the enhanced drop distribution.

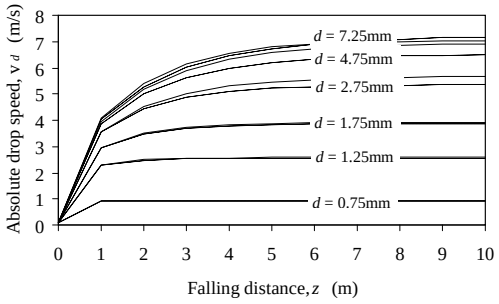

(c) Absolute drop speed for the enhanced drop distribution.

Figure I.7 : Comparison between *FLUENT*® results for the Dreyer (1994) and dynamic drag coefficient models.

The drop breakup model in *FLUENT*® uses a dynamic drag coefficient, which takes drop deformation into account. In Fig. I.7, the *FLUENT*® results for the enhanced polydisperse drop distribution obtained using the Dreyer (1994) drag coefficient (discussed in Appendix B) are compared with equivalent *FLUENT*® results based on the dynamic drag coefficient, giving the same temperatures but slightly higher loss coefficients ascribed to differences in the drop speeds. In Fig. I.7(c) it is shown that the *FLUENT*® drag model predicts lower absolute drop speeds and does not yield the expected constant terminal speed for drops of diameter d > 5mm as correctly predicted by the Dreyer (1994) model. The differences are however relatively small.

Fig. I.8 shows the effect of using the *FLUENT*® collision and breakup models on the *FLUENT*® results. It is observed that the effect on temperature is small, with the largest differences observed on the air-side between the rain zone inlet and outlet, which however converge at the outlet. The effect on the loss coefficient is negligible for the typical distribution, but measureable for the enhanced distribution. A change in drop size distribution is observed between the rain zone inlet and outlet, which would remain constant if there were no collisions. The Sauter mean diameter increases from d_{32} = 5.137 to 5.290 mm for the typical distribution and from d_{32} = 2.836 to 3.200 mm for the enhanced distribution. To check the collision model results, the monodisperse model is used to determine the rain zone performance for the mean of the inlet and outlet Sauter mean diameters of the enhanced distribution (d_{32} = 3.018 mm), yielding an increase in the cooling range of $\delta(\Delta T_w)$ = 0.41 ºC as opposed to $\delta(\Delta T_w)$ = 0.08 ºC obtained with the polydisperse collision model. Furthermore, the monodisperse model gave a $\delta(\Delta K_{fd})$ = 4 % whereas the polydisperse collision model predicts a decrease of $\delta(\Delta K_{fd})$ = 20 %. It is also found that mass is not conserved in the discrete phase when using the collision model. The *FLUENT*® collision model is therefore considered to be unreliable.

The effect of the stochastic tracking model was negligible and is therefore not presented.

Table I.3 gives the typical and enhanced drop distribution cooling range and loss coefficient data obtained for the following cases: monodisperse, polydisperse and Rosin-Rammler drop distributions solved with the steady DPM solver and employing the drag coefficient relation of Dreyer (1994); and polydisperse distribution solved with the unsteady DPM solver and the Dreyer (1994) and *FLUENT*® dynamic drag models and finally including the *FLUENT*® drop collision model. These results are compared with Eqs (I.1) and (I.2) of De Villiers (1998) solved by means of the Merkel method of analysis similar to the sample calculation for natural draught wet-cooling tower performance presented in Appendix K.

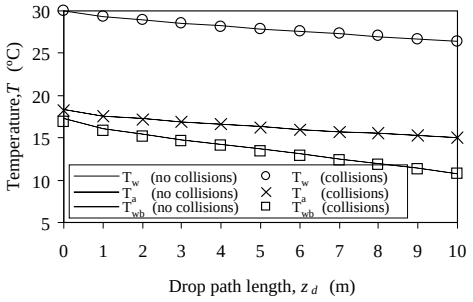

(a_1) Temperatures for the typical drop distribution.

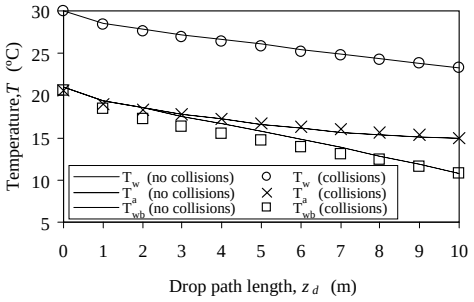

(a_2) Temperatures for the enhanced drop distribution.

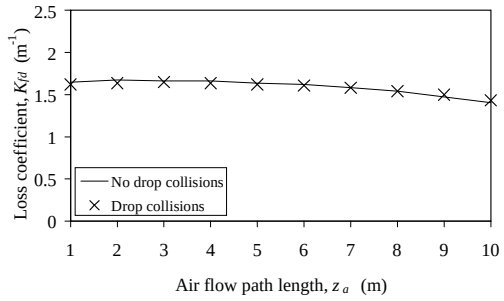

(b_1) Loss coefficient for the typical drop distribution.

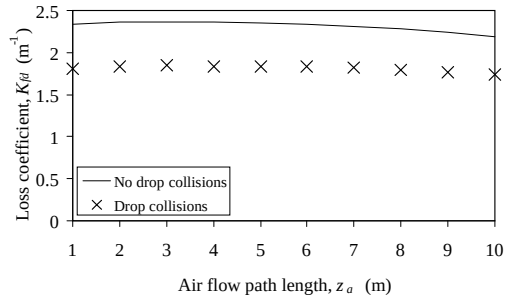

(b_2) Loss coefficient for the enhanced drop distribution.

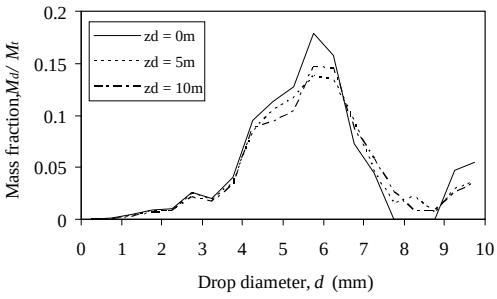

(c_1) Change in drop size distribution for the typical drop distribution.

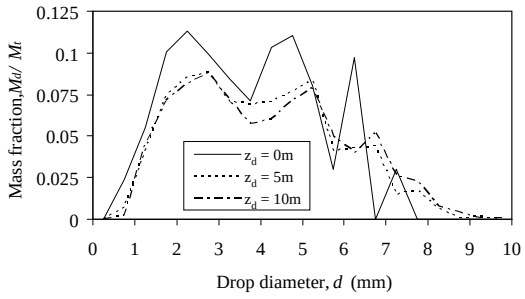

(c_2) Change in drop size distribution for the enhanced drop distribution.

Figure I.8 : Effect of the drop collision and breakup models on the *FLUENT*® results.

I.2.2 Crossflow rain zone

The *FLUENT*® results obtained for a crossflow rain zone, similar to the counterflow rain zone in the previous section with regard to water flow rate, injection area and rain zone height, are presented in this section for horizontal (φ = 0º) air speeds of v_a = 5.8 m/s and v_a = 6.3 m/s for the typical and enhanced drop distributions respectively. These air speeds yield the same air-side flow power consumptions as their opposing counterflow rain zones for the monodisperse drop distributions, thus providing a basis for comparing cooling performance.

Table I.3 : Counterflow rain zone cooling range and loss coefficient data for the typical and enhanced drop distributions with deviations from the polydisperse data given in brackets.

Drop distribution	Models			Typical drop distribution			Enhanced drop distribution		
	DPM	*Drag*	*Drop*	ΔT_w	K_{rz}	K_{fd}	ΔT_w	K_{rz}	K_{fd}
Monodisperse	Steady	Dreyer (1994)	-	3.60 (-0.8%)	13.46 (-4.4%)	13.44 (-4.3%)	6.92 (3.7%)	17.91 (-14.8%)	17.86 (-14.8%)
Polydisperse	Steady	Dreyer (1994)	-	3.63 (0%)	14.08 (0%)	14.04 (0%)	6.67 (0%)	21.02 (0%)	20.97 (0%)
Rosin-Rammler	Steady	Dreyer (1994)	-	4.05 (11.6%)	14.47 (2.8%)	14.47 (3.1%)	5.88 (-11.8%)	18.66 (-11.2%)	18.61 (-11.3%)
Polydisperse	Unsteady	Dreyer (1994)	-	3.63 (0%)	14.08 (0%)	14.04 (0%)	6.67 (0%)	21.02 (0%)	20.97 (0%)
Polydisperse	Unsteady	*FLUENT*® Dynamic	Breakup	3.68 (1.4%)	14.80 (5.1%)	14.77 (5.2%)	6.73 (0.9%)	21.98 (4.6%)	21.94 (4.6%)
Polydisperse	Unsteady	*FLUENT*® Dynamic	Breakup, collision	3.59 (-1.1%)	14.31 (1.6%)	14.28 (1.7%)	6.65 (-0.3%)	17.58 (-16.4%)	17.44 (-16.8%)
Monodisperse De Villiers (1998)	Steady	Dreyer (1994)	-	3.26 (-10%)	14.41 (2.3%)	-	6.18 (-7.3%)	20.01 (-4.8%)	-

The air-side flow power consumption is determined from

$$P_a = V \Delta p_t \tag{I.10}$$

Fig. I.9 shows negligible differences between the drop speeds and drop temperature change in terms of drop path length for the monodisperse drop distribution, determined using the numerical model for single drops (App. B and C) and a corresponding *FLUENT*® monodisperse model that excludes momentum, mass and energy exchange between the drops and the airstream.

The effect of momentum, mass and energy exchange between the drops and the airstream is presented in Figs I.10 to I.12 illustrating drop trajectories, colour mapped to show drop temperature, and contour plots of air dry-bulb temperature, humidity ratio, static pressure and absolute air speed.

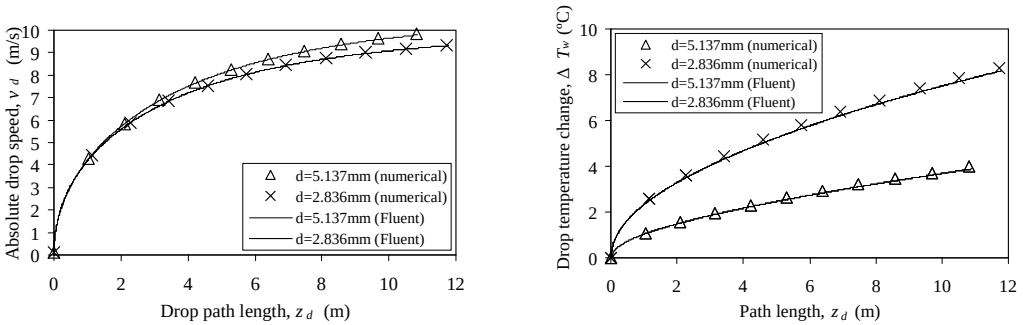

(a) Drop speed. (b) Drop temperature change.

Figure I.9 : Comparison between *FLUENT*® data for a crossflow rain zone without momentum, mass and energy exchange with the air and corresponding numerical single drop data (App. B and C).

Table I.4 gives the typical and enhanced drop distribution mass mean cooling range and loss coefficient data obtained for the following cases: monodisperse, polydisperse and Rosin-Rammler drop distributions solved with the steady DPM solver and employing the drag coefficient relation of Dreyer (1994); and polydisperse distribution solved with the unsteady DPM solver and the dynamic drag coefficient model of *FLUENT*® with and without the *FLUENT*® drop collision model and the Dreyer (1994) drag model.

Table I.4 : Crossflow rain zone cooling range and loss coefficient data for the typical and enhanced drop distributions showing the deviation from the polydisperse data in brackets.

Drop distribution	Models			Typical drop distribution			Enhanced drop distribution		
	DPM	*Drag*	*Drop*	ΔT_w	K_{rz}	K_{fd}	ΔT_w	K_{rz}	K_{fd}
Monodisperse	Steady	Dreyer (1994)	-	3.44 (-0.6%)	0.547 (-0.7%)	0.442 (0.9%)	6.88 (6.8%)	0.588 (2.3%)	0.340 (7.9%)
Polydisperse	Steady	Dreyer (1994)	-	3.46 (0%)	0.551 (0%)	0.438 (0%)	6.44 (0%)	0.575 (0%)	0.315 (0%)
Rosin-Rammler	Steady	Dreyer (1994)	-	3.89 (12.4%)	0.560 (1.6%)	0.428 (-2.2%)	6.02 (-6.5%)	0.567 (-1.4%)	0.346 (9.8%)
Polydisperse	Unsteady	Dreyer (1994)	-	3.46 (0%)	0.552 (0.2%)	0.438 (0%)	6.57 (2.0%)	0.575 (0%)	0.317 (0.6%)
Polydisperse	Unsteady	*FLUENT*® Dynamic	Breakup	3.47 (-0.3%)	0.526 (-4.5%)	0.380 (-13.2%)	6.59 (2.3%)	0.590 (2.6%)	0.303 (-3.8%)
Polydisperse	Unsteady	*FLUENT*® Dynamic	Breakup, collision	3.39 (-2.0%)	0.544 (-1.2%)	0.408 (-6.8%)	6.27 (-2.6%)	0.567 (-1.4%)	0.333 (5.7%)

I.2.3 Cross-counterflow rain zone of a counterflow natural draught wet-cooling tower

The *FLUENT*® results obtained for a cross-counterflow rain zone as found in counterflow natural draught wet-cooling towers with square and rounded inlets are presented in this section. The *FLUENT*® model developed in Appendix H.3 to investigate the influence of variables on the cooling tower inlet flow characteristics is used, which has the following geometry: d_i = 104.84 m; t_s = 1 m; r_i/d_i = 0.02 or 0; θ = 12 º; K_{fi} = 12.2 (isotropic resistance) and d_i/H_i = 10. The main difference is that a DPM model is now included to simulate the rain zone, based on the same operating conditions as the purely counterflow rain zone investigated above i.e. the average vertical air speed at the fill outlet is v_a = 2 m/s.

Figs I.13 and I.14 illustrate the drop trajectories, colour mapped to show drop temperature; contour plots of air dry-bulb temperature, humidity ratio, static pressure and absolute air speed; and air flow pathlines, colour mapped to show absolute drop speed, for a counterflow natural draught wet-cooling tower with isotropic fill resistance and a rounded and square inlet respectively. The mean cooling ranges, ΔT_w, and sum of the inlet and rain zone loss coefficients referred to fill conditions, $(K_{ci} + K_{rz})_{fi}$, are presented in Tables I.5 and I.6 for the rounded and square inlet respectively. The *FLUENT*® loss coefficients are determined from the numerical data using the following form of the energy equation:

$$\left(K_{ct}+K_{rz}\right)_{fi} \approx \frac{p_a\text{-}\left(p+\alpha_e\rho_a v_{am}^2/2\right)_{vc} - \int_0^{H_{vc}} \rho_a g \mathrm{d}z}{\left(\rho_a v_{am}^2/2\right)_{fi}} - K_{fi} \qquad \text{(I.11)}$$

The Eqs (I.3) to (I.6) of De Villiers (1998), are solved using the Merkel method of analysis similar to the solution of natural draught wet-cooling tower performance presented in Appendix K.

From the results in Table I.5, it can be seen that the cooling range and loss coefficient data differs measurably from the *FLUENT*® values. An interesting observation is that the inlet loss correction factor, C_{rz}, of De Villiers increases with a decrease in drop size in the rain zone. This loss coefficient, which accounts for the damping effect of the rain zone on the inlet loss coefficient and differences between the modelled inlet and rain zone loss coefficients and the empirical relations of De Villiers used to predict the inlet loss coefficient based on actual experimental data, is intuitively expected to become smaller due to the higher rain zone flow resistance. This notion is confirmed by the *FLUENT*® results, which show a much smaller increase in $(K_{ci}+K_{rz})_{fi}$ than De Villiers (2001) for a decrease in drop diameter, suggesting a reduction in C_{rz}.

Table I.5 : Cross-counterflow rain zone cooling range and loss coefficient data for the typical and enhanced drop distributions in a counterflow NDWCT with a rounded inlet.

Drop distribution	Cooling range		Inlet and rain zone loss coefficient				
	FLUENT®	De Villiers (1998)	*FLUENT*®	De Villiers (2001)			
	ΔT_w	ΔT_w	$K_{ctfi}+K_{rzfi}$	K_{ctfi}	C_{rz}	K_{rzfi}	$K_{ctfi}+K_{rzfi}$
No rain zone	-	-	4.1	6.0	-	-	6.0
Typical	3.29 (0%)	3.06 (-7.0%)	12.8 (0%)	3.8	0.64	10.0	13.9 (7.9%)
Enhanced	5.92 (0%)	6.06 (2.4%)	14.5 (0%)	5.0	0.85	12.3	17.3 (19.3%)

Table I.6 : Cross-counterflow rain zone cooling range and loss coefficient data for the typical and enhanced drop distributions in a counterflow NDWCT with a square inlet.

Drop distribution	Cooling range		Inlet and rain zone loss coefficient				
	FLUENT®	De Villiers (1998)	*FLUENT*®	De Villiers (2001)			
	ΔT_w	ΔT_w	$K_{ctfi}+K_{rzfi}$	K_{ctfi}	C_{rz}	K_{rzfi}	$K_{ctfi}+K_{rzfi}$
No rain zone	-	-	8.4	9.6	-	-	9.6
Typical	3.34 (0%)	3.05 (-8.7%)	17.3 (0%)	6.1	0.63	10.3	16.4 (-5.5%)
Enhanced	6.09 (0%)	6.04 (-1.0%)	17.4 (0%)	8.0	0.85	12.6	20.6 (18.3%)

I.3 SUMMARY OF RESULTS

Two-dimensional *FLUENT*® models are developed for purely counterflow and crossflow wet-cooling tower rain zones and cross-counterflow rain zones encountered in counterflow natural draught wet-cooling towers, using *FLUENT*®. The *FLUENT*® models are validated using the single drop numerical models developed in Appendices B and C, and for the counterflow and cross-counterflow rain zones, the cooling range and loss coefficient results are compared with data obtained by solving the semi-empirical model of De Villiers (1998) using the Merkel method of analysis. Two different drop distributions are investigated which are determined experimentally, where the "typical drop" distribution has a Sauter mean drop diameter of d_{32} = 5.137 mm and the "enhanced" drop distribution has a drop size of d_{32} = 2.836 mm.

The results are summarized as follows:

- ⇨ A comparison between the monodisperse *FLUENT*® results without momentum, mass and energy transfer between drops and the airstream, show that the differences to the numerical single drop model of Appendices B and C are minor.
- ⇨ The *FLUENT*® results determined for monodisperse (Sauter mean diameter), polydisperse and Rosin-Rammler drop size distributions, using the time independent DPM model and including momentum, mass and energy transfer exchange between drops and the airstream, shows that the differences are relatively small, with the largest deviations observed for the loss coefficient of the monodisperse enhanced distributions and the cooling range of the Rosin-Rammler distribution, which are above 10%.
- ⇨ Differences between using the time dependent and time independent DPM models are negligible.
- ⇨ Differences between using the drag model of Dreyer (1994) and the dynamic drag model of *FLUENT*®, both including the effects of drop deformation on the drag coefficient, are relatively small. The *FLUENT*® drag model predicts lower absolute drop speeds and does not yield the expected constant terminal speed for drops of diameter d > 5mm as correctly predicted by the Dreyer (1994) model, but the effect is small.
- ⇨ Using the *FLUENT*® drop collision and breakup models, it is observed that the effect on the water and air-side temperatures is small. The effect on the loss coefficient is negligible for the typical distribution, but significant for the enhanced distribution. As expected, a change in drop size distribution is observed between the rain zone inlet and outlet as expected, which would otherwise remain constant for no collisions. Checking the results using the average Sauter mean diameter and monodisperse *FLUENT*® model, reveals that the *FLUENT*® collision model over-predicts cooling and significantly under-predicts the loss coefficient. Furthermore, it is found that mass is not conserved in the discrete phase and the collision model is therefore deemed to be unreliable.
- ⇨ The effect of the stochastic tracking model was found to be negligible, ascribed to large drops and large void fractions.

- ⇨ A cross flow rain zone with the same air-side flow power consumption as an equivalent counterflow rain zone, reveals that the cooling is slightly less for the crossflow rain zone but that the loss coefficient of the counterflow rain zone is 25 and 36 time greater than that of a cross flow rain zone for the typical and enhanced drop distributions respectively. The reason for these large differences is that in the case of the counterflow rain zone, the total drop drag force acts in the direction of the air flow, resulting in dissipation of flow work, whereas in the crossflow rain zone the drag force acting in the direction of airflow is only a small component of the total drag force. A further interesting observation is that the crossflow loss coefficient decreases with drop diameter as opposed to an increase in counterflow loss coefficient, explaining the reason for the differences in the above numbers.
- ⇨ For the cross-counterflow rain zone, a comparison between the *FLUENT*® results and the solution of Eq. (I.3) to (I.6) reveals significant deviations. An interesting observation is that the inlet loss correction factor, C_{rz}, of De Villiers increases with a decrease in drop size in the rain zone, whereas the *FLUENT*® results suggest that it should decrease. Considering the increased damping effect on the inlet loss coefficient resulting from the higher flow resistance of the enhanced drop distribution, one would expect this coefficient to decrease as per the *FLUENT*® results.

I.4 CONCLUSIONS AND RECOMMENDATIONS

The deviations between *FLUENT*® and empirical data for cooling tower rain zones are found to be relatively small, considering the uncertainties in the experimental data and the numerical models.

From the results, the following can be concluded:

- ⇨ *FLUENT*® is an excellent tool to model cooling tower rain zones.
- ⇨ Monodisperse drop distributions based on the Sauter mean drop diameter give representative results for corresponding polydisperse drop distributions, as found by Pierce (2007).
- ⇨ The differences between the polydisperse drop distribution results and the Rosin-Rammler distribution results suggest that the Rosin-Rammler distribution should be avoided, as stated in Terblanche et al. (2009).
- ⇨ Results obtained for the *FLUENT*® dynamic drag model compare favourably with results using the Dreyer (1994) deformed drop drag model.
- ⇨ The *FLUENT*® drop collision model gives inconsistent results with regard to cooling performance, pressure drop and conservation of mass for the conditions investigated. The effect of drop collisions on the average Sauter mean drop diameter should be investigated further.
- ⇨ Similar cooling performance can be obtained in a crossflow rain zone as a counterflow rain zone for the same flow power consumption, ascribed to the higher air speeds in the crossflow rain zone which compensates for the lower drop residence time.

⇨ The rain zone performance model of De Villiers (1998) for cross-counterflow rain zones gives conservative loss coefficients compared to *FLUENT*® especially for the enhanced drop distribution. Similar trends are observed for the counterflow models, which suggest differences between the CFD models. A grid independence analysis done with *FLUENT*® showed that a grid size of at least 0.1 x 0.1 m is required and the integration time step should be sufficiently small to resolve the DPM model. The grid used by De Villiers for the cross-counterflow rain zone is about 0.5 x 0.5 m over most of the rain zone. Furthermore, De Villiers employs the standard k-ε turbulence model whereas the *FLUENT*® model uses the k-ε realizable model, which could also have an effect.

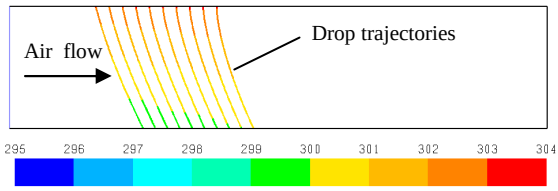

(a_1) Drop trajectory showing temperature in K for the typical drop distribution.

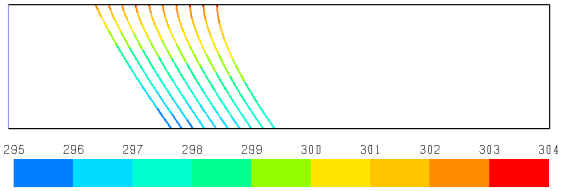

(a_2) Drop trajectory showing temperature in K for the enhanced drop distribution.

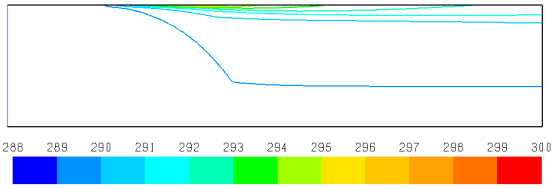

(b_1) Air temperature in K for the typical drop distribution.

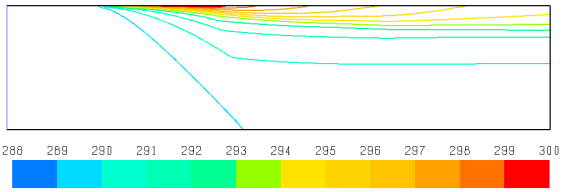

(b_2) Air temperature in K for the enhanced drop distribution.

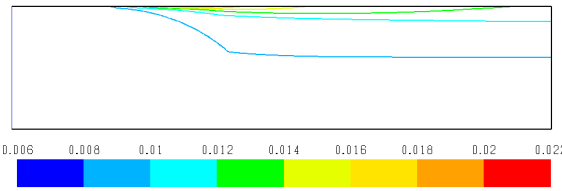

(c_1) Humidity ratio in kg/kg d.a. for the typical drop distribution.

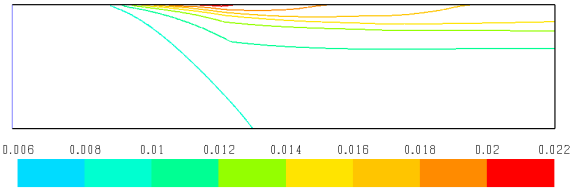

(c_2) Humidity ratio in kg/kg d.a. for the enhanced drop distribution.

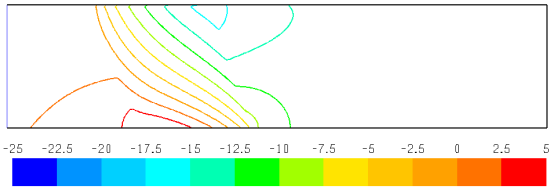

(d_1) Static pressure in N/m^2 for the typical drop distribution.

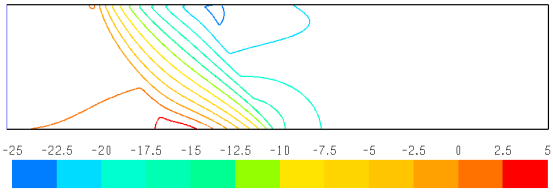

(d_2) Static pressure in N/m^2 for the enhanced drop distribution.

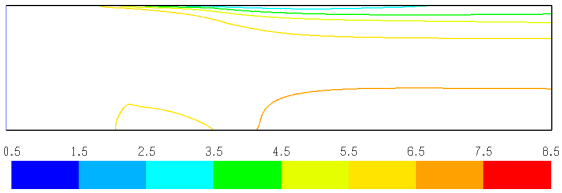

(e_1) Air speed in m/s for the typical drop distribution.

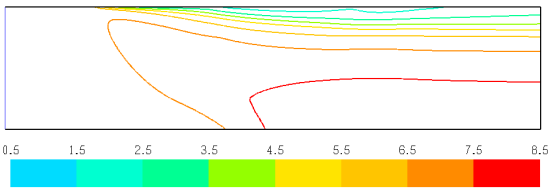

(e_2) Air speed in m/s for the enhanced drop distribution.

Figure I.10 : Contour plots for monodisperse crossflow rain zones with typical and enhanced drop distributions for the steady DPM model and the drag model of Dreyer (1994).

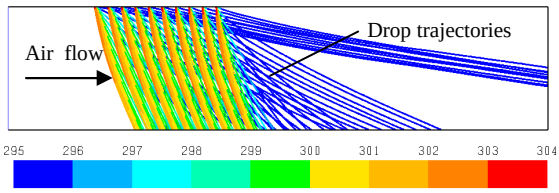

(a_1) Drop trajectory showing temperature in K for the typical drop distribution.

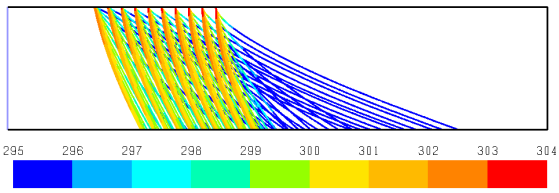

(a_2) Drop trajectory showing temperature in K for the enhanced drop distribution.

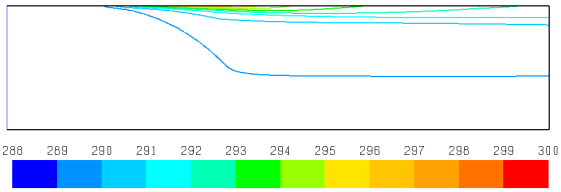

(b_1) Air temperature in K for the typical drop distribution.

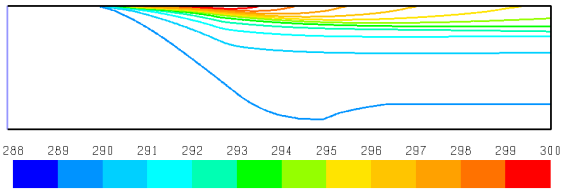

(b_2) Air temperature in K for the enhanced drop distribution.

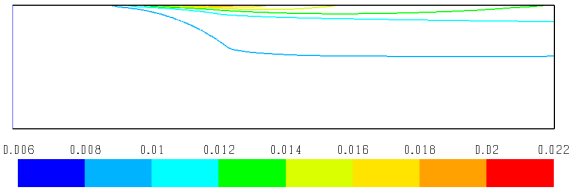

(c_1) Humidity ratio in kg/kg d.a. for the typical drop distribution.

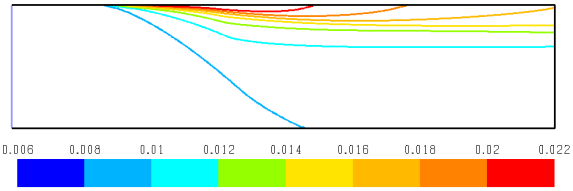

(c_2) Humidity ratio in kg/kg d.a. for the enhanced drop distribution.

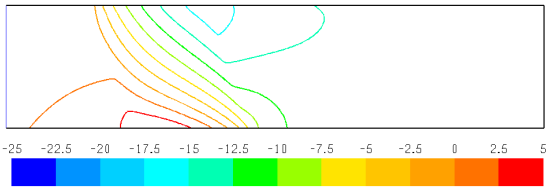

(d_1) Static pressure in N/m^2 for the typical drop distribution.

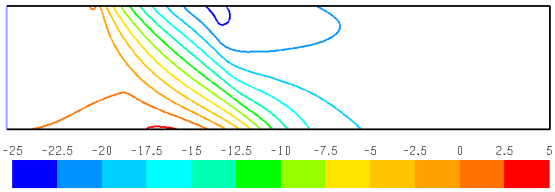

(d_2) Static pressure in N/m^2 for the enhanced drop distribution.

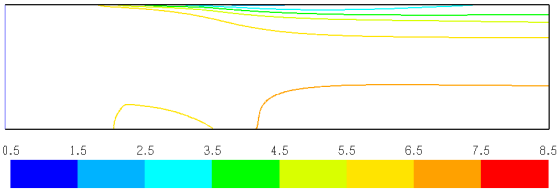

(e_1) Air speed in m/s for the typical drop distribution.

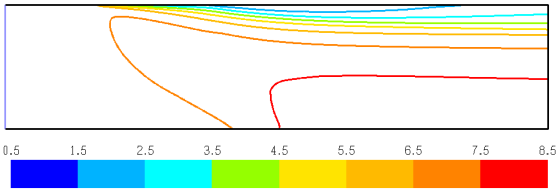

(e_2) Air speed in m/s for the enhanced drop distribution.

Figure I.11 : Contour plots for polydisperse crossflow rain zones with typical and enhanced drop distributions for the steady DPM model and the drag model of Dreyer (1994).

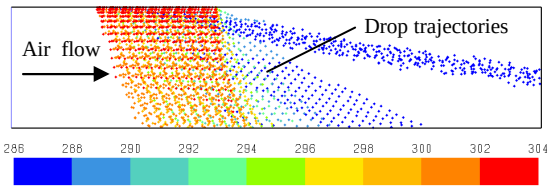

(a_1) Drop trajectory showing temperature in K for the typical drop distribution.

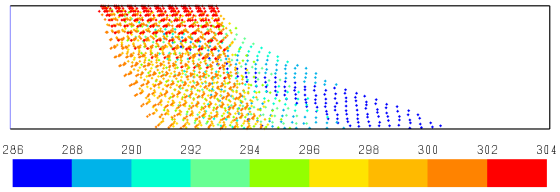

(a_2) Drop trajectory showing temperature in K for the enhanced drop distribution.

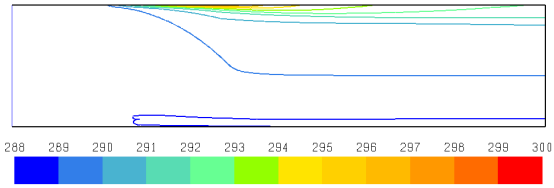

(b_1) Air temperature in K for the typical drop distributin.

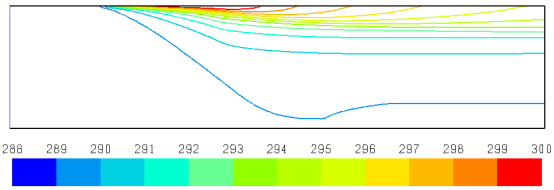

(b_2) Air temperature in K for the enhanced drop distribution.

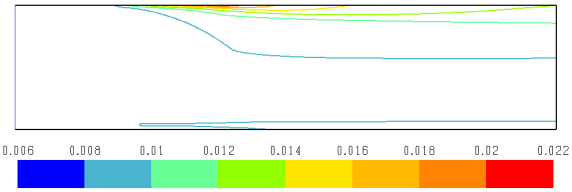

(c_1) Humidity ratio in kg/kg d.a. for the typical drop distribution.

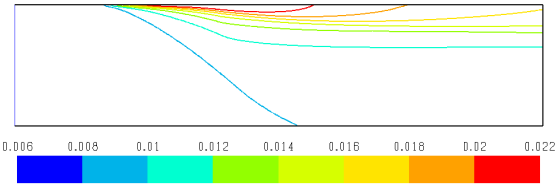

(c_2) Humidity ratio in kg/kg d.a. for the enhanced drop distribution.

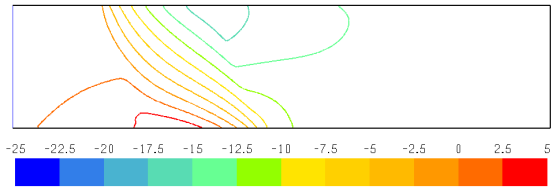

(d_1) Static pressure in N/m^2 for the typical drop distribution.

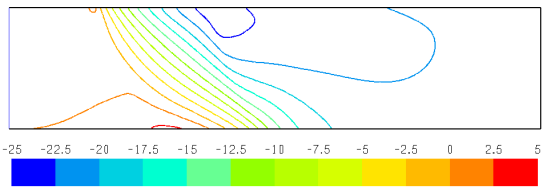

(d_2) Static pressure in N/m^2 for the enhanced drop distribution.

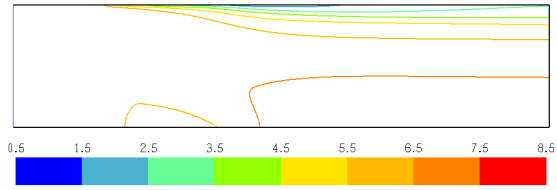

(e_1) Air speed in m/s for the typical drop distribution.

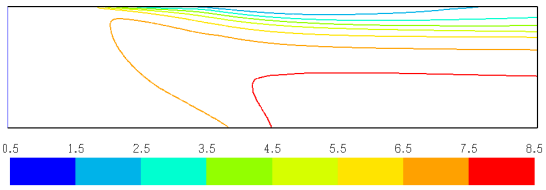

(e_2) Air speed in m/s for the enhanced drop distribution.

Figure I.12 : Contour plots for polydisperse crossflow rain zones with typical and enhanced drop distributions for the unsteady DPM model and the dynamic drag model of *FLUENT*®.

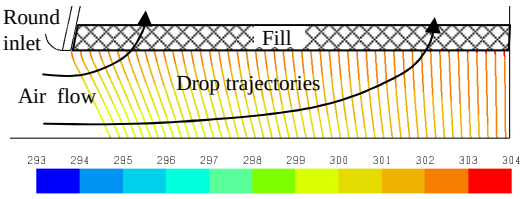

(a_1) Drop trajectory showing temperature in K for the typical drop distribution.

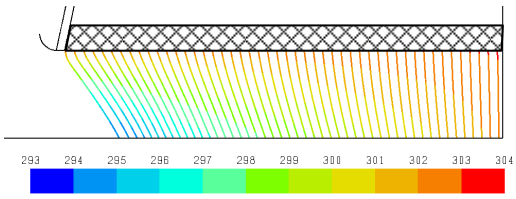

(a_2) Drop trajectory showing temperature in K for the enhanced drop distribution.

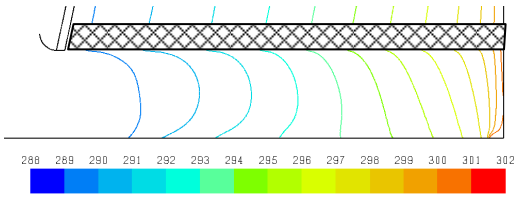

(b_1) Air temperature in K for the typical drop distribution.

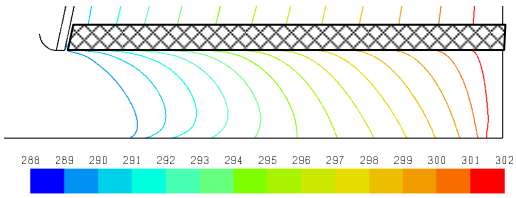

(b_2) Air temperature in K for the enhanced drop distribution.

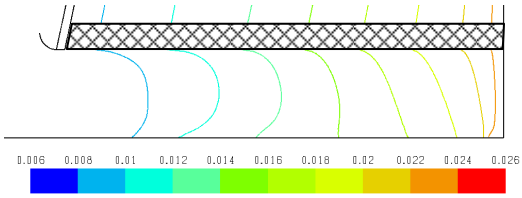

(c_1) Humidity ratio in kg/kg d.a. for the typical drop distribution.

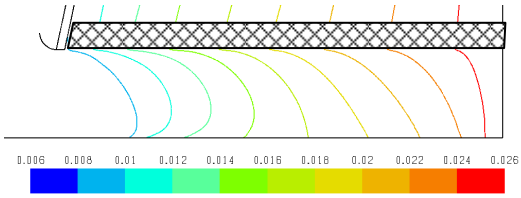

(c_2) Humidity ratio in kg/kg d.a. for the enhanced drop distribution.

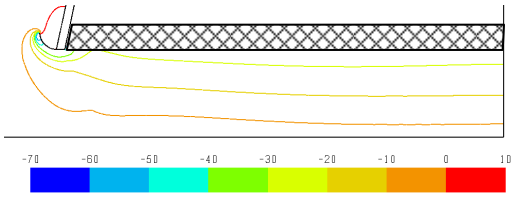

(d_1) Static pressure in N/m^2 for the typical drop distribution.

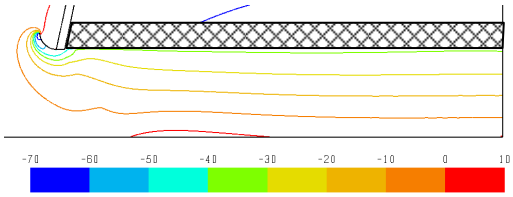

(d_2) Static pressure in N/m^2 for the enhanced drop distribution.

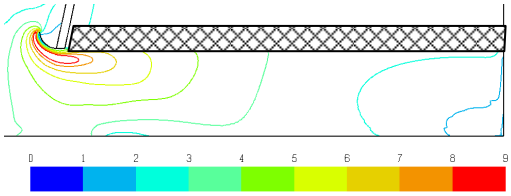

(e_1) Air speed in m/s for the typical drop distribution.

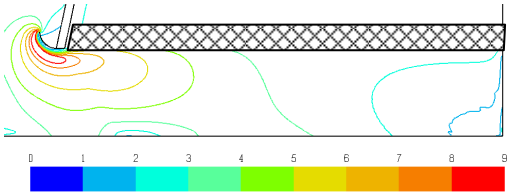

(e_2) Air speed in m/s for the enhanced drop distribution.

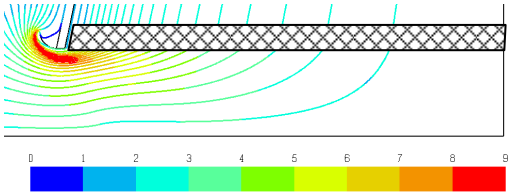

(e_1) Pathlines showing air speed in m/s for the typical drop distribution.

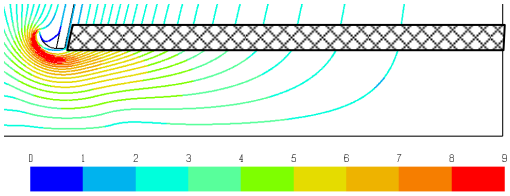

(f_2) Pathlines showing air speed in m/s for the enhanced drop distribution.

Figure I.13 : Contour plots for monodisperse cross-counterflow rain zones with rounded inlets and typical and enhanced drop distributions for the steady DPM model and the drag model of Dreyer (1994).

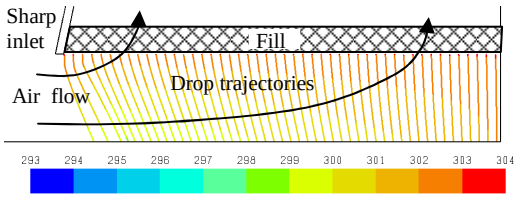

(a_1) Drop trajectory showing temperature in K for the typical drop distribution.

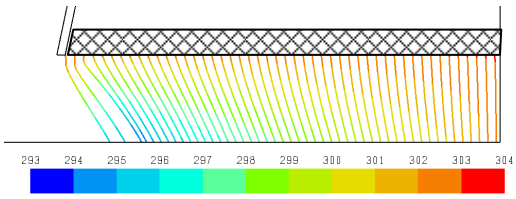

(a_2) Drop trajectory showing temperature in K for the enhanced drop distribution.

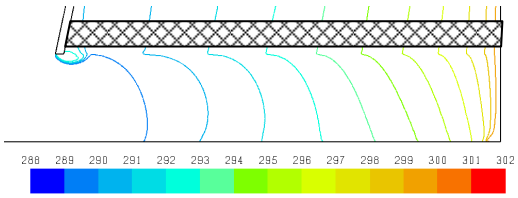

(b_1) Air temperature in K for the typical drop distribution.

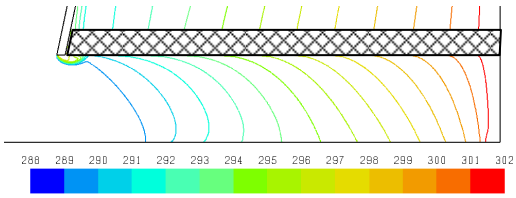

(b_2) Air temperature in K for the enhanced drop distribution.

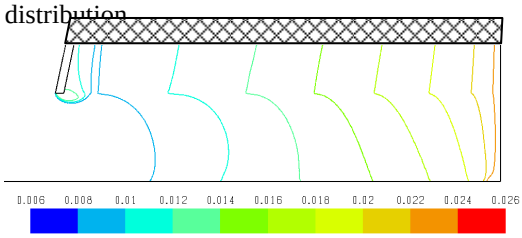

(c_1) H al drop distribution.

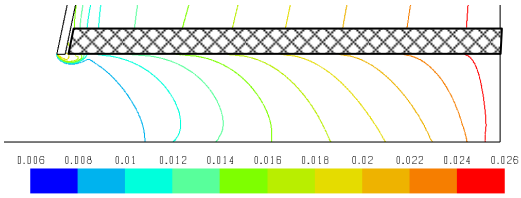

(c_2) Humidity ratio in kg/kg d.a. for the enhanced drop distribution.

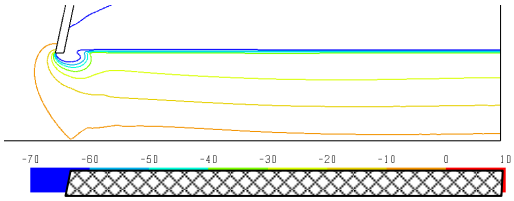

(d_1) Static pressure in N/m^2 for the typical drop distribution.

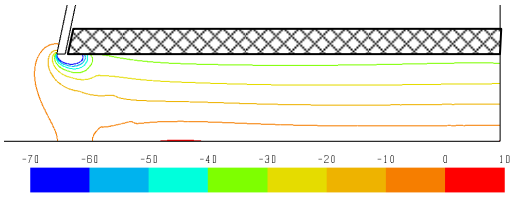

(d_2) Static pressure in N/m^2 for the enhanced drop distribution.

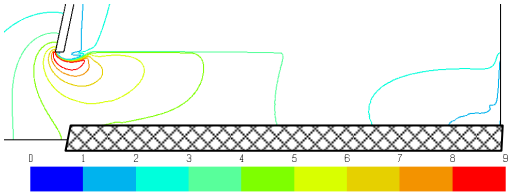

(e_1) Air speed in m/s for the typical drop distribution.

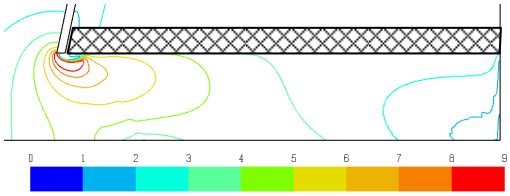

(e_2) Air speed in m/s for the enhanced drop distribution.

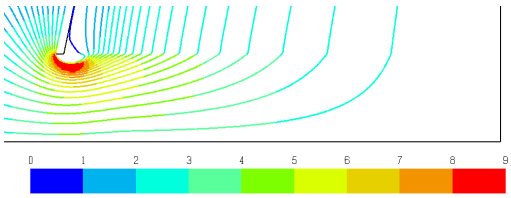

(e_1) Pathlines showing air speed in m/s for the typical drop distribution.

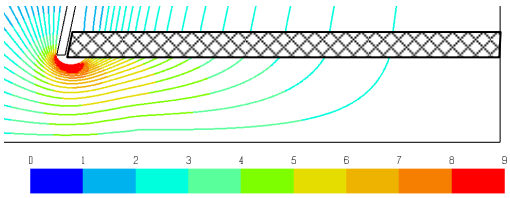

(f_2) Pathlines showing air speed in m/s for the enhanced drop distribution.

Figure I.14 : Contour plots for monodisperse cross-counterflow rain zones with square inlets and typical and enhanced drop distributions for the steady DPM model and the drag model of Dreyer (1994).

J

HEAT AND MASS TRANSFER IN CROSS-COUNTERFLOW FILLS

J.1 INTRODUCTION

In counter- and crossflow cooling towers with isotropic or anisotropic fill resistance, where the fill is porous in all flow directions such as trickle and splash fills, and is sometimes installed to hang down into the rain zone, the air flow through the fill is oblique or in cross-counterflow to the water flow, particularly at the cooling tower inlet and when the fill loss coefficient is small. The fill Merkel number for cross-counter flow will therefore be between that of purely counter- and crossflow fills.

Kloppers [2005(2)] presents a critical analysis for counterflow fill models based on the Merkel (1925), Poppe (Poppe and Rögener, 1991) and e-NTU (Jaber and Webb, 1989) methods of analysis and proposes a fundamental crossflow model based on the Poppe method. Williamson [2008(1), 2008(2), 2008(3)], and Klimanek, (2008, 2009, 2010) developed one-dimensional counterflow film fill models based on the Poppe method of analysis, to simulate natural draught wet-cooling tower performance using *FLUENT*®, where Williamson used the Multiphase Mixture Model and Klimanek the Multiphase Euler-Euler Model.

When using CFD to model natural draught wet-cooling tower performance for isotropic fill resistance, two- or three-dimensional models are however required to determine fill performance. The main objectives of this appendix are therefore to develop a two-dimensional Eulerian fill performance model for *FLUENT*® and to verify the results.

In the following sections, the governing fundamental partial differential equations are derived to determine the cooling water temperature, water evaporation rate, air temperature and air humidity ratio in two-dimensional cross-counterflow fills for saturated and supersaturated air. The equations are presented in cylindrical co-ordinates for circular (axisymmetric) cooling towers and Cartesian co-ordinates for rectangular cooling towers. To solve these equations, cross-counterflow transfer characteristics or Merkel numbers are required which cannot be measured in existing fill test facilities. A relation is therefore proposed to determine Merkel numbers for oblique air flows by linear interpolation and extrapolation of purely cross- and counterflow Merkel numbers in terms of the air flow angle. The model is compared to analytical Merkel numbers obtained for different air flow angles using the single drop model of Appendix C.

A computational model and an Eulerian *FLUENT*® model that employs a user defined function (UDF) routine to calculate the heat and mass transfer, are developed to model fill performance. For the computational model, the

differential equations are discretized according to the linear upwind method to calculate the required values of the independent variables at discrete nodes on a computational grid. Discretized equations are presented for a two-dimensional grid applicable to rectangular cooling towers. For the Eulerian *FLUENT*® model, a UDF is developed to calculate the water temperature, the energy source term and the vapour species mass source term for each cell of a computational grid, from local air velocity, air temperature and vapour mass fraction data. The calculated source terms are transferred to the respective cells and utilised by the *FLUENT*® solver to solve the global flow field. The results of the two numerical models are compared and verified with the aid of an Euler-Lagrange *FLUENT*® model.

J.2 GOVERNING EQUATIONS FOR HEAT AND MASS TRANSFER IN THE FILL OF A CIRCULAR COOLING TOWER FOR UNSATURATED AIR

Consider the circular ring in Fig. J.1 representing an elementary control volume in the fill region of an axisymmetric circular wet-cooling tower. A vertical section through this control volume is presented in Fig. J.2, which is used to illustrate the parameters required for the derivation of the governing equations in this section.

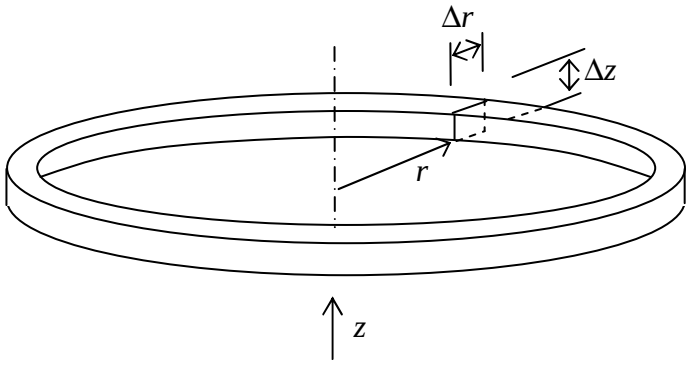

Figure J.1: Circular ring elementary control volume in an axi-symmetrical circular cooling tower.

A dry air mass balance for the above control volume yields,

$$\left(G_{a,r+\Delta r}-G_{a,r}\right)2\pi r\Delta z+\left(G_{a,z+\Delta z}-G_{a,z}\right)2\pi r\Delta r+G_{a,r+\Delta r}\,2\pi\Delta r\Delta z=0 \qquad \text{(J.1)}$$

Divide Eq. (J.1) by $2\pi r\Delta r\Delta z$,

$$\frac{\left(G_{a,r+\Delta r}-G_{a,r}\right)}{\Delta r}+\frac{\left(G_{a,z+\Delta z}-G_{a,z}\right)}{\Delta z}+\frac{G_{a,r+\Delta r}}{r}=0 \qquad \text{(J.2)}$$

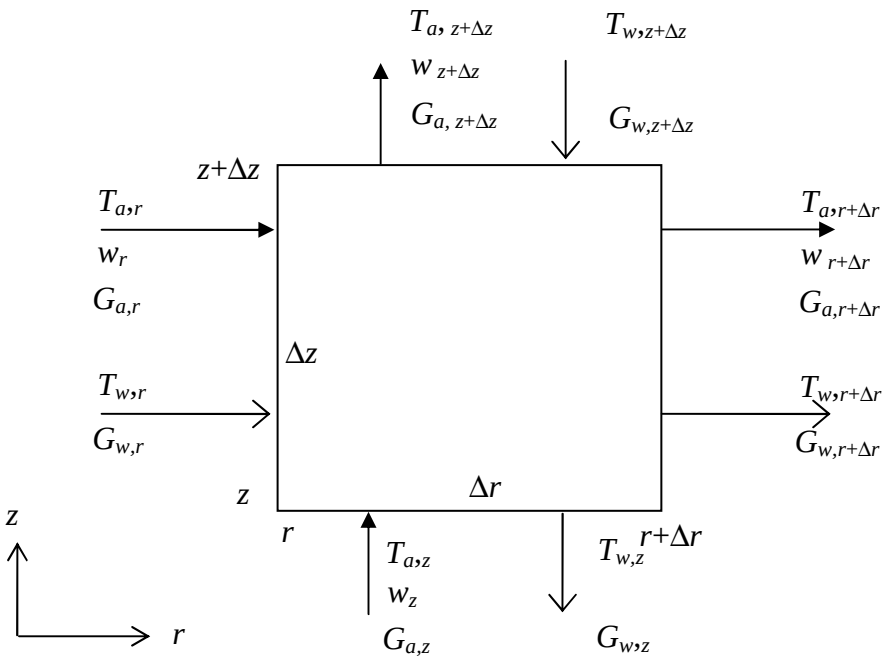

Figure J.2: Vertical section through the elementary control volume of a cross-counterflow fill region in a circular cooling tower.

and let Δr, $\Delta z \to 0$ to obtain,

$$\frac{\partial G_{a,z}}{\partial z}+\frac{\partial G_{a,r}}{\partial r}+\frac{G_{a,r}}{r}=0 \tag{J.3}$$

Assume that the radial water mass velocity is $G_{w,r}$ = 0 kg/s m^2 since the water flow in a fill is essentially vertically downwards and the horizontal momentum transfer to the water by the air flow is unknown. This could possibly be determined experimentally, but would require a detailed investigation of each type of fill to be modelled, which is not in the scope of this thesis.

A water mass balance for the control volume in Fig. J.2 can therefore be written as

$$\begin{aligned}&\left(G_{w,z+\Delta z}-G_{w,z}\right)2\pi r\Delta r\\&=\left(G_{a,r+\Delta r}w_{r+\Delta r}-G_{a,r}w_r\right)2\pi r\Delta z+\left(G_{a,z+\Delta z}w_{z+\Delta z}-G_{a,z}w_z\right)2\pi r\Delta r\\&\quad+G_{a,r+\Delta r}w_{r+\Delta r}2\pi\Delta r\Delta z\end{aligned} \tag{J.4}$$

Divide Eq. (J.4) by $2\pi r\Delta r\Delta z$ to obtain

$$\begin{aligned}\frac{\left(G_{w,z+\Delta z}-G_{w,z}\right)}{\Delta z}&=\frac{\left(G_{a,r+\Delta r}w_{r+\Delta r}-G_{a,r}w_r\right)}{\Delta r}+\frac{\left(G_{a,z+\Delta z}w_{z+\Delta z}-G_{a,z}w_z\right)}{\Delta z}\\&\quad+\frac{G_{a,r+\Delta r}w_{r+\Delta r}}{r}\end{aligned} \tag{J.5}$$

Let Δr, $\Delta z \rightarrow 0$, differentiate and substitute Eq. (J.3) to obtain the following differential equation:

$$\frac{\partial G_w}{\partial z} = G_{a,r}\frac{\partial w}{\partial r} + G_{a,z}\frac{\partial w}{\partial z} \tag{J.6}$$

From the definition of mass transfer rate used by Merkel (1925), the evaporation rate can also be expressed as

$$\frac{\partial G_w}{\partial z} = h_d a_{fi}\left(w_{sw} - w\right) \tag{J.7}$$

where the $h_d a_{fi}$ is determined from the empirical Merkel number relation proposed in Section J.4.

The heat and mass transfer from the water at the air/water interface, inside the control volume, is expressed in terms of heat and mass transfer coefficients as

$$\begin{aligned} &c_{pw}\left(T_{w,z+\Delta z}G_{w,z+\Delta z} - T_{w,z}G_{w,z}\right)2\pi r\Delta r \\ &= ha_{fi}\left(T_w - T_a\right)2\pi r\Delta r\Delta z + i_{v(T_w)}h_d a_{fi}\left(w_{sw} - w\right)2\pi r\Delta r\Delta z \end{aligned} \tag{J.8}$$

Divide by $2\pi r\Delta r\Delta z$,

$$c_{pw}\frac{\left(G_{w,z+\Delta z}T_{w,z+\Delta z} - G_{w,z}T_{w,z}\right)}{\Delta z} = ha_{fi}\left(T_w - T_a\right) + i_{v(T_w)}h_d a_{fi}\left(w_{sw} - w\right) \tag{J.9}$$

Let Δr, $\Delta z \rightarrow 0$ and apply the chain rule of differentiation to obtain,

$$\begin{aligned} &c_{pw}\frac{\partial\left(G_w T_w\right)}{\partial z} = c_{pw}\left(G_w\frac{\partial T_w}{\partial z} + T_w\frac{\partial G_w}{\partial z}\right) \\ &= ha_{fi}\left(T_w - T_a\right) + i_{v(T_w)}h_d a_{fi}\left(w_{sw} - w\right) \end{aligned} \tag{J.10}$$

From Eqs (J.7) and (J.10), it follows that the differential equation for water temperature is expressed as

$$\frac{\partial T_w}{\partial z} = \frac{c_{pma}}{c_{pw}}\frac{h_d a_{fi}}{G_w}\left[Le_f\left(T_w - T_a\right) + \frac{i_{fg(T_w)}}{c_{pma}}\left(w_{sw} - w\right)\right] \tag{J.11}$$

where $Le_f = h/c_{pma}h_d$ is the Lewis factor which can be determined according to the relation of Bosnjakovic (1965) given by Eq. (J.12), or can be assumed to be $Le_f = 1$ as done by Merkel (1925), depending on the method applied to determine the fill characteristics. The fill transfer characteristic, $h_d a_{fi}/G_w$, is determined from the empirical Merkel number (*Me*) relation proposed in Section J.4.

$$Le_f = \frac{h}{h_d\, c_{pma}}$$
$$= \left(\frac{k_{av}(1+w)}{\rho_{av} c_p D}\right)^{1-n} \left(\frac{v_a}{v_{av}}\right)^{m-n} \left(\frac{w_{sw}+0.622}{w+0.622}-1\right) / ln\left(\frac{w_{sw}+0.622}{w+0.622}\right) \tag{J.12}$$

To determine the change in air temperature in the fill zone, consider the sensible heat and mass transfer to the air, which can be expressed as

$$\begin{aligned} &G_{a,r}\, i_{ma,r}\, 2\pi r\Delta z + G_{a,z}\, i_{ma,z}\, 2\pi r\Delta r \\ &-G_{a,r+\Delta r}\, i_{ma,r+\Delta r}\, 2\pi (r+\Delta r)\Delta z - G_{a,z+\Delta z}\, i_{ma,z+\Delta z}\, 2\pi r\Delta r \\ &= -\left[ha_{fi}\left(T_w - T_a\right) + i_{v(T_w)} h_d a_{fi}\left(w_{sw} - w\right)\right] 2\pi r\Delta r\Delta z \end{aligned} \tag{J.13}$$

Divide Eq. (J.13) by $2\pi r \Delta r \Delta z$, to yield

$$\begin{aligned} &\frac{G_{a,r+\Delta r}\, i_{ma,r+\Delta r} - G_{a,r}\, i_{ma,r}}{\Delta r} + \frac{G_{a,z+\Delta z}\, i_{ma,z+\Delta z} - G_{a,z}\, i_{ma,z}}{\Delta z} + \frac{G_{a,r+\Delta r}\, i_{ma,r+\Delta r}}{r} \\ &= ha_{fi}\left(T_w - T_a\right) + i_{v(T_w)} h_d a_{fi}\left(w_{sw} - w\right) \end{aligned} \tag{J.14}$$

Let Δr, $\Delta z \rightarrow 0$, differentiate and substitute Eq. (J.3), to find that

$$G_{a,r}\frac{\partial i_{ma}}{\partial r} + G_{a,z}\frac{\partial i_{ma}}{\partial z} = ha_{fi}\left(T_w - T_a\right) + i_{v(T_w)} h_d a_{fi}\left(w_{sw} - w\right) \tag{J.15}$$

Substitute Eq. (A.3.6b) for air enthalpy in terms of air temperature and humidity ratio and differentiate. Then substitute Eqs (J.3), (J.6), (J.7) and the definition of Lewis factor given in Eq. (J.12) and re-arrange, to obtain the following partial differential equation for the air temperature:

$$G_{a,r}\frac{\partial T_a}{\partial r} + G_{a,z}\frac{\partial T_a}{\partial z} = h_d a_{fi}\left(T_w - T_a\right)\left[Le_f + \frac{c_{pv}}{c_{pma}}\left(w_{sw} - w\right)\right] \tag{J.16}$$

The differential equation for air humidity ratio is determined by substituting Eq. (J.7) into Eq. (J.6) as follows:

$$G_{a,r}\frac{\partial w}{\partial r} + G_{a,z}\frac{\partial w}{\partial z} = h_d a_{fi}\left(w_{sw} - w\right) \tag{J.17}$$

To solve the above governing equations for a given type of fill, the boundary values for water temperature, air temperature and air humidity ratio are required for each inlet boundary cell, as prescribed from experimental data or obtained from CFD data. The air mass velocity vector must also be known for each cell, also either specified or obtained from CFD data. Finally, the fill transfer characteristic or Merkel number needs to be determined using the method proposed in Section J.4.

J.3 GOVERNING EQUATIONS FOR HEAT AND MASS TRANSFER IN THE FILL OF A CIRCULAR COOLING TOWER FOR SUPERSATURATED AIR

Again consider the circular ring in Fig. J.1 and vertical section through this control volume as presented in Fig. J.2. By following the same derivation procedure as in Section J.2, however now assuming that the air is supersaturated, a dry air mass balance for the control volume in Fig. J.2 given the same equation as Eq. (J.3). A water mass balance however yields the following differential equation:

$$\frac{\partial G_w}{\partial z} = G_{a,r}\frac{\partial w_s}{\partial r} + G_{a,z}\frac{\partial w_s}{\partial z} + G_{a,r}\frac{\partial (w - w_s)}{\partial r} + G_{a,z}\frac{\partial (w - w_s)}{\partial z} \tag{J.18}$$

where the first two terms on the right hand side represent the amount of water vapour taken up by the air and the last two terms represent the mist that condenses out of the airstream.

For supersaturated air, Eq. (J.7) becomes

$$\frac{\partial G_w}{\partial z} = h_d a_{fi} (w_{sw} - w_s) \tag{J.19}$$

and Eq. (J.11) becomes

$$\frac{\partial T_w}{\partial z} = \frac{c_{pma}}{c_{pw}}\frac{h_d a_{fi}}{G_w}\left[Le_f (T_w - T_a) + \frac{i_{fg(T_w)}}{c_{pma}}(w_{sw} - w_s) \right] \tag{J.20}$$

The Lewis factor for supersaturated air is expressed as

$$\begin{aligned} Le_f &= \frac{h}{h_d\, c_{pma}} \\ &= \left(\frac{k_{av}(1+w_s)}{\rho_{av} c_p D} \right)^{1-n} \left(\frac{v_a}{v_{av}} \right)^{m-n} \left(\frac{w_{sw}+0.622}{w_s+0.622} - 1 \right) / ln\left(\frac{w_{sw}+0.622}{w_s+0.622} \right) \end{aligned} \tag{J.21}$$

Consider the enthalpy of supersaturated air to be

$$i_{ma,ss} = c_{pa}T_a + w_{sa}\left(i_{fgwo} + c_{pv}T_a\right) + (w - w_{sa})c_{pw}T_a \tag{J.22}$$

Substitute Eq. (J.22) into Eq. (J.15) and carry out the same operations as for Eq. (J.16) to yield

$$G_{a,r}\frac{\partial T_a}{\partial r}+G_{a,z}\frac{\partial T_a}{\partial z}$$
$$=h_d a_{fi} Le_f\left(T_w-T_a\right)\frac{c_{pma,s}}{c_{pma,ss}}+\left[\frac{i_{fg(T_w)}+c_{pw}\left(T_w-T_a\right)}{c_{pma,ss}}\right]h_d a_{fi}\left(w_{sw}-w_s\right) \quad \text{(J.23)}$$
$$-\frac{i_{fg(T_a)}}{c_{pma,ss}}\left(G_{a,r}\frac{\partial w_s}{\partial r}+G_{a,z}\frac{\partial w_s}{\partial z}\right)$$

where

$$c_{pma,ss}=c_{pa}+w_s c_{pv}+\left(w-w_s\right)c_{pw}=c_{pma,s}+\left(w-w_{sa}\right)c_{pw} \quad \text{(J.24)}$$

and w_s is a function of T_a.

Eq. (J.17) is expressed as

$$G_{a,r}\frac{\partial w}{\partial r}+G_{a,z}\frac{\partial w}{\partial z}=h_d a_{fi}\left(w_{sw}-w_s\right) \quad \text{(J.25)}$$

After confirming that the air is supersaturated, by comparing the cell humidity ratio to that of saturated air at the cell dry bulb temperature, a similar procedure, as described in Section J.2, is followed to solve Eqs (J.18) to (J.25).

J.4 GOVERNING EQUATIONS FOR HEAT AND MASS TRANSFER IN THE FILL OF A RECTANGULAR COOLING TOWER FOR UNSATURATED AIR

Consider the control volume in the fill region of a rectangular wet-cooling tower, as presented in Fig. J.3.

By following the same method as discussed in Section J.2, a dry air mass balance for the control volume in Fig. J.3 gives

$$\frac{\partial G_{a,z}}{\partial z}+\frac{\partial G_{a,x}}{\partial x}=0 \quad \text{(J.26)}$$

The other governing equations are similar to those of circular axi-symmetric cooling towers, where the only difference is that the radial co-ordinate, *r*, is replaced with the Cartesian co-ordinate, *x*.

Eq. (J.6) therefore becomes

$$\frac{\partial G_w}{\partial z}=G_{a,x}\frac{\partial w}{\partial x}+G_{a,z}\frac{\partial w}{\partial z} \quad \text{(J.27)}$$

and Eq. (J.11) remains unchanged,

$$\frac{\partial T_w}{\partial z}=\frac{c_{pma}}{c_{pw}}\frac{h_d a_{fi}}{G_w}\left[Le_f\left(T_w-T_a\right)+\frac{i_{fg(T_w)}}{c_{pma}}\left(w_{sw}-w\right)\right] \quad \text{(J.28)}$$

Eq. (J.16) becomes

$$G_{a,x}\frac{\partial T_a}{\partial x}+G_{a,z}\frac{\partial T_a}{\partial z}=h_d a_{fi}\left(T_w-T_a\right)\left[Le_f+\frac{c_{pv}}{c_{pma}}\left(w_{sw}-w\right)\right] \tag{J.29}$$

and Eq. (J.17) is written as follows:

$$G_{a,x}\frac{\partial w}{\partial x}+G_{a,z}\frac{\partial w}{\partial z}=h_d a_{fi}\left(w_{sw}-w\right) \tag{J.30}$$

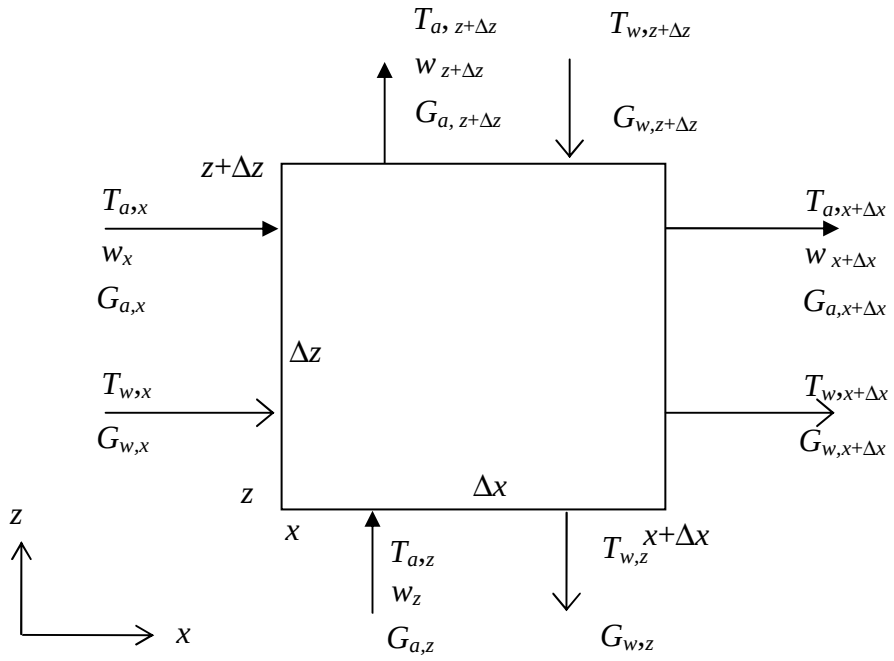

Figure J.3: Control volume of a cross-counterflow fill region in a rectangular cooling tower per unit width.

J.5 GOVERNING EQUATIONS FOR HEAT AND MASS TRANSFER IN THE FILL OF A RECTANGULAR COOLING TOWER FOR SUPERSATURATED AIR

Again consider the elementary control volume presented in Fig. J.3. By following the same derivation procedure as above, however now assuming that the air is supersaturated, a dry air mass balance gives the same equation as Eq. (J.26) but a water mass balance yields

$$\frac{\partial G_w}{\partial z}=G_{a,x}\frac{\partial w_s}{\partial x}+G_{a,z}\frac{\partial w_s}{\partial z}+G_{a,x}\frac{\partial\left(w-w_s\right)}{\partial x}+G_{a,z}\frac{\partial\left(w-w_s\right)}{\partial z} \tag{J.31}$$

Eq. (J.28) becomes

$$\frac{\partial T_w}{\partial z} = \frac{c_{pma}}{c_{pw}} \frac{h_d a_{fi}}{G_w} \left[Le_f \left(T_w - T_a \right) + \frac{i_{fg(T_w)}}{c_{pma}} \left(w_{sw} - w_s \right) \right] \tag{J.32}$$

Eq. (J.29) becomes

$$\begin{aligned} & G_{a,x} \frac{\partial T_a}{\partial x} + G_{a,z} \frac{\partial T_a}{\partial z} \\ & = h_d a_{fi} Le_f \left(T_w - T_a \right) \frac{c_{pma,s}}{c_{pma,ss}} + \left[\frac{i_{fg(T_w)} + c_{pw} \left(T_w - T_a \right)}{c_{pma,ss}} \right] h_d a_{fi} \left(w_{sw} - w_s \right) \\ & - \frac{i_{fg(T_a)}}{c_{pma,ss}} \left(G_{a,x} \frac{\partial w_s}{\partial x} + G_{a,z} \frac{\partial w_s}{\partial z} \right) \end{aligned} \tag{J.33}$$

and Eq. (J.30) is written as

$$G_{a,x} \frac{\partial w}{\partial x} + G_{a,z} \frac{\partial w}{\partial z} = h_d a_{fi} \left(w_{sw} - w_s \right) \tag{J.34}$$

J.6 MERKEL NUMBER FOR CROSS-COUNTERFLOW FILLS

The remaining unknown for solving the above governing equations for circular and rectangular wet-cooling towers, is the fill transfer characteristic or Merkel number, defined as

$$Me = \frac{h_d a_{fi} L_{fi}}{G_w} \tag{J.35}$$

The Merkel number is obtained from fill performance test data measured in a fill test facility and is generally expressed as a function of G_w, G_a, T_{wi} and L_{fi}. Due to practical and economic reasons, these tests are performed in purely counter- and crossflow configuration only, where the counterflow Merkel number will differ from corresponding crossflow data for a particular fill. These differences are mainly due to variations in the fill geometry along the air flow paths, as well as the longer residence time of the water in counterflow due to the additional vertical drag on the drops, which has the effect of increasing the interfacial surface area in trickle and splash fills. The differences between cross- and counterflow Merkel numbers are however generally found to be relatively small for splash and trickle fills.

To find a suitable Merkel number for fills with oblique air flow, it is therefore proposed to interpolate between available cross- and counterflow Merkel numbers based on absolute air speed, using the following equation:

$$Me = \frac{h_d a_{fi} \Delta z}{G_w} = \left\{ \left(\frac{Me}{L_{fi}} \right)_{counter} + \left[\left(\frac{Me}{L_{fi}} \right)_{cross} - \left(\frac{Me}{L_{fi}} \right)_{counter} \right] \left(\frac{90^o - \varphi}{90^o} \right) \right\} \Delta z \tag{J.36}$$

where the air flow angle, φ, is the flow angle to the horizontal.

J.6 SOLVING THE SYSTEM OF PARTIAL DIFFERENTIAL EQUATIONS

The above differential equations are solved numerically by means of a computational model and ultimately by an Eulerian *FLUENT*® model that employs a user defined function (UDF) routine to calculate the heat and mass transfer. For both these models, consider Fig. J.4 showing a computational grid for a cross-counterflow fill, which is divided evenly into three intervals or cells in the vertical and horizontal directions for illustration.

J.6.1 Computational model

For the computational model, the above differential equations are discretized according to the first order upwind method to calculate the dependent variables at discrete nodes on a computational grid.

To illustrate this method, consider the property, ϕ, at the central node *P* in cell (i,j), which is also referred to as $\phi_{P(i,j)}$, as shown in cell (2,2) of Fig. J.4. The cell (*i*,*j*) is connected to four adjacent cells, of which the interfaces are depicted as *n* (north), *s* (south), *e* (east) and *w* (west). The central nodes of the adjacent cells are written as: *N*(*i*,*j*) or (*i*+1,*j*); *S*(*i*,*j*) or (*i*-1,*j*); *E*(*i*,*j*) or (*i*,*j*+1); and *W*(*i*,*j*) or (*i*,*j*-1) for the northern, southern, eastern and western cells respectively.

The derivatives of $\phi_{P(i,j)}$ with respect to *r* and *z* are discretized in terms of the interfacial nodal values by making use of a first order Taylor series, written as

$$\left.\frac{\partial\phi}{\partial r}\right|_{P(i,j)} \approx \frac{\phi_{e(i,j)} - \phi_{w(i,j)}}{\Delta r} \tag{J.37}$$

$$\left.\frac{\partial\phi}{\partial z}\right|_{P(i,j)} \approx \frac{\phi_{n(i,j)} - \phi_{s(i,j)}}{\Delta z} \tag{J.38}$$

The values of ϕ at the cell faces can be determined by linear extrapolation and/ or interpolation of central node data, as follows:

$$\phi_{w(i,j)} = \frac{\left(\phi_{W(i,j)} + \phi_{P(i,j)}\right)}{2} = \frac{\left(\phi_{(i,j-1)} + \phi_{(i,j)}\right)}{2} \tag{J.39}$$

$$\phi_{e(i,j)} = \phi_{P(i,j)} + \frac{\left(\phi_{P(i,j)} - \phi_{W(i,j)}\right)}{2} = \phi_{(i,j)} + \frac{\left(\phi_{(i,j)} - \phi_{(i,j-1)}\right)}{2} \tag{J.40}$$

$$\phi_{s(i,j)} = \frac{\left(\phi_{S(i,j)} + \phi_{P(i,j)}\right)}{2} = \frac{\left(\phi_{(i-1,j)} + \phi_{(i,j)}\right)}{2} \tag{J.41}$$

$$\phi_{n(i,j)} = \phi_{P(i,j)} + \frac{\left(\phi_{P(i,j)} - \phi_{S(i,j)}\right)}{2} = \phi_{(i,j)} + \frac{\left(\phi_{(i,j)} - \phi_{(i-1,j)}\right)}{2} \tag{J.42}$$

These equations are substituted into Eqs (J.37) and (J.38) to obtain discretized relations for the partial derivatives in terms of nodal values at the cell centres.

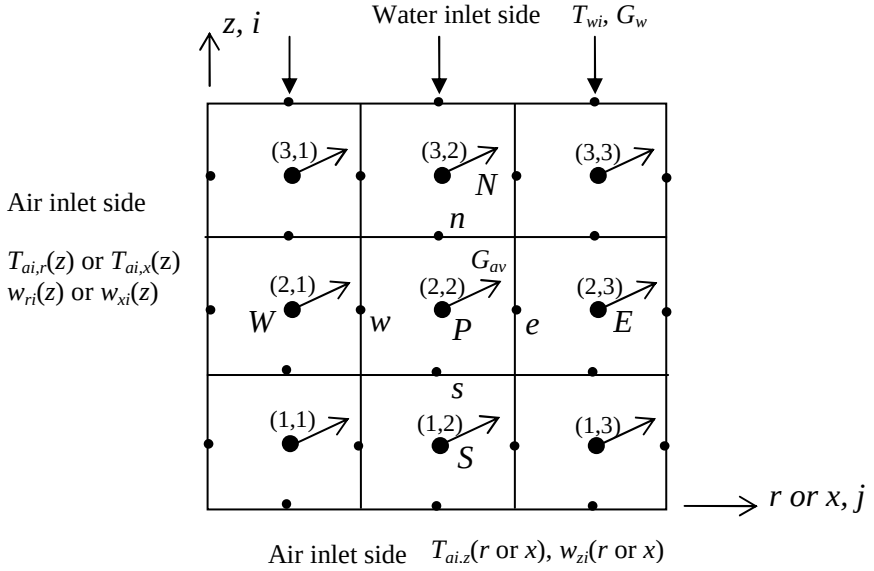

Figure J.4: Example of a cross-counterflow fill that is divided into three intervals in each direction.

To illustrate the discretization of the above governing equations we consider Eqs (J.7), (J.28), (J.29) and (J.30) in Cartesian co-ordinates, applicable to rectangular cooling towers. These equations are selected as they are used for evaluating cross- and counterflow fill performance data as well as for comparison with *FLUENT*® results.

$$G_{w(i,j)} = \frac{G_{w(i-1,j)}}{\left[1 - Me\left(w_{sw} - w\right)\Delta z\right]_{(i,j)}} \tag{J.43}$$

$$T_{w(i,j)} = T_{w(i-1,j)} + \left\{ \frac{c_{pma}}{c_{pw}} Me \left[Le_f \left(T_w - T_a\right) + \frac{i_{fg(T_w)}}{c_{pma}} \left(w_{sw} - w\right) \right] \right\}_{(i,j)} \tag{J.44}$$

$$T_{a(i,j)} = \frac{\left(G_{a,x(i,j)} \frac{\Delta z}{\Delta x} T_{a(i,j-1)} + G_{a,z(i,j)}\, T_{a(i-1,j)} \right)}{\left(G_{a,x(i,j)} \frac{\Delta z}{\Delta x} + G_{a,z(i,j)} \right)} + \frac{Me\, G_w \left(T_w - T_a\right)}{\left(G_{a,x(i,j)} \frac{\Delta z}{\Delta x} + G_{a,z(i,j)} \right)} \left[Le_f + \frac{c_{pv}}{c_{pma}} \left(w_{sw} - w\right) \right]_{(i,j)} \tag{J.45}$$

$$w_{(i,j)} = \frac{\left(G_{a,x(i,j)} \dfrac{\Delta z}{\Delta x} w_{(i,j-1)} + G_{a,z(i,j)} w_{(i-1,j)} \right)}{\left(G_{a,x(i,j)} \dfrac{\Delta z}{\Delta x} + G_{a,z(i,j)} \right)} + \frac{\left[G_w Me \left(w_{sw} - w \right) \right]_{(i,j)}}{\left(G_{a,x(i,j)} \dfrac{\Delta z}{\Delta x} + G_{a,z(i,j)} \right)} \tag{J.46}$$

where $\Delta x = L_x / n_x$ and $\Delta z = L_z / n_z$ with L_x and L_z the fill lengths and n_x and n_z the number of cells in the *x*- and *z*-directions respectively.

At the fill air inlet boundaries, the values of air temperature and air humidity ratio are known at the cell face nodes from specified or measured data. These values can therefore be substituted directly into Eqs (J.37) and (J.38).

At the fill boundaries, Eq. (J.29) can therefore be discretized as follows, assuming that the horizontal and vertical components of the air velocity vector are both positive:

Since cell (1,1) will have two boundary faces, the air temperature in this cell can be determined from

$$\begin{aligned} T_{a(1,1)} = & \frac{\left(G_{a,x(1,1)} \dfrac{\Delta z}{\Delta x} T_{aBC(1,1)} + G_{a,z(1,1)} T_{aBC(1,1)} \right)}{\left(G_{a,x(1,1)} \dfrac{\Delta z}{\Delta x} + G_{a,z(1,1)} \right)} \\ & + \frac{1}{2} \frac{Me\, G_w \left(T_w - T_a \right)}{\left(G_{a,x(1,1)} \dfrac{\Delta z}{\Delta x} + G_{a,z(1,1)} \right)} \left[Le_f + \frac{c_{pv}}{c_{pma}} \left(w_{sw} - w \right) \right]_{(1,1)} \end{aligned} \tag{J.47}$$

The air temperature in cells (1,*j*), in the bottom row, are determined from

$$\begin{aligned} T_{a(1,j)} = & \frac{\left(G_{a,x(1,j)} \dfrac{\Delta z}{\Delta x} T_{a(1,j-1)} + 2 G_{a,z(1,j)} T_{aBC(1,j)} \right)}{\left(G_{a,x(1,j)} \dfrac{\Delta z}{\Delta x} + 2 G_{a,z(1,j)} \right)} \\ & + \frac{Me\, G_w \left(T_w - T_a \right)}{\left(G_{a,x(1,j)} \dfrac{\Delta z}{\Delta x} + 2 G_{a,z(1,j)} \right)} \left[Le_f + \frac{c_{pv}}{c_{pma}} \left(w_{sw} - w \right) \right]_{(1,j)} \end{aligned} \tag{J.48}$$

and for the cells (i,1) in the first column, from

$$T_{a(i,1)} = \frac{\left(G_{a,x} \frac{2\Delta z}{\Delta x} T_{aBC(i,1)} + G_{a,z} T_{a(i-1,j)} \right) + \left[Le_f G_w Me \left(T_w - T_a \right) \right]_{(i,1)}}{\left(G_{a,x} \frac{2\Delta z}{\Delta x} + G_{a,z} \right)} + \frac{Me\, G_w \left(T_w - T_a \right)}{\left(G_{a,x} \frac{2\Delta z}{\Delta x} + G_{a,z} \right)} \left[Le_f + \frac{c_{pv}}{c_{pma}} \left(w_{sw} - w \right) \right]_{(i,1)} \quad \text{(J.49)}$$

Similarly Eq. (J.30) can be discretized as follows to determine the cell centre node values of humidity ratio, w, in the boundary cells for the corner cell (1,1), cells in the bottom row (1,j) and cells in the first column (i,1) respectively:

$$w_{(1,1)} = \frac{\left(G_{a,x(1,1)} \frac{\Delta z}{\Delta x} w_{BC(1,1)} + G_{a,z(1,1)} w_{BC(1,1)} \right) + \left[G_w Me \left(w_{sw} - w \right) \right]_{(1,1)}}{\left(G_{a,x(1,1)} \frac{\Delta z}{\Delta x} + G_{a,z(1,1)} \right)} \quad \text{(J.50)}$$

$$w_{(1,j)} = \frac{\left(G_{a,x(1,j)} \frac{\Delta z}{\Delta x} w_{(1,j-1)} + 2 G_{a,z(1,j)} w_{BC(1,j)} \right) + \left[G_w Me \left(w_{sw} - w \right) \right]_{(1,j)}}{\left(G_{a,x(1,j)} \frac{\Delta z}{\Delta x} + 2 G_{a,z(1,j)} \right)} \quad \text{(J.51)}$$

$$w_{(i,1)} = \frac{\left(G_{a,x} \frac{2\Delta z}{\Delta x} w_{BC(i,1)} + G_{a,z} w_{(i-1,j)} \right) + \left[G_w Me \left(w_{sw} - w \right) \right]_{(i,1)}}{\left(G_{a,x} \frac{2\Delta z}{\Delta x} + G_{a,z} \right)} \quad \text{(J.52)}$$

If the air is supersaturated at a point in the fill, the governing equations for supersaturated air must be solved instead of the above equations for unsaturated air.

J.6.2 Eulerian *FLUENT*® model

FLUENT® solves the conservation equations for mass, momentum, energy and species mixing and the k-ε realizable turbulence model for the global flow field comprising a mixture of air and water vapour, by employing the double precision, two-dimensional, steady state, segregated solver and the SIMPLE algorithm for the pressure-velocity coupling. To maximize numerical accuracy, second order discretization is employed for all the governing equations. The heat and mass transfer between the water and the air, is determined by means of a user defined function (UDF), which allocates a reference number to each cell in the transfer zone and iteratively calculates the water temperature (Eq. J.53) and mass velocity (Eq. J.54) changes, as well as the air-side energy source term (Eq. J.55) and

vapour species mass source term (Eq. J.56) for each cell from local air velocity, air temperature and vapour mass fraction data, extracted from each cell by the UDF.

$$\Delta T_{w(i,j)} = \left\{ \frac{c_{pma}}{c_{pw}} Me \left[Le_f \left(T_w - T_a \right) + \frac{i_{fg(T_w)}}{c_{pma}} \left(w_{sw} - w \right) \right] \right\}_{(i,j)} \tag{J.53}$$

$$\Delta G_{w(i,j)} = \left\{ G_w Me \left(w_{sw} - w \right) \Delta z \right\}_{(i,j)} \tag{J.54}$$

$$S_q = \left\{ \frac{Me\, G_w \left(T_w - T_a \right)}{\Delta z} \left[Le_f c_{pma} + c_{pv} \left(w_{sw} - w \right) \right] \right\}_{(i,j)} \tag{J.55}$$

$$S_m = \left\{ \frac{G_w Me}{\Delta z} \left(w_{sw} - w \right) \right\}_{(i,j)} \tag{J.56}$$

The above user defined energy and vapour mass source terms appear in the energy and species transport equations solved by *FLUENT*®. These source terms are transferred from the UDF to the cells, to yield a change in air temperature and vapour species mass fraction in the global flow field. The water temperature and change in mass velocity due to evaporation data is obtained directly from the UDF.

J.7 MODEL VERIFICATION PROCEDURE

The computational and *FLUENT*® models developed in this appendix make use of purely counter- and crossflow fill Merkel numbers to predict cross-counterflow fill performance. To verify the model results, fill performance characteristics and data are required for all three flow configurations. Since existing fill test facilities are however designed for purely counter- and/ or crossflow testing, suitable experimental data is unavailable and thus an alternative method is required to obtain the data. It is shown in previous sections that *FLUENT*® can be used effectively to predict rain zone performance for any given flow configuration by making use of a monodisperse Lagrangian discrete phase model. It is also found that the Merkel numbers obtained from *FLUENT*® data using the Merkel method of analysis and the effectiveness-NTU method for counter- and crossflow respectively, are essentially the same as corresponding average Merkel numbers obtained using the single drop model of Appendix C.

A method is therefore proposed by which the performance characteristics and data are generated using a Lagrangian *FLUENT*® model with uniform heat and mass transfer coefficients, a rectangular transfer zone and unidirectional airflow. Uniform transfer coefficients are achieved by means of monodisperse drops falling at terminal speed. For a rain zone to be rectangular, the horizontal displacement of the drops due to drag must be insignificant. This is achieved by using low air speeds and large drops. From the single drop displacement model, presented in Appendix B, it is observed that the horizontal drop displacement for

drops of diameter d > 5 mm is effectively the same, because they have the same terminal speed. However, to maximize heat and mass transfer, the drops need to be small and thus a drop diameter of d = 5 mm is taken. For unidirectional airflow, the air flow direction is fixed in the present models, however for the Lagrangian *FLUENT*® model calculations, the air speed and direction are fixed in the x- and z-directions.

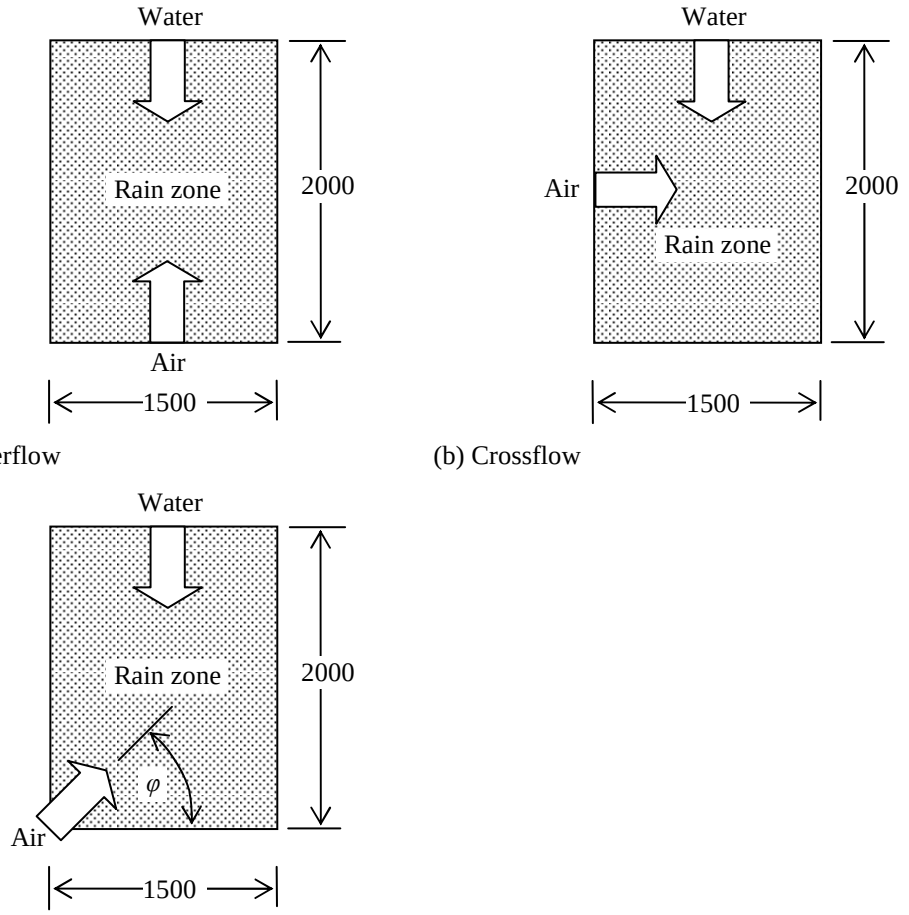

(a) Counterflow

(b) Crossflow

(c) Cross-counterflow

Figure J.5: Computational domain used to compare the different models.

To verify the computational and Eulerian *FLUENT*® models, referred to as the present models, the results are compared to data from an equivalent Lagrangian *FLUENT*® model, based on the dimensions of the counter- and crossflow test sections in the Stellenbosch University fill test facility, as depicted in Figure J.5. The following input values are used: an inlet water mass velocity of G_{wi} = 7 kg/sm^2, to obtain maximum heat and mass transfer while still producing unsaturated air outlet conditions; initial drop speeds of $v_{d0} = v_T$; a drop injection angle of θ = -90º to the horizontal; a monodisperse drop diameter of d = 5 mm; an absolute air speed of v_a = 1 m/s; different air flow angles (φ) to the horizontal; an atmospheric pressure of p_a = 101325 Pa; an ambient temperature of T_a = 288.15 K

(15 ºC); a relative humidity of ϕ = 60% and a water inlet temperature of T_{wi} = 313.15 K (40 ºC). Furthermore, the following reference models are used: the Dreyer (1994) relation for the drag coefficient of accelerating deformed drops (Eq. B.12); the Ranz and Marshall (1952) relations for the heat and mass transfer coefficients (Eqs C.12 and C.22); the Fuller (VDI-Wärmeatlas, 2006) relation for the diffusion coefficient (Eq. C.42); Eq. (C.5) for determining the rate of mass transfer; and the Lewis factor relation according to Bosnjakovic (1965) (Eq. C.33) to determine the relationship between the convective heat transfer and mass transfer coefficients.

The basic procedure to verify the present models is as follows:

- ⇨ Average counter-, cross-, and cross-counterflow Merkel numbers are determined using the single drop model of Appendix C, which are compared to Merkel numbers obtained using Eq. (J.36).
- ⇨ These Merkel numbers are applied in the present models to determine the water and air outlet temperatures and air outlet humidity ratio data, which are compared.
- ⇨ The present model results are compared to corresponding Lagrangian *FLUENT*® results.

J.8 COMPARISON OF RESULTS

The terminal drop speeds and Merkel numbers obtained from the single drop model of Appendix C for different air flow angles, ranging from counter- to co-currentflow (-90 ≤ φ ≤ 90 º), and the above input conditions, are presented in Table J.1. The results are compared to interpolated data from Eq. (J.36) and it can be seen that the maximum deviations between the exact and interpolated values (flow angles of 0 ≤ φ ≤ 90 º), is about δMe = 2 %. Similar results are observed for extrapolated Merkel numbers (flow angles of -90 ≤ φ < 0 º), applicable to regions of flow separation or recirculation as found at cooling tower inlets.

Table J.1 : Single drop terminal drop speeds and average Merkel numbers for different air flow angles.

Air flow angle	Terminal drop speed	Merkel number Single drop model (App. C)	Merkel number Eq. (J.14)	Merkel number deviation
Φ (º)	v_T (m/s)	Me (-)	Me (-)	δMe (%)
90	8.1	0.045494	0.045494	0
67.5	8.2	0.045089	0.044266	-1.8
45	8.4	0.043938	0.043038	-2.0
22.5	8.7	0.042330	0.041810	-1.2
0	9.1	0.040582	0.040582	0
-45	9.8	0.037608	0.038125	1.4
-90	10.1	0.036465	0.035669	-2.2

The *Me* values for positive air flow angles are applied in the present computational model to determine mean cooling range, dry bulb temperature change and humidity ratio change in the x- and z-directions, as presented in Table J.2 for a computational grid size of 0.0125 x 0.0125 m. Similar results are obtained and presented in Table J.3 for the present Eulerian *FLUENT*® model for a grid size of 0.1 x 0.1 m. The differences in grid size are ascribed to the second order discretization scheme used in *FLUENT*® as opposed to single order in the computational model, which results that grid independence is reached sooner in *FLUENT*®. In previous appendices, it is shown that for the global flow field in cooling towers, sufficient grid independence is achieved with grid sizes of 0.15 x 0.15 m. However to verify grid independence for two-dimensional heat and mass transfer, the results obtained with the present computational model for different grid sizes are presented in Table J.4, where it can be seen that sufficient grid independence is achieved with a grid size of 0.0125 x 0.0125 m.

Table J.2 : Present computational model results for different flow angles using analytical single drop Merkel numbers.

Air flow angle	Mean cooling range	Mean dry bulb temperature difference		Mean humidity ratio difference	
φ (º)	ΔT_{wm} (ºC)	$\Delta T_{am,z}$ (ºC)	$\Delta T_{am,x}$ (ºC)	$\Delta w_{am,z}$ (kg/kg da)	$\Delta w_{am,x}$ (kg/kg da)
90	1.18	5.64	N/A	0.009515	N/A
67.5	1.18	4.41	3.12	0.007426	0.005227
45	1.17	3.06	3.65	0.005159	0.006109
22.5	1.14	2.33	3.72	0.003937	0.006227
0	1.09	N/A	3.95	N/A	0.006637

Table J.3 : Present Eulerian *FLUENT*® model results for different flow angles using analytical single drop Merkel numbers.

Air flow angle	Mean cooling range	Mean dry bulb temperature difference		Mean humidity ratio difference	
φ (º)	ΔT_{wm} (ºC)	$\Delta T_{am,z}$ (ºC)	$\Delta T_{am,x}$ (ºC)	$\Delta w_{am,z}$ (kg/kg da)	$\Delta w_{am,x}$ (kg/kg da)
90	1.18	5.65	N/A	0.009511	N/A
45	1.17	3.03	3.64	0.005095	0.006090
0	1.09	N/A	3.99	N/A	0.006627

Table J.4 : Present computational model results for different grid sizes for a air flow angle of φ = 45 º.

Grid size	Mean cooling range	Mean dry bulb temperature difference		Mean humidity ratio difference		Energy balance
Δx and Δz (m)	ΔT_{wm} (ºC)	$\Delta T_{am,z}$ (ºC)	$\Delta T_{am,x}$ (ºC)	$\Delta w_{am,z}$ (kg/kg da)	$\Delta w_{am,x}$ (kg/kg da)	EB (%)
0.1	1.174	3.00	3.45	0.005790	0.005072	4.7
0.05	1.171	3.04	3.56	0.005957	0.005130	2.4
0.025	1.170	3.05	3.61	0.006055	0.005152	1.2
0.0125	1.170	3.06	3.65	0.006109	0.005159	0.5

Corresponding Lagrangian *FLUENT*® results are presented in Table J.5 for a grid size of 0.1 x 0.1 m, showing minor deviations compared to the present models. These differences can be attributed to grid size; small differences in the mean Merkel number; the numerical methods employed; the handling of thermophysical properties; the air speed that is kept constant in the *FLUENT*® model; and differences in the relationship between the heat and mass transfer coefficients.

Table J.5 : *FLUENT*® DPM data for comparison with the present model results.

Air flow angle	Mean cooling range	Mean dry bulb temperature difference		Mean humidity ratio difference	
φ (º)	ΔT_{wm} (ºC)	$\Delta T_{am,z}$ (ºC)	$\Delta T_{am,x}$ (ºC)	$\Delta w_{am,z}$ (kg/kg da)	$\Delta w_{am,x}$ (kg/kg da)
90	1.20	5.65	N/A	0.009537	N/A
45	1.19	3.01	3.65	0.005089	0.006118
0	1.11	N/A	3.93	N/A	0.006622

Cross-counterflow (φ = 45 º) contour plots for water temperature, air dry bulb temperature and humidity ratio are presented in Figs J.6 and J.7, showing good comparison between the present models and the Lagrangian *FLUENT*® model . The grid points on these graphs represent the cell centre node values of the computational grid.

J.9 SUMMARY OF RESULTS AND CONCLUSIONS

Two-dimensional computational and *FLUENT*® Eulerian models are developed to calculate fill performance in cross-counterflow or oblique airflow conditions using a newly proposed equation to determine cross-counterflow Merkel numbers by linear interpolation of purely cross- and counterflow Merkel numbers. A comparison between these models shows small deviations, attributed mainly to differences in grid size, numerical methods and discretization schemes employed. These models are verified by comparing the results obtained using average Merkel numbers for single drops (Appendix C), to Lagrangian *FLUENT*® results. The marginal differences between the *FLUENT*® Eulerian and *FLUENT*® Lagrangian models are attributed to small differences in the mean Merkel number; the numerical methods employed; the handling of thermophysical properties; the air speed that is kept constant in the *FLUENT*® DPM; and differences in the relationship between the heat and mass transfer coefficients.

In conclusion, the Eulerian *FLUENT*® model developed in this section provides an improved method to predict the performance of wet-cooling towers with isotropic fill resistance, where the air flow is oblique, which allows for better optimization of cooling tower performance.

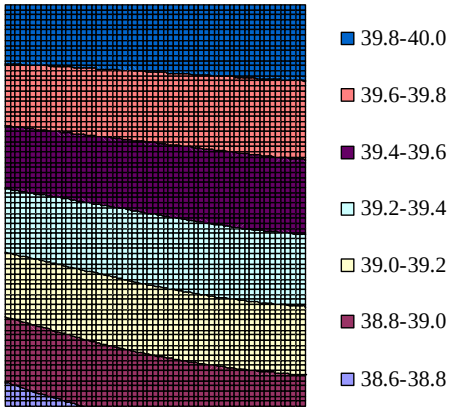

(a_1) Water temperature in ºC (present model).

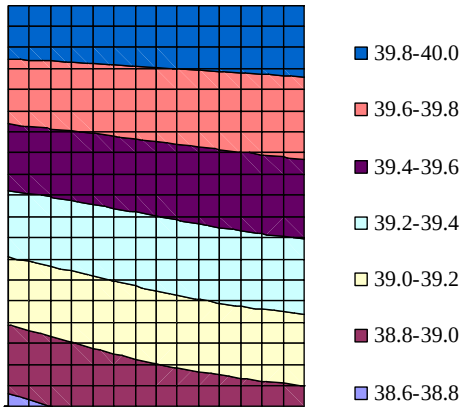

(a_2) Water temperature in ºC (*FLUENT*® Eulerian model).

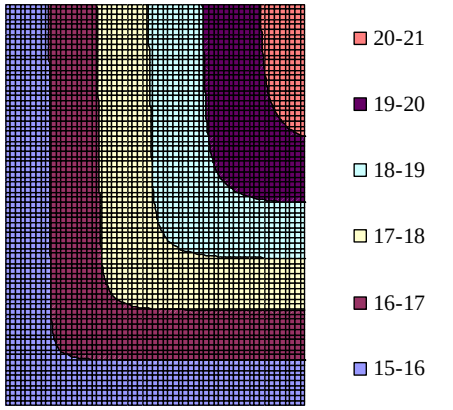

(b_1) Dry bulb temperature in ºC (present model).

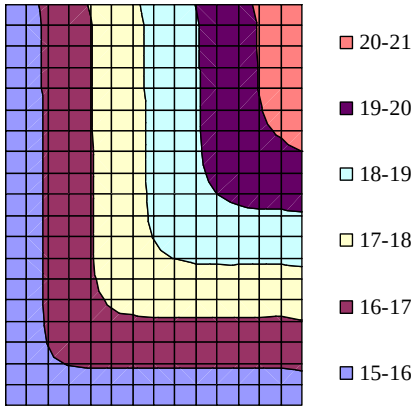

(b_2) Dry bulb temperature in ºC (*FLUENT*® Eulerian model).

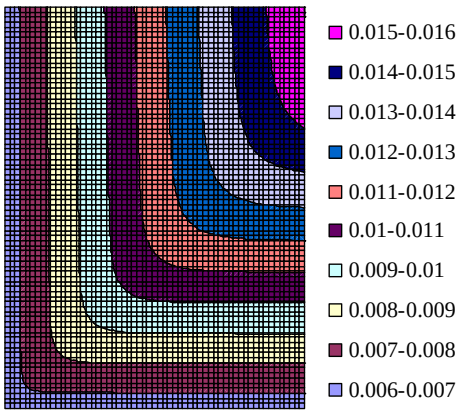

(c_1) Humidity ratio in kg/kg da (present model).

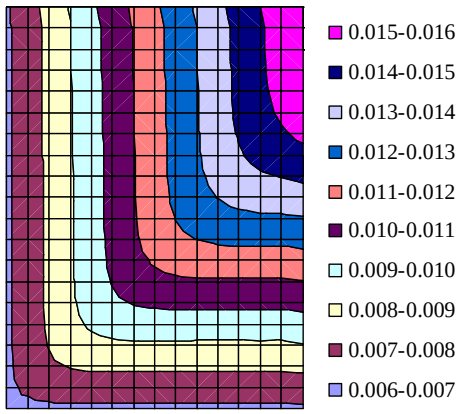

(c_2) Humidity ratio in kg/kg da (*FLUENT*® Eulerian model).

Figure J.6: Cross-counterflow contour plots for the present model and *FLUENT*® Eulerian model for the flow domain in Fig. J.6.

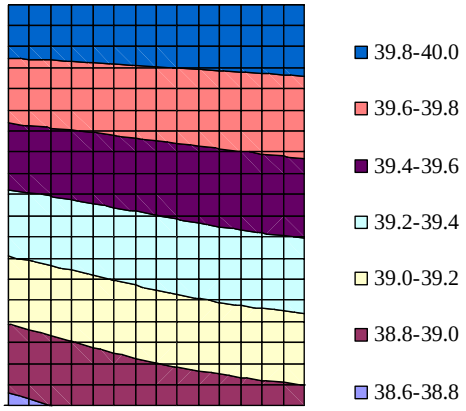

(a_1) Water temperature in ºC (*FLUENT*® Eulerian model).

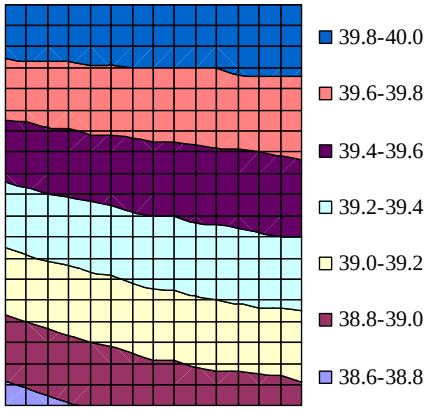

(a_2) Water temperature in ºC (*FLUENT*® Lagrangian model).

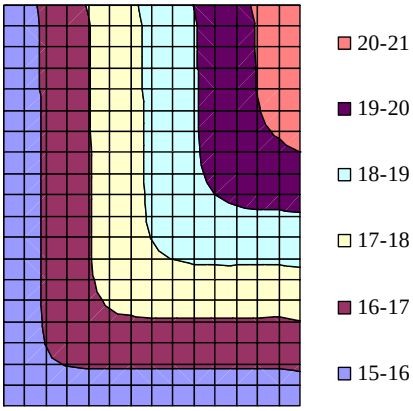

(b_1) Dry bulb temperature in ºC (*FLUENT*® Eulerian model).

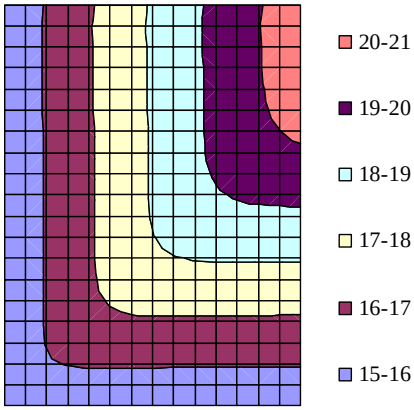

(b_2) Dry bulb temperature in ºC (*FLUENT*® Lagrangian model).

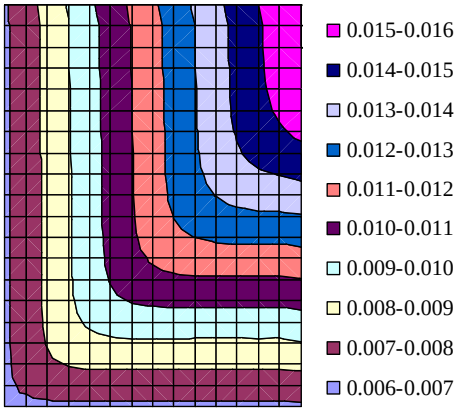

(c_1) Humidity ratio in kg/kg da (*FLUENT*® Eulerian model).

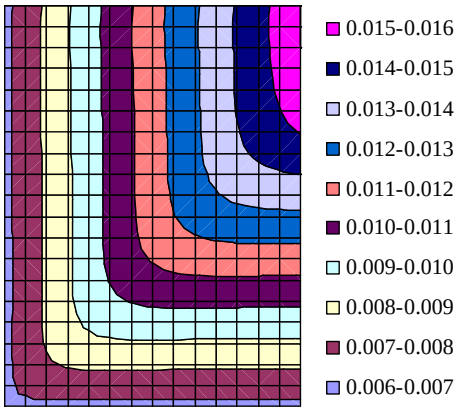

(c_2) Humidity ratio in kg/kg da (*FLUENT*® Lagrangian model).

Figure J.7: Cross-counterflow contour plots for the present model and *FLUENT*® DPM model for the flow domain in Fig. J.6.

K

PERFORMANCE EVALUATION OF A NATURAL DRAUGHT WET-COOLING TOWER EMPLOYING THE MERKEL METHOD OF ANALYSIS

The heat rejection rate and the cooling water evaporation loss in a hyperbolic natural draught counterflow wet-cooling tower, as shown in figure K.1, are determined by employing the Merkel method of analysis for determining the heat and mass transfer in the fill, following the example 7.3.2 in Kröger (2004). The results are used for verification of a one-dimensional code developed mainly for the validation of CFD models and for investigation of the effects of improvements to the theoretical models employed in this code on cooling tower performance. As the calculations are done using Mathcad 2001i Professional, the equations are given in the Mathcad format.

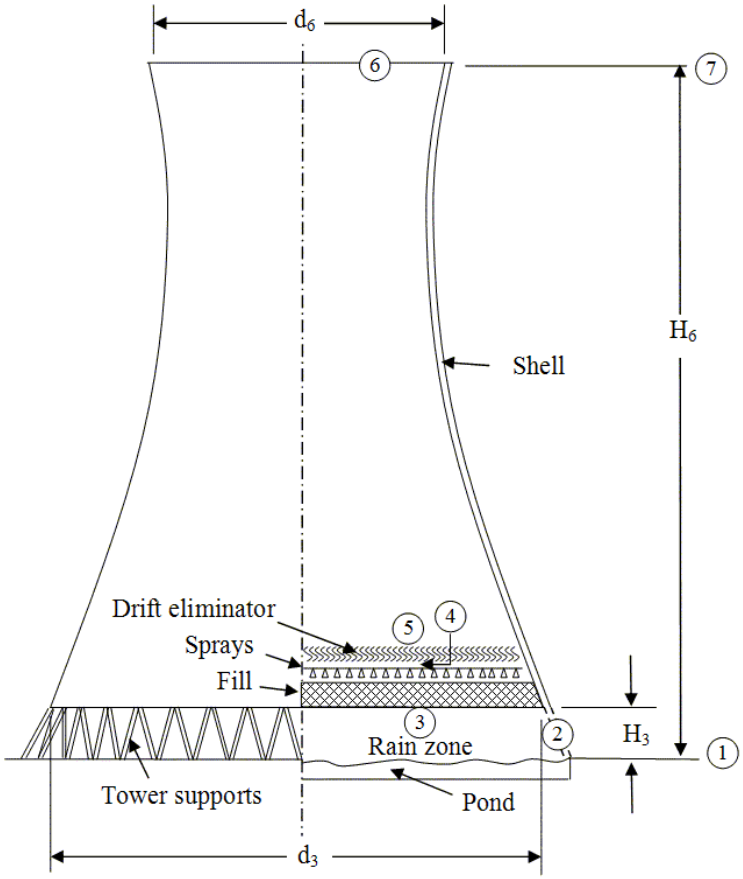

Figure K.1: Counterflow natural draught wet-cooling tower.

K.1 DESIGN DATA

K.1.1 Cooling tower dimensions

Tower height	$H_6 = 147$ m
Tower inlet height	$H_3 = 10$ m
Tower inlet diameter	$d_3 = 104.5$ m
Shell base cross-sectional area	$A_3 = \frac{\pi d_3^2}{4}$
	$A_3 = 8577$ m^2
Tower outlet diameter	$d_6 = 60.85$ m
Tower outlet cross-sectional area	$A_6 = \frac{\pi d_6^2}{4}$
	$A_6 = 2908$ m^2
Fill height	$L_{fi} = 2.504$ m
Spray zone height	$L_{sp} = 0.5$ m
Inlet rounding	$r_i = 0.02 \cdot d_3$ m
Number of tower supports	$n_{ts} = 72$
Length of tower supports	$L_{ts} = 11.6$ m
Diameter of tower supports	$d_{ts} = 0.8$ m
Drag coefficient of tower supports (round)	$C_{Dts} = 1.0$
Shell thickness (inlet)	$t_s = 1.0$ m

K.1.2 Ambient conditions

Atmospheric pressure at ground level	$p_{a1} = 84100$ Pa
Air temperature at ground level	$T_{a1} = 288.6$ K
	$T_{a1} - 273.15 = 15.45$ °C
Wetbulb temperature at ground level	$T_{awb1} = 284.2$ K
	$T_{awb1} - 273.15 = 11.05$ °C
Ambient temperature gradient from ground	$DALR = -0.00975$ K/m

K.1.3 Operating conditions

Inlet water temperature	$T_{wi} = 313.15$ K
	$T_{wi} - 273.15 = 40$ °C
Water massflow rate	$m_w = 12500$ kg/s

K.1.4 Performance characteristics

The cooling tower is fitted with an expanded metal fill for which the performance characteristics are:

Fill transfer coefficient

$$Me_{fi}(G_w, G_a) = 0.25575 \cdot L_{fi} \cdot G_w^{-0.094} \cdot G_a^{0.6023}$$

Fill loss coefficient

$$K_{fdm1}(G_w, G_a) = 1.851 \cdot L_{fi} \cdot G_w^{1.2752} \cdot G_a^{-1.0356}$$

Effective frontal area of the fill	$A_{fr} = 8300$ m^2
Mean drop diameter in the rain zone	$d_d = 0.0035$ m
Fill support system and contraction loss coefficient based on A_{fr}	$K_{fs} = 0.5$
Water distribution loss coefficient	$K_{wd} = 0.5$
Drift eliminator loss coefficient	$K_{de}(Ry) = 27.4892 \cdot Ry^{-0.14247}$
Kinetic energy coefficient at tower outlet	$\alpha_{e6} = 1.01$

K.2 SOLUTION

This problem can only be solved by following an iterative procedure to find a solution that will satisfy both the energy and draft equations. A converged solution is obtained when the chosen values for the variables below satisfy these equations.

K.2.1 Iteration parameters

Air-vapour mass flow rate through the fill	$m_{av15} = 16810.89$ kg/s
Air pressure after the drift eliminators	$p_{a5} = 83937.7$ Pa
Air temperature after the drift eliminators	$T_{a5} = 299.587$ K
Air pressure at the tower outlet	$p_{a6} = 82650.6$ Pa
Mean re-cooled water outlet temperature	$T_{wo} = 294.538$ K
	$T_{wo} - 273.15 = 21.389$ °C

K.2.2 Thermophysical properties

The thermophysical properties of the air at (1), employing the equations given in Appendix A, are as follows:

Specified inlet drybulb temperature	$T_{a1} = 288.6$ K
Specified air inlet wetbulb temperature	$T_{awb1} = 284.2$ K
Humidity ratio (equation A.3.5)	$w_1 = 0.008127$ kg/kg d.a.
Humidity ratio of saturated air at T_{wo} (equation A.3.5)	$w_{s1} = 0.019515$ kg/kg d.a.
Density (equation A.3.1)	$\rho_{av1} = 1.01012$ kg/m^3
Dynamic viscocity (equation A.3.3)	$\mu_{av1} = 1.7857 \times 10^{-5}$ Pa.s
Enthalpy (equation A.3.6b)	$i_{ma1} = 36114.7$ J/kg
Specific heat (equation A.1.2)	$c_{pa1} = 1006.4$ J/kg K
Specific heat (equation A.2.2)	$c_{pv1} = 1869.2$ J/kg K

If the air is assumed to be saturated immediately after the drift eliminator, the wetbulb temperature at (5) will be equal to the given drybulb temperature at this elevation, therefore

Wetbulb temperature	$T_{awb5} = T_{a5}$

The corresponding thermophysical properties at (5) can be determined using the equations given in Appendix A.

Vapour pressure (equation A.2.1)	$p_{v5} = 3448.43$ Pa
Humidity ratio (equation A.3.5)	$w_5 = 0.026787$ kg/kg d.a.
Density (equation A.3.1)	$\rho_{av5} = 0.960724$ kg/m^3
Dynamic viscocity (equation A.3.3)	$\mu_{av5} = 1.81732 \times 10^{-5}$ Pa.s
Enthalpy (equation A.3.6b)	$i_{ma5} = 94947.3$ J/kg
Specific heat (equation A.1.2)	$c_{pa5} = 1006.6$ J/kg K
Specific heat (equation A.2.2)	$c_{pv5} = 1873.8$ J/kg K
The mean pressure of the air-vapor in the fill $p_{a15} = \frac{p_{a1} + p_{a5}}{2}$	$p_{a15} = 84018.9$ Pa

The approximate harmonic mean density of the air-vapor in the fill

$$\rho_{av15} = \left(\frac{2}{\frac{1}{\rho_{av1}} + \frac{1}{\rho_{av5}}} \right) \qquad \rho_{av15} = 0.984804 \ \text{kg/m}^3$$

and the mean air temperature

$$T_{a15} = \frac{T_{a1} + T_{a5}}{2} \qquad T_{a15} = 294.094 \ \text{K}$$

$$T_{a15} - 273.16 = 20.934 \ ^{o}\text{C}$$

The thermophysical properties of water at the outlet temperature T_{wo} are as follows:

Density (equation A.4.1) $\rho_{wo} = 997.867 \ \text{kg/m}^3$

Surface tension (equation A.4.7) $\sigma_{wo} = 0.072564 \ \text{N/m}$

The mean water temperature is

$$T_{wm} = \frac{T_{wi} + T_{wo}}{2} \qquad T_{wm} = 303.844 \ \text{K}$$

$$T_{wm} - 273.15 = 30.694 \ ^{o}\text{C}$$

Specific heat at T_{wm} (equation A.4.2) $c_{pwm} = 4178.3 \ \text{J/kg K}$

K.2.3 Flow rates

The dry air mass flow rate can be determined from the following relation:

$$m_{av15} = \frac{m_a \cdot (1 + w_1) + m_a \cdot (1 + w_5)}{2} \qquad m_{av15} = 16810.9 \ \text{kg/s}$$

or $$m_a = \frac{2 \cdot m_{av15}}{2 + w_1 + w_5} \qquad m_a = 16522.5 \ \text{kg/s}$$

The respective flow rates upstream and downstream of the fill are thus

$$m_{av1} = m_a \cdot (1 + w_1) \qquad m_{av1} = 16656.7 \ \text{kg/s}$$

and $$m_{av5} = m_a \cdot (1 + w_5) \qquad m_{av5} = 16965 \ \text{kg/s}$$

The corresponding mass velocities are

$$G_{av15} = \frac{m_{av15}}{A_{fr}} \qquad G_{av15} = 2.025408 \ \text{kg/s m}^2$$

$$G_a = \frac{m_a}{A_{fr}} \qquad G_a = 1.990658 \ \text{kg/s m}^2$$

$$G_{av1} = \frac{m_{av1}}{A_{fr}} \qquad G_{av1} = 2.006836 \ \text{kg/s m}^2$$

$$G_{av5} = \frac{m_{av5}}{A_{fr}} \qquad G_{av5} = 2.043981 \ \text{kg/s m}^2$$

$$G_w = \frac{m_w}{A_{fr}} \qquad G_w = 1.506024 \ \text{kg/s m}^2$$

K.2.4 Transfer coefficients or Merkel numbers

De Villiers (1997) proposes an equation that expresses the transfer coefficient of the rain zone of this particular tower approximately. The *a* coefficients appearing in this equation for the rain zone transfer coefficient and the pressure drop, required later on, are as follows:

$$a_\mu = 3.061 \cdot 10^{-6} \cdot \left(\frac{\rho_{wo}^{\,4} \cdot g^9}{\sigma_{wo}} \right)^{0.25} \qquad a_\mu = 1.000034$$

$$a_\rho = \frac{998}{\rho_{wo}} \qquad a_\rho = 1.000133$$

$$a_v = 73.298 \cdot \left(\frac{g^5 \cdot \sigma_{wo}^{\,3}}{\rho_{wo}^{\,3}} \right)^{0.25} \qquad a_v = 1.000828$$

$$a_L = 6.122 \cdot \left(\frac{g \cdot \sigma_{wo}}{\rho_{wo}} \right)^{0.25} \qquad a_L = 1.000257$$

It can be seen that the values of these coefficients are close to unity.
The diffusion coefficient at air inlet conditions

$$D_1 = \frac{0.04357 \cdot T_{a1}^{\,1.5} \cdot \left(\frac{1}{28.97} + \frac{1}{18.016} \right)^{0.5}}{p_{a1} \cdot \left(29.9^{0.333} + 18.8^{0.333} \right)^2}$$

$$D_1 = 2.29972 \times 10^{-5} \ \text{m}^2/\text{s}$$

The Schmidt number is

$$Sc_1 = \frac{\mu_{av1}}{\rho_{av1} \cdot D_1} \qquad Sc_1 = 0.768704$$

The air-vapor velocity before the fill

$$v_{av3} = \frac{m_{av1}}{\rho_{av1} \cdot A_{fr}} \qquad v_{av3} = 1.986725$$

Vapor gas constant $R_v = 461.52$ J/kg K

With these values find

$$A_{rz1} = 12 \cdot \left(\frac{D_1}{v_{av3} \cdot d_d}\right) \cdot \left(\frac{H_3}{d_d}\right) \cdot \left(\frac{p_{a1}}{\rho_{wo} \cdot R_v \cdot T_{a1}}\right) \cdot Sc_1^{0.33} \cdot \left(\frac{ln\left(\frac{w_{s1} + 0.622}{w_1 + 0.622}\right)}{w_{s1} - w_1}\right)$$

$$A_{rz1} = 0.103465$$

$$A_{rz2} = 0.90757 \cdot a_\rho \cdot \rho_{av1} - 30341.04 \cdot a_\mu \cdot \mu_{av1} - 0.37564$$

$$A_{rz2} = -5.783892 \times 10^{-4}$$

$$A_{rz3} = 0.55 + 41.7215\left(a_L \cdot d_d\right)^{0.80043} \qquad A_{rz3} = 1.001489$$

$$A_{rz4} = \left(3.11 \cdot e^{0.15 a_v \cdot v_{av3}} - 3.13\right) \cdot \left[3.741 \cdot \left(a_L \cdot H_3\right)^{-1.23456} + 0.713\right]$$

$$A_{rz4} = 0.987464$$

$$A_{rz5} = e^{5.3759 \cdot e^{-0.2092 \cdot a_L \cdot H_3} \cdot ln\left(0.3719 \cdot e^{0.0019055 \cdot a_L \cdot d_3} + 0.55\right)}$$

$$A_{rz5} = 1.002562$$

Substitution of the above equations into the following equation yields the transfer coefficient applicable to the rain zone.

$$Me_{rz} = A_{rz1} \cdot \left(A_{rz2} + 4.04016 A_{rz3} \cdot A_{rz4} \cdot A_{rz5}\right)$$

$$Me_{rz} = 0.414391$$

The transfer coefficient applicable to the fill is

$$Me_{fi} = Me_{fi}\left(G_w, G_a\right) \qquad Me_{fi} = 0.932866$$

and for the spray zone is

$$Me_{sp} = 0.2 \cdot L_{sp} \cdot \left(\frac{G_a}{G_w}\right)^{0.5} \qquad Me_{sp} = 0.114969$$

The overall transfer coefficient is the sum of the transfer coefficients of the rain, fill and spray zones respectively.

$$Me_{CT} = Me_{rz} + Me_{fi} + Me_{sp} \qquad Me_{CT} = 1.462226$$

where according to Merkel

$$Me_{CT} = \int_{T_{wo}}^{T_{wi}} \frac{c_{pw}}{i_{masw} - i_{ma}}\, dT_w$$

If the four-point form of the Chebyshev integral is applied to this relation, the integral on the right side can be expressed as

$$\int_{T_{wo}}^{T_{wi}} \frac{c_{pw}}{i_{masw} - i_{ma}}\, dT_w = \frac{c_{pwm}\cdot\left(T_{wi} - T_{wo}\right)}{4}\cdot\left(\frac{1}{\Delta i_a} + \frac{1}{\Delta i_b} + \frac{1}{\Delta i_c} + \frac{1}{\Delta i_d}\right)$$

The enthalpy differentials are dependent on the following intermediate temperatures:

$T_{wa} = T_{wo} + 0.1\cdot\left(T_{wi} - T_{wo}\right)$ $\quad T_{wa} = 296.3997$ K

$T_{wb} = T_{wo} + 0.4\cdot\left(T_{wi} - T_{wo}\right)$ $\quad T_{wb} = 301.9831$ K

$T_{wc} = T_{wo} + 0.6\cdot\left(T_{wi} - T_{wo}\right)$ $\quad T_{wc} = 305.7054$ K

$T_{wd} = T_{wo} + 0.9\cdot\left(T_{wi} - T_{wo}\right)$ $\quad T_{wd} = 311.2888$ K

The humidity ratios of saturated air at the intermediate water temperatures are:

$w_{sa} = w\left(T_{wa}, T_{wa}, p_{a15}, p_v\left(T_{wa}\right)\right)$ $\quad w_{sa} = 0.02196$ kg/kg d.a.

$w_{sb} = w\left(T_{wb}, T_{wb}, p_{a15}, p_v\left(T_{wb}\right)\right)$ $\quad w_{sb} = 0.030981$ kg/kg d.a.

$w_{sc} = w\left(T_{wc}, T_{wc}, p_{a15}, p_v\left(T_{wc}\right)\right)$ $\quad w_{sc} = 0.038776$ kg/kg d.a.

$w_{sd} = w\left(T_{wd}, T_{wd}, p_{a15}, p_v\left(T_{wd}\right)\right)$ $\quad w_{sd} = 0.053977$ kg/kg d.a.

From these values the enthalpies of saturated air at the intermediate water temperatures are determined as follows:

$i_{maswa} = i_{ma}\left(T_{wa}, w_{sa}\right)$ $\quad i_{maswa} = 7.92914\times 10^4$ J/kg

$i_{maswb} = i_{ma}\left(T_{wb}, w_{sb}\right)$ $\quad i_{maswb} = 1.08199\times 10^5$ J/kg

$i_{maswc} = i_{ma}\left(T_{wc}, w_{sc}\right)$ $\quad i_{maswc} = 1.32141\times 10^5$ J/kg

$i_{maswd} = i_{ma}\left(T_{wd}, w_{sd}\right)$ $\quad i_{maswd} = 1.77292\times 10^5$ J/kg

The intermediate air enthalpies are also calulated using these values.

$$i_{maa} = \frac{m_w\cdot c_{pwm}\cdot\left(T_{wa} - T_{wo}\right)}{m_a} + i_{ma1} \quad i_{maa} = 4.199799\times 10^4 \text{ J/kg}$$

$$i_{mab} = \frac{m_w\cdot c_{pwm}\cdot\left(T_{wb} - T_{wo}\right)}{m_a} + i_{ma1} \quad i_{mab} = 5.964779\times 10^4 \text{ J/kg}$$

$$i_{mac} = \frac{m_w\cdot c_{pwm}\cdot\left(T_{wc} - T_{wo}\right)}{m_a} + i_{ma1} \quad i_{mac} = 7.141433\times 10^4 \text{ J/kg}$$

$$i_{mad} = \frac{m_w \cdot c_{pwm} \cdot \left(T_{wd} - T_{wo}\right)}{m_a} + i_{ma1} \quad i_{mad} = 8.906413 \times 10^4 \text{ J/kg}$$

With these values, find the difference in enthalpy

$$\Delta i_a = i_{maswa} - i_{maa} \qquad \Delta i_a = 3.729345 \times 10^4 \text{ J/kg}$$

$$\Delta i_b = i_{maswb} - i_{mab} \qquad \Delta i_b = 4.855096 \times 10^4 \text{ J/kg}$$

$$\Delta i_c = i_{maswc} - i_{mac} \qquad \Delta i_c = 6.072679 \times 10^4 \text{ J/kg}$$

$$\Delta i_d = i_{maswd} - i_{mad} \qquad \Delta i_d = 8.82278 \times 10^4 \text{ J/kg}$$

Substitution into the Chebyshev integral yields

$$Me_{CT} = \frac{c_{pwm} \cdot \left(T_{wi} - T_{wo}\right)}{4} \cdot \left(\frac{1}{\Delta i_a} + \frac{1}{\Delta i_b} + \frac{1}{\Delta i_c} + \frac{1}{\Delta i_d}\right)$$

$$Me_{CT} = 1.462227$$

This value is almost identical to the value obtained by adding the transfer coefficients of the three wet zones which means the chosen water outlet temperature is correct.

K.2.5 Energy balance

The heat rejected by the cooling tower is given by

$$Q_w = m_w \cdot c_{pwm} \cdot \left(T_{wi} - T_{wo}\right) \qquad Q_w = 9.720606 \times 10^8 \text{ W}$$

The correctness of the chosen temperature of the saturated air leaving the spray zone, T_{a5}, can be confirmed from the relation

$$Q_a = m_a \cdot \left(i_{ma5} - i_{ma1}\right) \qquad Q_a = 9.720584 \times 10^8 \text{ W}$$

The values of Q are in agreement, which means the chosen value for T_{a5} is correct.

K.2.6 Loss coefficients

The loss coefficient due to the tower supports referred to the fill is determined from

$$K_{ts} = \frac{C_{Dts} \cdot L_{ts} \cdot d_{ts} \cdot n_{ts}}{\pi d_3 \cdot H_3} \qquad K_{ts} = 0.203523$$

$$K_{tsfi} = \left[\frac{C_{Dts} \cdot L_{ts} \cdot d_{ts} \cdot n_{ts} \cdot A_{fr}^{\,2}}{\left(\pi d_3 \cdot H_3\right)^3} \right] \cdot \left(\frac{\rho_{av15}}{\rho_{av1}} \right) \cdot \left(\frac{m_{av1}}{m_{av15}} \right)^2$$

$$K_{tsfi} = 1.245123$$

The specified loss coefficient due to the fill support structure and the contraction loss into the fill is referred to the mean density through the fill, i.e.,

$$K_{fsfi} = K_{fs} \cdot \left(\frac{\rho_{av15}}{\rho_{av1}} \right) \cdot \left(\frac{m_{av1}}{m_{av15}} \right)^2 \qquad K_{fsfi} = 0.478569$$

According to the specified fill loss coefficient

$$K_{fdm} = K_{fdm1}\left(G_w, G_a\right) \qquad K_{fdm} = 3.829756$$

The actual fill loss coefficient applicable to the cooling tower is given by

$$K_{fi} = K_{fdm} + \left(\frac{G_{av5}^{\,2}}{\rho_{av5}} - \frac{G_{av1}^{\,2}}{\rho_{av1}} \right) \cdot \frac{\rho_{av15}}{G_{av15}^{\,2}}$$

$$K_{fi} = 3.916569$$

The expansion loss coefficient after the fill is given by

$$K_{ctefi} = \left(1 - \frac{A_{fr}}{A_3} \right)^2 \cdot \left(\frac{\rho_{av15}}{\rho_{av5}} \right) \cdot \left(\frac{m_{av5}}{m_{av15}} \right)^2$$

$$K_{ctefi} = 0.001087$$

The loss coefficient through the spray zone is given by

$$K_{spfi} = L_{sp} \cdot \left[0.4 \cdot \left(\frac{G_w}{G_a} \right) + 1 \right] \cdot \left(\frac{\rho_{av15}}{\rho_{av5}} \right) \cdot \left(\frac{m_{av5}}{m_{av15}} \right)^2$$

$$K_{spfi} = 0.679934$$

For the water distribution system, it follows from the specified loss coefficient that

$$K_{wdfi} = K_{wd} \cdot \left(\frac{\rho_{av15}}{\rho_{av5}} \right) \cdot \left(\frac{m_{av5}}{m_{av15}} \right)^2 \qquad K_{wdfi} = 0.521975$$

The loss coefficient for a type *c* drift eliminator based on fill conditions is

$$Ry = \frac{m_{av5}}{A_{fr} \cdot \mu_{av5}} \qquad Ry = 1.124722 \times 10^{5}$$

$$K_{defi} = K_{de}(Ry) \cdot \left(\frac{\rho_{av15}}{\rho_{av5}} \right) \cdot \left(\frac{m_{av5}}{m_{av15}} \right)^{2}$$

$$K_{defi} = 5.472925$$

The sum of the loss coefficients in the vicinity of the fill is

$$K_{ct\_fi} = K_{fsfi} + K_{fi} + K_{ctefi} + K_{spfi} + K_{wdfi} + K_{defi}$$

$$K_{ct\_fi} = 11.071059$$

The inlet loss coefficient for a circular cooling tower with splash type isotropic fill operating in the absence of a rain zone and based on fill conditions can be determined according to the following applicable equation proposed by De Villiers and presented in Kröger (2004).

$$A_{ctfi1} = 0.011266 \cdot e^{\frac{0.093 d_3}{H_3}} \cdot K_{ct\_fi}^{2} - 0.3105 \cdot e^{\frac{0.1085 d_3}{H_3}} \cdot K_{ct\_fi}$$

$$A_{ctfi1} = -7.032934$$

$$A_{ctfi2} = -1.7522 + 4.5614 \cdot e^{\frac{0.131 \cdot d_3}{H_3}} \qquad A_{ctfi2} = 16.17967$$

$$A_{ctfi3} = \frac{10970.2 \cdot e^{-0.2442 K_{ct\_fi}} + 1391.3}{\frac{d_3}{H_3} - 15.7258} + 1205.54 \cdot e^{-0.23 K_{ct\_fi}} + 109.314$$

$$A_{ctfi3} = -199.171951$$

$$A_{ctfi4} = \frac{2 \cdot r_i}{d_3} - \frac{0.01942}{\frac{d_3}{H_3} - 27.929} - 0.016866$$

$$A_{ctfi4} = 0.024245$$

$$A_{ctfi5} = \left(A_{ctfi1} + A_{ctfi2} + asinh\left(A_{ctfi3} \cdot A_{ctfi4} \right) \right)$$

$$A_{ctfi5} = 6.86841$$

$$K_{ctfinorz} = A_{ctfi5}\cdot\left[\left(\frac{\rho_{av15}}{\rho_{av1}}\right)\cdot\left(\frac{m_{av1}}{m_{av15}}\right)^2\cdot\left(4\cdot\frac{A_{fr}}{\pi\, d_3{}^2}\right)^2\right]$$

$$K_{ctfinorz} = 6.156612$$

This value must be multiplied by a correction factor C_{rz} as given by the following equation to obtain the correct inlet loss coefficient in the presence of a rain zone.

$$A_{crz1} = 0.2394 + 80.1\cdot\left(\frac{0.0954}{\frac{d_3}{H_3}} + d_d\right)\cdot e^{0.395\frac{G_w}{G_{av1}}} - 0.3195\cdot\frac{G_w}{G_{av1}}$$

$$A_{crz1} = 1.360276$$

$$A_{crz2} = 966\cdot\left(\frac{d_d}{\frac{d_3}{H_3}}\right)\cdot e^{0.686\frac{G_w}{G_{av1}}} \qquad A_{crz2} = 0.541385$$

$$A_{crz3} = \left(1 - 0.06825\cdot G_w\right)\cdot K_{ct\_fi}{}^{0.09667}\cdot e^{8.7434\left(\frac{1}{d_3}-0.01\right)}$$

$$A_{crz3} = 1.127723$$

$$C_{rz} = \left(A_{crz1} - A_{crz2}\right)\cdot A_{crz3} \qquad C_{rz} = 0.923482$$

Thus $K_{ctfi} = C_{rz}\cdot K_{ctfinorz}$ $\qquad K_{ctfi} = 5.685517$

The loss coefficient for the rain zone referred to the fill conditions is calculated using the following equation which also makes use of the identical *a* coefficients defined for the rain zone tranfer coefficient equation of De Villiers used above.

$$B_{rz1} = \left(0.22460 - 0.31467\cdot a_\rho\cdot\rho_{av1} + 5263.04\cdot a_\mu\cdot\mu_{av1}\right)$$

$$B_{rz1} = 0.000688$$

$$B_{rz2} = 0.775526\cdot\left(1.4824163\cdot e^{71.52\, a_L\cdot d_d} - 0.91\right)$$

$$B_{rz2} = 0.771022$$

$$B_{rz3} = \left(0.39064 \cdot e^{0.010912 a_L \cdot d_3} - 0.17\right) \cdot \left[2.0892 \cdot \left(a_v \cdot v_{av3}\right)^{-1.3944} + 0.14\right]$$

$$B_{rz3} = 0.99033$$

$$B_{rz4} = \left(0.8449 \cdot ln\left(a_L \cdot \frac{d_3}{2}\right) - 2.312\right) \quad B_{rz4} = 1.030675$$

$$B_{rz5} = \left(0.3724 \cdot ln\left(a_v \cdot v_{av3}\right) + 0.7263\right) \cdot ln\left[206.757 \cdot \left(a_L \cdot H_3\right)^{-2.8344} + 0.43\right]$$

$$B_{rz5} = -0.305751$$

$$K_{rz} = 3 \cdot a_v \cdot \left(\frac{G_w}{\rho_{wo}}\right) \cdot \left(\frac{H_3}{d_d}\right) \cdot \left(B_{rz1} + B_{rz2} \cdot B_{rz3} \cdot e^{B_{rz4} \cdot B_{rz5}}\right)$$

$$K_{rz} = 7.222625$$

$$K_{rzfi} = K_{rz} \cdot \left(\frac{\rho_{av15}}{\rho_{av1}}\right) \cdot \left(\frac{m_{av1}}{m_{av15}}\right)^2 \left(\frac{4 \cdot A_{fr}}{\pi {d_3}^2}\right)^2$$

$$K_{rzfi} = 6.474118$$

The effective diameter in the absence of a rain zone can be determined from

$$d_{e3} = d_3 \cdot \left[1.27 - 0.16722 \cdot ln\left(\frac{d_3}{H_3}\right) + \left(0.043653 \cdot ln\left(\frac{d_3}{H_3}\right) - 0.062658\right) \cdot ln\left(K_{ct\_fi}\right)\right]$$

$$d_{e3} = 101.7 \text{ m}$$

The corresponding effective frontal fill area is

$$A_{fre} = \frac{\pi {d_{e3}}^2}{4} \qquad A_{fre} = 8123.9 \text{ m}^2$$

At this stage it is possible to confirm the values of p_{a3} and p_{a5} according to the equations

$$p_{a3} = p_{a1} \cdot \left(1 - \frac{0.00975 \cdot H_3}{T_{a1}}\right)^{3.5 \cdot \left(1 + w_1\right) \cdot \left(1 - \frac{w_1}{w_1 + .62198}\right)} \ldots$$

$$+ -\left(K_{tsfi} + K_{rzfi} + K_{fsfi} + K_{ctfi}\right) \cdot \frac{\left(\frac{m_{av15}}{A_{fr}}\right)^2}{2 \cdot \rho_{av15}}$$

$$p_{a3} = 83972.2 \text{ Pa}$$

$$p_{a5} = p_{a1}\cdot\left[1 - \frac{0.00975\cdot\left(H_3 + \frac{L_{fi}}{2}\right)}{T_{a1}}\right]^{3.5\cdot(1+w_1)\cdot\left(1-\frac{w_1}{w_1+.62198}\right)} \quad \ldots$$

$$+ -\left(K_{tsfi} + K_{rzfi} + K_{fsfi} + K_{fi} + K_{ctefi} + K_{spfi} + K_{wdfi} + K_{defi} + K_{ctfi}\right)\cdot\frac{\left(\frac{m_{av15}}{A_{fr}}\right)^2}{2\cdot\rho_{av15}}$$

$$p_{a5} = 83937.7 \text{ Pa}$$

This value for p_{a5} is in agreement with that used in previous calculations in this example. The temperature lapse rate in the tower is determined from

$$A_{\xi Ta51} = w_5^{2.}\cdot p_{a5}\cdot e^{\frac{5406.1915}{T_{a5}}} \qquad A_{\xi Ta51} = 4.138\times 10^9$$

$$A_{\xi Ta52} = \left(w_5 + 0.622\right)\cdot R_a\cdot T_{a5} \qquad A_{\xi Ta52} = 55799.3$$

$$i_e = i_{fg}(273.15) - \left(c_{pw}\left(\frac{T_{a5}+273.15}{2}\right) - c_{pv}\left(\frac{T_{a5}+273.15}{2}\right)\right)\cdot\left(T_{a5} - 273.15\right)$$

$$i_e = 2.440296\times 10^6 \text{ J/kg}$$

$$c_{pma5} = c_{pa}\left(T_{a5}\right) + w_5\cdot c_{pv}\left(T_{a5}\right) \qquad c_{pma5} = 1057.44 \text{ J/kg K}$$

These equations are substituted into the following equation to obtain the temperature lapse rate inside the tower.

$$\xi_{Ta5} = \frac{-\left(1 + w_5\right)\cdot g\cdot\left(1 + \frac{0.42216\cdot 10^{-11}\cdot A_{\xi Ta51}\cdot i_e}{A_{\xi Ta52}}\right)}{\left(c_{pma5} + 3.6693\cdot 10^{-8}\cdot A_{\xi Ta51}\cdot\frac{i_e}{T_{a5}^{\ 2}}\right)}$$

$$\xi_{Ta5} = -0.003423 \text{ K/m}$$

The temperature lapse rate in the tower is determined from

$$T_{a6} = T_{a5} + \xi_{Ta5}\cdot\left(H_6 - H_3 - L_{fi} - L_{sp}\right)$$

$$T_{a6} = 299.129 \text{ K}$$

The corresponding density of the air-vapor mixture at this temperature is

$$\rho_{av6} = \rho_{av}\left(w_5, p_{a6}, T_{a6}\right) \qquad \rho_{av6} = 0.947442 \ \text{kg/m}^3$$

The ambient temperature at elevation (7) can be calculated from the dry adiabatic lapse rate as follows with $H_7 = H_6$.

$$T_{a7} = T_{a1} - 0.00975 \cdot H_6 \qquad T_{a7} = 287.167 \ \text{K}$$

The pressure at (7) can be determined from

$$p_{a7} = p_{a1} \cdot \left(1 - 0.00975 \cdot \frac{H_6}{T_{a1}}\right)^{3.5 \cdot \left(1+w_1\right) \cdot \left(1 - \frac{w_1}{w_1 + 0.62198}\right)}$$

$$p_{a7} = 82654.3 \ \text{Pa}$$

The corresponding density of the ambient air at elevation (7), assuming a uniform ambient humidity ratio w_1, is

$$\rho_{av7} = \rho_{av}\left(w_1, p_{a7}, T_{a7}\right) \qquad \rho_{av7} = 0.997713 \ \text{kg/m}^3$$

With no cold inflow, these values yield the following densimetric Froude number:

$$Fr_D = \frac{1}{\rho_{av6} \cdot \left(\rho_{av7} - \rho_{av6}\right) g \cdot d_6} \cdot \left(\frac{m_{av5}}{A_6}\right)^2$$

$$Fr_D = 1.198217$$

The pressure at (6) can then be determined from

$$p_{a6} = p_{a7} + \left(0.02 \cdot Fr_D^{-1.5} - \frac{0.14}{Fr_D}\right) \cdot \left(\frac{1}{\rho_{av6}}\right) \cdot \left(\frac{m_{av5}}{A_6}\right)^2$$

$$p_{a6} = 82650.6 \ \text{Pa}$$

For comparison with CFD, the pressure p_{a5} needs to be determined at an elevation above the drift eliminators, located at H = 13.5 m, as follows:

$$p_{a5\_13.5m} = p_{a5} \cdot \left[1 + \xi_{Ta5} \cdot \frac{\left[13.5 - \left(H_3 + \frac{L_{fi}}{2}\right)\right]}{T_{a5}}\right]^{-\left[0.021233 \frac{\left(1+w_5\right)}{\xi_{Ta5} \cdot \left(w_5 + 0.622\right)}\right]}$$

$$p_{a5\_13.5m} = 83917 \ \text{Pa}$$

K.2.7 Draught equation

The draught equation may now be solved using the above values. Upon substitution, the left side of the equation yields,

$$A_{LS1} = p_{a1}\cdot\left[1 - \frac{0.00975\cdot\left(H_3 + \frac{L_{fi}}{2}\right)}{T_{a1}}\right]^{3.5\cdot(1+w_1)\cdot\left(1-\frac{w_1}{w_1+0.62198}\right)}$$

$$A_{LS1} = 83988.705309$$

$$A_{LS2} = \left[1 + \frac{\xi_{Ta5}\cdot\left(H_6 - H_3 - \frac{L_{fi}}{2}\right)}{T_{a5}}\right]^{\frac{-0.02123(1+w_5)}{\xi_{Ta5}\cdot(w_5+0.622)}}$$

$$A_{LS2} = 0.984879$$

$$LS_{draft} = A_{LS1}\cdot A_{LS2} - p_{a7} - (p_{a6} - p_{a7})$$

$$LS_{draft} = 68.1217$$

The total loss coefficient referred to fill conditions is obtained by adding all the appropriate loss coefficients as follows:

$$K_{total} = K_{tsfi} + K_{rzfi} + K_{fsfi} + K_{ctfi} + K_{fi} + K_{ctefi} + K_{spfi} + K_{wdfi} + K_{defi}$$

$$K_{total} = 24.4758$$

The corresponding pressure drop is therefore

$$\Delta p_{losses} = K_{total}\cdot\frac{1}{2\cdot\rho_{av15}}\cdot\left(\frac{m_{av15}}{A_{fr}}\right)^2$$

$$\Delta p_{losses} = 50.977975 \text{ Pa}$$

$$RS_{draft} = \Delta p_{losses}\cdot\left[1 + \frac{\xi_{Ta5}\cdot\left(H_6 - H_3 - \frac{L_{fi}}{2}\right)}{T_{a5}}\right]^{\frac{-0.021233(1+w_5)}{\xi_{Ta5}\cdot(w_5+0.622)}} + \frac{\alpha_{e6}}{2\cdot\rho_{av6}}\cdot\left(\frac{m_{av5}}{A_6}\right)^2$$

$$RS_{draft} = 68.34659$$

Since the value of the right-side of the draft equation is essentially the same as the left side, the chosen value for the air-vapor mass flow rate is correct.
The approximate amount of water lost due to evaporation is given by

$$m_{w\_evap} = m_a \cdot (w_5 - w_1) \qquad m_{w\_evap} = 308.304 \text{ kg/s}$$

Taking into consideration this rate of evaporation, a more accurate value of the heat transfer rate can be found according to the following equation:

$$Q = m_w \cdot c_{pwm} \cdot (T_{wi} - 273.15) - (m_w - m_{w\_evap}) \cdot c_{pwm} \cdot (T_{wo} - 273.15)$$

$$Q = 9.996131 \times 10^8 \text{ W}$$

The difference between this value and that obtained without taking evaporation into account is

$$\frac{Q - Q_w}{Q_w} \cdot 100 = 2.83 \ \%$$

L

PERFORMANCE EVALUATION OF A NATURAL DRAFT WET-COOLING TOWER RAIN ZONE EMPLOYING THE MERKEL METHOD OF ANALYSIS

The rain zone performance is determined in this appendix by following the same method as in Appendix K and using various values calculated in Appendix K. The objective is to calculate the mean rain zone water inlet temperature, air outlet temperature and air outlet humidity ratio. An iterative process is required to find a solution that will satisfy both the energy and draft equations. A converged solution is obtained when the following variables satisfy these equations.

L.1 SOLUTION

L.1.1 Iteration parameters

Air temperature leaving the rain zone	$T_{a3} = 290.25$ K
Air wetbulb temperature leaving the rain zone	$T_{awb3} = 288.15$ K
Air humidity ratio leaving the rain zone	$w_3 = 0.012078$ kg/kg d.a.
Air enthalpy leaving the rain zone	$i_{ma3} = 47814$ J/kg
Mean rain zone water inlet temperature	$T_{wi\_rz} = 298.24$ K
	$T_{wi\_rz} - 273.15 = 25.1$ ºC

L.1.2 Rain zone transfer characteristic or Merkel number

From Appendix K, the rain zone transfer coefficient is

$$Me_{rz} = \int_{T_{wo}}^{T_{wi\_rz}} \frac{c_{pw}}{i_{masw} - i_{ma}} \, dT_w \qquad Me_{rz} = 0.414391$$

If the four-point form of the Chebyshev integral is applied to this relation, the integral on the right side can be expressed as

$$\int_{T_{wo}}^{T_{wi\_rz}} \frac{c_{pw}}{i_{masw} - i_{ma}}\, dT_w = \frac{c_{pwm13}\cdot\left(T_{wi\_rz} - T_{wo}\right)}{4}\cdot\left(\frac{1}{\Delta i_a} + \frac{1}{\Delta i_b} + \frac{1}{\Delta i_c} + \frac{1}{\Delta i_d}\right)$$

The mean pressure is denoted by

$$p_{a13} = \frac{p_{a1} + p_{a3}}{2} \qquad p_{a13} = 84036.1 \text{ Pa}$$

The enthalpy differentials are dependent on the following intermediate temperatures:

$$T_{wa} = T_{wo} + 0.1\cdot\left(T_{wi\_rz} - T_{wo}\right) \qquad T_{wa} = 294.9082 \text{ K}$$
$$T_{wb} = T_{wo} + 0.4\cdot\left(T_{wi\_rz} - T_{wo}\right) \qquad T_{wb} = 296.0175 \text{ K}$$
$$T_{wc} = T_{wo} + 0.6\cdot\left(T_{wi\_rz} - T_{wo}\right) \qquad T_{wc} = 296.757 \text{ K}$$
$$T_{wd} = T_{wo} + 0.9\cdot\left(T_{wi\_rz} - T_{wo}\right) \qquad T_{wd} = 297.8662 \text{ K}$$

The humidity ratios of saturated air at the intermediate water temperatures are:

$$w_{sa} = w\left(T_{wa}, T_{wa}, p_{a13}, p_v\left(T_{wa}\right)\right) \qquad w_{sa} = 0.019992 \text{ kg/kg d.a.}$$
$$w_{sb} = w\left(T_{wb}, T_{wb}, p_{a13}, p_v\left(T_{wb}\right)\right) \qquad w_{sb} = 0.021436 \text{ kg/kg d.a.}$$
$$w_{sc} = w\left(T_{wc}, T_{wc}, p_{a13}, p_v\left(T_{wc}\right)\right) \qquad w_{sc} = 0.022451 \text{ kg/kg d.a.}$$
$$w_{sd} = w\left(T_{wd}, T_{wd}, p_{a13}, p_v\left(T_{wd}\right)\right) \qquad w_{sd} = 0.024055 \text{ kg/kg d.a.}$$

From these values the enthalpies of saturated air at the intermediate water temperatures are determined as follows:

$$i_{maswa} = i_{ma}\left(T_{wa}, w_{sa}\right) \qquad i_{maswa} = 7.27255\times 10^4 \text{ J/kg}$$
$$i_{maswb} = i_{ma}\left(T_{wb}, w_{sb}\right) \qquad i_{maswb} = 7.75582\times 10^4 \text{ J/kg}$$
$$i_{maswc} = i_{ma}\left(T_{wc}, w_{sc}\right) \qquad i_{maswc} = 8.0916\times 10^4 \text{ J/kg}$$
$$i_{maswd} = i_{ma}\left(T_{wd}, w_{sd}\right) \qquad i_{maswd} = 8.61679\times 10^4 \text{ J/kg}$$

The intermediate air enthalpies are also calulated using these values.

$$i_{maa} = \frac{m_w\cdot c_{pwm}\cdot\left(T_{wa} - T_{wo}\right)}{m_a} + i_{ma1} \quad i_{maa} = 3.728351\times 10^4 \text{ J/kg}$$
$$i_{mab} = \frac{m_w\cdot c_{pwm}\cdot\left(T_{wb} - T_{wo}\right)}{m_a} + i_{ma1} \quad i_{mab} = 4.078988\times 10^4 \text{ J/kg}$$

$$i_{mac} = \frac{m_w \cdot c_{pwm} \cdot \left(T_{wc} - T_{wo}\right)}{m_a} + i_{ma1} \quad i_{mac} = 4.312746 \times 10^4 \text{ J/kg}$$

$$i_{mad} = \frac{m_w \cdot c_{pwm} \cdot \left(T_{wd} - T_{wo}\right)}{m_a} + i_{ma1} \quad i_{mad} = 4.663383 \times 10^4 \text{ J/kg}$$

With these values, find the difference in enthalpy

$$\Delta i_a = i_{maswa} - i_{maa} \quad \Delta i_a = 3.544201 \times 10^4 \text{ J/kg}$$

$$\Delta i_b = i_{maswb} - i_{mab} \quad \Delta i_b = 3.676828 \times 10^4 \text{ J/kg}$$

$$\Delta i_c = i_{maswc} - i_{mac} \quad \Delta i_c = 3.778849 \times 10^4 \text{ J/kg}$$

$$\Delta i_d = i_{maswd} - i_{mad} \quad \Delta i_d = 3.953409 \times 10^4 \text{ J/kg}$$

Substitution into the Chebyshev integral yields

$$Me_{rz} = \frac{c_{pwm13} \cdot \left(T_{wi\_rz} - T_{wo}\right)}{4} \cdot \left(\frac{1}{\Delta i_a} + \frac{1}{\Delta i_b} + \frac{1}{\Delta i_c} + \frac{1}{\Delta i_d}\right)$$

$$Me_{rz} = 0.4143282$$

L.1.3 Rain zone energy balance

The heat rejected by the cooling tower is given by

$$Q_{w\_rz} = m_w \cdot c_{pwm13} \cdot \left(T_{wi\_rz} - T_{wo}\right) \quad Q_{w\_rz} = 1.933 \times 10^8 \text{ W}$$

The correctness of the temperature of the air leaving the rain zone, T_{a3}, can be confirmed from

$$Q_{a\_rz} = m_a \cdot \left(i_{ma3} - i_{ma1}\right) \qquad Q_{a\_rz} = 1.933 \times 10^8 \text{ W}$$

The values of Q are in agreement, which means the value for T_{a3} is correct.

L.1.4 Spray and fill zone Merkel number

The fill and spray zone transfer coefficient is

$$Me_{fs} = \int_{T_{wi\_rz}}^{T_{wi}} \frac{c_{pw}}{i_{masw} - i_{ma}} \, dT_w$$

$$Me_{fs} = Me_{fi} + Me_{sp} \qquad Me_{fs} = 1.047836$$

Again using the four-point form of the Chebyshev integral ,

$$\int_{T_{wi\_rz}}^{T_{wi}} \frac{c_{pw}}{i_{masw} - i_{ma}}\, dT_w = \frac{c_{pwm35}\cdot\left(T_{wi} - T_{wi\_rz}\right)}{4}\cdot\left(\frac{1}{\Delta i_a} + \frac{1}{\Delta i_b} + \frac{1}{\Delta i_c} + \frac{1}{\Delta i_d}\right)$$

The mean pressure is denoted by

$$p_{a35} = \frac{p_{a3} + p_{a5}}{2} \qquad p_{a35} = 83954.9 \text{ Pa}$$

The enthalpy differentials are dependent on the following intermediate temperature:

$$T_{wa} = T_{wi\_rz} + 0.1\cdot\left(T_{wi} - T_{wi\_rz}\right) \qquad T_{wa} = 299.727 \text{ K}$$
$$T_{wb} = T_{wi\_rz} + 0.4\cdot\left(T_{wi} - T_{wi\_rz}\right) \qquad T_{wb} = 304.202 \text{ K}$$
$$T_{wc} = T_{wi\_rz} + 0.6\cdot\left(T_{wi} - T_{wi\_rz}\right) \qquad T_{wc} = 307.184 \text{ K}$$
$$T_{wd} = T_{wi\_rz} + 0.9\cdot\left(T_{wi} - T_{wi\_rz}\right) \qquad T_{wd} = 311.659 \text{ K}$$

The humidity ratios of saturated air at the intermediate water temperatures are:

$$w_{sa} = w\left(T_{wa}, T_{wa}, p_{a35}, p_v\left(T_{wa}\right)\right) \qquad w_{sa} = 0.027012 \text{ kg/kg d.a.}$$
$$w_{sb} = w\left(T_{wb}, T_{wb}, p_{a35}, p_v\left(T_{wb}\right)\right) \qquad w_{sb} = 0.035458 \text{ kg/kg d.a.}$$
$$w_{sc} = w\left(T_{wc}, T_{wc}, p_{a35}, p_v\left(T_{wc}\right)\right) \qquad w_{sc} = 0.042387 \text{ kg/kg d.a.}$$
$$w_{sd} = w\left(T_{wd}, T_{wd}, p_{a35}, p_v\left(T_{wd}\right)\right) \qquad w_{sd} = 0.055207 \text{ kg/kg d.a.}$$

From these values the enthalpies of saturated air at the intermediate water temperatures are determined as follows.

$$i_{maswa} = i_{ma}\left(T_{wa}, w_{sa}\right) \qquad i_{maswa} = 9.56704 \times 10^4 \text{ J/kg}$$
$$i_{maswb} = i_{ma}\left(T_{wb}, w_{sb}\right) \qquad i_{maswb} = 1.22024 \times 10^5 \text{ J/kg}$$
$$i_{maswc} = i_{ma}\left(T_{wc}, w_{sc}\right) \qquad i_{maswc} = 1.43003 \times 10^5 \text{ J/kg}$$
$$i_{maswd} = i_{ma}\left(T_{wd}, w_{sd}\right) \qquad i_{maswd} = 1.80868 \times 10^5 \text{ J/kg}$$

The intermediate air enthalpies are also calulated using these values.

$$i_{maa} = \frac{m_w \cdot c_{pwm35}\cdot\left(T_{wa} - T_{wi\_rz}\right)}{m_a} + i_{ma3} \qquad i_{maa} = 5.252778 \times 10^4 \text{ J/kg}$$
$$i_{mab} = \frac{m_w \cdot c_{pwm35}\cdot\left(T_{wb} - T_{wi\_rz}\right)}{m_a} + i_{ma3} \qquad i_{mab} = 6.666914 \times 10^4 \text{ J/kg}$$

$$i_{mac} = \frac{m_w \cdot c_{pwm35} \cdot \left(T_{wc} - T_{wi\_rz}\right)}{m_a} + i_{ma3} \qquad i_{mac} = 7.609672 \times 10^4 \text{ J/kg}$$

$$i_{mad} = \frac{m_w \cdot c_{pwm35} \cdot \left(T_{wd} - T_{wi\_rz}\right)}{m_a} + i_{ma3} \qquad i_{mad} = 9.023808 \times 10^4 \text{ J/kg}$$

With these values, find the required enthalpy differentials

$$\Delta i_a = i_{maswa} - i_{maa} \quad \Delta i_a = 4.314265 \times 10^4 \text{ J/kg}$$

$$\Delta i_b = i_{maswb} - i_{mab} \quad \Delta i_b = 5.535519 \times 10^4 \text{ J/kg}$$

$$\Delta i_c = i_{maswc} - i_{mac} \quad \Delta i_c = 6.690652 \times 10^4 \text{ J/kg}$$

$$\Delta i_d = i_{maswd} - i_{mad} \quad \Delta i_d = 9.063034 \times 10^4 \text{ J/kg}$$

Substitution into the Chebyshev integral yields

$$Me_{fsz} = \frac{c_{pwm35} \cdot \left(T_{wi} - T_{wi\_rz}\right)}{4} \cdot \left(\frac{1}{\Delta i_a} + \frac{1}{\Delta i_b} + \frac{1}{\Delta i_c} + \frac{1}{\Delta i_d}\right)$$

$$Me_{fsz} = 1.047128$$

This value is almost identical to the value obtained by adding the transfer coefficients o three wet zones which means the water outlet temperature is correct.

L.1.5 Spray and fill zone energy balance

The heat rejected by the cooling tower is given by

$$Q_{w\_fsz} = m_w \cdot c_{pwm35} \cdot \left(T_{wi} - T_{wi\_rz}\right) \quad Q_{w\_fsz} = 7.7883 \times 10^8 \text{ W}$$

The correctness of the temperature of the air leaving the rain zone, T_{a3}, can be confirme from the relation

$$Q_{a\_fsz} = m_a \cdot \left(i_{ma5} - i_{ma3}\right) \qquad Q_{a\_fsz} = 7.7876 \times 10^8 \text{ W}$$

The values of Q are in agreement, which means the value for T_{a3} is correct.

M

EVALUATION OF DIFFERENT NATURAL DRAUGHT FLOW DRIVING POTENTIAL MODELS

M.1 INTRODUCTION

The flow driving potential or available pressure difference to drive the flow in natural draught wet-cooling towers, required to overcome flow losses, is effectively the aerostatic or total pressure difference between the air inside and outside the tower at fill level, due to the difference in mean density of the colder ambient air outside the tower and the warmer moist air inside the tower. To determine the mean densities, the air temperature and aerostatic pressure must be known as functions of elevation. Different atmospheric temperature and pressure models are presented in the following section, which are subsequently used to determine wet-cooling tower flow driving potential based on the air conditions at the tower inlet and fill outlet determined for the reference natural draught wet-cooling tower in App. K. The results are ultimately compared to investigate the effect of the different models on the driving potential.

M.2 ATMOSPHERIC TEMPERATURE AND PRESSURE RELATIONS

Depending on prevailing ambient conditions, there are appropriate models to determine atmospheric temperature and pressure as functions of elevation. In this section, the relations are presented for the following assumed conditions: isentropic dry air; dry adiabatic lapse rate, isentropic and isothermal air, each with constant humidity ratio; power function temperature inversion; and isentropic supersaturated air.

The vertical atmospheric temperature distribution for isentropic dry air is commonly referred to as the dry adiabatic lapse rate (DALR), given in Kröger (2004) as

$$T_{az} = T_{a1} - 0.00975z \tag{M.1}$$

The corresponding DALR pressure difference relation can be expressed as

$$p_{a1} - p_{az} = p_{a1}\left[1-\left(1-0.00975\frac{z}{T_{a1}}\right)^{3.5}\right] \tag{M.2}$$

For a DALR temperature however assuming that the air contains water vapour with a constant humidity ratio, the aerostatic pressure difference can be determined from

$$p_{a1} - p_{az} = p_{a1}\left[1-\left(1-0.00975\frac{z}{T_{a1}}\right)^{3.5(1+w_1)\left(1-\frac{w_1}{w_1+0.62198}\right)}\right] \tag{M.3}$$

For atmospheric air containing water vapour, assuming constant humidity ratio, Kröger (2004) gives the following relations:

$$T_{az} = T_{a1} - 0.00975\frac{(1+w_1)}{(1+1.9w_1)}z \tag{M.4}$$

$$p_{a1} - p_{az} = p_{a1}\left[1-\left(1-0.00975\frac{(1+w_1)z}{(1+1.9w_1)T_{a1}}\right)^{2.1778(1+1.9w_1)/(w_1+0.62198)}\right] \tag{M.5}$$

A vertical flow analysis in a gravitational field done with *FLUENT®*, revealed that *FLUENT®* has a deficiency when modelling the temperature change (lapse rate) of vertical air flow giving an isothermal solution. In order to define the boundary conditions for the *FLUENT®* cooling tower model discussed in following appendices, the following pressure difference relation is therefore proposed for isothermal air with a constant humidity ratio:

$$p_{a1} - p_{az} = p_{a1}\left\{1-\exp\left[-0.021233\frac{(w_1+1)z}{(w_1+0.62198)T_{a1}}\right]\right\} \tag{M.6}$$

Kloppers and Kröger (2005) proposed the following relations for a power function temperature inversion:

$$T_{az} = (T_{a1}+273.15)(z/z_1)^{b_T} \tag{M.7}$$

$$p_{a1} - p_{az} = p_{a1}\left\{1-\exp\left[-g\,z_1^{b_T}\Big/\left\{(273.15+T_1)R(1-b_T)\right\}\left(z^{(1-b_T)}-z_1^{(1-b_T)}\right)\right]\right\} \tag{M.8}$$

where T_1 is in °C and is measured one to two meters above the ground while the exponent b_T is obtained from a power function curve fit through measured data, which passes through a temperature measurement at a higher elevation.

For saturated air rising isentropically in a cooling tower, resulting in super-saturation of the air and subsequent condensation of water vapour to form a mist, as encountered at the fill outlet inside wet-cooling towers, Kröger (2004) derived the following relations:

$$T = T_{sc} + \xi_T z_s \tag{M.9}$$

$$p_{sc} - p_{az} \approx p_{sc}\left\{1-\left[1+\xi_T\frac{z_s}{T_{sc}}\right]^{-0.021233(1+w_s)/\left[\xi_T(w_{sc}+0.622)\right]}\right\} \tag{M.10}$$

where

$$\xi_T = \frac{-(1+w_s)g\left[1+0.42216\times10^{-11}\,p\exp(5406.1915/T)\,i_e/\left\{(w_s+0.622)RT\right\}\right]}{c_{pma}+3.6693\times10^{-8}\,w_s^2\,p\exp(5406.1915/T)\,i_e/T} \tag{M.11}$$

and

$$i_e = i_{fgwo} - \left(c_{pw} - c_{pv}\right)\left(T - 273.15\right) \tag{M.12}$$

M.3 FLOW DRIVING POTENTIAL

The oldest and simplest form of the driving potential in natural draft cooling towers, which is still used today to approximate the draught, is

$$\Delta p_{\mathrm{a}} = \left(\rho_{\mathrm{avi}} - \rho_{\mathrm{avo}}\right) gH = \sum K \frac{\rho_{\mathrm{av}} v_{\mathrm{av}}{}^2}{2} = \sum K \frac{m_{\mathrm{av}}{}^2}{2\rho_{\mathrm{av}} A^2} \tag{M.13}$$

where ρ_{avo} is the air density at the fill elevation outside the cooling tower and ρ_{avi} is the density inside at the fill elevation. For the reference tower in Appendix K, this simple model can be expressed as

$$\Delta p_{\mathrm{a}} = \left(\rho_{\mathrm{av1}} - \rho_{\mathrm{av5i}}\right) g\left(H_6 - H_3 + \frac{L_{\mathrm{fi}}}{2}\right) = \sum K \frac{m_{\mathrm{av15}}{}^2}{2\rho_{\mathrm{av15}} A^2} \tag{M.14}$$

where ρ_{av5i} is the mean density of the air-vapour mixture inside the tower at the mean fill elevation.

The more rigorous definition is however the difference between the aerostatic pressure inside and outside the tower at elevation 5, shown in Fig. (K.1), which can be written as

$$\begin{aligned} \Delta p_{\mathrm{a}} &= p_{\mathrm{a34,o}} - p_{\mathrm{a34,i}} = \left[\left(p_{\mathrm{a1}} - p_{\mathrm{a7}}\right) - \left(p_{\mathrm{a1}} - p_{\mathrm{a34}}\right)\right]_{\mathrm{o}} - \left[\left(p_{\mathrm{a34}} - p_{\mathrm{a6}}\right) + \left(p_{\mathrm{a6}} - p_{\mathrm{a7}}\right)\right]_{\mathrm{i}} \\ &= \sum K \frac{m_{\mathrm{av15}}{}^2}{2\rho_{\mathrm{av15}} A^2} + \alpha_{\mathrm{e6}} \frac{\left(\frac{m_{\mathrm{av6}}}{A_{\mathrm{fr}}}\right)^2}{2\rho_{\mathrm{av6}}} \end{aligned} \tag{M.15}$$

The $(p_{\mathrm{a1}} - p_{\mathrm{a7}})$ and $(p_{\mathrm{a1}} - p_{\mathrm{a34}})$ terms can be determined by consistently applying one of the Eqs (M.2), (M.3), (M.5), (M.6) or (M.8) evaluated at an elevation of $z = H_6$ and $(H_3 + L_{\mathrm{fi}}/2)$ respectively and a temperature of T_{a1}. The pressure difference between the fill outlet and cooling tower outlet, $(p_{\mathrm{a34}} - p_{\mathrm{a6}})$, is determined from Eq. (M.10) for a temperature of $T_{sc}=T_{a5}$ and an elevation of $z = (H_6 - H_3 - L_{\mathrm{fi}}/2)$. However for direct comparison with a *FLUENT*® single phase model, Eq. (M.6) can be used instead. The outlet loss, $(p_{\mathrm{a6}} - p_{\mathrm{a7}})$ is determined from the following equation proposed by Kröger (2004):

$$\left(p_{\mathrm{a6}} - p_{\mathrm{a7}}\right) = \left(0.02 Fr_{\mathrm{D}}^{-1.5} - \frac{0.14}{Fr_{\mathrm{D}}}\right) \frac{\left(\frac{m_{\mathrm{av5}}}{A_6}\right)^2}{\rho_{\mathrm{av6}}} \tag{M.16}$$

where

$$Fr_D = \left(m_{av5}/A_6\right)^2 / \left[\rho_{av6}\left(\rho_{av7} - \rho_{av6}\right) g d_6\right] \tag{M.17}$$

The flow potential and pressure differences in Eq. (M.15) are determined for the different models and presented in Table M.1.

Table M.1 : The effect of different pressure distribution models on natural draft wet-cooling tower driving potential.

Model description			Pressure difference, N/m^2					
Drive potential	Atmosphere	Inside	$(p_{a1}- p_{a7})$	$(p_{a1}- p_{a34})$	$(p_{a34}- p_{a6})$	$(p_{a6}- p_{a7})$	Δp_a	Deviation
Eq. (M.14) (App. K dry air)			---	---	---	---	53.0	-21%
Eq. (M.14) (App. K air-vapour mixture)			---	---	---	---	66.9	0%
Eq. (M.15)	Eq. (M.2)	Eq. (M.10)	1452.8	111.8	1269.2	-3.6	73.1	9%
Eq. (M.15)	Eq. (M.3)	Eq. (M.10)	1445.7	111.3	1269.2	-3.6	66.7	-1%
Eq. (M.15)	Eq. (M.5)	Eq. (M.10)	1446.3	111.3	1269.2	-3.6	67.2	0%
Eq. (M.15)	Eq. (M.6)	Eq. (M.10)	1442.7	111.3	1269.2	-3.6	63.6	-5%
Eq. (M.15)	Eq. (M.8)	Eq. (M.10)	1383.4	91.0	1269.2	-3.6	8.7	-87%
Eq. (M.15)	Eq. (M.5)	Eq. (M.6)	1446.3	111.3	1268.4	-3.6	68.0	1%

M.4 CONCLUSIONS

In Table M.1, pressure differences and drive potentials results are presented for different pressure distribution models which are compared to the reference constant humidity model, used in the natural draught wet-cooling tower calculation in Appendix K. It can be seen that the simple model gives different results if the densities are determined for dry air than if they are determined for an air-vapour mixture, where the latter gives almost the same result as the reference model. The temperature inversion model differs significantly from the other models, which only deviate marginally from each other.

N

AXISYMMETRIC CFD MODEL OF A NATURAL DRAUGHT WET-COOLING TOWER

N.1 INTRODUCTION

In the design of a modern natural draft wet-cooling tower, structural and performance characteristics must be considered. Air flow distortions and resistances must be minimised and heat and mass transfer maximised to achieve optimal cooling which requires that the cooling towers must be modelled two dimensionally and ultimately three dimensionally, to be optimised. CFD models found in literature (Al-Waked, 2006, 2007, 2010, Williamson, 2008a, 2008b, 2008c, and Klimanek, 2008, 2009, 2010) are limited to cooling towers packed with film or orthotropic fills which are porous in one direction only and have relatively high loss coefficients. This simplifies the numerical analysis considerably due to reduced flow separation at the air inlet and vertical flow through the fill, which can be modelled by means of the simple Merkel or Poppe methods of analysis using available fill characteristics. Many cooling towers are however packed with trickle and splash fills which have anisotropic flow resistances, which means that the fills are porous in all flow directions and thus air flow can be oblique through the fill, especially near the cooling tower air inlet where the flow turns through about 90º inside the fill after it has entered the tower. Fill performance characteristics are however limited to purely counter- and crossflow configuration due to the availability of fill test facilities. A two-dimensional fill performance model was therefore developed as presented in Appendix J.

This appendix presents a new steady state axisymmetric CFD model for a natural draught wet-cooling tower packed with anisotropic fills, developed within *FLUENT*® version 6.3. This model, which is applicable to general design conditions with no cross-wind, is validated by comparing the results to corresponding one-dimensional model data according to Appendices K and L for a stainless steel expanded metal fill and results obtained for trickle fill employing the same method of analysis.

The proposed *FLUENT*® model, which is developed to optimise natural draught wet-cooling towers, can predict the performance of natural draft wet-cooling towers for any given design configuration. It can therefore be applied to investigate the effects on cooling tower performance due to variation of: atmospheric temperature and humidity distribution, air inlet and outlet geometries, air inlet height, cooling tower diameter, radial water loading and fill height, fill and spray zone configuration, Lewis factor, cross- to counterflow Merkel number ratio, saturation level of the air leaving the fill, and rain zone drop size distribution. Furthermore the effects of boiler flue gas discharge in the centre of

the tower and damage or removal of fill in certain concentric sections of the cooling tower can be investigated.

This appendix gives a description of the *FLUENT*® model and compares the numerical results obtained for different cases to corresponding one dimensional data obtained with the computational model of which a sample calculation is presented in Appendix K.

It is assumed that the reader has sound background knowledge of CFD, however additional information can be found in *ANSYS-FLUENT* (2006).

N.2 CFD MODEL DESCRIPTION

In this section, the flow domain, boundary definitions, mesh type and size, models and input values of the *FLUENT*® model are presented and discussed. The cooling tower geometry and dimensions of the model are shown in Fig N.1, and are based on the reference cooling tower presented in Appendix K.

N.2.1 Flow domain, boundary definitions and mesh

GAMBIT® (the *FLUENT*® meshing tool) is used to create the flow geometry and mesh and to define the boundaries and flow regions, as depicted in Figures N.1 and N.2.

The fill region has a uniform quadrilateral mesh of 0.025 x 0.025 m cells. From the fill border, the cell size increases at a constant growth rate of 5% to a size of 0.1 x 0.1 m in the rain and drift eliminator zones by making use of growth functions and the quad pave meshing scheme. In previous appendices, it was shown that when modelling cooling tower inlet losses and rain zone performance, sufficient grid independence is achieved with cell sizes of 0.1 x 0.1 m, as also employed by Williamson (2008).

However, to achieve acceptable energy balances below 1 % for the new fill model, smaller cells are required in the fill region.

The non-equilibrium wall function is used for the boundary layer calculation along the wall boundaries, which requires that the centroids of wall adjacent cells should be within the log-law layer, i.e. $30 < y^+ < 300$. To achieve this, the wall cell height needs to be 0.05 m for the ground and pond boundaries and 0.025 m for the shell walls.

To minimise the number of cells and maximize accuracy, the quad pave meshing scheme is used in the remaining regions, which develops from a mesh size of 0.125 m at the border of the rain and drift eliminator regions and where the mesh connects to the wall boundary layer mesh, increasing with a growth rate of 5 % to a maximum cell size of 2 m in regions of low air speed and velocity gradients.

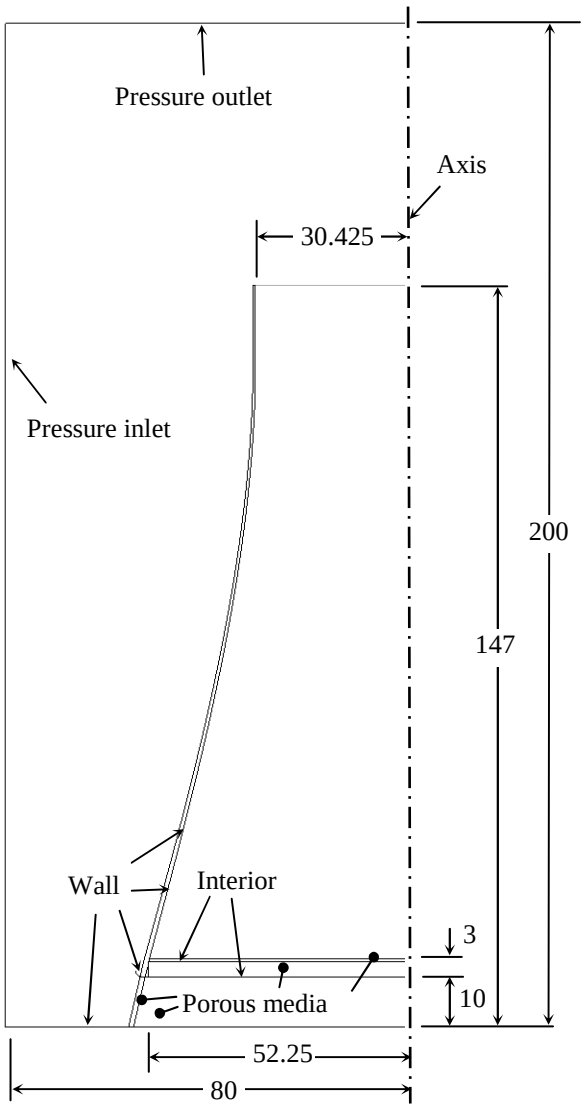

Figure N.1 : Axisymmetric computational flow domain showing main dimensions in metres and boundary definitions.

N.2.2 Numerical models, input data and user defined functions

In essence, the *FLUENT*® model developed in this appendix is a steady two-dimensional axisymmetric model comprising a single phase (mixture of air and water vapour) Eulerian model with species transport for the gas (continuous) phase flow and Lagrangian particle tracking or discrete phase model (DPM) for the water drops in the rain zone. For the continuous phase, the conservation equations for mass, momentum, energy and species mixing, with buoyancy; the k-ε realizable turbulence model, and the non-equilibrium wall function model are solved by employing the double precision, axisymmetric, steady state, segregated solver and the SIMPLE algorithm for the pressure-velocity coupling. Second order discretization is employed for all the governing equations and a body-force-weighted scheme for pressure interpolation.

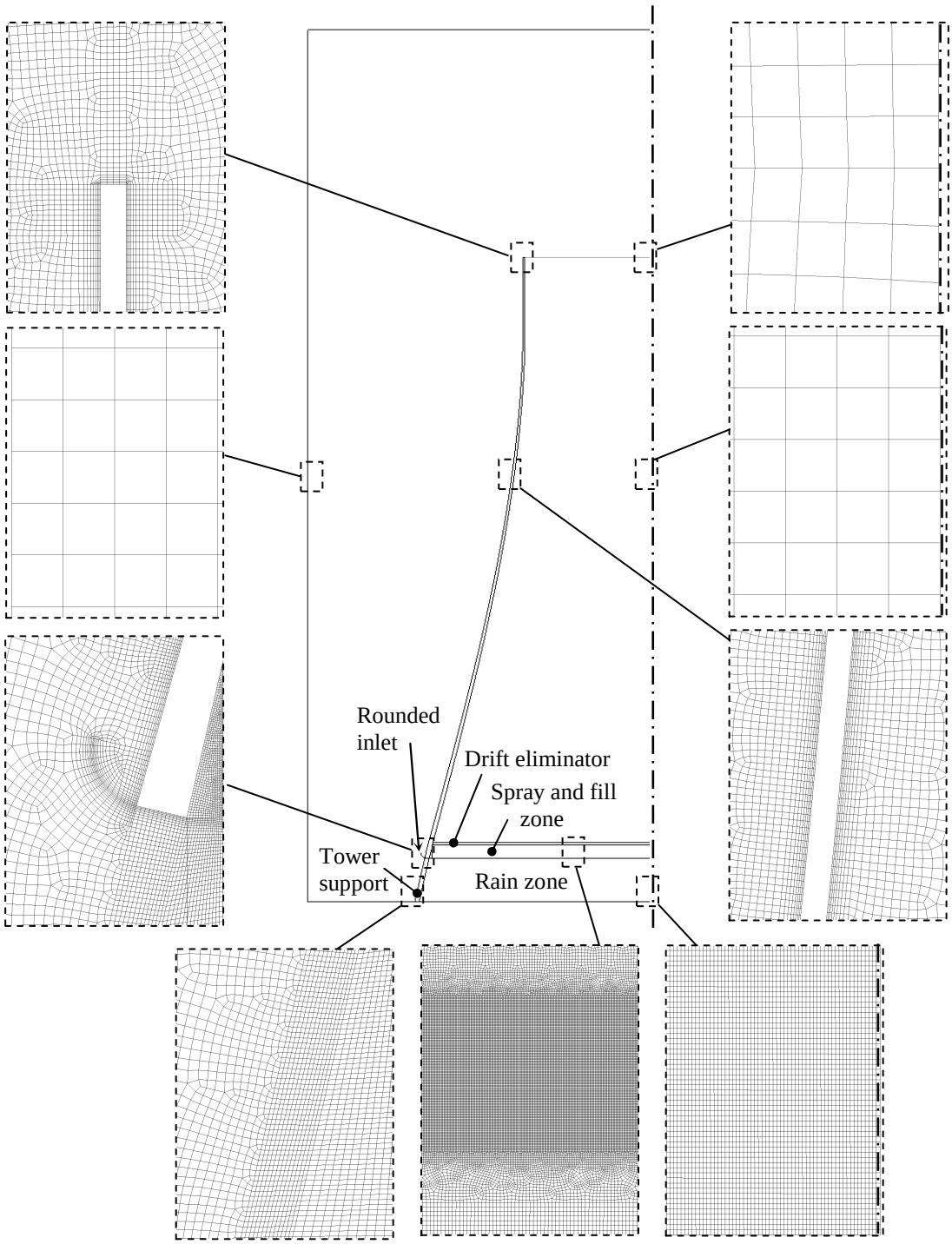

Figure N.2 : Axisymmetric computational flow domain showing enlarged mesh details in certain areas.

The heat and mass transfer in the fill zone is solved by utilizing a user defined function (UDF) routine based on the method of analysis proposed in Appendix J. The model assumes a Lewis factor of Le_f = 1 in order to make use of Merkel

method fill characteristics. This UDF, which is called at the end of every *FLUENT*® iteration, creates cell reference numbers and reads the flow properties ($v_{a,r}$, $v_{a,z}$, p_a, T_a and m_v/m_{av}) in individual cells in the fill and spray zone region. It then calculates the thermophysical properties (w, w_{sa}, w_{sw}, c_{pma}, c_{pv}, c_{pw}, i_{fg}, k_{av}, ρ_{av}, G_a) according to the equations in Appendix A and subsequently determines the Merkel number, loss coefficient, Lewis factor, cooling water temperature, cooling water mass velocity, energy source term, momentum source term and vapour species mass source term for each cell in the fill and spray zones. The respective Merkel numbers for the spray and fill zones are determined from the following relations:

$$\mathrm{Me}_{\mathrm{sp(i,j)}} = \left\{ 0.2\left(\frac{\mathrm{G_a}}{\mathrm{G_w}}\right)^{1/2} \Delta \mathrm{z} \right\}_{\mathrm{(i,j)}} \tag{N.1}$$

$$\mathrm{Me}_{\mathrm{fi(i,j)}} = \left\{ 0.25575\mathrm{G_w^{-0.094}G_a^{0.6023}}\left[\mathrm{X} + (1-\mathrm{X})\left(\frac{\varphi}{90^{\mathrm{o}}}\right)\right]\Delta \mathrm{z} \right\}_{\mathrm{(i,j)}} \tag{N.2}$$

for the stainless steel expanded metal fill and

$$\mathrm{Me}_{\mathrm{fi(i,j)}} = \left\{ 1.64107\mathrm{G_w^{-0.712}G_a^{0.576}}\left[\mathrm{X} + (1-\mathrm{X})\left(\frac{\varphi}{90^{\mathrm{o}}}\right)\right]\Delta \mathrm{z} \right\}_{\mathrm{(i,j)}} \tag{N.3}$$

for trickle fill, where

$$\mathrm{X}_{\mathrm{(i,j)}} = \left\{ \frac{\mathrm{Me_{cross}}}{\mathrm{Me_{counter}}} \right\}_{\mathrm{(i,j)}} \tag{N.4}$$

The spray and fill zone loss coefficients are determined from:

$$\mathrm{K}_{\mathrm{sp(i,j)}} = \left\{ 0.4\left(\frac{\mathrm{G_w}}{\mathrm{G_a}}\right) + 1 \right\}_{\mathrm{(i,j)}} \tag{N.5}$$

$$\mathrm{K}_{\mathrm{fi(i,j)}} = \left\{ 1.851\mathrm{G_w^{1.2752}G_a^{-1.0356}} + 0.19142 \right\}_{\mathrm{(i,j)}} \tag{N.6}$$

for the expanded metal fill and

$$\mathrm{K}_{\mathrm{fi(i,j)}} = \left\{ 20.817\mathrm{G_w^{0.071}G_a^{-0.253}} \right\}_{\mathrm{(i,j)}} \tag{N.7}$$

for the trickle fill.

The cooling water temperature change in each cell is determined from the following equations for unsaturated and supersaturated air respectively:

$$\delta \mathrm{T}_{\mathrm{w(i,j)}} = \left\{ \frac{\mathrm{c_{pma}}}{\mathrm{c_{pw}}} \mathrm{Me}\left[\mathrm{Le_f}\left(\mathrm{T_w} - \mathrm{T_a}\right) + \frac{\mathrm{i_{fg}}}{\mathrm{c_{pma}}}\left(\mathrm{w_{sw}} - \mathrm{w}\right)\right] \right\}_{\mathrm{(i,j)}} \tag{N.8}$$

$$\delta \mathrm{T}_{\mathrm{w,ss(i,j)}} = \left\{ \frac{\mathrm{c_{pma}}}{\mathrm{c_{pw}}} \mathrm{Me}\left[\mathrm{Le_f}\left(\mathrm{T_w} - \mathrm{T_a}\right) + \frac{\mathrm{i_{fg}}}{\mathrm{c_{pma}}}\left(\mathrm{w_{sw}} - \mathrm{w_s}\right)\right] \right\}_{\mathrm{(i,j)}} \tag{N.9}$$

The vapour species mass source terms for unsaturated and saturated air are calculated from:

$$S_{m(i,j)} = \left\{ \frac{Me\, G_w}{\Delta z} \left(w_{sw} - w \right) \right\}_{(i,j)} \tag{N.10}$$

$$S_{m,ss(i,j)} = \left\{ \frac{Me\, G_w}{\Delta z} \left(w_{sw} - w_s \right) \right\}_{(i,j)} \tag{N.11}$$

and the respective air energy source terms from:

$$S_{q(i,j)} = \left\{ \frac{Me\, G_w}{\Delta z} \left(T_w - T_a \right) \left[Le_f c_{pma} + c_{pv} \left(w_{sw} - w \right) \right] \right\}_{(i,j)} \tag{N.12}$$

$$S_{q,ss(i,j)} = \left\{ \frac{Me\, G_w}{\Delta z} \left(T_w - T_a \right) \left[Le_f c_{pma} + c_{pv} \left(w_{sw} - w_s \right) + c_{pw} \left(w - w_s \right) \right] \right\}_{(i,j)} \tag{N.13}$$

The fill and spray zone momentum source terms in the r- and z-directions respectively are determined from:

$$S_{mom,r(i,j)} = \left\{ -\frac{K_r \rho_a}{2} \left| v_{a,r} \right| v_{a,r} \right\}_{(i,j)} \tag{N.14}$$

$$S_{mom,z(i,j)} = \left\{ -\frac{K_z \rho_a}{2} \left| v_{a,z} \right| v_{a,z} \right\}_{(i,j)} \tag{N.15}$$

Furthermore, the UDF calculates the rain zone inlet temperature and mass flow rate for the cells adjacent to the rain zone inlet. Certain values such as the energy, momentum and vapour species mass source terms and the rain zone inlet temperature and mass flow rate are stored in allocated user defined memory (UDM) in order to be transferred to *FLUENT*® by UDF DEFINE functions, before continuing with the next *FLUENT*® iteration. For the DPM, the trajectories of the drops as well as the heat and mass transfer to or from them are calculated by numerical integration of the governing motion and energy equations as discussed in Appendices B and C, with two-way interaction between the continuous and discrete phases. A UDF is employed to make use of the improved drop drag model of Dreyer (1994), which takes into account varying drop deformation due to acceleration of the drops.

The pressure distribution at the inlet boundary to the flow domain is defined by a PROFILE UDF which makes use of the isothermal pressure distribution according to Eq. (M.6).

The air-side flow resistances due to the cooling tower inlet and rain zone are solved directly by *FLUENT*. Other flow resistances, such as the cooling tower shell and fill support columns, fill, water spray, water distribution system and drift eliminators are modelled by means of porous zones defined in the regions where they are situated. Each porous zone is given the relevant loss coefficient (Kröger 2004) to calculate the losses across it. The loss coefficients for the tower and fill supports are constants whereas momentum source terms determined in the fill UDF, are employed for the fill, water spray, water distribution system and drift eliminators.

The *FLUENT*® input data for the models used, material properties, operating conditions, boundary conditions, DPM injections and solve controls, are summarised in Tables O.1 to O.8 in Appendix O.

N.3 VALIDATION OF RESULTS

In this section, the CFD results obtained with the above *FLUENT*® model are compared to corresponding data from the one-dimensional computational model in Appendix K for a round inlet and expanded metal (EM) fill. Similar comparisons are also done for the cases of a square inlet, different Sauter mean drop diameters in the rain zone, and different cooling tower inlet heights. Finally the one-dimensional results obtained for trickle fill, using the same method of analysis presented in Appendix K, are compared to corresponding *FLUENT*® data for two different rain zone drop diameters.

N.3.1 Comparison between one-dimensional model and the *FLUENT*® model for expanded metal fill and a round inlet

Table N.1 shows the one-dimensional model results from Appendices K and L in the first data column and data for different comparable CFD cases in the adjacent columns, for the expanded metal fill.

Case N.1 is for a counter- to crossflow Merkel number ratio of X = 1.0, a fill zone grid size of 0.025 x 0.025 m, supersaturated air at the fill outlet and no-slip conditions at the wall boundaries. To verify grid independence, Case N.2 has a courser grid in the fill zone. For Case N.3 the supersaturated air leaving the fill is adjusted to saturation conditions keeping the air enthalpy constant, in order to be more comparable with the air outlet conditions obtained with one-dimensional model using the Merkel method of analysis, which could influence the draught. Cases N.4 and N.5 are for different counter- to crossflow Merkel number ratios of X = 0.9 and 0.8 respectively showing a 0.8 % and 2.0 % decrease in the cooling range respectively. For Case N.6, the wall boundaries are defined as slip as opposed to no-slip, to confirm that boundary layer effects on cooling tower performance are negligible.

The following graphs and figures show the variation of various parameters in the cooling tower and are based on Case N.4 in Table N.1. Fig. N.3 shows absolute and relative cooling water temperatures in the fill and rain zones. From Fig. N.3(a) it can be seen that the fill performance is poor in the outer ring region ($r/ r_{fi} > 0.925$) and that the maximum cooling range of $\Delta T_w/ \Delta T_{w,m} \approx 1.2$ and the minimum of $\Delta T_w/ \Delta T_{w,m} \approx 0.73$ are at $r/ r_{fi} \approx 0.925$ and $r/ r_{fi} = 0$ respectively, changing almost linearly along the radius from maximum to minimum. Fig. N.3(b) shows that the rain zone range is consistently about 20% of the overall cooling range along the radius. In Fig. N.3(c) a region of high cooling water temperature and thus reduced fill performance is observed near the cooling tower inlet.

The pathlines in Fig. N.8(a) illustrate that the atmospheric air is drawn into the tower from a region roughly half the height of the cooling tower. The velocity profiles in Fig. N.4(a) however show that most of the air seems to come from a region closer to the ground. From Fig. N.4(b), it can be seen that the radial velocity varies significantly, being almost double at the upper ring beam to that at ground level.

The enlarged vector and a streamline plots of the cooling tower inlet region presented in Figs N.8(b) and (c), show flow separation and air recirculation in the fill, which results in reduced fill performance in this region, as confirmed in Fig N.3. Furthermore, the air flow passing through the fill is found to be predominantly oblique, since the fill is isotropic with a low loss coefficient. This results in higher absolute air mass velocities in the fill than for orthotropic fill with vertical air flow, and consequently the Merkel number factor (Eq. N.3) is expected to influence the fill performance, as confirmed by the results in Table N.1.

Fig. N.5(a) shows that near the cooling tower shell, the axial air mass velocity is very low due to the flow separation and air recirculation, increasing to a maximum at $r/r_{ct,z} \approx 0.94$ before decreasing again to a almost uniform axial mass velocity at $r/r_{ct,z} < 0.82$. Comparing Figs N.5(a) and (b), the total mass velocity at the inlet below the fill is significantly higher than the axial velocity component ascribed to the obliqueness of the flow.

In Fig. N.6, the temperature and humidity ratio of the recirculating air are high as expected, both dropping sharply as one moves away from the flow separation bubble before gradually increasing towards the centre. Fig. N.7 shows that the flow driving potential is the highest in the centre of the cooling tower and right next to the shell wall. According to Fig. N.9(a), the largest static pressure difference between the air inside and outside the cooling tower is at the bottom of the tower above the fill. As the air flow accelerates, this difference decreases. This shows that a significant increase in draught potential can be achieved if the kinetic energy of the air leaving the cooling tower is decreased. This is however restricted to avoid cold inflow of air into the tower. Figures N.10 and N.11 show that the air density and the velocity magnitude above the fill are non-uniform.

N.3.2 Comparison between one-dimensional model and the *FLUENT*® model for expanded metal fill and a sharp inlet

Table N.2 shows the results from the one-dimensional model for a sharp inlet in the first data column and data for corresponding CFD cases with different Merkel number ratios (X = 1.0, 0.9 and 0.8) in the adjacent columns. It can be seen that *FLUENT*® predicts higher cooling water outlet temperatures than the one-dimensional model.

Similar to the previous section, the following figures are based on the Case N.8 in Table N.2 for X = 0.9. Fig. N.11(a) reveals worse fill performance in the outer ring region ($r/ r_{fi} < 0.9$) than for the round inlet, that a maximum cooling range of $\Delta T_w/ \Delta T_{w,m} \approx 1.3$ and a minimum of $\Delta T_w/ \Delta T_{w,m} \approx 0.8$ occurs at $r/ r_{fi} \approx 0.9$ and

Table N.1 Comparison between one-dimensional model and CFD model data for a rounded inlet.

Description	Symbol	Units	1-D	CFD					
Case no.	---	---	A	N.1	N.2	N.3	N.4	N.5	N.6
Fill type	---	---	EM	Expanded metal (EM)					
Merkel number ratio	X	---	1	1	1	1	0.9	0.8	1
Air outlet condition	---	---	Sat.	Supersat.	Supersat.	Saturated	Supersat.	Supersat.	Supersat.
Fill grid size	Δr or Δz	m	---	0.025	0.050	0.025	0.025	0.025	0.025
Wall boundary condition	---	---	Slip	No-slip	No-slip	No-slip	No-slip	No-slip	Slip
Air inlet geometry	---	---	Round	Round	Round	Round	Round	Round	Round
Air mass flow rate	m_{av5}	kg/s	16965	17331	17356	17199	17262	17188	17412
Air pressure	p_{a1}	Pa	84100	84100	84100	84100	84100	84100	84100
	p_{a3}	Pa	83973	83976	83976	83976	83976	83976	83976
	$p_{a5@13.5m}$	Pa	83917	83919	83918	83919	83919	83919	83918
	p_{a6}	Pa	82651	82650	82650	82650	82650	82650	82650
	p_{a7}	Pa	82654	82654	82654	82654	82654	82654	82654
Air temperature	T_{a1}	ºC	15.45	15.45	15.45	15.45	15.45	15.45	15.45
	T_{a3}	ºC	17.10	17.20	17.20	17.22	17.25	17.32	17.19
	T_{a5}	ºC	26.44	25.99	26.12	26.15	26.03	25.96	26.06
	T_{a6}	ºC	25.98	25.99	26.12	26.15	26.03	25.96	26.06
	T_{a7}	ºC	14.02	15.45	15.45	15.45	15.45	15.45	15.45
Air humidity ratio	w_1	kg/kg_{da}	0.00813	0.00813	0.00813	0.00813	0.00813	0.00813	0.00813
	w_3	kg/kg_{da}	0.01208	0.01160	0.01157	0.01161	0.01167	0.01173	0.0116
	w_5	kg/kg_{da}	0.02680	0.02772	0.02779	0.02632	0.02759	0.02746	0.02766
	w_6	kg/kg_{da}	0.02680	0.02772	0.02779	0.02632	0.02759	0.02746	0.02766
	w_7	kg/kg_{da}	0.00813	0.00813	0.00813	0.00813	0.00813	0.00813	0.00813
Air density	ρ_{av1}	kg/m^3	1.010	1.010	1.010	1.010	1.010	1.010	1.01
	ρ_{av3}	kg/m^3	0.998	1.001	1.001	1.001	1.001	1.000	1.001
	ρ_{av5}	kg/m^3	0.960	0.962	0.961	0.962	0.962	0.962	0.962
	ρ_{av6}	kg/m^3	0.947	0.947	0.947	0.948	0.947	0.948	0.947
	ρ_{av7}	kg/m^3	0.998	0.993	0.993	0.993	0.993	0.993	0.993
Water mass flow rate	m_{wi}	kg/s	12500	12500	12500	12500	12500	12500	12500
Water temperature	T_{wi}	ºC	40.00	40.00	40.00	40.00	40.00	40.00	40.00
	$T_{wi,rz}$	ºC	25.09	24.81	24.90	24.49	25.07	25.35	24.78
	T_{wo}	ºC	21.39	21.35	21.42	21.4	21.54	21.75	21.33

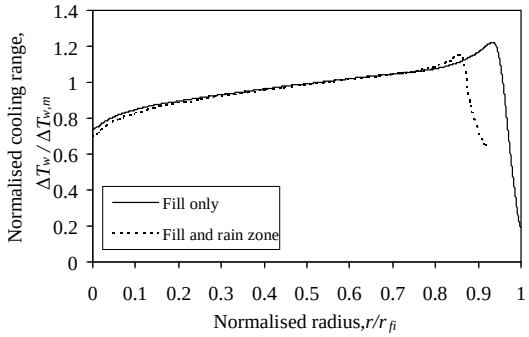

(a) Graph of normalised cooling range plotted against normalised radius.

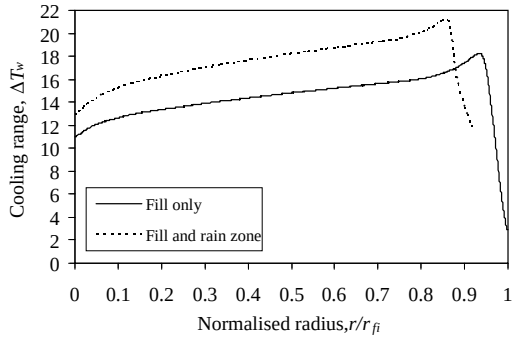

(b) Graph of cooling range plotted against normalised radius.

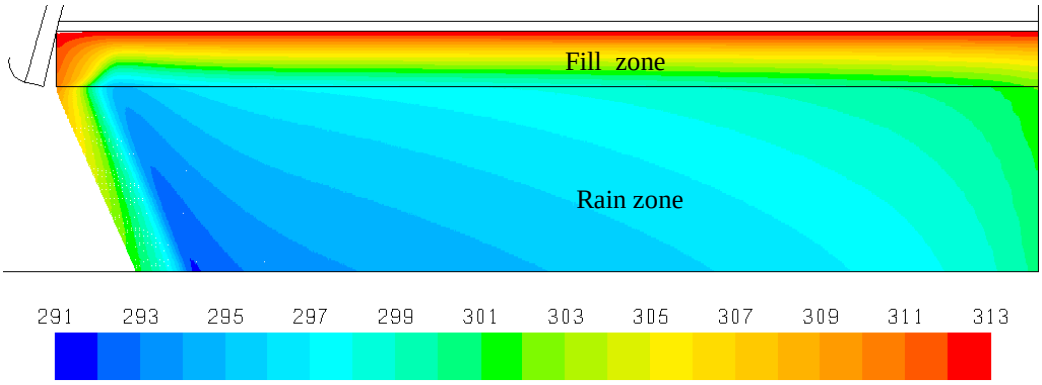

(c) Contour plot of cooling water temperature.

Figure N.3 : Cooling water temperature profiles.

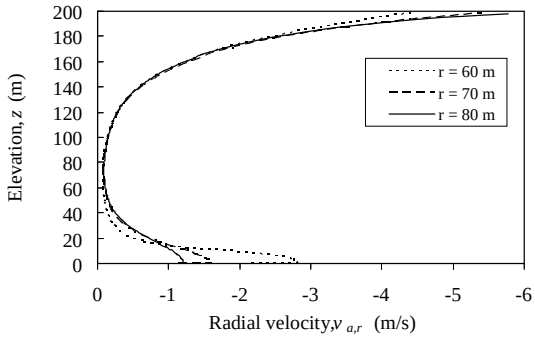

(a) Outside the NDWCT.

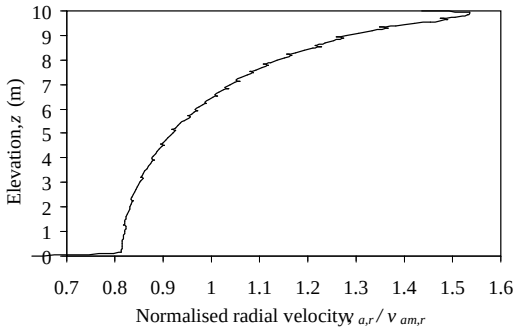

(b) Below the air inlet.

Figure N.4 : Radial component air velocity profiles upstream of the air inlet.

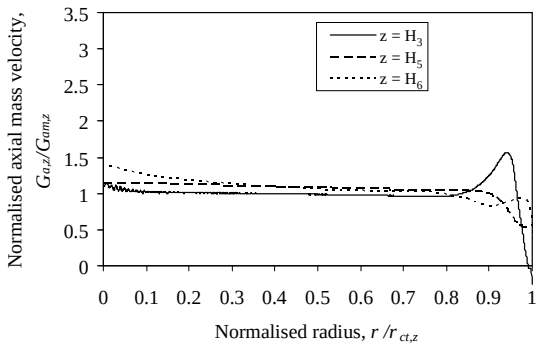

(a) Normalised axial air mass velocity as a function of normalised radius.

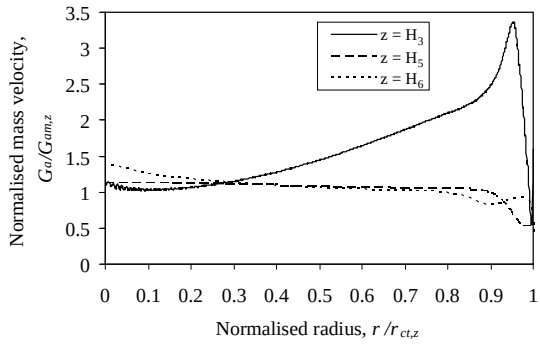

(b) Normalised total air mass velocity as a function of normalised radius.

Figure N.5 : Air mass velocity profiles at different elevations inside the NDWCT.

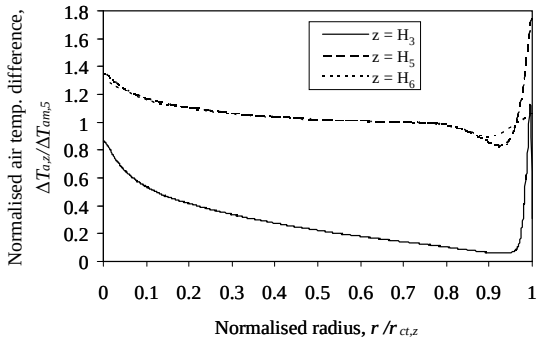

(a) Normalised air temperature change as a function of normalised radius.

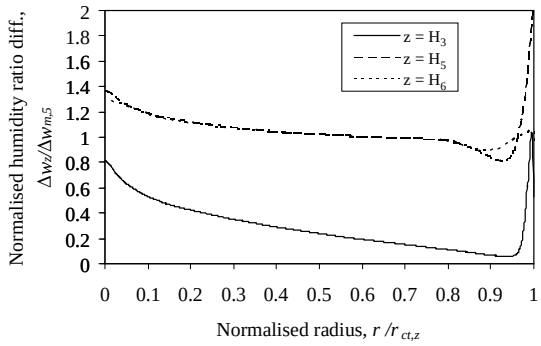

(b) Normalised air humidity ratio change as a function of normalised radius.

Figure N.6 : Air temperature and humidity ratio change at different elevations inside the NDWCT.

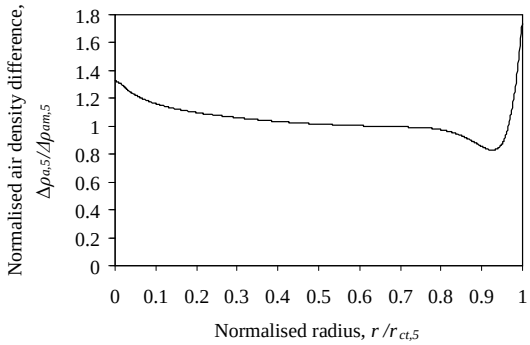

Figure N.7 : Air density difference between the air inside and outside the cooling tower at the elevation where the air leaves the drift eliminators.

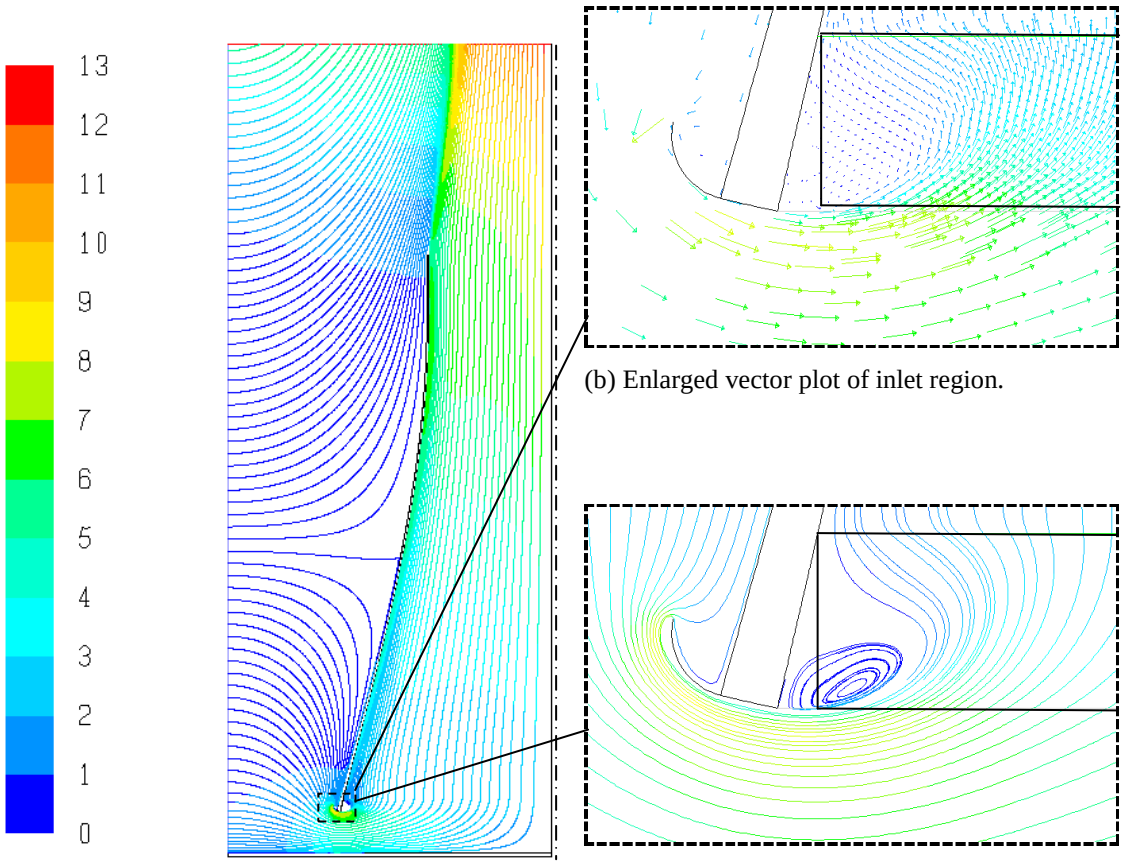

(a) Stream line plot

(b) Enlarged vector plot of inlet region.

(c) Enlarged stream line plot of air inlet region.

Figure N.8 : Streamline and vector plots for the airflow through the NDWCT in m/s.

$r/r_{fi} = 0$ respectively, also changing almost linearly from maximum to minimum. Fig. N.12(b) also shows that the rain zone cooling range is about 20% of the overall cooling range along the radius.

Figures N.12 to N.17 show similar results to Figures N.3 to N.8, with the main difference being the larger flow separation and recirculation region present for the sharp compared to the rounded inlet, which reduces the cooling tower performance significantly. The flow recirculation in the fill is not accounted for in the one-dimensional model and therefore the higher deviation from the CFD results.

From Fig. N.13(b) it is observed that for the sharp inlet the radial inlet velocity profile is far more uniform than for the rounded inlet. Fig. N.14(a) shows that the peak axial mass velocity is higher but the peak absolute velocity is lower than for the round inlet. Due to the added flow recirculation at the inlet, the air temperature and humidity ratio at the air inlet is higher than for the rounded inlet.

N.3.3 Comparison between the one-dimensional model and the *FLUENT*® model for expanded metal fill and different rain zone drop sizes

Table N.3 compares the results from the one-dimensional model for expanded metal fill, a round inlet, and rain zone drop diameters of d = 2.5, 3.5 and 5.5 mm to corresponding CFD cases assuming a Merkel number ratio of X = 0.9, which are found to compare relatively well. It is observed that a change in drop size from d = 5.5 mm to 2.5 mm, results in a increase in cooling range of $\delta(\Delta T_{cw})$ = 2.2 ºC (12 %).

N.3.4 Comparison between the one-dimensional model and the *FLUENT*® model for expanded metal fill and different cooling tower inlet heights

Table N.4 compares the results from the one-dimensional model for expanded metal fill, a rounded inlet, and cooling tower inlet heights of H_3 = 10, 9 and 8 m to corresponding CFD cases assuming a Merkel number ratio of X = 0.9. It is found that a change in air inlet height from H_3 = 10 m to 8 mm, results in a decrease in cooling range of $\delta(\Delta T_{cw})$ = 0.6 ºC (3.1 %).

N.3.5 Comparison between the one-dimensional model and the *FLUENT*® model for expanded metal fill to investigate the effect of a pond wall and stiffening ring structure at the tower outlet

Table N.5 compares the results from the one-dimensional model for expanded metal fill and a rounded inlet, to CFD results obtained when adding a pond wall and stiffening profiles at the tower outlet according to Harte (2002), as shown in Fig. N.18. The one dimensional data is particularly useful to evaluate the effect of the stiffening profile inside the shell, as this reduces the flow area at the tower outlet. It is found that the effect of the pond wall and stiffening profile at the outlet is an increase in cooling range of $\delta(\Delta T_{cw})$ = 0.05 ºC (0.3 %) and a decrease of 0.29 ºC (1.6%) respectively.

N.3.6 Comparison between the one-dimensional model and the *FLUENT*® model for trickle type fill and different rain zone drop diameters

Table N.6 compares the results from the one-dimensional model for trickle fill with a uniform fill height (L_{fi} = 0.68 m to achieve the same thermal performance as Case N.1), a round inlet, and rain zone drop diameters of d = 5.5 mm and 2.5 mm, to corresponding CFD cases, assuming a Merkel number ratio of X = 0.9.

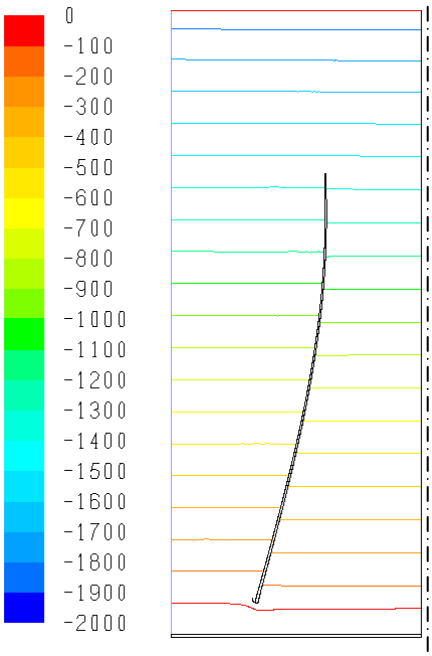

(a) Static pressure

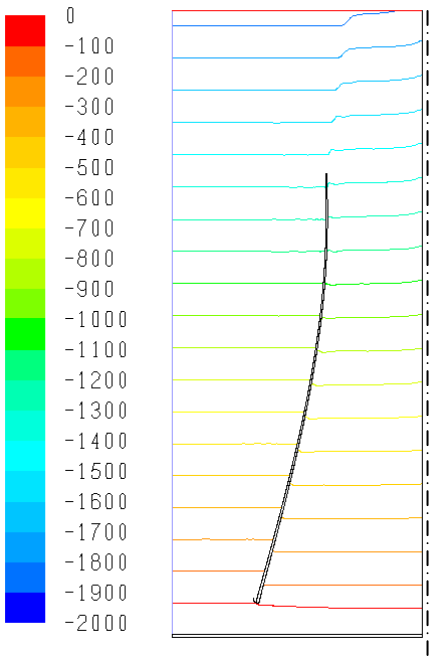

(b) Total pressure

Figure N.9 : Pressure (N/m^2) contours.

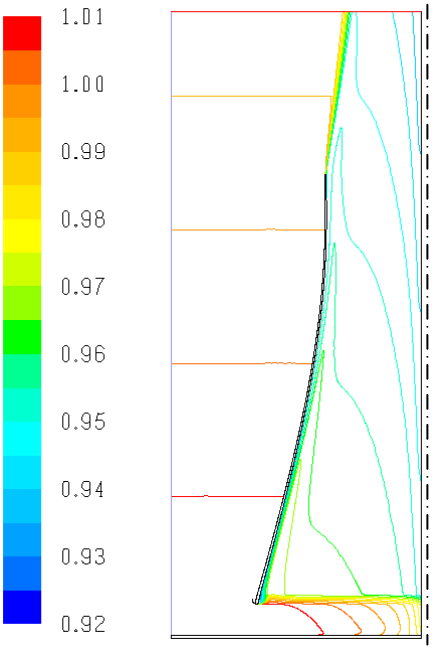

Figure N.10 : Density (kg/m^3) contours.

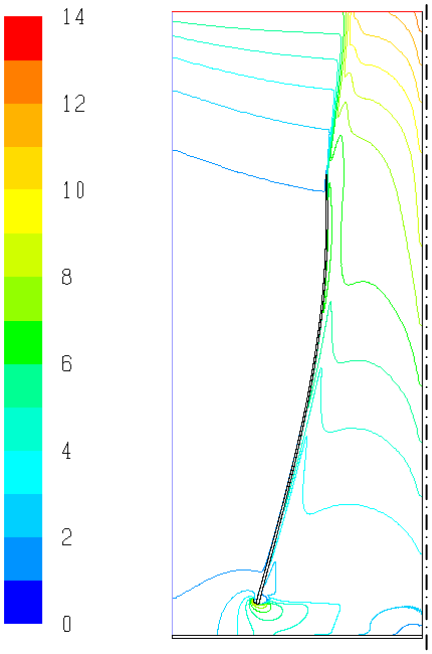

Figure N.11 : Velocity magnitude (m/s) contours.

Table N.2 Comparison between one-dimensional model and CFD model data for a sharp inlet.

Description	Symbol	Unit	1-D	CFD		
Case no.	---	---	B	N.7	N.8	N.9
Fill type	---	---	EM	EM	EM	EM
Merkel number ratio	X	---	1	1	0.9	0.8
Air outlet condition	---	---	Sat.	Supersat.	Supersat.	Supersat.
Fill grid size	Δr or Δz	m	---	0.025	0.025	0.025
Wall boundary condition	---	---	Slip	No-slip	No-slip	No-slip
Air inlet geometry	---	---	Square	Square	Square	Square
Air mass flow rate	m_{av5}	kg/s	16237	16647	16588	16528
Air pressure	p_{a1}	Pa	84100	84100	84100	84100
	p_{a3}	Pa	83968	83975	83975	83975
	$p_{a5@13.5m}$	Pa	83913	83917	83917	83918
	p_{a6}	Pa	82651	82650	82650	82650
	p_{a7}	Pa	82654	82654	82654	82654
Air temperature	T_{a1}	ºC	15.45	15.45	15.45	15.45
	T_{a3}	ºC	17.34	17.70	17.78	17.83
	T_{a5}	ºC	26.77	26.20	26.15	26.18
	T_{a6}	ºC	26.32	26.20	26.15	26.18
	T_{a7}	ºC	14.02	15.45	15.45	15.45
Air humidity ratio	w_1	kg/kg_{da}	0.00813	0.00813	0.00813	0.00813
	w_3	kg/kg_{da}	0.01228	0.01257	0.01263	0.01269
	w_5	kg/kg_{da}	0.02735	0.02780	0.02769	0.02756
	w_6	kg/kg_{da}	0.02735	0.02780	0.02769	0.02756
	w_7	kg/kg_{da}	0.00813	0.00813	0.00813	0.00813
Air density	ρ_{av1}	kg/m^3	1.01	1.01	1.01	1.01
	ρ_{av3}	kg/m^3	1.000	0.998	0.998	0.998
	ρ_{av5}	kg/m^3	0.959	0.962	0.962	0.962
	ρ_{av6}	kg/m^3	0.946	0.947	0.947	0.948
	ρ_{av7}	kg/m^3	0.998	0.993	0.993	0.993
Water mass flow rate	m_{wi}	kg/s	12500	12500	12500	12500
Water temperature	T_{wi}	ºC	40	40	40	40
	$T_{wi,rz}$	ºC	25.42	25.68	25.91	26.15
	T_{wo}	ºC	21.66	22.01	22.18	22.34

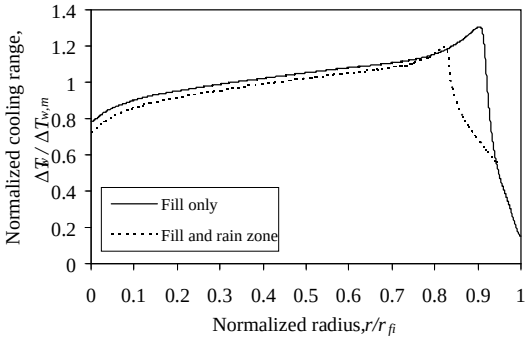

(a) Graph of normalised cooling range plotted against normalised radius.

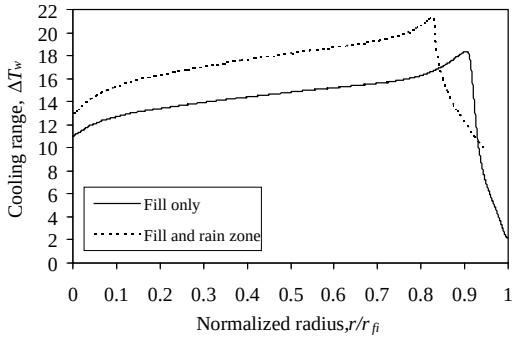

(b) Graph of cooling range plotted against normalised radius.

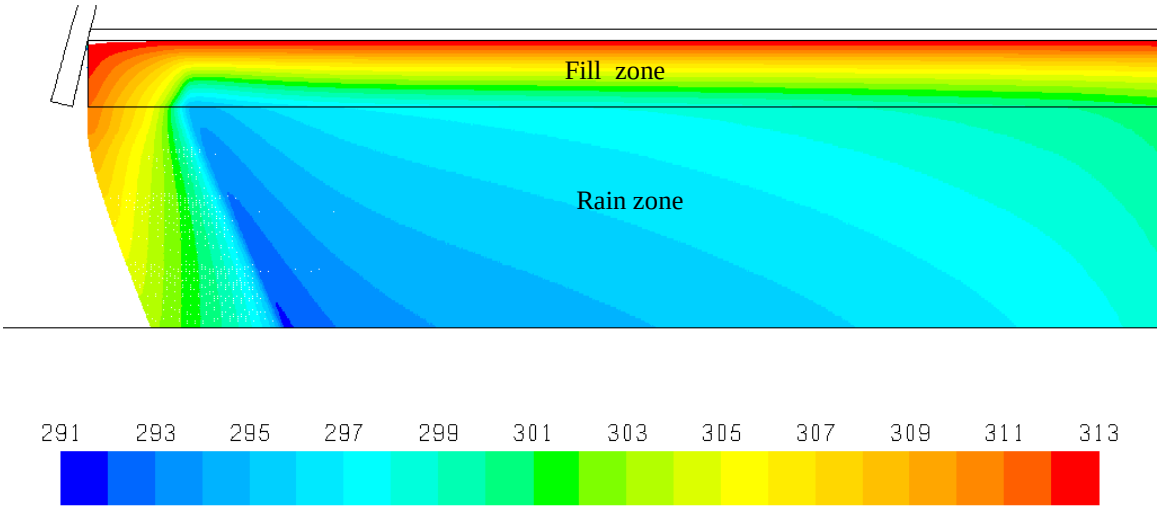

(c) Contour plot of cooling water temperature.

Figure N.12 : Cooling water temperature profiles for a sharp inlet.

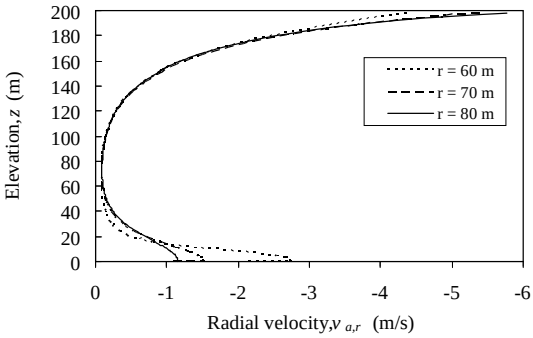

(a) Outside the NDWCT.

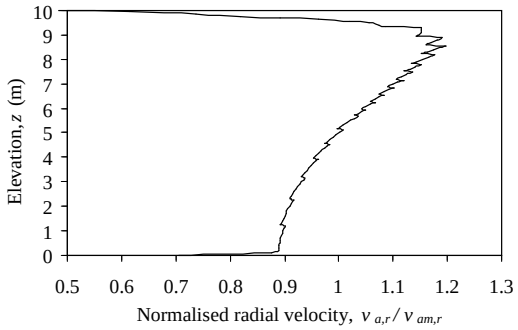

(b) Below the air inlet.

Figure N.13 : Radial component air velocity profiles upstream of the air inlet.

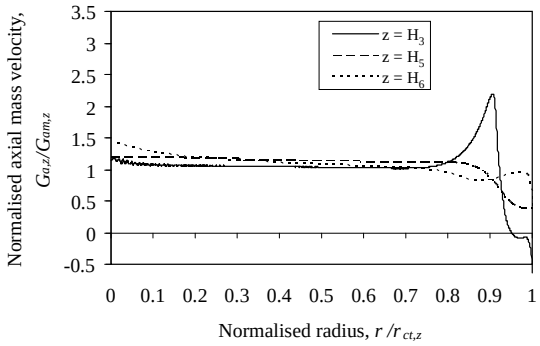

(a) Normalised axial air mass velocity as a function of normalised radius.

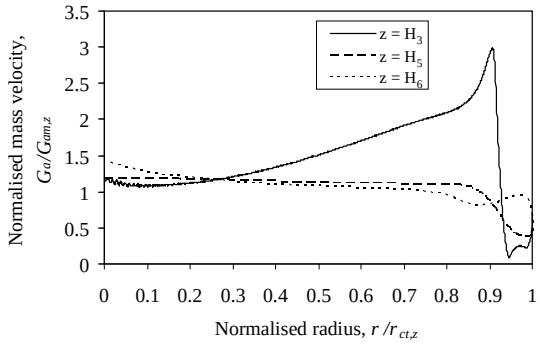

(b) Normalised total air mass velocity as a function of normalised radius.

Figure N.14 : Air mass velocity profiles at different elevations inside the NDWCT.

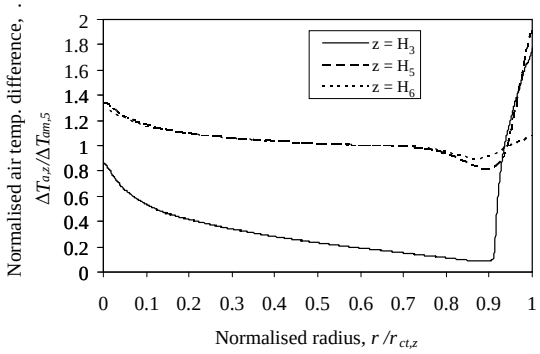

(a) Normalised air temperature change as a function of normalised radius.

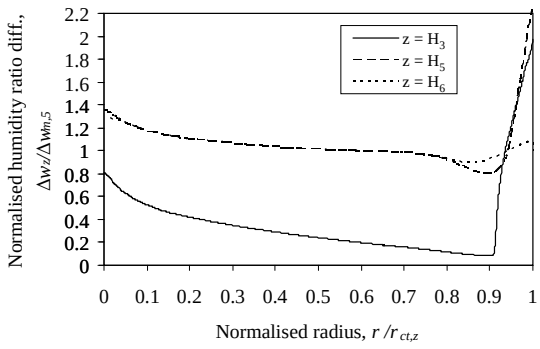

(b) Normalised air humidity ratio change as a function of normalised radius.

Figure N.15 : Air temperature and humidity ratio change at different elevations inside the NDWCT.

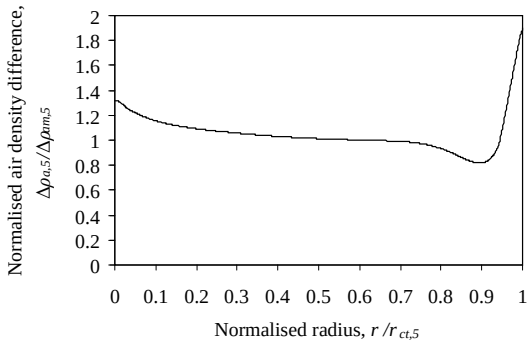

Figure N.16 : Air density difference between the air inside and outside the cooling tower at the elevation where the air leaves the drift eliminators.

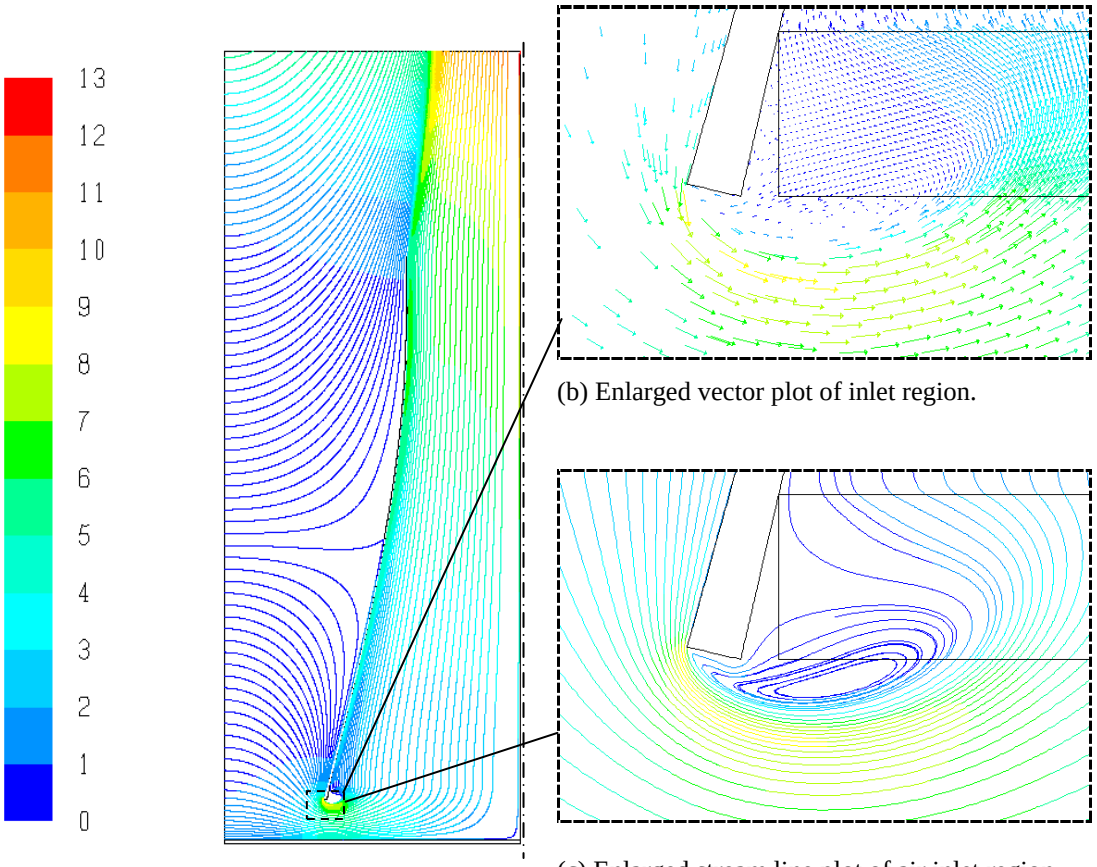

(a) Stream line plot

(b) Enlarged vector plot of inlet region.

(c) Enlarged stream line plot of air inlet region.

Figure N.17 : Streamline and vector plots for the airflow through the NDWCT in m/s.

Table N.3 Comparison between one-dimensional model and CFD model data for a rounded inlet and different drop sizes.

Description	Symbol	Units	1-D	CFD	1-D	CFD	1-D	CFD
Case no.	---	---	A	N.4	C	N.10	D	N.11
Fill type	---	---	EM	EM	EM	EM	EM	EM
Merkel number ratio	X	---	---	0.9	---	0.9	---	0.9
Air outlet condition	---	---	Sat.	Supersat.	Sat.	Supersat.	Sat.	Supersat.
Fill grid size	Δr or Δz	m	---	0.025	---	0.025	---	0.025
Wall boundary condition	---	---	---	No-slip	---	No-slip	---	No-slip
Air inlet geometry	---	---	Round	Round	Round	Round	Round	Round
Rain zone drop diameter	d	mm	3.5	3.5	2.5	2.5	5.5	5.5
Air mass flow rate	m_{av5}	kg/s	16965	17262	17029	17255	16928	17230
Air pressure	p_{a1}	Pa	84100	84100	84100	84100	84100	84100
	p_{a3}	Pa	83973	83976	83967	83974	83976	83978
	$p_{a5@13.5m}$	Pa	83917	83919	83913	83917	83920	83921
	p_{a6}	Pa	82651	82650	82651	82650	82651	82650
	p_{a7}	Pa	82654	82654	82654	82654	82654	82654
Air temperature	T_{a1}	ºC	15.45	15.45	15.45	15.45	15.45	15.45
	T_{a3}	ºC	17.10	17.25	19.02	18.14	15.32	16.47
	T_{a5}	ºC	26.44	26.03	27.18	26.45	25.78	25.46
	T_{a6}	ºC	25.98	26.03	26.73	26.45	25.31	25.46
	T_{a7}	ºC	14.02	15.45	14.02	15.45	14.02	15.45
Air humidity ratio	w_1	kg/kg_{da}	0.00813	0.00813	0.00813	0.00813	0.00813	0.00813
	w_3	kg/kg_{da}	0.01208	0.01167	0.01381	0.01333	0.01064	0.01014
	w_5	kg/kg_{da}	0.02680	0.02759	0.02805	0.02873	0.02572	0.02660
	w_6	kg/kg_{da}	0.02680	0.02759	0.02805	0.02873	0.02572	0.02660
	w_7	kg/kg_{da}	0.00813	0.00813	0.00813	0.00813	0.00813	0.00813
Air density	ρ_{av1}	kg/m^3	1.010	1.010	1.010	1.010	1.010	1.010
	ρ_{av3}	kg/m^3	0.998	1.001	0.993	0.996	1.008	1.004
	ρ_{av5}	kg/m^3	0.960	0.962	0.957	0.956	0.963	0.964
	ρ_{av6}	kg/m^3	0.947	0.947	0.944	0.945	0.950	0.949
	ρ_{av7}	kg/m^3	0.998	0.993	0.998	0.993	0.998	0.993
Water mass flow rate	m_{wi}	kg/s	12500	12500	12500	12500	12500	12500
Water temperature	T_{wi}	ºC	40.00	40.00	40.00	40.00	40.00	40.00
	$T_{wi,rz}$	ºC	25.09	25.07	25.80	25.66	24.46	24.54
	T_{wo}	ºC	21.39	21.54	20.08	20.39	22.50	22.60

Table N.4 Comparison between one-dimensional model and CFD model data for expanded metal fill, a rounded inlet, and different cooling tower inlet heights.

Description	Symbol	Units	1-D	CFD	1-D	CFD	1-D	CFD
Case no.	---	---	A	N.4	E	N.12	F	N.13
Fill type	---	---	EM	EM	EM	EM	EM	EM
Merkel number ratio	X	---	---	0.9	---	0.9	---	0.9
Air outlet condition	---	---	Sat.	Supersat.	Sat.	Supersat.	Sat.	Supersat.
Fill grid size	Δr or Δz	m	---	0.025	---	0.025	---	0.025
Wall boundary condition	---	---	---	No-slip	---	No-slip	---	No-slip
Air inlet geometry	---	---	Round	Round	Round	Round	Round	Round
Cooling tower inlet height	H_3	m	10	10	9	9	8	8
Air mass flow rate	m_{av5}	kg/s	16965	17262	16560	17260	16072	16883
Air pressure	p_{a1}	Pa	84100	84100	84100	84100	84100	84100
	p_{a3}	Pa	83973	83976	83981	83986	83988	83994
	p_{a5}	Pa	83917	83919	83925	83929	83924	83937
	p_{a6}	Pa	82651	82650	82660	82660	82670	82670
	p_{a7}	Pa	82654	82654	82664	82664	82674	82674
Air temperature	T_{a1}	ºC	15.45	15.45	15.45	15.45	15.45	15.45
	T_{a3}	ºC	17.10	17.25	17.01	17.19	16.93	17.20
	T_{a5}	ºC	26.44	26.03	26.54	25.88	26.68	25.95
	T_{a6}	ºC	25.98	26.03	26.07	25.88	26.22	25.95
	T_{a7}	ºC	14.02	15.45	14.03	15.45	14.02	15.45
Air humidity ratio	w_1	kg/kg_{da}	0.00813	0.00813	0.00813	0.00813	0.00813	0.00813
	w_3	kg/kg_{da}	0.01208	0.01167	0.01200	0.01153	0.01193	0.01154
	w_5	kg/kg_{da}	0.02680	0.02759	0.02696	0.02748	0.02719	0.02763
	w_6	kg/kg_{da}	0.02680	0.02759	0.02696	0.02748	0.02719	0.02763
	w_7	kg/kg_{da}	0.00813	0.00813	0.00813	0.00813	0.00813	0.00813
Air density	ρ_{av1}	kg/m^3	1.010	1.010	1.010	1.010	1.010	1.010
	ρ_{av3}	kg/m^3	0.998	1.001	1.001	1.001	1.001	1.001
	ρ_{av5}	kg/m^3	0.960	0.962	0.960	0.962	0.960	0.962
	ρ_{av6}	kg/m^3	0.947	0.947	0.947	0.948	0.947	0.947
	ρ_{av7}	kg/m^3	0.998	0.993	0.998	0.993	0.998	0.993
Water mass flow rate	m_{wi}	kg/s	12500	12500	12500	12500	12500	12500
Water temperature	T_{wi}	ºC	40.00	40.00	40.00	40.00	40.00	40.00
	$T_{wi,rz}$	ºC	25.09	25.07	25.18	25.01	25.34	24.40
	T_{wo}	ºC	21.39	21.54	21.66	21.65	22.00	22.11

Table N.5 Comparison between one-dimensional model and CFD model data for expanded metal fill, a rounded inlet, and different tower pond and air outlet geometries.

Description	Symbol	Units	1-D	CFD	CFD	1-D	CFD
Case no.	---	---	A	N.4	N.14	G	N.15
Fill type	---	---	EM	EM	EM	EM	EM
Merkel number ratio	X	---	---	0.9	0.9	---	0.9
Air outlet condition	---	---	Sat.	Supersat.	Supersat.	Sat.	Supersat.
Fill grid size	Δr or Δz	m	---	0.025	0.025	---	0.025
Wall boundary condition	---	---	---	No-slip	No-slip	---	No-slip
Air inlet geometry	---	---	Round	Round	Round	Round	Round
Pond geometry	---	---	Flat	Flat	1m wall	Flat	Flat
Air outlet geometry	---	---	Cyl.	Cyl.	Cyl.	Cyl.	Stiff. ring
Cooling tower outlet diameter	d_6	m	60.85	60.85	60.85	58.85	59.85
Air mass flow rate	m_{av5}	kg/s	16965	17262	17265	16656	16201
Air pressure	p_{a1}	Pa	84100	84100	84100	84100	84100
	p_{a3}	Pa	83973	83976	83976	83973	83978
	p_{a5}	Pa	83917	83919	83919	83918	83923
	p_{a6}	Pa	82651	82650	82650	82651	82655
	p_{a7}	Pa	82654	82654	82654	82654	82664
Air temperature	T_{a1}	ºC	15.45	15.45	15.45	15.45	15.45
	T_{a3}	ºC	17.10	17.25	17.33	17.20	17.43
	T_{a5}	ºC	26.44	26.03	25.95	26.58	26.35
	T_{a6}	ºC	25.98	26.03	25.95	26.12	26.35
	T_{a7}	ºC	14.02	15.45	15.45	14.02	15.45
Air humidity ratio	w_1	kg/kg_{da}	0.00813	0.00813	0.00813	0.00813	0.00813
	w_3	kg/kg_{da}	0.01208	0.01167	0.01179	0.01216	0.01192
	w_5	kg/kg_{da}	0.02680	0.02759	0.02764	0.02703	0.02844
	w_6	kg/kg_{da}	0.02680	0.02759	0.02764	0.02703	0.02844
	w_7	kg/kg_{da}	0.00813	0.00813	0.00813	0.00813	0.00813
Air density	ρ_{av1}	kg/m^3	1.010	1.010	1.010	1.010	1.010
	ρ_{av3}	kg/m^3	0.998	1.001	1.001	1.000	1.000
	ρ_{av5}	kg/m^3	0.960	0.962	0.962	0.960	0.960
	ρ_{av6}	kg/m^3	0.947	0.947	0.947	0.947	0.946
	ρ_{av7}	kg/m^3	0.998	0.993	0.993	0.998	0.993
Water mass flow rate	m_{wi}	kg/s	12500	12500	12500	12500	12500
Water temperature	T_{wi}	ºC	40.00	40.00	40.00	40.00	40.00
	$T_{wi,rz}$	ºC	25.09	25.07	25.14	25.23	25.52
	T_{wo}	ºC	21.39	21.54	21.49	21.50	21.94

Table N.6 Comparison between one-dimensional model and CFD model data for trickle type fill, a rounded inlet, and different drop diameters in the rain zone.

Description	Symbol	Units	1-D	CFD	1-D	CFD
Case no.	---	---	H	N.16	I	N.17
Fill type	---	---	Trickle	Trickle	Trickle	Trickle
Merkel number ratio	X	---	---	0.9	---	0.9
Air outlet condition	---	---	Sat.	Supersat.	Sat.	Supersat.
Fill grid size	Δr or Δz	m	---	0.025	---	0.025
Wall boundary condition	---	---	---	No-slip	---	No-slip
Air inlet geometry	---	---	Round	Round	Round	Round
Rain zone drop diameter	d	mm	5.5	5.5	2.5	2.5
Air mass flow rate	m_{av5}	kg/s	15835	15983	15812	15925
Air pressure	p_{a1}	Pa	84100	84100	84100	84100
	p_{a3}	Pa	83978	83981	83972	83977
	$p_{a5@13.5m}$	Pa	83910	83911	83903	83907
	p_{a6}	Pa	82650	82650	82650	82649
	p_{a7}	Pa	82654	82664	82654	82654
Air temperature	T_{a1}	ºC	15.45	15.45	15.45	15.45
	T_{a3}	ºC	15.17	16.33	18.79	17.92
	T_{a5}	ºC	27.22	26.73	28.40	27.59
	T_{a6}	ºC	26.76	26.73	27.95	27.59
	T_{a7}	ºC	14.02	15.45	14.02	15.45
Air humidity ratio	w_1	kg/kg_{da}	0.00813	0.00813	0.00813	0.00813
	w_3	kg/kg_{da}	0.01052	0.00993	0.01359	0.01306
	w_5	kg/kg_{da}	0.02811	0.02908	0.03022	0.03103
	w_6	kg/kg_{da}	0.02811	0.02908	0.03022	0.03103
	w_7	kg/kg_{da}	0.00813	0.00813	0.00813	0.00813
Air density	ρ_{av1}	kg/m^3	1.010	1.010	1.010	1.010
	ρ_{av3}	kg/m^3	1.008	1.005	0.994	0.997
	ρ_{av5}	kg/m^3	0.957	0.958	0.952	0.955
	ρ_{av6}	kg/m^3	0.944	0.944	0.939	0.940
	ρ_{av7}	kg/m^3	0.998	0.998	0.998	0.993
Water mass flow rate	m_{wi}	kg/s	12500	12500	12500	12500
Water temperature	T_{wi}	ºC	40.00	40.00	40.00	40.00
	$T_{wi,rz}$	ºC	23.13	23.34	24.60	24.54
	T_{wo}	ºC	21.42	21.65	19.53	19.87

N.4 CONCLUSIONS

From the above results, the following conclusions can be made:

⇨ Relatively small differences are observed between the one-dimensional model results for a round inlet (Case A) and corresponding *FLUENT*® data (Cases N.1, N.4 and N.5) presented in Table N.1. Closer examination reveals that this

is rather fortuitous, since the physics of the two models differ considerably. This is confirmed by the significant difference observed when comparing the one-dimensional results for a sharp inlet (Case B) with equivalent *FLUENT*® data (Cases N.7-N.9) in Table N.2. In the one-dimensional model, the fill characteristics are determined using the mean vertical air mass velocity and the effect of flow separation on fill performance is not taken into consideration. In the *FLUENT*® model however, local fill characteristics are calculated for each cell in the rain, fill and spray zones based on absolute mass velocity values, and the entire flow field is solved numerically, including the flow recirculation in the fill due to flow separation at the cooling tower inlet, showing measurable radial variation in cooling water temperature, air flow rate, air temperature and humidity ratio. In the *FLUENT*® model, the higher local Merkel numbers due to oblique flow through the fill however seem to cancel out the adverse effects of the flow recirculation.

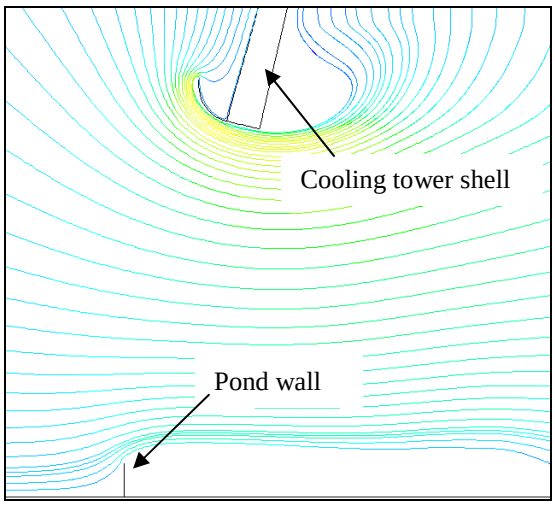

(a) Cooling tower inlet with pond wall.

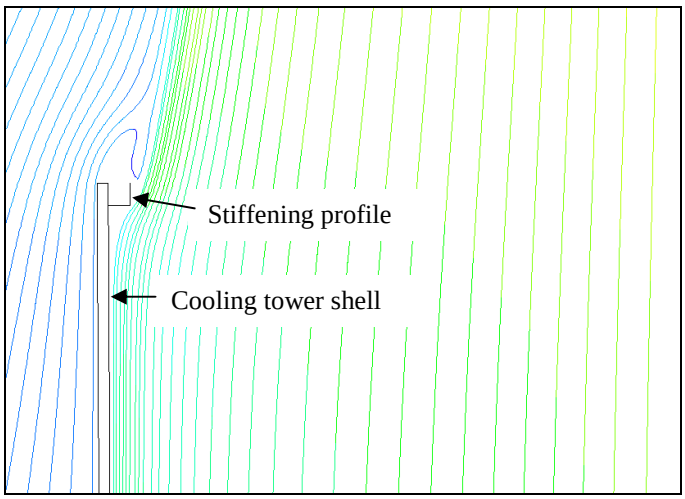

(b) Cooling tower outlet with stiffening profile inside the shell.

Figure N.18 : Streamline plot showing the effect of a pond wall and stiffening structures at the tower outlet on the flow patterns.

- ⇨ The rain zone drop size has a significant effect on cooling tower performance, where the effect of a diameter change from d = 5.5 mm to 2.5 mm results in an increase in cooling range of $\delta(\Delta T_{cw})$ = 2.2 ºC (12 %) for the expanded metal fill compared to an increase of $\delta(\Delta T_{cw})$ = 1.8 ºC (9.6 %) for the trickle fill.
- ⇨ A grid size of 0.025 m in the fill region yields energy balances below 1% and is therefore considered to be sufficiently fine.
- ⇨ Changing the properties of the air leaving the fill from supersaturated to saturated conditions by means of heat and vapour species source terms, which are adjusted iteratively in each cell downstream and adjacent to the drift eliminator zone to achieve the same enthalpy, shows a negligible change in performance.

- ⇨ The difference between using no-slip and slip wall boundaries was also, as expected, found to be negligible.
- ⇨ The effects of a pond wall and stiffening structure inside the shell at the tower outlet is a change in cooling range of $\delta(\Delta T_{cw})$ = 0.05 ºC (0.3 %) and 0.29 ºC (1.6%) respectively.
- ⇨ The effect of decreasing the inlet height is found to be a decrease in cooling range of $\delta(\Delta T_{cw})$ = 0.1 ºC (0.6 %) and 0.6 ºC (3.1 %) for a reduction in inlet height of ΔH_3 = 1 m and 2 m respectively.

From the various cases investigated, it can be seen that by reducing the flow losses and size of the recirculation region at the air inlet, by varying the radial water loading and fill height, and by reducing the drop size in the rain zone, cooling tower performance can be enhanced significantly. By reducing the cooling tower inlet height, the pumping head and possibly cooling tower costs are reduced. The effect of changing the inlet geometry, rain zone drop size and inlet height are summarised in Table N.7.

Table N.7 Evaluation of results obtained from different design parameter changes.

Parameter changed	From	To	Change in cooling range
Inlet geometry	Square	Round	0.6 ºC (3.5%)
Rain zone drop size	d = 3.5 mm	d = 2.5 mm	1.2 ºC (6.2%)
Rain zone drop size	d = 5.5 mm	d = 2.5 mm	2.2 ºC (12%)
Pond	Flat	Incl. pondwall	0.05 ºC (0.3%)
Tower outlet	Cylindrical	Incl. a stiffening ring inside the shell	-0.29 ºC (-1.6%)
Inlet height	H_3 = 10 m	H_3 = 9 m	-0.1 ºC (-0.6%)
Inlet height	H_3 = 10 m	H_3 = 8 m	-0.6 ºC (-3.1%)

O

INPUT DATA TO THE TWO-DIMENSIONAL CFD MODEL OF A NATURAL DRAUGHT WET-COOLING TOWER

N.1 INTRODUCTION

This appendix provides tables containing the input data for the two-dimensional CFD model presented and discussed in Appendix N.

N.2 CFD MODEL INPUT DATA

The *FLUENT*® input data for the models used, material properties, operating conditions, boundary conditions, DPM injections and solve controls, are summarised in Tables O.1 to O.8 below.

Table O.1 : Activated *FLUENT*® model input data.

Description	Setting	Input value
Solver	Pressure based	---
Formulation	Implicit	---
Space	Axisymmetric	---
Time	Steady	---
Velocity formulation	Absolute	---
Gradient option	Green-Gauss cell based	---
Porous formulation	Superficial velocity	---
Multiphase/ Model	Off	---
Energy	Activated	---
Viscous/ Model	k-ε Realizable	---
Viscous/ Near-wall treatment	Non-equilibrium wall functions	---
Viscous/ Options	Full buoyancy effects	
Species/ Model	Species transport	---
Species/ Options	Inlet diffusion	---
Species/ Options	Diffusion energy source	---
Species/ Mixture material	Mixture-template	---
Species/ Number of volumetric species	---	2
DPM/ Interaction	Interaction with continuous phase	---
DPM/ Interaction	Number of continuous phase interactions per DPM iteration	---
DPM/ Tracking/ Tracking parameters	Max. number of steps	50 000
DPM/ Tracking/ Tracking parameters	Step length factor	5
DPM/ Tracking/ Drag parameters/ Drag law	UDF (Dreyer 1994)	---
DPM/ Numerics/ Options	Accuracy control tolerance	1e-9
DPM/ Numerics/ Options	Max. refinements	20
DPM/ Numerics/ Tracking scheme selection	Automated/ High order scheme/ Trapezoidal	---
DPM/ Numerics/ Tracking scheme selection	Automated/ Low order scheme/ Implicit	---

Table O.2 : Activated *FLUENT*® material (mixture) input data.

Description	Setting	Input value	Units
Material type	Mixture	---	---
Properties/ Mixture species	Names/ Selected species	h2o, air	---
Properties/ Density	Ideal gas	---	kg/m^3
Properties/ Specific heat	Mixing law	---	J/kgK
Properties/ Thermal conductivity	Constant	0.0256	W/mK
Properties/ Viscosity	Constant	1.8e-05	kg/ms
Properties/ Mass diffusivity	Constant	2.3e-0.5	m^2/s

Table O.3 : Activated *FLUENT*® material (fluid) input data.

Description	Setting	Input value	Units
Material type	Fluid	---	---
Properties/ Specific heat	Constant	1006.43	J/kgK
Properties/ Molecular weight	Constant	28.966	kg/kgmol
Properties/ Reference temperature	Constant	298.15	K

Table O.4 : Activated *FLUENT*® material (droplet particle) input data.

Description	Setting	Input value	Units
Material type	Droplet particle	---	---
Fluent droplet particle materials	Water-liquid	---	---
Properties/ Density	Constant	997.46	Kg/m^3
Properties/ Specific heat	Constant	4182	J/kgK
Properties/ Thermal conductivity	Constant	0.608	W/mK
Properties/ Latent heat	Constant	2450000	J/kg
Properties/ Vaporization temperature	Polynomial	{0; 1}	K
Properties/ Boiling point	Constant	373	K
Properties/ Volatile component fraction	Constant	100	%
Properties/ Binary diffusivity	Constant	2.3e-05	m^2/s
Properties/ Saturation vapour pressure	Polynomial	{2752231; -40834.89; 228.34; -0.5706257; 0.0005380}	N/m^2
Properties/ Heat of pyrolysis	Constant	0	J/kg

Table O.5 : Activated *FLUENT*® operating condition input data.

Description	Setting	Input value	Units
Pressure/ Operating pressure	---	84100	N/m^2
Reference pressure location	X; Y	0; 81	m
Gravity	Gravity	---	---
Gravitational acceleration	X; Y	-9.8; 0	m/s^2
Boussinesq parameters	Operating temperature	288.6	K
Boussinesq parameters	Operating density	0	kg/m^3

Table O.6 : Activated *FLUENT*® boundary condition input data.

Description	Boundary type	Setting	Input value	Units
Domain inlet	Pressure inlet	Momentum/ Gauge total pressure	UDF	N/m^2
		Momentum/ Turbulence intensity	2	%
		Momentum/ Turbulent length scale	0.1	m
		Thermal/ Total temperature	288.6	K
		Species/ Species mass fraction	0.008061496	kg/kg
Domain outlet	Pressure outlet	Momentum/ Gauge pressure	-1965	N/m^2
Tower centreline	Axis	---	---	---
Ground	Wall	Momentum/ Specified shear/ X and Y	0	N/m^2
Pond	Wall	Momentum/ Specified shear/ X and Y	0	N/m^2
		DPM/ Escape	---	---
Shell	Wall	Momentum/ Specified shear/ X and Y	0	N/m^2
Round inlet	Wall	Momentum/ Specified shear/ X and Y	0	N/m^2
Ambient air	Fluid	---	---	---
Tower supports	Fluid	Porous zone/ Power law/ C0 and C1	0.10279; 2	---
Rain zone	Fluid	---	---	---
Fill and spray zone	Fluid	Source terms/ Axial momentum	UDF	N/m^2
		Source terms/ Radial momentum	UDF	N/m^2
		Source terms/ H_2O species mass	UDF	kg/sm^3
		Source terms/ Energy	UDF	W/m^3
Drift eliminator	Fluid	Porous zone/ Power law/ C0 and C1	5.74794; 2	---
		Source terms/ H_2O species mass	UDF	kg/sm^3
		Source terms/ Energy	UDF	W/m^3
Cooling tower	Fluid	---	---	---
Cooling water inlet	Interior	---	---	---
Rainzone inlet	Interior	---	---	---

Table O.7 : Activated *FLUENT*® DPM injection input data.

Description	Setting	Input value	Units
Injection type	Surface	---	---
Release from surface	Rain zone inlet	---	---
Particle type	Droplet	---	---
Material	Water-liquid	---	---
Diameter distribution	Uniform	---	---
Evaporating species	H_20	---	---
Point properties/ X-velocity	---	-0.1	m/s
Point properties/ Y-velocity	---	0	m/s
Point properties/ Diameter	---	0.0035	mm
Point properties/ Temperature	---	UDF (298.3)	K
Point properties/ Total flow rate	---	UDF (12500)	kg/s
Point properties	Scale flow rate by face area	---	---
UDF/ User-defined functions/ Initialization	UDF	---	---

Table O.8 : Activated *FLUENT*® solve control input data.

Description	Setting
Controls/ Solution/ Equations	Select all
Controls/ Solution/ Under-relaxation factors	Default
Controls/ Solution/ Pressure-velocity coupling	SIMPLE
Controls/ Solution/ Discretization/ Pressure	Body force weighted
Controls/ Solution/ Discretization/ Density	Second order upwind
Controls/ Solution/ Discretization/ Momentum	Second order upwind
Controls/ Solution/ Discretization/ Turbulence kinetic energy	Second order upwind
Controls/ Solution/ Discretization/ Turbulence dissipation rate	Second order upwind
Controls/ Solution/ Discretization/ H_2O	Second order upwind
Controls/ Solution/ Discretization/ Energy	Second order upwind

P

INVESTIGATION OF THE EFFECTS OF RADIALLY VARIABLE WATER MASS VELOCITIES AND FILL HEIGHTS ON NATURAL DRAUGHT WET-COOLING TOWER PERFORMANCE

P.1 INTRODUCTION

From the *FLUENT*® results presented in Appendix N, it can be seen that the water temperature, air mass velocity, air temperature and humidity ratio vary considerably along the radius and that due to flow separation, there is also significant air recirculation in the fill at the air inlet. In this appendix, the effects of employing two different water mass velocities and two fill heights along the radius on cooling tower performance are investigated for the cooling tower presented in Appendix K. For this investigation the cross-sectional area of the fill region is therefore divided into a central core area and an annulus and the elevations of the spray and rain zone inlets are kept radially constant, as shown in Fig. P.1.

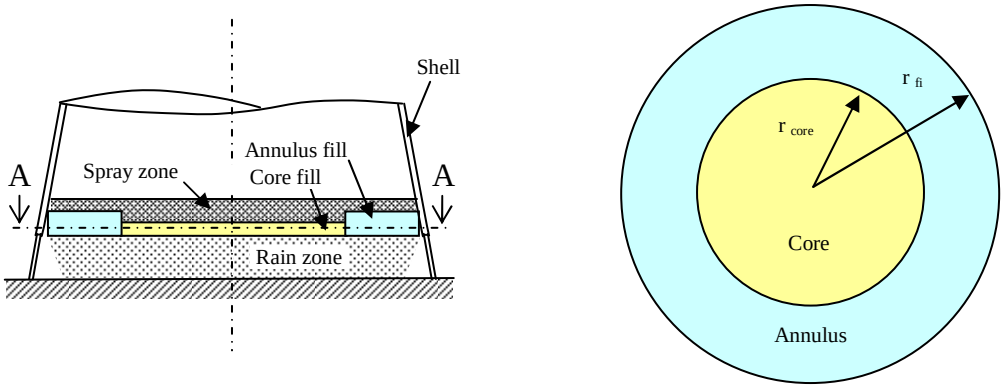

(a) Schematic showing the spray, fill and rain zone configuration. (b) Section A-A.

Figure P.1 : Schematic showing the core and outer fill area.

A mass velocity is specified for the annulus and the core mass velocity is determined from the following equation to obtain the specified total cooling water mass flow rate:

$$G_{w,core} = \frac{m_{wi} - G_{w,annulus} A_{fr,annulus}}{A_{fr,core}} \qquad (P.1)$$

Different annular water mass velocities are investigated for a fixed radius and the results are compared to Case N.4 based on a uniform water distribution, taken

from Table N.1. The lowest cooling water outlet temperature case is then used to investigate the effect of different core diameters.

Similarly different concentric fill height combinations are investigated for different core radii based on a uniform water mass velocity distribution. The core fill height is determined from the specified annulus fill height by means of the following equation:

$$L_{fi,core} = \frac{Vol_{fi,uniform} - (A_{fr} L_{fi})_{annulus}}{A_{fr,core}} \qquad (P.2)$$

Ultimately, the two best results are combined to show the overall effect on cooling tower performance.

P.2 WATER MASS VELOCITY DISTRIBUTION RESULTS

Table P.1 shows the CFD data obtained for different annular water mass velocities for a constant core radius of $r_{w,core}$ = 45 m and uniform fill height, compared to uniform water mass velocity data from Table N.1. It can be seen that Case P.3 yields the lowest cooling water outlet temperature, but that the effect is negligible.

In Figure P.2, the normalised radial cooling range, air axial mass velocity, air temperature and humidity ratio profiles of Case P.3 in Table P.1 are compared to corresponding graphs of Case N.4 from Table N.1. It can be seen that the all the profiles become more uniform near the air inlet when the water mass velocity in the annulus is increased. The opposite occurs when the core mass velocity is higher than that of the annulus, which is not shown here.

Table P.2 compares CFD data obtained for different core radii and a constant annular water mass velocity of $G_{w,annulus}$ = 1.7 kg/s m^2, to Case N.4 in Table N.1. It can be seen that the effect of changing the core radius is minimal and that the lowest outlet water temperatures are obtained with a core radius of about $r_{w,core}$ = 43 m. However, the effect on outlet water temperature is negligible.

P.3 VARIABLE FILL HEIGHT DISTRIBUTION RESULTS

Table P.3 shows the CFD data obtained for different concentric fill heights compared to Case N.4 in Table N.1 based on uniform fill height. An annulus fill height of $L_{fi,annulus}$ = 1.5 m yields the highest cooling range, even though it has the lowest air flow rate. This can be ascribed to less of the fill volume being subjected to flow recirculation at the air inlet, thus increasing the effective fill volume. For the $L_{fi,annulus}$ = 3.0 m case, it is found that the cooling range is also slightly better than for uniform fill height due to the higher air flow rate and reduced flow recirculation due to the increased flow resistance at the inlet. The profile plots of these two cases are presented in Fig. P.3.

Table P.4 shows the CFD data obtained for different core radii based on an annular fill height of $L_{fi,annulus}$ = 2.0 m, again compared to Case N.4 in Table N.1. It can be seen that a reduction in $r_{fi,core}$ results in an increase in ΔT_{cw}.

Table P.5 shows the CFD data obtained for different core radii based on an annular fill height of $L_{fi,annulus}$ = 3.0 m, compared to Case N.4 in Table N.1, which is based on uniform fill height. As in Table P.4, a reduction in $r_{fi,core}$ results in an increase in ΔT_{cw}.

P.4 COMBINATION OF THE MOST FAVOURABLE WATER AND FILL HEIGHT DISTRIBUTION CONDITIONS FOR THE EXPANDED METAL FILL

Table P.6 shows CFD data for expanded metal (Case P.19) when combining the conditions that gave the best results in the above cases i.e. water mass velocities of $G_{w,annulus}$ = 1.7 kg/sm^2 and $G_{w,core}$ = 1.464 kg/sm^2 for a core radius of $r_{w,core}$ = 43 m, and fill heights of $L_{fi,annulus}$ = 3.0 m and $L_{fi,core}$ = 0.871 m for a fill core radius of $r_{core,Lfi}$ = 25 m, which are compared to Case N.4 from Table N.1. It can be seen that the increase in cooling range is essentially the sum of the individual increases in cooling range obtained for Cases P.8 and P.16.

A similar exercise was done for the case when the cooling tower is packed with trickle fill instead of expanded metal however with a fill height that yields the same mean cooling range as the expanded metal with the one-dimensional model. Case P.21 is the CFD data obtained for the same water distribution, fill height ratios and core radii as for the expanded metal fill, compared to Case N.14, where it is however observed that the cooling range decreases. From the graphs in Fig. P.4, it can be seen that for the trickle fill, the cooling range in the fill core region is significantly lower than that obtained for the expanded metal fill. This can be ascribed to the fact that for towers packed with trickle fill, the fill dominates the performance since the drop size in the rain zone is d = 5.5 mm as opposed to d = 3.5 mm for the expanded metal fill and the spray zone height in the core region is L_{sp} = 1.079 compared to L_{sp} = 2.629 for the expanded metal fill. The higher loss coefficient results in a reduction in air flow rate and a slightly smaller flow recirculation region.

Case P.20 in Table P.6 shows that a radially constant spray zone height of L_{sp} = 0.5, as depicted in Fig. P.5 for the above water and fill depth distributions, results in a reduction in cooling range.

P.5 CONCLUSIONS

From the above results, the following conclusions can be made:

- ⇨ The effect of variable water mass velocity is shown to be negligible for the particular cooling tower configuration investigated.
- ⇨ The effect of fill height is however found to be significant when the spray and rain zone inlet are at constant elevations, where the largest performance enhancement was achieved by maximising the fill height in the annulus while minimising the core radius.

- ⇨ When combining the water and fill height distributions that gave the best results, the net increase in cooling range is found to be the sum of the increase when water and fill height is changed separately.
- ⇨ The water and fill distributions that gave the best results for the expanded metal fill, however results in a performance reduction for the trickle fill. It is therefore important to note that cooling tower optimisation studies should be conducted on a case-by-case basis and that the spray and rain zone characteristics play an important role in the outcome of the optimisation.

Table P.1 : CFD data for different water mass velocities based on a core radius of r_{core} = 45 m.

Description	Symbol	Units	Case					
			N.4	P.1	P.2	P.3	P.4	P.5
Annulus water mass velocity	$G_{w,annulus}$	kg/s m^2	1.5	1.4	1.6	1.7	1.8	1.9
Core water mass velocity	$G_{w,core}$	kg/s m^2	---	1.527	1.464	1.433	1.402	1.371
Core radius	$r_{w,core}$	m	0	45	45	45	45	45
Air mass flow rate	m_{av5}	kg/s	17262	17158	17292	17305	17293	17259
Air pressure	p_{a1}	Pa	84100	84100	84100	84100	84100	84100
	p_{a3}	Pa	83976	83977	83976	83976	83976	83976
	$p_{a5@13.5m}$	Pa	83919	83920	83919	83919	83919	83919
	p_{a6}	Pa	82650	82650	82650	82650	82650	82650
	p_{a7}	Pa	82654	82654	82654	82654	82654	82654
Air temperature	T_{a1}	ºC	15.45	15.45	15.45	15.45	15.45	15.45
	T_{a3}	ºC	17.25	17.25	17.25	17.25	17.27	17.29
	T_{a5}	ºC	26.03	25.91	25.87	25.86	25.86	25.85
	T_{a6}	ºC	26.03	25.89	25.87	25.86	25.86	25.85
	T_{a7}	ºC	15.45	15.45	15.45	15.45	15.45	15.45
Air humidity ratio	w_1	kg/kg$_{da}$	0.00813	0.00813	0.00813	0.00813	0.00813	0.00813
	w_3	kg/kg$_{da}$	0.01167	0.01164	0.01164	0.01165	0.01167	0.0117
	w_5	kg/kg$_{da}$	0.02759	0.02756	0.02748	0.02746	0.02746	0.02746
	w_6	kg/kg$_{da}$	0.02759	0.02756	0.02748	0.02746	0.02746	0.02746
	w_7	kg/kg$_{da}$	0.00813	0.00813	0.00813	0.00813	0.00813	0.00813
Air density	ρ_{av1}	kg/m^3	1.010	1.010	1.010	1.010	1.010	1.01
	ρ_{av3}	kg/m^3	1.001	1.000	1.000	1.000	1.000	1.000
	ρ_{av5}	kg/m^3	0.962	0.962	0.962	0.962	0.962	0.962
	ρ_{av6}	kg/m^3	0.947	0.947	0.948	0.948	0.948	0.948
	ρ_{av7}	kg/m^3	0.993	0.993	0.993	0.993	0.993	0.993
Water mass flow rate	m_{wi}	kg/s	12500	12500	12500	12500	12500	12500
Water temperature	T_{wi}	ºC	40.00	40.00	40.00	40.00	40.00	40.00
	$T_{wi,rz}$	ºC	25.07	25.09	25.05	25.06	25.10	25.17
	T_{wo}	ºC	21.53	21.57	21.51	21.50	21.52	21.55

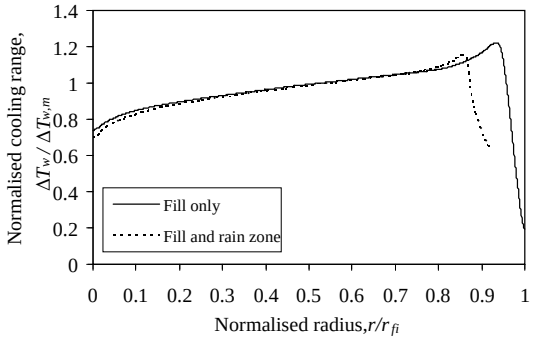

(a_1) Normalised cooling range profile (Case N.4).

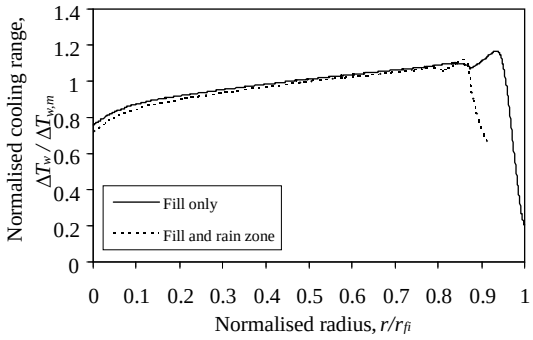

(a_2) Normalised cooling range profile (Case P.3).

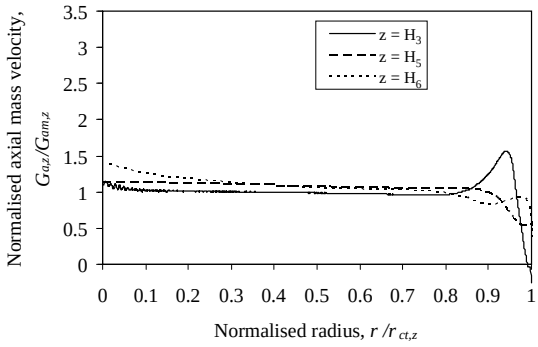

(b_1) Normalised axial air mass velocity profile (Case N.4).

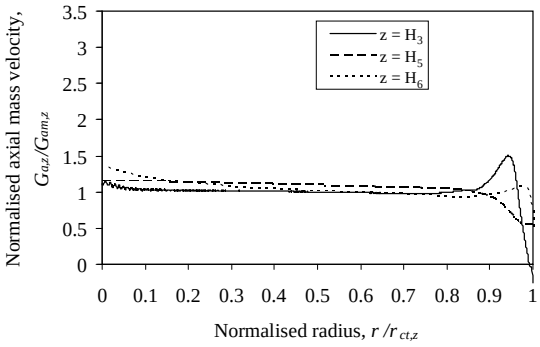

(b_2) Normalised axial air mass velocity profile (Case P.3).

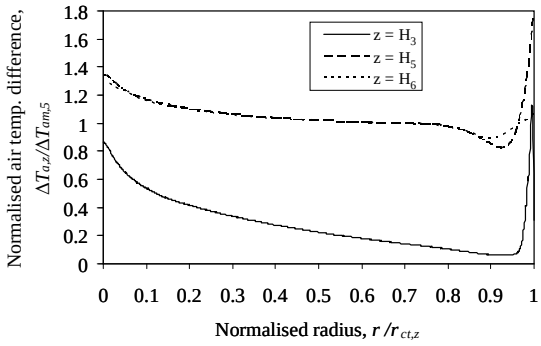

(c_1) Normalised air temperature profile (Case N.4).

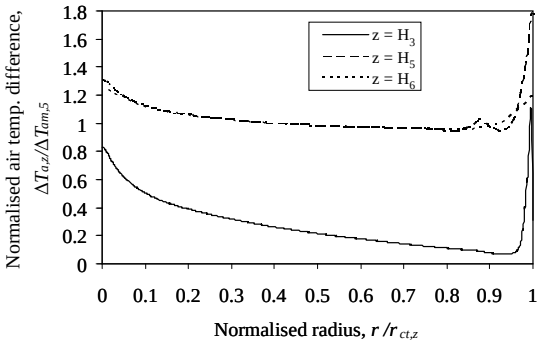

(c_2) Normalised air temperature profile (Case P.3).

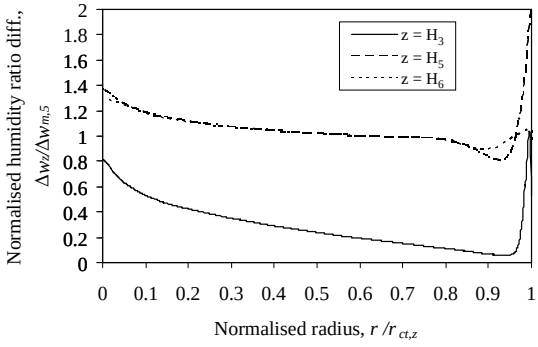

(d_1) Normalised air humidity ratio profile (Case N.4).

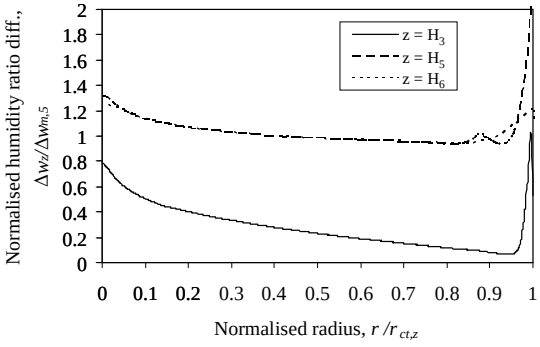

(d_2) Normalised air humidity ratio profile (Case P.3).

Figure P.2 : Comparison between profile plots for a uniform mass distribution and an annular water mass velocity of $G_{w,annulus}$ = 1.7 kg/s m^2 with a core radius of $r_{w,core}$ = 45 m.

Table P.2 : CFD data for different core diameters based on a annular water mass velocities of 1.7 kg/s m^2.

Description	Symbol	Units	Case						
			N.4	P.6	P.7	P.8	P.9	P.3	P.10
Annulus water mass velocity	$G_{w,annulus}$	kg/s m^2	1.5	1.7	1.7	1.7	1.7	1.7	1.7
Core water mass velocity	$G_{w,core}$	kg/s m^2	---	1.527	1.527	1.464	1.433	1.433	1.371
Core radius	$r_{fi,core}$	m	0	35	42	43	44	45	46
Air mass flow rate	m_{av5}	kg/s	17262	17244	17305	17309	17309	17305	17296
Air pressure	p_{a1}	Pa	84100	84100	84100	84100	84100	84100	84100
	p_{a3}	Pa	83976	83976	83976	83976	83976	83976	83976
	$p_{a5@13.5m}$	Pa	83919	83919	83919	83919	83919	83919	83919
	p_{a6}	Pa	82650	82650	82650	82650	82650	82650	82650
	p_{a7}	Pa	82654	82654	82654	82654	82654	82654	82654
Air temperature	T_{a1}	ºC	15.45	15.45	15.45	15.45	15.45	15.45	15.45
	T_{a3}	ºC	17.25	17.29	17.26	17.26	17.26	17.25	17.25
	T_{a5}	ºC	26.03	25.87	25.86	25.86	25.86	25.86	25.86
	T_{a6}	ºC	26.03	25.87	25.86	25.86	25.86	25.86	25.86
	T_{a7}	ºC	15.45	15.45	15.45	15.45	15.45	15.45	15.45
Air humidity ratio	w_1	kg/kg_{da}	0.00813	0.00813	0.00813	0.00813	0.00813	0.00813	0.00813
	w_3	kg/kg_{da}	0.01167	0.01171	0.01166	0.01166	0.01165	0.01165	0.01165
	w_5	kg/kg_{da}	0.02759	0.02750	0.02747	0.02747	0.02746	0.02746	0.02746
	w_6	kg/kg_{da}	0.02759	0.02749	0.02747	0.02747	0.02746	0.02746	0.02746
	w_7	kg/kg_{da}	0.00813	0.00813	0.00813	0.00813	0.00813	0.00813	0.00813
Air density	ρ_{av1}	kg/m^3	1.010	1.010	1.010	1.010	1.010	1.010	1.01
	ρ_{av3}	kg/m^3	1.001	1.000	1.000	1.000	1.000	1.000	1.000
	ρ_{av5}	kg/m^3	0.962	0.962	0.962	0.962	0.962	0.962	0.962
	ρ_{av6}	kg/m^3	0.947	0.948	0.948	0.948	0.948	0.948	0.948
	ρ_{av7}	kg/m^3	0.993	0.993	0.993	0.993	0.993	0.993	0.993
Water mass flow rate	m_{wi}	kg/s	12500	12500	12500	12500	12500	12500	12500
Water temperature	T_{wi}	ºC	40.00	40.00	40.00	40.00	40.00	40.00	40.00
	$T_{wi,rz}$	ºC	25.07	25.14	25.07	25.06	25.06	25.06	25.07
	T_{wo}	ºC	21.53	21.53	21.50	21.50	21.50	21.50	21.51

Table P.3 : CFD data for different concentric fill heights based on a core radius of $r_{w,core}$ = 45 m and a uniform water mass velocities of G_w = 1.5 kg/s m^2.

Description	Symbol	Units	Case			
			N.4	P.11	P.12	P.13
Annulus fill height	$L_{fi,annulus}$	m	2.504	1.5	2.0	3.0
Core fill height	$L_{fi,core}$	m	---	2.830	2.668	2.343
Core radius	$r_{fi,core}$	m	0	45	45	45
Air mass flow rate	m_{av5}	kg/s	17262	17158	17212	17298
Air pressure	p_{a1}	Pa	84100	84100	84100	84100
	p_{a3}	Pa	83976	83976	83976	83976
	$p_{a5@13.5m}$	Pa	83919	83919	83919	83919
	p_{a6}	Pa	82650	82650	82650	82650
	p_{a7}	Pa	82654	82654	82654	82654
Air temperature	T_{a1}	ºC	15.45	15.45	15.45	15.45
	T_{a3}	ºC	17.25	17.20	17.22	17.20
	T_{a5}	ºC	26.03	26.05	25.96	25.92
	T_{a6}	ºC	26.03	26.03	25.96	25.92
	T_{a7}	ºC	15.45	15.45	15.45	15.45
Air humidity ratio	w_1	kg/kg_{da}	0.00813	0.00813	0.00813	0.00813
	w_3	kg/kg_{da}	0.01167	0.01158	0.01160	0.01158
	w_5	kg/kg_{da}	0.02759	0.02782	0.02766	0.02759
	w_6	kg/kg_{da}	0.02759	0.02782	0.02766	0.02759
	w_7	kg/kg_{da}	0.00813	0.00813	0.00813	0.00813
Air density	ρ_{av1}	kg/m^3	1.010	1.010	1.010	1.010
	ρ_{av3}	kg/m^3	1.001	1.000	1.000	1.000
	ρ_{av5}	kg/m^3	0.962	0.961	0.962	0.962
	ρ_{av6}	kg/m^3	0.947	0.947	0.947	0.947
	ρ_{av7}	kg/m^3	0.993	0.993	0.993	0.993
Water mass flow rate	m_{wi}	kg/s	12500	12500	12500	12500
Water temperature	T_{wi}	ºC	40.00	40.00	40.00	40.00
	$T_{wi,rz}$	ºC	25.07	24.76	24.90	24.88
	T_{wo}	ºC	21.53	21.32	21.43	21.40

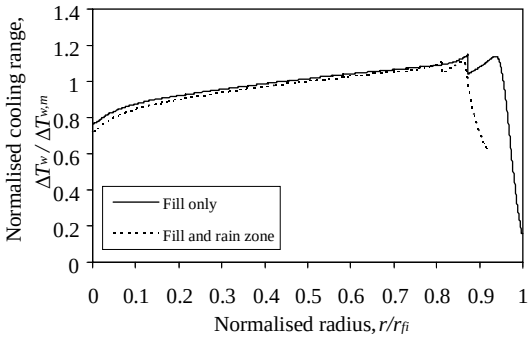

(a_1) Normalised cooling range profile (Case P.11).

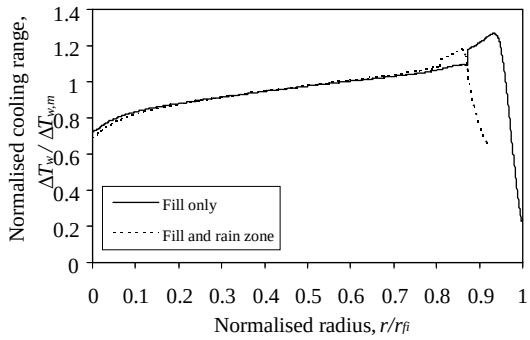

(a_2) Normalised cooling range profile (Case P.13).

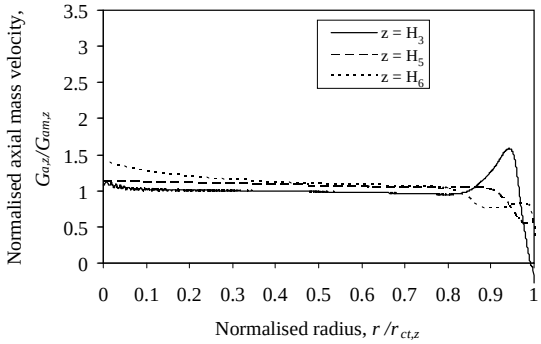

(b_1) Normalised axial air mass velocity profile (Case P.11).

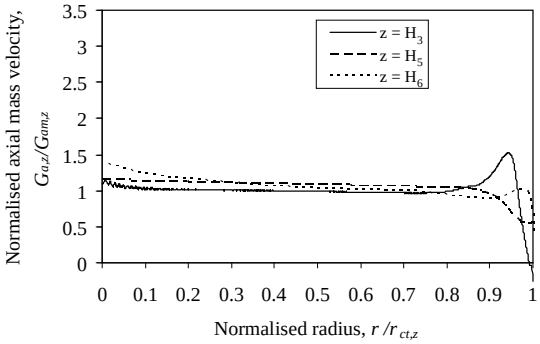

(b_2) Normalised axial air mass velocity profile (Case P.13).

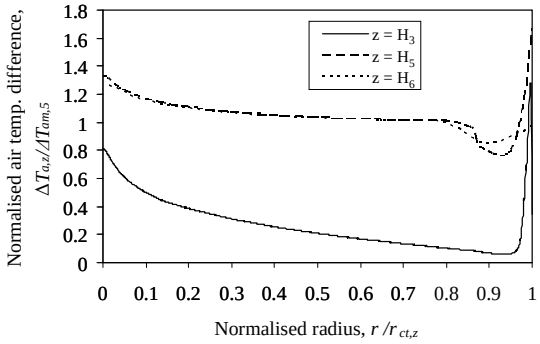

(c_1) Normalised air temperature profile (Case P.11).

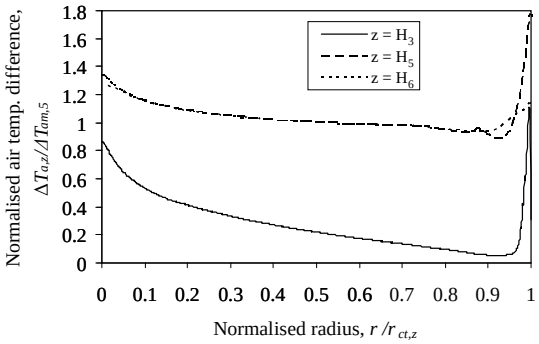

(c_2) Normalised air temperature profile (Case P.13).

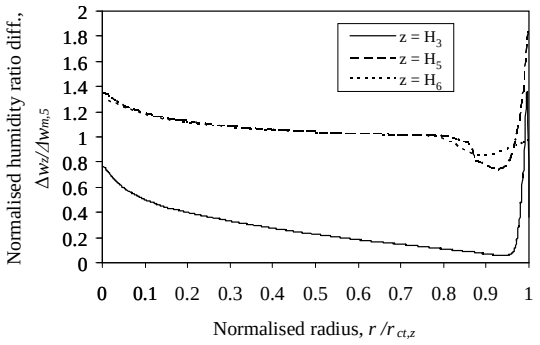

(d_1) Normalised air humidity ratio profile (Case P.11).

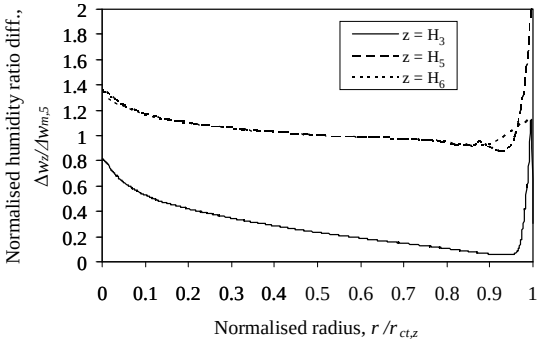

(d_2) Normalised air humidity ratio profile (Case P.13).

Figure P.3 : Comparison between profile plots for annular fill heights of $L_{fi,annulus}$ = 1.5 m and 3 m with a core radius of r_{core} = 45 m.

Table P.4 : CFD data for different core radii based on a annular fill height of $L_{fi,annulus}$ = 2.0 m and a uniform water mass velocities of G_w = 1.5 kg/s m^2.

Description	Symbol	Units	Case			
			N.4	P.14	P.12	P.15
Annulus fill height	$L_{fi,annulus}$	m	2.504	2.0	2.0	2.0
Core fill height	$L_{fi,core}$	m	---	3.104	2.668	2.612
Core radius	$r_{fi,core}$	m	0	35	45	47
Air mass flow rate	m_{av5}	kg/s	17262	17154	17212	17235
Air pressure	p_{a1}	Pa	84100	84100	84100	84100
	p_{a3}	Pa	83976	83976	83976	83976
	$p_{a5@13.5m}$	Pa	83919	83919	83919	83919
	p_{a6}	Pa	82650	82650	82650	82650
	p_{a7}	Pa	82654	82654	82654	82654
Air temperature	T_{a1}	ºC	15.45	15.45	15.45	15.45
	T_{a3}	ºC	17.25	17.20	17.22	17.22
	T_{a5}	ºC	26.03	26.04	25.96	25.94
	T_{a6}	ºC	26.03	26.04	25.96	25.94
	T_{a7}	ºC	15.45	15.45	15.45	15.45
Air humidity ratio	w_1	kg/kg$_{da}$	0.00813	0.00813	0.00813	0.00813
	w_3	kg/kg$_{da}$	0.01167	0.01157	0.01160	0.01161
	w_5	kg/kg$_{da}$	0.02759	0.02780	0.02766	0.02761
	w_6	kg/kg$_{da}$	0.02759	0.02780	0.02766	0.02761
	w_7	kg/kg$_{da}$	0.00813	0.00813	0.00813	0.00813
Air density	ρ_{av1}	kg/m^3	1.010	1.010	1.010	1.010
	ρ_{av3}	kg/m^3	1.001	1.000	1.000	1.000
	ρ_{av5}	kg/m^3	0.962	0.961	0.962	0.962
	ρ_{av6}	kg/m^3	0.947	0.947	0.947	0.947
	ρ_{av7}	kg/m^3	0.993	0.993	0.993	0.993
Water mass flow rate	m_{wi}	kg/s	12500	12500	12500	12500
Water temperature	T_{wi}	ºC	40.00	40.00	40.00	40.00
	$T_{wi,rz}$	ºC	25.07	24.79	24.90	24.93
	T_{wo}	ºC	21.53	21.36	21.43	21.44

Table P.5 : CFD data for different core radii based on a annular fill height of $L_{fi,annulus}$ = 3.0 m and a uniform water mass velocities of G_w = 1.5 kg/s m^2.

Description	Symbol	Units	Case				
			N.4	P.16	P.17	P.13	P.18
Annulus fill height	$L_{fi,annulus}$	m	2.504	3.0	3.0	3.0	3.0
Core fill height	$L_{fi,core}$	m	---	0.871	1.914	2.343	2.398
Core radius	$r_{fi,core}$	m	0	25	35	45	47
Air mass flow rate	m_{av5}	kg/s	17262	17314	17318	17298	17275
Air pressure	p_{a1}	Pa	84100	84100	84100	84100	84100
	p_{a3}	Pa	83976	83976	83976	83976	83976
	$p_{a5@13.5m}$	Pa	83919	83918	83918	83919	83919
	p_{a6}	Pa	82650	82650	82650	82650	82650
	p_{a7}	Pa	82654	82654	82654	82654	82654
Air temperature	T_{a1}	ºC	15.45	15.45	15.45	15.45	15.45
	T_{a3}	ºC	17.25	17.13	17.16	17.20	17.22
	T_{a5}	ºC	26.03	26.03	25.98	25.92	25.90
	T_{a6}	ºC	26.03	26.03	25.98	25.92	25.90
	T_{a7}	ºC	15.45	15.45	15.45	15.45	15.45
Air humidity ratio	w_1	kg/kg$_{da}$	0.00813	0.00813	0.00813	0.00813	0.00813
	w_3	kg/kg$_{da}$	0.01167	0.01151	0.01153	0.01158	0.01160
	w_5	kg/kg$_{da}$	0.02759	0.02783	0.02773	0.02759	0.02756
	w_6	kg/kg$_{da}$	0.02759	0.02783	0.02773	0.02759	0.02756
	w_7	kg/kg$_{da}$	0.00813	0.00813	0.00813	0.00813	0.00813
Air density	ρ_{av1}	kg/m^3	1.010	1.010	1.010	1.010	1.010
	ρ_{av3}	kg/m^3	1.001	1.000	1.000	1.000	1.000
	ρ_{av5}	kg/m^3	0.962	0.961	0.962	0.962	0.962
	ρ_{av6}	kg/m^3	0.947	0.947	0.947	0.947	0.947
	ρ_{av7}	kg/m^3	0.993	0.993	0.993	0.993	0.993
Water mass flow rate	m_{wi}	kg/s	12500	12500	12500	12500	12500
Water temperature	T_{wi}	ºC	40.00	40.00	40.00	40.00	40.00
	$T_{wi,rz}$	ºC	25.07	24.56	24.68	24.88	24.95
	T_{wo}	ºC	21.53	21.16	21.25	21.40	21.46

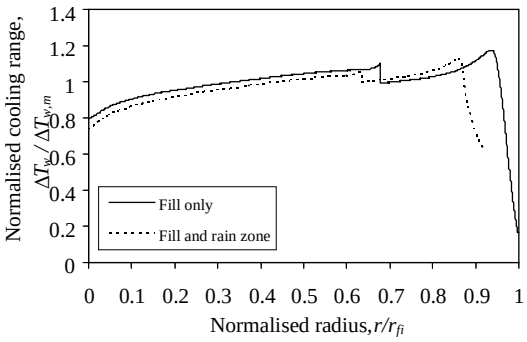

(a_1) Normalised cooling range profile (Case P.14).

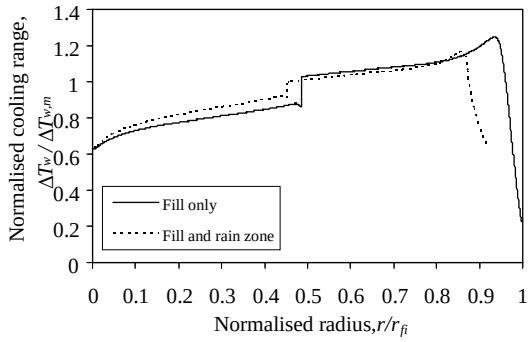

(a_2) Normalised cooling range profile (Case P.16).

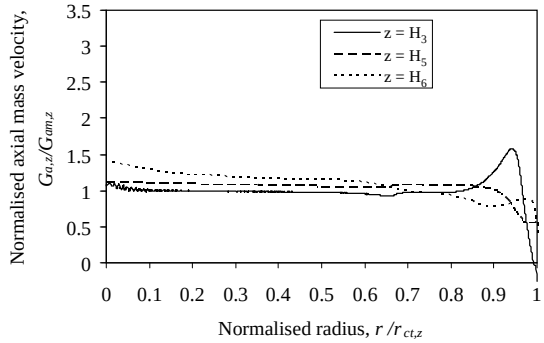

(b_1) Normalised axial air mass velocity profile (Case P.14).

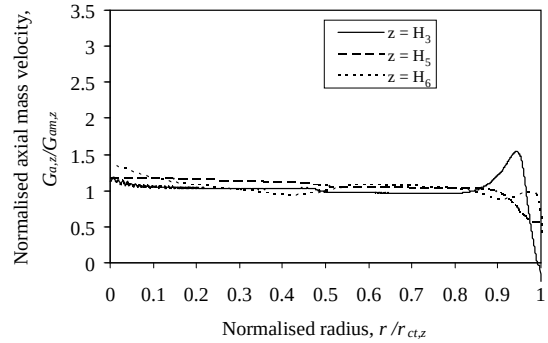

(b_2) Normalised axial air mass velocity profile (Case P.16).

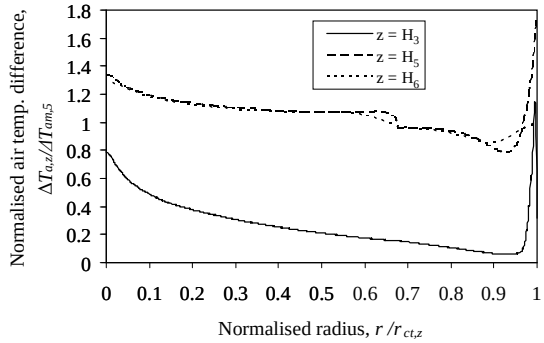

(c_1) Normalised air temperature profile (Case P.14).

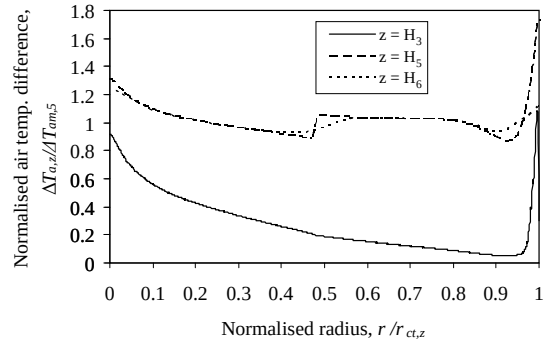

(c_2) Normalised air temperature profile (Case P.16).

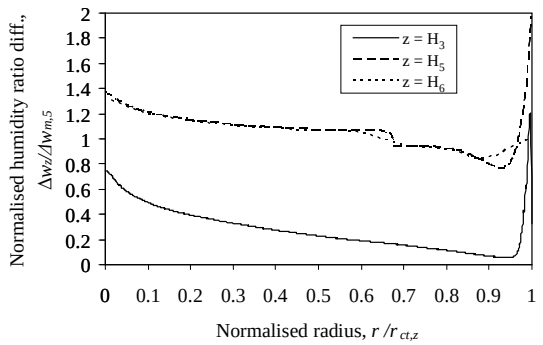

(d_1) Normalised air humidity ratio profile (Case P.14).

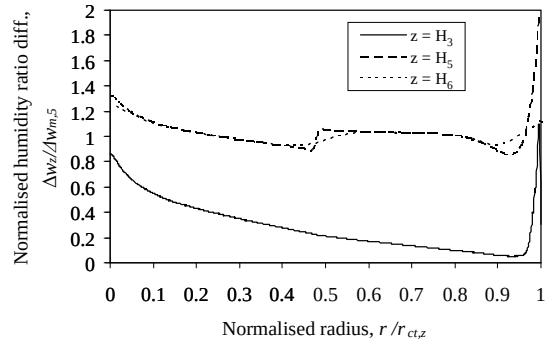

(d_2) Normalised air humidity ratio profile (Case P.16).

Figure P.3 : Comparison between profile plots for annular fill heights of $L_{fi,annulus}$ = 2.0 m and 3.0 m with core radii of $r_{fi,core}$ = 35 m and 25 m.

Table P.6 : CFD data for expanded metal and trickle fills obtained by combining the water and fill height distributions that gave the best results for the expanded metal fill, when each was varied independently.

Description	Symbol	Units	N.4	P.19	P.20	N.14	P.21
Fill type	---	---	ES	ES	ES	Trickle	Trickle
Merkel number ratio	X	---	0.9	0.9	0.9	0.9	0.9
Air outlet condition	---	---	Supersat.	Supersat.	Supersat.	Supersat.	Supersat.
Fill grid size	Δr or Δz	m	0.025	0.025	0.025	0.025	0.025
Wall boundary condition	---	---	No-slip	No-slip	No-slip	No-slip	No-slip
Air inlet geometry	---	---	Round	Round	Round	Round	Round
Rain zone drop diameter	D	mm	3.5	3.5	3.5	5.5	5.5
Annulus water mass velocity	$G_{w,annulus}$	kg/sm^2	1.5	1.7	1.7	1.5	1.7
Core water mass velocity	$G_{w,annulus}$	kg/sm^2	---	1.464	1.464	---	1.464
Water core radius	$r_{w,core}$	m	0	43	43	0	43
Annulus fill height	$L_{fi,annulus}$	m	2.504	3	3	0.68	0.815
Core fill height	$L_{fi,core}$	m	---	0.871	0.871	---	0.236
Annulus spray height	$L_{sp,annulus}$	m	0.5	0.5	0.5	0.5	0.5
Core spray height	$L_{sp,core}$	m	---	2.629	0.5	---	1.079
Fill core radius	$r_{fi,core}$	M	--	25	25	--	25
Air mass flow rate	m_{av5}	kg/s	17262	17321	17026	15983	15509
Air pressure	p_{a1}	Pa	84100	84100	84100	84100	84100
	p_{a3}	Pa	83976	83976	83976	83981	83981
	$p_{a5@13.5m}$	Pa	83919	83918	83920	83911	83914
	p_{a6}	Pa	82650	82650	82650	82650	82649
	p_{a7}	Pa	82654	82654	82654	82664	82664
Air temperature	T_{a1}	ºC	15.45	15.45	15.45	15.45	15.45
	T_{a3}	ºC	17.25	17.15	17.15	16.33	16.44
	T_{a5}	ºC	26.03	26.04	25.71	26.73	26.67
	T_{a6}	ºC	26.03	26.02	25.71	26.73	26.67
	T_{a7}	ºC	15.45	15.45	15.45	15.45	15.45
Air humidity ratio	w_1	kg/kg_{da}	0.00813	0.00813	0.00813	0.00813	0.00813
	w_3	kg/kg_{da}	0.01167	0.01153	0.01192	0.00993	0.01011
	w_5	kg/kg_{da}	0.02759	0.02786	0.02727	0.02908	0.02914
	w_6	kg/kg_{da}	0.02759	0.02786	0.02727	0.02908	0.01914
	w_7	kg/kg_{da}	0.00813	0.00813	0.00813	0.00813	0.00813
Air density	ρ_{av1}	kg/m^3	1.010	1.010	1.010	1.010	1.010
	ρ_{av3}	kg/m^3	1.001	1.001	1.000	1.005	1.004
	ρ_{av5}	kg/m^3	0.962	0.961	0.963	0.958	0.959
	ρ_{av6}	kg/m^3	0.947	0.947	0.948	0.944	0.944
	ρ_{av7}	kg/m^3	0.993	0.993	0.993	0.998	0.998
Water mass flow rate	m_{wi}	kg/s	12500	12500	12500	12500	12500
Water temperature	T_{wi}	ºC	40.00	40.00	40.00	40.00	40.00
	$T_{wi,rz}$	ºC	25.07	24.56	25.62	23.34	23.92
	T_{wo}	ºC	21.53	21.12	21.83	21.65	22.11

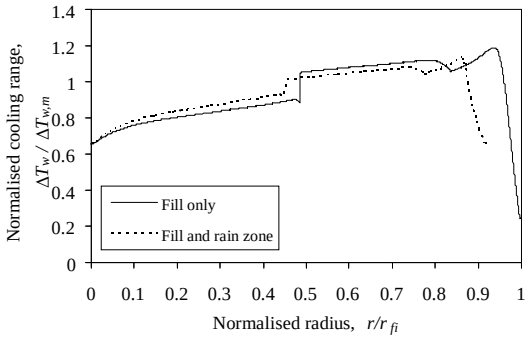

(a_1) Normalised cooling range profile (Case P.19).

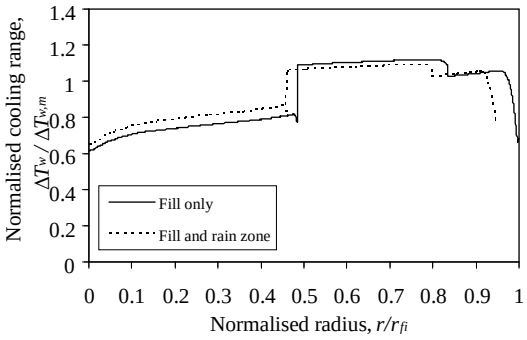

(a_2) Normalised cooling range profile (Case P.21).

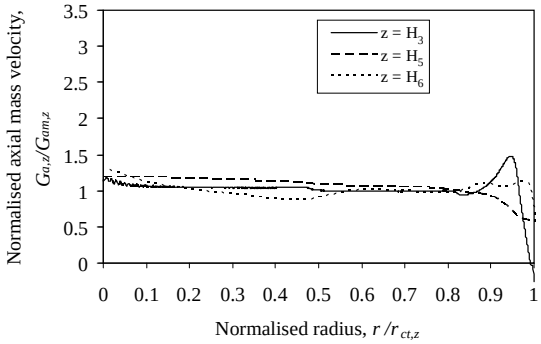

(b_1) Normalised axial air mass velocity profile (Case P.19).

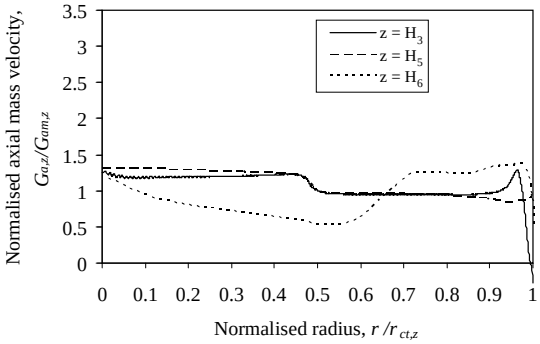

(b_2) Normalised axial air mass velocity profile (Case P.20).

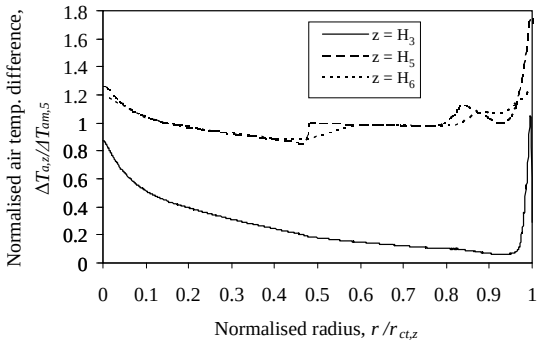

(c_1) Normalised air temperature profile (Case P.19).

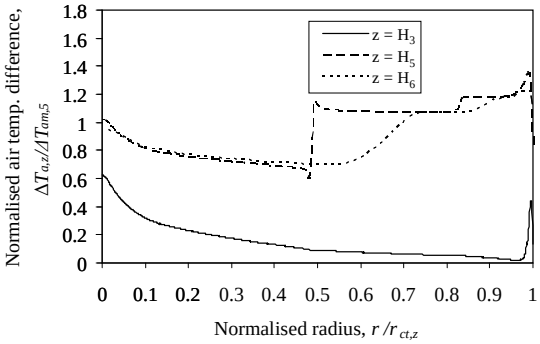

(c_2) Normalised air temperature profile (Case P.21).

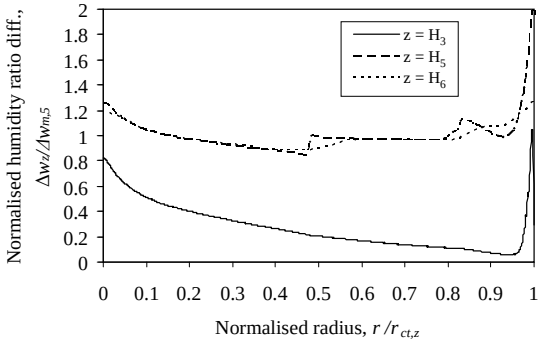

(d_1) Normalised air humidity ratio profile (Case P.19).

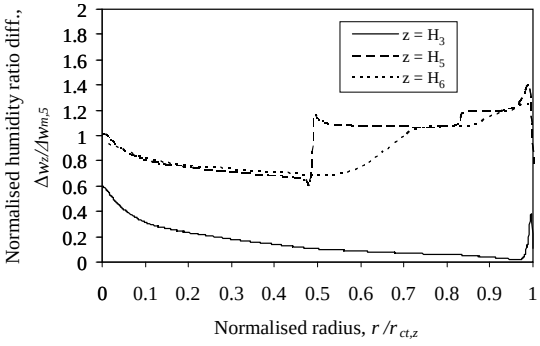

(d_2) Normalised air humidity ratio profile (Case P.21).

Figure P.4 : Comparison between profile plots for expanded metal and trickle fill combining the water and fill height distributions that gave the best results for the expanded metal fill when each was varied independently.

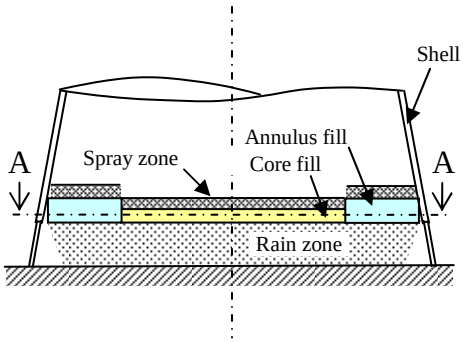

Figure P.5 : Schematic showing the spray, fill and rain zone configuration when the spray height is constant.

Q

A METHOD FOR DETERMINING THE PERFORMANCE CHARACTERISTICS OF COOLING TOWER SPRAY ZONES

Q.1 INTRODUCTION

Spray zone performance characteristics such as water distribution onto the fill, drop size distribution in the spray zone and pump head play an important role in cooling tower performance. A non-uniform distribution of water onto the fill material causes reduced performance in the fill and rain zones and has a negative effect on the performance of the spray zone itself. The water flow distribution is dependent on nozzle design, nozzle spacing, spray direction and operating conditions such as water and air flow rates. The drop size distribution in the spray zone directly affects the heat and mass transfer in the spray zone and is dependent mainly on nozzle design, nozzle operating pressure and the collision and agglomeration of drops in regions where sprays of adjacent nozzles overlap.

The only transfer characteristic and loss coefficient data found in literature are by Lowe and Christie (1961), which are however limited to 1 mm drops. This appendix therefore presents a method to model a cooling tower spray zone for different operating conditions and configurations using flow distribution, drop size distribution and nozzle inlet pressure data measured for a single nozzle, to determine the flow distribution and the transfer characteristics of a grid of nozzles with overlapping sprays, required to predict cooling tower performance, which was developed in collaboration with Viljoen (2006). The experimental apparatus, test results, computational models and CFD models used to model the spray zone of a grid of commercial full cone medium pressure swirl nozzles, are discussed. Ultimately, correlations are presented for the Merkel number and loss coefficient, which are the performance characteristics typically required for cooling tower design.

Q.2 MODELLING PROCEDURE

The basic procedure followed to model a cooling tower spray zone is as follows:

- ⇨ Measure the water flow distribution and drop size distribution produced by a single nozzle for different operating conditions and installation considerations.
- ⇨ Employ a numerical model, as presented in Appendix B, that solves the motion equations for a single drop falling through upward flowing air, to predict the drop initial speed and initial angle at the nozzle outlet by making use of the nozzle inlet water pressure as well as water flow distribution and drop size distribution data measured at a specific level below the nozzle.

- ⇨ Predict the temperature change of a single drop falling through upward flowing air, by solving the energy equations simultaneously with the motion equations above, as presented in Appendix C.
- ⇨ Predict the water distribution at a given level produced by a grid of equally spaced nozzles with overlapping sprays by numerical superposition of single nozzle water distribution data and a given nozzle spacing. Use this model to optimize the nozzle spacing.
- ⇨ Develop a CFD model to predict single spray nozzle performance using the numerically determined drop initial conditions at the nozzle outlet and verify the results with the above single drop motion and cooling model data.
- ⇨ Develop a CFD model of a multi-nozzle spray zone for a given nozzle spacing using single nozzle data and verify the flow distribution results with the superposition model data.
- ⇨ Determine the spray zone transfer characteristics (Merkel numbers) from the multi-nozzle CFD results using the Merkel method of analysis.
- ⇨ Determine the spray zone loss coefficient from the CFD results from the volume flow weighted mean total air-side pressure difference.

Q.3 EXPERIMENTAL WORK

In order to model a spray zone, performance data is required for a single spray nozzle i.e. water flow distribution at different levels, drop size distribution in the spray zone and nozzle inlet pressure, for different water flow rates.

For illustration, the flow and drop size distributions of a single nozzle and a grid of four spray nozzles are measured in a counterflow cooling tower test rig shown in Figs Q.1. Water is supplied to the nozzle by a centrifugal pump at a set flow rate and constant pressure. The water is sprayed into the test section by the spray nozzle/s and falls down to a pond under gravity, from which it is pumped back to the nozzle. Air is drawn upwards through the test section by an induced draught axial flow fan at a set flow rate to simulate air conditions encountered in a counter flow cooling tower.

Figure Q.2 shows the sprays obtained by means of a medium pressure and a low pressure nozzle.

To measure the water distribution of a medium pressure nozzle for different air flow rates, a measurement rake is used which comprises a row of measuring cups with a diameter of d_{cup} = 40 mm which are spaced at 60 mm intervals, as shown schematically in Fig. Q.3(a). The rake is mounted on a guide rail for it to be moved through the test section to obtain a grid of measurement points. Water from the spray nozzle is collected in the measuring cups and drains through plastic tubing to a set of buckets, as shown in Fig. Q.1, which are used to measure the water flow rate collected simultaneously in each cup.

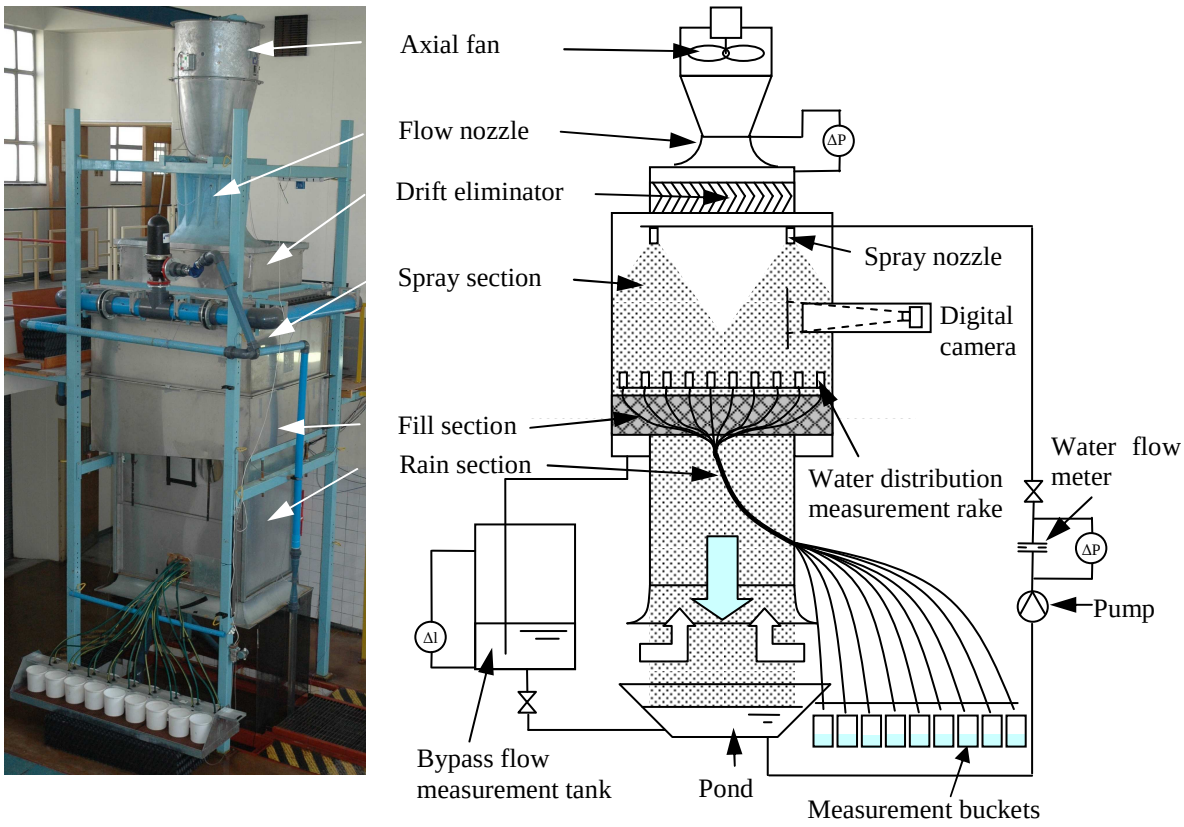

(a) Photo. (b) Schematic representation.

Figure Q.1: Cooling tower test rig.

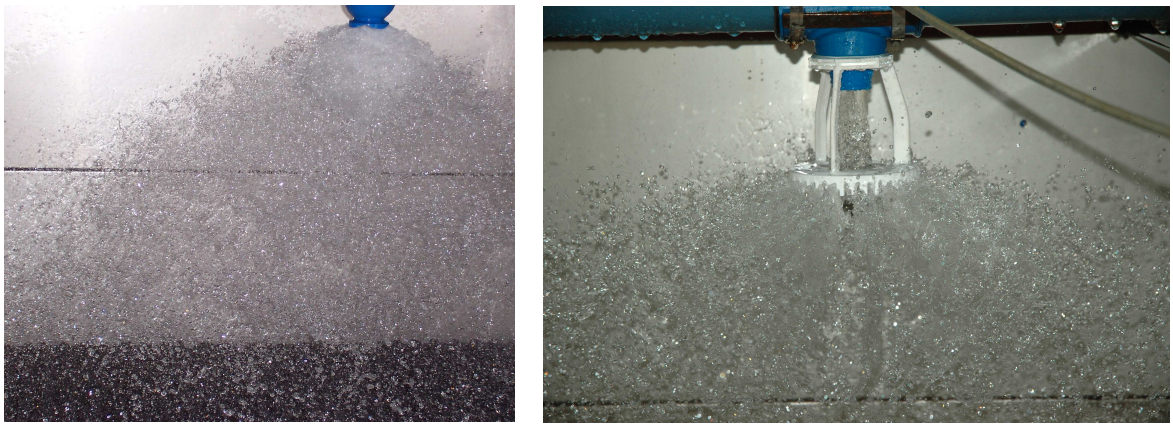

(a) Medium pressure nozzle. (b) Low pressure nozzle.

Figure Q.2: Nozzle sprays.

The mass velocity of water draining from each cup is determined from

$$G_w = \frac{V_{bucket}\,\rho_w}{A_{cup}\Delta t} \qquad \text{(Q.1)}$$

For low pressure nozzles, as depicted in Fig. Q.2(b), the spray trajectories originate radially from a fixed openings, as opposed to the swirling flow leaving the medium pressure nozzle in Fig. Q.2(a). This and the larger drop diameters produced by low pressure nozzles results in significant measurement uncertainties when using the rake of Fig. Q.3(a). Sector or rectangular troughs therefore need to be used as shown in Figs Q.3(b) and (c), where the water caught in each measurement compartment drains through a hose pipe to the bucket flow measurement system (Fig. Q.1).

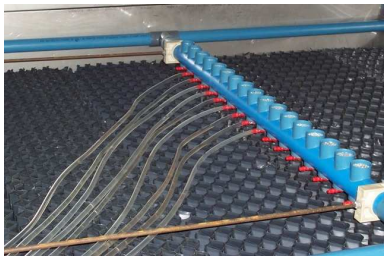

(a) Rake of cups.

(b) Sector trough.

(c) Rectangular trough.

Figure Q.3: Different catchment systems to measure spray nozzle flow distribution.

In Fig. Q.4, the radial water distribution data of a single full cone medium pressure swirl nozzle is presented for a flow rate of 4.5 l/s, water pressure head of 2.6 m and at a level of 0.470 m below the nozzle. The water distribution is measured at conditions with and without air flow and it can be seen that for an air velocity of v_a = 3 m/s, the radial position of the peak moves radially outward by about 10% whereas the spray diameter remains almost the same, compared to the case of no air flow. These two cases can be used to validate the flow distributions obtained with the various models.

The drop size distribution is measured using a digital camera, shielding pipe and background plate as shown in Fig. Q.5.

The shielding pipe protrudes horizontally through the wall into the test section, protecting the camera from moisture. Digital images are taken of the drops falling past the open end of the pipe against a background plate. These images are processed by means of software developed at Stellenbosch University, used to detect the drop edges and to determine the number of pixels enclosed by each detected edge. Knowing the distance from the camera lens to the front and back of the image zone, calibration values are determined in terms of mm/ pixel and used to calculate the area enclosed by the edge and subsequently the drop diameter. Knowing the size of each drop on the digital image, the drop size distribution is

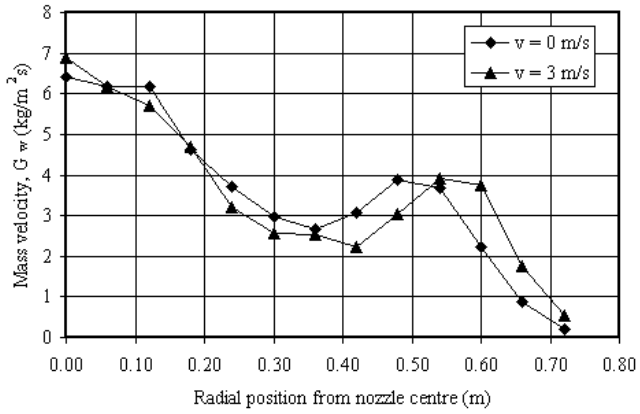

Figure Q.4 : Radial water distribution measured with and without counterflow air.

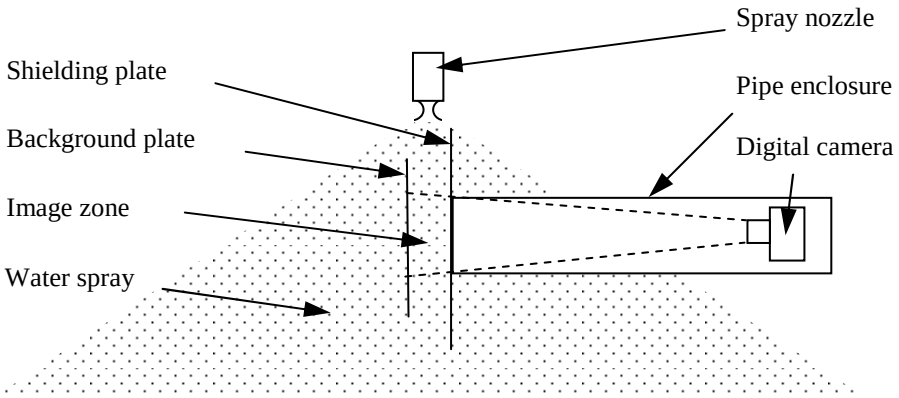

Figure Q.5 : Schematic of drop size distribution measurement apparatus.

determined and the Sauter mean diameter, d_{32} (ASTM E799-92), calculated accordingly. Moussiopoulos and Ernst (1987) used the Sauter mean diameter for modelling the performance of spray cooling ponds and found good agreement with field measurements. This diameter definition is therefore also used for modelling the performance of spray zones.

The mass fraction Y_d, is defined as the mass of drops of which the diameters are greater than diameter d as a fraction of the total drop mass.

Figure Q.6 shows the cumulative distribution of Y_d for the medium pressure nozzle obtained without air flow. The distribution shows that 60% of the total mass has a drop size larger than 3.5 mm and that the largest drops are in the order of 7.8 mm. The corresponding Sauter mean diameter is d_{32} = 3.25 mm.

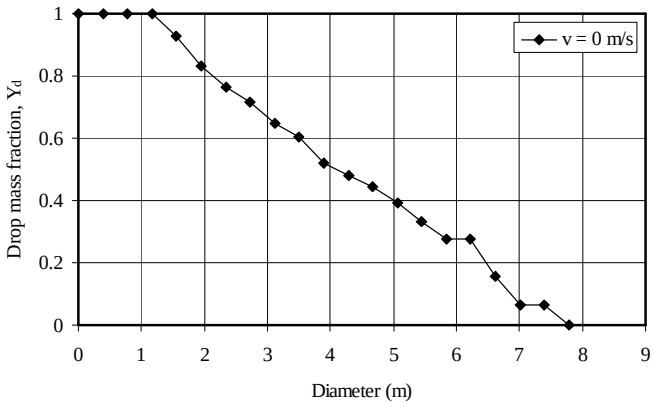

Figure Q.6 : Cumulative drop mass fraction (Y_d) distribution for a medium pressure nozzle.

Q.4 SINGLE NOZZLE SPRAY SIMULATION MODEL

Two different single nozzle spray models were developed, where the first model assumes that the drops exit the nozzle at constant velocity, and the second assumes a constant injection angle. Calculating the drop trajectory and temperature change of a single drop with given initial conditions by means of the single drop motion and heat transfer models presented in Appendices B and C respectively, forms the basis of all these models.

Two different numerical models were developed to model the effect of different cooling tower operating conditions and installation parameters on the nozzle spray. The following assumptions are made: all drop trajectories originate from a single point; there are no drop collisions; each drop exists and interacts with ambient air in the same way as a single drop; the ambient air temperature remains constant; the relative humidity of ambient air remains constant; the air speed remains uniform and constant; the drop diameter remains constant and the drop diameters are uniform. The common user input data required for these models includes the following: the ambient air temperature, the ambient air wet bulb temperature, the atmospheric pressure, the vertical air speed, the drop diameter, the nozzle to fill height, the time step, the spray diameter, the number of spray trajectories, and the water mass velocity of each spray trajectory.

The spray diameter at the fill level is sub-divided into evenly spaced concentric rings, where the number of incremental rings is equal to the number of spray trajectories. The end position of each trajectory lies on the central circle of a ring element and the mass velocity of each trajectory is used to calculate the number of drops represented by each trajectory. The drop temperature change along each trajectory, as well as the total mass and energy transfer is then calculated.

The constant initial speed model is one of the two models, which assumes that all the drop trajectories have the same initial drop speed given as input by the user.

The model iterates the angle (θ) at which each trajectory leaves the nozzle until the required trajectory end positions on the fill are obtained.

The other model is the constant initial angle model, which assumes that all the drop trajectories have the same initial angle (θ) given as input by the user. The model iterates the initial drop speed of each trajectory so that the required trajectory end position on the fill is obtained.

Figure Q.7 shows the drop initial conditions at the nozzle outlet obtained from the two different models when simulating the medium pressure nozzle, where each symbol on the curves represents the trajectory for a given concentric ring. The Sauter mean diameter calculated from the measured drop size distribution data was used to simulate the drops.

Different types of nozzles have different mechanisms of spraying water and can therefore be simulated with different drop initial conditions. The medium pressure nozzle investigated in this paper is found to be best represented by the constant speed code which is subsequently used for the spray simulations in the following sections.

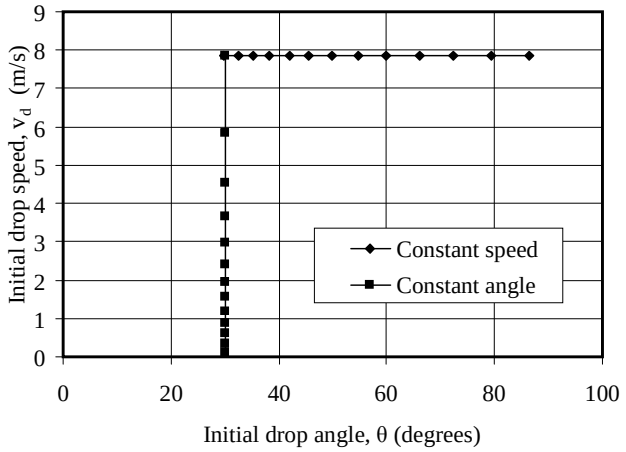

Figure Q.7. Drop initial angle and speed at nozzle outlet for the different codes.

Q.5. WATER DISTRIBUTION PREDICTION BY SUPERPOSITION

A computer model is developed which uses the experimental water distribution or numerical simulation data of a single nozzle to obtain the overall water distribution produced by a grid of nozzles, by means of superposition. The distance between the nozzles can be varied to find the optimal nozzle spacing based on the most uniform water distribution obtained. As the code uses single nozzle data, it does not take into account certain interference effects caused by the overlapping of spray patterns from adjacent nozzles, such as: drop collision, drop coalescence and airflow disturbances, which could have a noticeable affect on the water distribution.

This code requires single nozzle water distribution data and nozzle spacing as input data. The mass velocity for the single nozzle in terms of local co-ordinates is then defined as

$$G_{w,Local}(x,y) = f_1(x,y) \qquad \text{(Q.2)}$$

The overall water distribution produced by the overlapping sprays from four nozzles is calculated by superimposing the water distribution data of the four single nozzles using equation (Q.3). This is done by converting the local co-ordinates (x,y) to global co-ordinates (X,Y) and then summing the mass velocities to obtain an overall water distribution matrix in terms of the global co-ordinate system. For a grid of m x n nozzles with nozzle spacing L, the water mass velocity is therefore expressed as

$$G_{w,Global}(X,Y) = \sum_{i=0}^{m-1}\sum_{j=0}^{n-1} G_{w,Local}(X - iL, Y - jL) \qquad \text{(Q.3)}$$

The optimal distribution is obtained when the standard deviation is minimized.

Figure Q.8 shows that the water distribution along a section between two nozzles, determined by superposition of single nozzle experimental data, compares favourably with corresponding measured data of a four nozzle arrangement for both the no air flow case and the v_a = 3 m/s case.

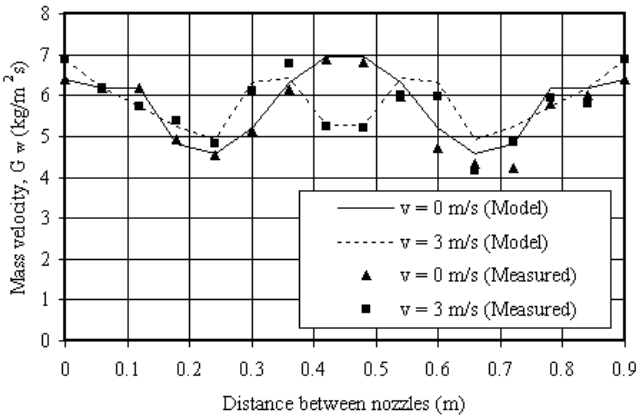

Figure Q.8 : Water distributions obtained by superimposing single nozzle water distributions.

Q.6 NOZZLE SPRAY CFD SIMULATION

The commercial CFD code *FLUENT*® (version 6.2.16) is used to simulate a spray zone produced by four nozzles. The advantage of using CFD is that the interaction between the drops and the continuous phase can be modelled, thus taking the respective changes in continuous phase temperature, velocity and humidity ratio into consideration, providing a more realistic solution.

Firstly, a single nozzle is simulated three-dimensionally using the drop initial conditions at the nozzle outlet as obtained with the aid of the single drop trajectory models of Section Q.4.

An Eulerian model is adopted for the continuous gaseous phase (mixture of air and water vapour) flow and a Lagrangian model for the discrete phase (water drop) flow, dispersed in the continuous phase to simulate the spray.

For the continuous phase, the conservation equations for mass, momentum, energy and species mixing and the standard k-ε turbulence model are solved by employing the double precision, steady state, segregated solver and the SIMPLE algorithm for the pressure-velocity coupling. Second order discretization is employed for all the governing equations.

For the discrete phase (DP), the trajectories of the drops as well as the heat and mass transfer to or from them are calculated by numerical integration of the governing motion and energy equations, with two-way interaction between the continuous and discrete phases. The air-side flow resistance due to the spray zone is solved directly by *FLUENT*®.

Firstly, a converged solution is obtained for the air flow without any spray interaction. To validate the CFD results, the discrete phase model is then superimposed onto this air flow solution, to be directly comparable with the single drop model results. The discrete phase model injections are defined using the initial spray angles, spray speeds and mass flows as calculated with the constant speed model. This is used to define a number of concentric conical spray sheets consisting of drops with a uniform Sauter mean diameter. These injected cones then form the spray model that is solved in conjunction with the continuous phase. After validation, the model is solved with discrete phase model and continuous phase interaction.

The spray zone can be simulated for the required number of single spray nozzles where the optimal spacing can be calculated with the aid of the superposition code. From the CFD simulation the air side pressure drop over the spray zone, water temperature change and mass transfer rate in the spray zone are obtained. Figures Q.9 shows the air velocity vectors and drop trajectories on a vertical plane between two nozzles.

Q.7 SPRAY ZONE PERFORMANCE CHARACTERISTICS

The modelling procedure described above is used to simulate a down spraying spray zone at different water and air mass velocities as well as different Sauter mean diameters.

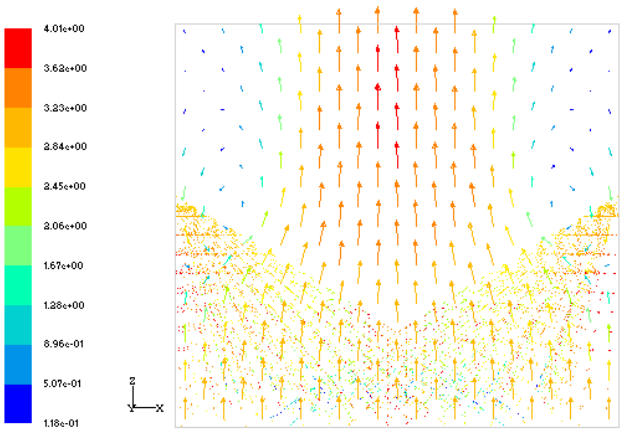

Figure Q.9 : Drop trajectories and air velocity vectors for a grid of down-spraying nozzles.

The heat and mass transfer is presented by the transfer characteristic which is obtained by solving the following Merkel equation by means of the four point Chebyshev integral, as presented in Kröger (2004):

$$Me_{sp} = \frac{h_{dsp} a_{sp} L_{sp}}{G_w} = \int_{T_{wo}}^{T_{wi}} \frac{c_{pw} dT_w}{(i_{masw} - i_{ma})} \qquad (Q.4)$$

The air-side pressure drop data is presented by a loss coefficient defined as

$$K_{sp} = \frac{2\Delta p_{tsp}}{\rho_a v_a^2} \qquad (Q.5)$$

All the CFD spray simulations in this paper are based on the constant initial drop speed approach, a nozzle spacing of 0.9 m, the water distribution data measured without air flow, as presented in Fig. Q.3, and a spray zone depth of L_{sp} = 0.47 m. The simulations are performed at the following conditions assumed typical for a natural draught wet-cooling tower: atmospheric pressure of p_a = 101325 Pa, ambient temperature of T_a = 305 K and a relative humidity of φ_a = 100%. The water inlet temperature was T_{wi} = 313 K. The following cases are investigated: water mass velocities of G_w = 1.5, 3.5 and 5.5 kg/m^{2}s; air mass velocities of G_a = 1.16, 2.32 and 3.48 kg/m^{2}s and a Sauter mean diameter of d_{32} = 3.25 mm.

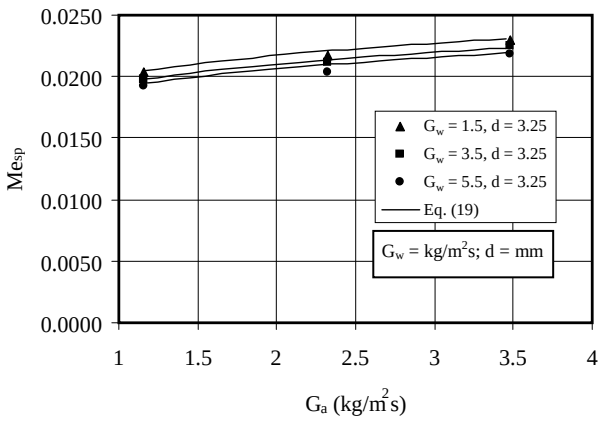

Figure Q.10 : Spray zone Merkel number for different air and water mass velocities.

Figure Q.10 shows that the Merkel number and the effect of water and air mass velocities on Merkel number are relatively small for this specific nozzle.

The Merkel number data is correlated in terms of Sauter mean drop diameter and air and water mass velocity to yield the following relation applicable to the spray zone simulated:

$$Me_{sp} = \frac{h_{dsp} a_{sp} L_{sp}}{G_w} = 7.54\times10^{-6} G_a^{0.11} G_w^{-0.04} d^{-1.38} \qquad \text{(Q.6)}$$

Figure Q.11 shows the loss coefficients for different air and water mass velocities as well as drop diameters. As the drop diameter decreases the pressure drop over the spray zone increases due to the larger number of drops in the domain.

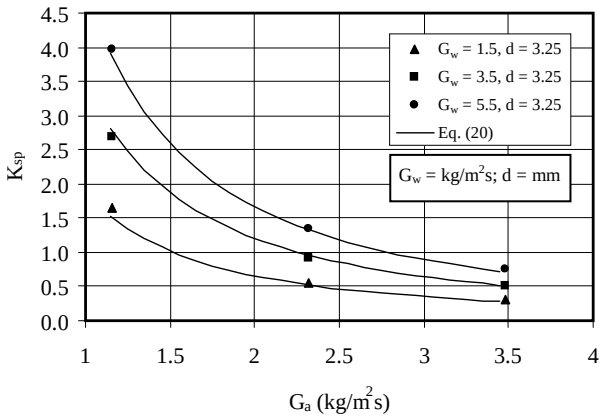

Figure Q.11 : Spray zone Loss coefficient for different air and water mass velocities.

The loss coefficient data obtained is correlated in terms of Sauter mean drop diameter and air and water mass velocity to yield the following relation:

$$K_{sp} = 0.0065 G_a^{-1.54} G_w^{0.72} d^{-0.94} \qquad \text{(Q.7)}$$

Similar results were obtained from measured flow distribution data by using the single drop model presented in Appendices B and C. Since the drop trajectories and mass flow rate assigned to each representative trajectory leaving a specific nozzle have been determined above, the Merkel number of a single nozzle spray zone can also be determined in terms of local coordinates on the plane of the flow distribution measurements, written as

$$Me_{sp,Local}(x,y) = f_2(x,y) \qquad \text{(Q.8)}$$

For a grid of nozzles, the Merkel number can be superimposed and written in terms of global coordinates as

$$Me_{sp,Global}(X,Y) = \frac{\sum_{i=0}^{m-1}\sum_{j=0}^{n-1} Me_{sp,Local}(X-iL,Y-jL)\, G_{w,Local}(X-iL,Y-jL)}{\sum_{i=0}^{m-1}\sum_{j=0}^{n-1} G_{w,Local}(X-iL,Y-jL)} \qquad (Q.9)$$

The mean spray zone Merkel number can then be determined from

$$Me_{sp} = \frac{\int_{Y_1}^{Y_2}\int_{X_1}^{X_2} Me_{sp,Global}(X,Y)\, G_{w,Global}(X,Y)\, dXdY}{\int_{Y_1}^{Y_2}\int_{X_1}^{X_2} G_{w,Global}(X,Y)\, dXdY} \qquad (Q.10)$$

Similarly the specific loss coefficient of a single nozzle spray zone can be written in terms of local coordinates on the plane of the flow distribution measurements as

$$\left(\frac{K}{G_w}\right)_{sp,Local}(x,y) = f_3(x,y) \qquad (Q.11)$$

For a grid of nozzles, the specific loss coefficient in terms of global coordinates becomes

$$\left(\frac{K}{G_w}\right)_{sp,Global}(X,Y) = \frac{\sum_{i=0}^{m-1}\sum_{j=0}^{n-1}\left(\frac{K}{G_w}\right)_{sp,Local}(X-iL,Y-jL)\, G_{w,Local}(X-iL,Y-jL)}{\sum_{i=0}^{m-1}\sum_{j=0}^{n-1} G_{w,Local}(X-iL,Y-jL)} \qquad (Q.12)$$

The mean spray zone Merkel number can then be determined from

$$\left(\frac{K}{G_w}\right)_{sp} = \frac{\int_{Y_1}^{Y_2}\int_{X_1}^{X_2}\left(\frac{K}{G_w}\right)_{sp,Global}(X,Y)\, G_{w,Global}(X,Y)\, dXdY}{\int_{Y_1}^{Y_2}\int_{X_1}^{X_2} G_{w,Global}(X,Y)\, dXdY} \qquad (Q.13)$$

Q.8 CONCLUSIONS

A method to simulate cooling tower spray zones using CFD is presented in this study. Experimental data, a single nozzle computational spray model, a superposition model and a CFD model are used to simulate down-spraying spray zones for different air and water mass velocities as well as Sauter mean drop diameters. The Merkel number and loss coefficient obtained from the simulation data were correlated for a down-spraying spray zone. These correlations make provision for different air and water mass velocities as well as drop diameters but do not take variation in spray zone depth into consideration. Furthermore they are specific to the nozzle tested and will differ for other nozzle types e.g. low pressure nozzles. Since it is virtually impossible to accurately measure spray zone performance, the approach described in this paper provides a fairly simple but effective method to obtain spray zone performance characteristics.

Finally, a model is proposed with which the spray zone Merkel number and specific loss coefficient can be determined from measured drop size, flow distribution and nozzle pressure data using the single drop numerical model developed in Appendices B and C.

R

INVESTIGATION OF THE EFFECT OF TURBINE EXHAUST PRESSURE ON POWER PLANT PERFORMANCE

R.1 INTRODUCTION

Cooling system performance has a significant effect on the efficiency of a power plant. To verify this, heat balance diagrams were obtained for two power plant units which have the same boilers, and high pressure (HP) and intermediate pressure (IP) steam turbine cylinders but different low pressure (LP) steam turbines and LP regeneration heat exchangers, optimised for different steam turbine exhaust/ condenser pressures. This provides a special opportunity to investigate the effect of the steam turbine exhaust pressure on the generator output and subsequently the efficiency of real power plants.

In the following section, data obtained from these heat balance diagrams are presented and used to determine the percentage changes in gross efficiency and condenser load per unit change in saturation temperature of the turbine exhaust steam.

R.2 GROSS EFFICIENCY AND CONDENSER LOAD VARIATION PERCENTAGE WITH STEAM TURBINE EXHAUST STEAM TEMPERATURE CHANGE

Table R.1 shows the comparison between the relevant performance data of the two cycles. It is found that the percentage change in gross efficiency per unit change in saturation temperature of the steam turbine exhaust/ condenser steam is $(\Delta\eta_{gross}/\ \eta_{gross}) / \Delta T_{cond}$ x 100 % = -0.34 %/K and that the condenser load variation is $(\Delta Q_{out}/\ Q_{out}) / \Delta T_{cond}$ x 100 % = 0.26 %/K. Figure R.1 shows the expansion curves of both steam turbines, where it can be seen that the curves lie close to each other except for the section between the steam turbine exhaust and the last LP steam turbine extraction which deviate due to the different number of LP turbine stages.

Table R.1: Power plant performance data

Description	Symbol	Units	ST 1	ST 2	Diff.	Dev.
Total heat input	Q_{in}	MW_{th}	1.000	0.987	0.0134	1.36 %
Generator output	P_{gross}	MW_{e}	0.452	0.416	0.0361	8.68 %
Total heat output	Q_{out}	MW_{th}	0.543	0.574	-0.0316	-5.50 %
Gross efficiency	η_{gross}	%	45.2 %	42.2 %	3.0%	7.23 %
Condenser pressure	P_{cond}	kPa	5.5	16.1	-10.6	-65.84 %
Condenser temperature	T_{cond}	ºC	34.5	55.4	-20.94	

R.3 CONCLUSIONS

From the above results it follows that a decrease in steam turbine exhaust pressure corresponding to a 3 ºC change in saturation temperature results in a 1 % increase in the gross power plant efficiency and a 0.8 % decrease in condenser heat load.

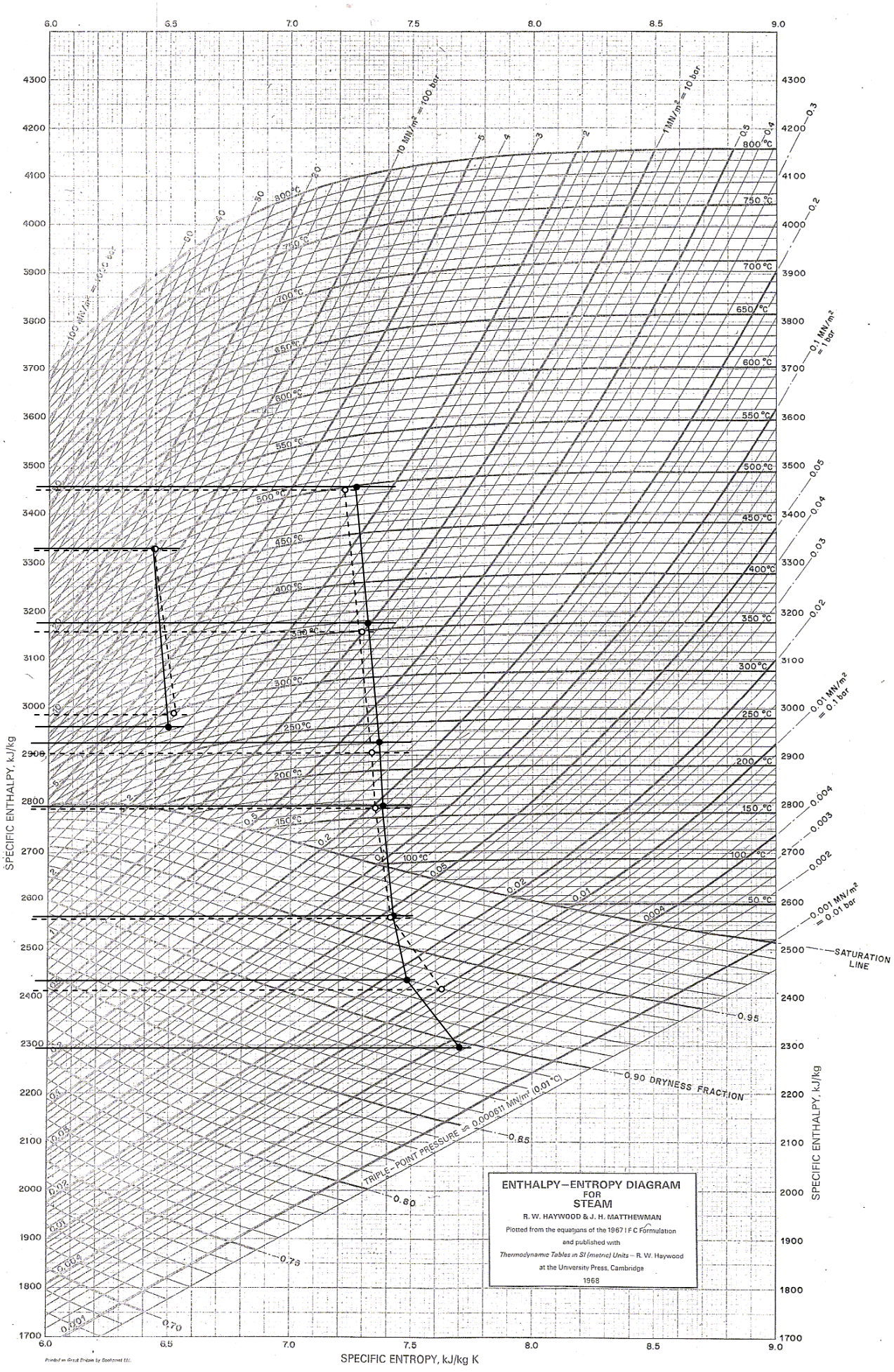

Figure R.1: Expansion curves of the LP cylinders of two power plants drawn on a Mollier diagram.